Doctoral Dissertation

博士論文

High-Precision Motion Control for Nonminimum Phase Systems with Applications to Positioning Stages

（非最小位相系に対する精密位置決め制御法と位置決めステージへの応用）

by

37-157069 **Wataru Ohnishi**

Dissertation Submitted to

Department of Electrical Engineering and Information Systems

for the Degree of

Doctor of Philosophy

at

The University of Tokyo

December 2017

Supervisor:

Professor Hiroshi Fujimoto

邦文概要

精密位置決め技術は，半導体や液晶パネル製造装置をはじめ，工作機械，産業用ロボット，ハードディスク装置などに欠かせない技術である。その高速高精度の位置決め性能が製品の性能に直結しており，その要求性能は年々厳しくなっている。このような装置は，目標値追従特性と外乱抑圧性能を両立させるため，フィードフォワード制御器とフィードバック制御器をあわせ持つ 2 自由度制御を行うのが一般的である。そこで，制御対象が非最小位相系である場合，高性能なフィードバック制御器，フィードバック制御器を設計することが難しくなるという課題がある。非最小位相系は，i) 不安定零点を持つ系，ii) 遅延を持つ系，に大別される。

第 1 章においては，序論として精密位置決め制御の背景を述べた。そして，非最小位相系がもたらす制約を，理論と応用の両方の観点から述べた。さらに，メカトロ機器の制御に用いられるディジタル制御が本質的に持っている零次ホールドによって生じる不安定な離散化零点が問題であることを述べた上で，その厳密な安定逆系の設計法であるマルチレートフィードフォワード制御法について概観した。そして，本博士論文の概要を述べた。

本博士論文は，第 I 部において，i) 不安定零点 を持つ制御対象へのフィードフォワード制御法について述べた。また，第 II 部において，ii) 遅延 を持つ制御対象の例としてとりあげた空気圧アクチュエータを用いた入力遅延と内部遅延の補償法を述べた。

第 I 部の第 2 章においては，無限時間の Preview (未来の軌道を予見すること) と Preactuation (指令値が変化するより前に制御入力を印加すること) および，マルチレートフィードフォワード制御によりあらゆる零点配置の制御対象に対し完全追従することが可能な制御法 Preactuation Perfect Tracking Control (PPTC) 法を提案した。本手法は，離散時間系の零点には，1) 連続時間系の零点由来の真性零点，2) 離散化により生じる離散化零点，の 2 つがあることに着目し，それを別々に補償することが特徴である。第 3 章においては，Preactuation を有限時間行うことを考え，Preactuation 中の出力を最適化し，Preactuation 後の完全追従を達成する手法を提案した。実際に軌道が印加される際の追従誤差が重要な半導体・液晶製造装置や工作機械において特に有効な手法である。さらに第 4 章においては，制御入力とプラント出力の制約を陽に考慮したうえで，最短時間 Preactuation 法を提案した。本手法により，Preactuation 時間と位置決め誤差，必要な制御入力のトレードオフの中で，要求仕様を満たす最短の Preactuation 時間を導出することが可能となった。また，第 5 章においては，Preactuation を一切用いないという条件の上で，制御入力の制約・プラント出力の制約を満たした最適な状態変数軌道生成法を提案し，従来の近似逆系に基づく

手法に比べて優れていることを示した。第 6 章においては，従来では高次モデルを用いることにより低下していた数値的安定性を，モード正準系を用いることにより向上させる手法を提案し，サンプル点間応答が改善する利点もあることを示した。

第 II 部においては，リニアモータの重量増大により，大型化が頭打ちになっている精密位置決めステージの現状を踏まえ，リニアモータを空気圧アクチュエータに置き換えるための制御手法を提案した。空気圧アクチュエータは精密位置決めステージの軽量化・低価格化・低発熱化に大いに有用であるが，入力遅延や内部遅延による位置依存・無限次の共振により高帯域なフィードバック制御ができず，精密位置決めに使われることは少ない。そこで，第 7 章では入力遅延に着目し，純積分器を持つ制御対象にも適用可能な修正スミス法を提案・適用した。スミス法は通常漸近安定な制御対象にしか用いることができず，また軌道追従制御問題に用いられることは少ない。実際の空気圧駆動ステージに適用し，位置決め誤差が改善されることを確認した。本手法は，空気圧アクチュエータのみならず，通信を介するために遅延がある制御対象や化学プラントなど広く適応可能である。さらに第 8 章では，空気圧アクチュエータのチャンバ長依存でかつ無限個存在する共振モードを，波動方程式を用いて内部遅延によりモデル化した。さらに，通常波動方程式では考慮することが難しいダンピングもモデル化する手法を示した。次に，このモデルから共振モードのみを取り出す操作を行い，その逆系を求めることで，波動方程式に起因する全ての共振モードを相殺するフィルタを提案した。本手法は，空気圧アクチュエータのみならず，柔軟ビームなど機械共振を持つ系にも適用可能である。

第 9 章では，本論文を振り返り，本論文の位置づけを述べた。提案した PPTC 法とその発展による不安定な真性零点の補償法，モード正準系に基づくマルチレートフィードフォワード制御法による不安定な離散化零点補償法を振り返り，精密位置決めステージを用いたシミュレーション・実験の結果から，提案手法が従来手法に対し大いに優れていると結論づけた。また，提案した入力遅延補償や内部遅延による位置依存の共振補償の有効性が，空気圧アクチュエータを用いた実験検証で明らかになったことから，リニアモータの重量増大により大型化が頭打ちになっている精密位置決めステージ設計へのブレイクスルーを与えたと結論づけた。従来は精密位置決めのため，システムが不安定零点や遅延を持たない最小位相系になるように制約を受け機構設計を行っていた。不安定零点を持たざるをえない場合は近似逆系を用いて完全追従を諦められており，また入力遅延や内部遅延を持つ空気圧アクチュエータを用いることは精密位置決めステージにおいて避けられていた。提案した一連の不安定真性零点・離散化零点補償法，入力遅延・内部遅延補償法により，機構設計の制約を緩和し，機構設計に対し新たな選択肢を提示できたと言える。

なお，本文は英語により記述されていることを付記する。

Acknowledgments

I would like to express my sincere gratitude to my supervisor, Professor Hiroshi Fujimoto for his advice, encouragement, and continuous support. He offered me a lot of opportunities to collaborate with industry and to participate in academic conferences and committees. I can not imagine that I could have accomplished this work without his kind help. I am very proud to belong to the Hori-Fujimoto laboratory during the period 2012 to 2018. I have met many excellent people there.

I deeply thank Professor Yoichi Hori for giving me valuable advice on this work and influencing my way of thinking. He taught me many things, not only related to my research but also how a researcher should be. I have the utmost respect for your insight and your ability to see the big picture, not only for control engineering but also for the future society.

I thank Dr. Kazuaki Saiki, Mr. Atsushi Hara, Mr. Kazuhiro Suzuki, and Dr. Koichi Sakata, who are with Nikon Corporation. They designed brilliant experimental setups and gave me helpful advice. Dr. Koichi Sakata helped me a lot, not only as a collaborating company researcher but also as a *senpai* of Hori-Fujimoto laboratory. In addition, Nikon offered me the opportunity to stay at the Nikon Research Corporation of America (NRCA). I deeply thank Dr. Bausan Yuan, Dr. Ping-Wei Chang, Dr. Pai-Hsueh Yang, Mr. Alex Poon, Dr. Yeong Choi, and Mr. Sandy Lee, who are with NRCA. They provided me a very interesting topic and helped me with both software and hardware. Dr. Bausan Yuan, Dr. Ping-Wei Chang, and Dr. Pai-Hsueh Yang are role models of control engineers to me. I would like to thank Mr. Nobutaka Magome, senior vice president of NRCA, who helped a lot with the paperwork and took care of my daily life in the U.S.A. I will never forget the total solar eclipse I observed with him. My stay for two times two months at NRCA changed my way of thinking.

I appreciate all members of the committee for precision servo systems (PSS) of IEE Japan, where I served as a secretary assistant. They gave a lot of feedback about this work from the viewpoint of both motion control theory and industrial applications.

I want to express my gratitude to Professors Yoichi Hori, Tatsuaki Hashimoto, Takafumi Koseki, Jumpei Baba, and Shin-ichiro Sakai of the University of Tokyo, who are members of the judging committee of my doctoral degree together with Professor Hiroshi Fujimoto. Their constructive comments in the preliminary judging meeting helped me a lot to improve this dissertation.

I am greatly thankful to the graduated and current members of my laboratory. Discussions with my colleagues Dr. Takayuki Shiraishi, Dr. Takayuki Miyajima, Dr. Hongzhong Zhu, Dr. Masato Kanematsu, Dr. Daisuke Gunji, Dr. Motoki Sato, Mr. Thomas Beauduin, Dr. Giorgio Lovison, Mr. Katsuhiro Hata, Mr. Yuma Yazaki, Mr. Shota Yamada, Mr. Tomoki Emmei, Mr. Yoshi Ri and all members of my laboratory, always stimulated me. Mr. Thomas Beauduin helped a lot with the system identification of the setup and the daily talks with him changed my way of thinking. I thank Ms. Yoko Matsushima, Ms. Kimiko Ueno, and Ms. Reina Imaizumi as Professor Fujimoto's secretaries for their sincere work. I appreciate the friendship with Dr. Takahiro Nakamura, who I know from EEIC in Komaba campus. I enjoyed my Ph.D. candidate life with him.

This dissertation would not have been possible without the financial support of the Japan Society for the Promotion of Science (JSPS), where I am supported as a research fellow. A part of this work was supported by JSPS KAKENHI Grant Number 15J08488.

Finally, I would like to thank my wife and my parents for their continuous encouragements and support.

Wataru Ohnishi

The University of Tokyo

December 2017

Contents

List of Figures

Chapter 1

Introduction

1.1 Back ground of high-precision motion control

High-precision motion control has an important role in the industry. Because motion accuracy and throughput are crucial factor for product quality and price, faster and more precise positioning are continuously required. It has a key role in, for instance, wafer scanner [1–3], flat panel display (FPD) scanner [4, 5], hard disk drives (HDD) [6], optical drive [7, 8], atomic force microscope (AFM) [9, 10], printing system [11,12], machine tools [13,14], galvano scanner [15], satellite [16], industrial robot [17], packaging machinery [18].

Literature [19] [20] mentions the design phases of motion control are:

1. design of reference trajectory;
2. design of controller to track the reference trajectory;
3. design of transient or settling controller to minimize the tracking error caused by various unmodeled dynamics or unpredicted plant fluctuations; and
4. design of controller to suppress external disturbances to ensure the controlled object remains on the target position.

To achieve a high-performance in all four phases, two-degrees of freedom control design, which consists of feedforward and feedback controllers, is important.

In phase 1, polynomial trajectories (including SMART trajectory [21]), Bézier curves, B-spline curves are widely used [22] for reference trajectory generation. Phase 1 also includes input shaping [23–25] to reduce plant vibration excited by the original reference signal, and reference governor [26–29], which is taking into account of constraints.

In phase 2, model-based or data-based feedforward controllers are used. The key of model-based feedforward controller is the inversion of a plant model [30] (see Part I for detail). Model-based

feedforward control also includes finite-state control (FSC) [31]. FSC and its extension methods are applied to HDD [32, 33], galvano scanner [15], and scanning stage [34, 35].

Phase 3 and 4 include feedback control design from classical control to modern control and further, with long history (see i.e. [20, 36–38]). Mechanical resonances, delays, unstable zeros (non-collocated system), model uncertainty limit the feedback control bandwidth. For mechanical resonances, notch filters and phase stabilization techniques [39, 40] are widely applied. Variable gain approach [2, 41], which is one of nonlinear control approach, is proposed to overcome the limitations of linear control scheme [36]. To deal with uncertainty of the plant and design less-conservative robust controller, connecting system identification and robust control approach is proposed [42].

One of the recent trends is utilizing additional sensors and actuators compared to rigid-body design approach (the numbers of sensors and actuators are same as motion degrees of freedom). Additionally, the high-resolution encoder becomes cheaper [17]. Hence, vibration suppression control methods for two-mass system using multiple encoders [43] and high-resolution encoder [44] are proposed. Active damping using additional actuators is proposed [45, 46]. Compared to the traditional notch filters, active damping leads to a faster decay of the vibration modes.

To minimize the cost and effort of mechanical design and controller to maximize the performance, integrated design of mechanism and control approaches are proposed [47–51]. Mechanical systems are designed to be minimum phase and have less delay as much as possible to have better feedback/feedforward performance. This is, in other words, constraints for a design of a system. The motivation of this thesis is to relax the constraints by control algorithms and to present new options for system design.

1.2 Effect of nonminimum phase systems

1.2.1 Definition of nonminimum phase systems

Systems with no unstable zeros or time delays are called “minimum phase systems”. Minimum phase systems have a unique relationship between the gain and phase of the frequency response, called the phase formula [36]. In other words, the minimum phase systems have the minimum possible phase lag for the given magnitude response.

On the other hand, systems with unstable zeros and/or time delays are called “nonminimum phase systems”. Compared to the minimum phase systems, nonminimum phase systems have an additional phase lag with the same gain. For each nonminimum phase system $G_{nmp}(s)$, there exist and all-pass system $G_{ap}(s)$ and a minimum phase system $G_{mp}(s)$ such that $G_{nmp}(s) = G_{ap}(s)G_{mp}(s)$ [36]. An

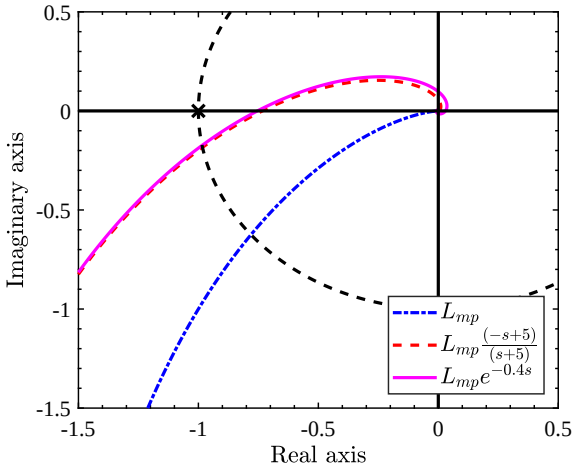

Figure 1.1 Reduced phase margin of the nonminimum phase systems. $L_{mp} = \frac{2}{s(s+1)}$.

example of an all-pass system with unstable zero is

$$G_{ap1}(s) = \frac{-s+a}{s+a}, \tag{1.1}$$

where $a > 0$. $|G_{ap1}(s)| = 1$ for all frequency, but $\angle G_{ap1}(s) = -2\arctan(\omega/a)$ [rad]. Similar thing can be said for the time delay.

$$G_{ap2}(s) = e^{-\tau s}, \tag{1.2}$$

where τ denotes the delay time [s]. $|G_{ap2}(s)| = 1$ for all frequency, but $\angle G_{ap2}(s) = -\omega\tau$ [rad]. These all-pass filters with unstable zeros or time delays contribute the additional phase lag compared to the minimum phase systems and reduce the phase margin (Fig. 1.1).

1.2.2 Limitations of system with unstable zeros

The zeros of the continuous-time system are determined by the matrices $\boldsymbol{A}, \boldsymbol{b}, \boldsymbol{c}$ in the state space representation of the plant. In other words, besides the dynamics of the plant, the arrangement of the sensors and the actuators also have a role in determining the zeros [52]. It is known that, for instance, the wafer stage of a semiconductor exposure apparatus [1], a hard disk drive (HDD) [53], a boost converter [54] have unstable zeros in continuous-time domain as shown in Fig. 1.2. In these cases, the unstable intrinsic zeros are generated by discretization. On the other hand, even when there is no unstable zero in the continuous time transfer function, the discretization zero is unstable when the relative degree is greater than two [55]. It is also clear from the Euler-Frobenius polynomials with a short-sampling time assumption [56–58] listed in Tab. 1.1. Therefore, the inverse system of the plant becomes unstable and perfect tracking control (PTC) cannot be achieved with the single-rate system framework [59].

Table 1.1 Zeros of Euler-Frobenius polynomial [58].

Relative order	Zeros
2	-1
3	$-2-\sqrt{3}$, $1/(-2-\sqrt{3})$
4	$-5-2\sqrt{6}$, -1, $1/(-5-2\sqrt{6})$
⋮	⋮

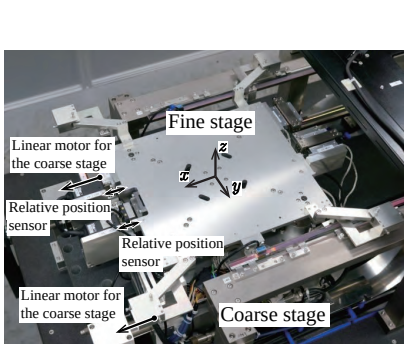

(a) High-precision positioning stages.

(b) Hard disk drives.

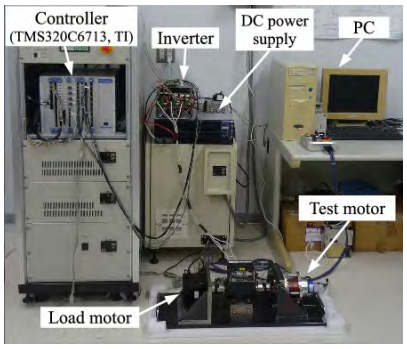

(c) Motors and converters.

(d) Robots.

(e) Cars (backward driving [60]).

(f) Aircraft (elevator deflection to pitch angle) [61].

Figure 1.2 System with unstable zeros (Photographs are from [62]).

To balance the robustness and the response speed, it is advised to have the gain margin is grater than 2 and the phase margin is grater than 30° [38]. When we have an unstable zero at $s = a$ ($a > 0$), the acceptable control performance in the sense of integral square error (ISE) optimal is limited to $\omega_c < a/2$, approximately [38, 63]. ω_c denotes the gain cross over frequency [rad/s]. The effect of unstable zeros for the sensitivity function is known as the second waterbed formula [64, 65].

Additionally, systems with unstable zeros gives rise to an initial undershoot when stepped (Fig. 1.3) [52, 66]. It is known that the number of the zero-crossings [67, 68] is same as the number of real unstable zeros. It is undesired phenomena for the reference tracking problem. Feedforward controller for reference tracking is commonly designed by the feedforward plant-injection (FFPI) or feedforward closed-loop-injection (FFCLI) architectures [69]. In both cases, the inversion system has unstable poles

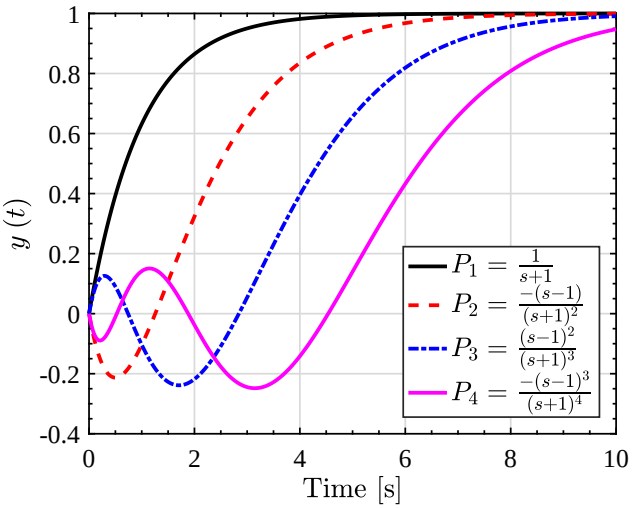

Figure 1.3 Step response comparison: P_1 is a first order transfer function without an unstable zero. P_2, P_3, and P_4 have one, two, and three unstable zero(s), respectively

and it is infeasible to implement. Therefore, approximate model-inverse methods are proposed (see Section 2.3.1). With the approximate model-inverse methods, the undershoot is inevitable because the unstable zeros remain the frequency responses from the reference r to the output y.

It is known that with preview[*1] and preactuation[*2], the tracking performance is improved [70–72]. Continuous-time approach [70, 71], ignoring the effect of zero-order hold, perfect tracking is not possible for digital control system (it is discussed in Section 2.6.6 and Fig. 2.22). Direct inversion for discrete time model, which compensate the discretization and intrinsic zeros at same time, brings high oscillations [73, 74].

1.2.3 Practical background of system with unstable zeros: high-precision positioning stages

High-precision scan stages play an important role in the manufacturing processes for semiconductors and liquid crystal displays [42, 75]. In these applications, high-precision stages have to control six degrees of freedom (DOFs: $x, y, z, \theta_x, \theta_y$, and θ_z) [76]. To reduce disturbances such as floor vibrations, contactless actuators (e.g. linear motors [1, 77] and voice coil motors [78]) and contactless gravity compensation (e.g. air bearings [79] and magnetic levitation [80–82]) are commonly used.

Since the rotation degrees of freedom are not mechanically constrained, coupling between the translational motion and rotational motion is not negligible. For instance, as shown in Fig. 1.4, the height

[*1] preknowledge of the future trajectory.
[*2] applying the control input before the command value changes.

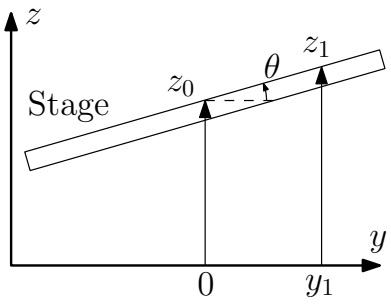

Figure 1.4 Stage z motion with coupling from θ direction.

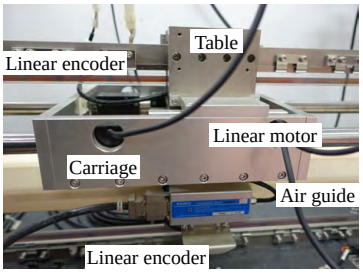

(a) High-precision positioning stage.

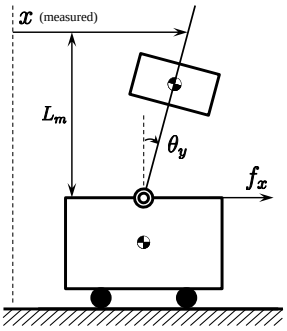

(b) Model of (a).

Figure 1.5 Experimental high-precision positioning stage and its model [83, 84].

of z_1 (point of interest) is

$$z_1 = z_0 + y_1\theta, \tag{1.3}$$

where z_0, y_1, and θ denote the height of the center of rotation of the stage, the position of the stage in y axis, and the pitching angle, respectively. Small pitching angle is assumed. Transfer function from z direction force f_z to z_1 is

$$\frac{z_1(s)}{f_z(s)} = \frac{z_0(s)}{f_z(s)} + y_1\frac{\theta(s)}{f_z(s)}. \tag{1.4}$$

Since y_1 can be positive or negative sign, the zeros of $\dfrac{z_1(s)}{f_z(s)}$ become unstable in some position [1].

Another example with unstable zeros is gantry stages shown in Fig. 1.5. The gantry stage structure is commonly used in X-Y large scale high-precision positioning stages [43,85]. The zeros of the transfer function is a function of the height of the measurement point L_m [83], e.g.

$$\frac{x(s)}{f(s)} = 3.048 \times 10^{10}\frac{(0.1228 - L_m)s^2 + 0.4102s + 3476}{s(s + 10000)(s + 1.846)(s^2 + 5.623s + 4.078 \times 10^4)}. \tag{1.5}$$

Depending on the mechanical design such as the height of the actuation point, measurement point, and the center of mass, the system can have unstable zeros. Hence, integrated design of mechanism and control approaches are proposed [47–50] to locate the zeros for the desired position from the viewpoint of control engineering. This is, in other words, a constraint for a mechanical design. The approaches proposed in Chapter 2–6 relax the constraints for mechanical design by improving the feedforward control performance utilizing preactuation and multirate feedforward control scheme.

Table 1.2 Plate size of the flat panel display manufacturing system.

Generation	4	6	8	10	10.5
Year	2000	2003	2005	2009	2018
Plate size [mm]	700×900	1500×1850	2200×2550	2880×3130	2940×3370
Ratio	1	4.4	8.9	14.3	15.7

1.2.4 Limitations of system with time delay

Systems with time delay are, for instance, chemical processes [86, 87], teleoperated systems [88], and pneumatic actuators [89]. As mentioned in Section 1.2.2, it is advised to have the gain margin is grater than 2 and the phase margin is grater than 30° [38]. When we have a time delay of τ ($\tau > 0$), the acceptable control performance in the sense of ISE optimal is limited to $\omega_c < 1/\tau$, approximately. Comparing the acceptable control performance mentioned in Section 1.2.2, the time delay τ has similar effect of unstable zero at $2/a$. It is clear from 1st order Padé approximation

$$e^{-\tau s} \simeq \frac{1 - \frac{\tau s}{2}}{1 + \frac{\tau s}{2}}, \tag{1.6}$$

which has a zero at $s = \frac{2}{\tau}$. General Padé approximation is given by [90]

$$e^{-\tau s} \simeq \frac{p_0 + p_1 s + \cdots + p_L s^L}{q_0 + q_1 s + \cdots + q_M s^M} \tag{1.7}$$

$$q_i = \frac{M!(L + M - i)!}{L!(M - i)!i!}(-\tau)^i \tag{1.8}$$

$$p_i = \frac{(-1)^i(L + M - i)!}{(L - i)!i!}(-\tau)^i, \tag{1.9}$$

where M and L denotes the order of approximations. Other approximation methods are, for instance, Laguerre approximation

$$e^{-\tau s} \simeq \left(\frac{1 - \frac{\tau s}{2L}}{1 + \frac{\tau s}{2L}}\right)^L \tag{1.10}$$

and Kauz approximation

$$e^{-\tau s} \simeq \left(\frac{1 - \frac{\tau s}{2L} + \frac{\tau^2 s^2}{8L^2}}{1 + \frac{\tau s}{2L} + \frac{\tau^2 s^2}{8L^2}}\right)^L. \tag{1.11}$$

The key issue is that time delays cannot be inverted in the causal framework.

1.2.5 Practical background of system with unstable zeros: pneumatic actuators for large-scale stages

There is a strong requirement for improving productivity for integral circuits [1] and flat panel displays [4, 91]. To improve the productivity, the size of the stage becomes larger [92–94], and the scanning speed and acceleration [1] are increased.

The required maximum force of the actuator f_{max} is about

$$f_{max} = ma_{max}, \tag{1.12}$$

where m and a_{max} denote the mass of the stage and the maximum acceleration of the reference trajectory. Considering that m becomes bigger by a larger stage and a_{max} becomes bigger by a higher acceleration profile, the required maximum force of the actuator f_{max} becomes bigger and bigger. This is one of the bottlenecks of the productivity improvement. The plate size of the flat panel display is listed in Tab. 1.2. It is clearly said that the plate size is reaching the ceiling.

To address the issue, a catapult stage structure, which allows both contact and separation between the fine and coarse stages, is proposed [34, 95, 96]. The fine stage of the catapult stage is lighter and simpler compared to the conventional dual-stage because the fine stage actuation is not necessary for the acceleration and deceleration regions in the scanning motion. This thesis considers replacing the linear motor in the coarse stage with a pneumatic actuator for a lighter and simpler stage. This pneumatically-actuated coarse stage can be used in the catapult configuration to create a new-generation lightweight dual stage that generates little heat and demonstrates high positioning accuracy.

A pneumatic actuator has advantages compared to a linear motor: 1) low heat generation [97], 2) high power-weight ratio [98], and 3) low cost [98]. Disadvantages include 1) time delay [99] and 2) nonlinear dynamics [100, 101] due to air dynamics and servo valves. Because of these disadvantages, pneumatic actuators are not commonly used in precision motion control applications [102]. This thesis address the problem of input delay and position dependent resonances shown in Fig. 1.6.

1.3 Review on multirate feedforward control

This section briefly reviews the multirate feedforward control. Details and notations are in Chapter 2. To address the unstable discretization zeros problem, a multirate feedforward control [103] (see Fig. 1.8) has been proposed to design stable inverse for unstable discretization zero(s) [55], which is generated by a zero-order-hold. This method generates a feedforward control input, which enables

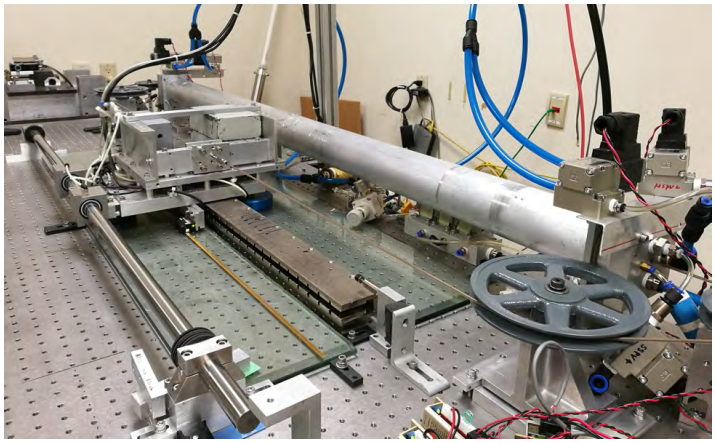

(a) Pneumatically actuated stage (see Fig. 8.1).

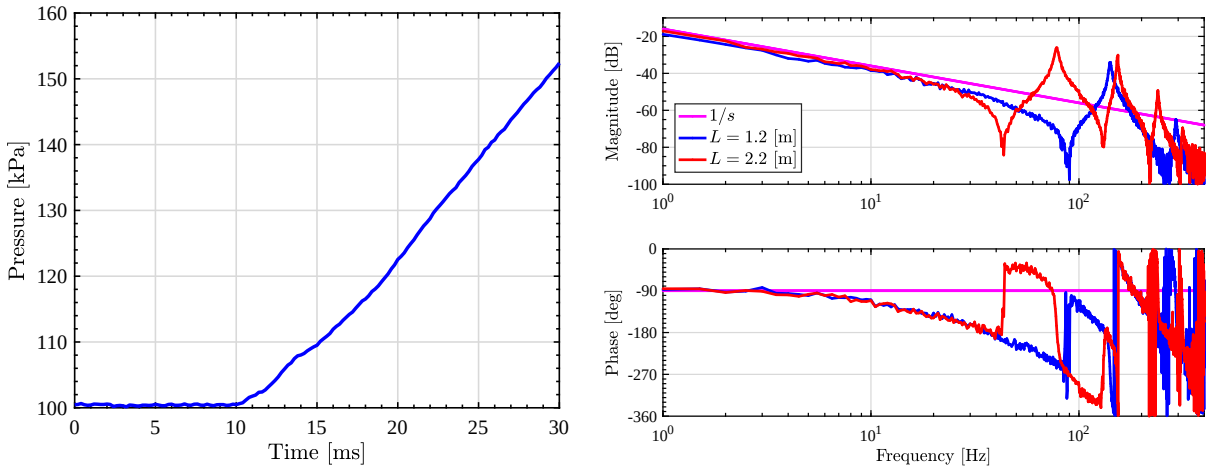

(b) Input delay (see Fig. 7.5).

(c) Position dependent resonances. (see Fig. 8.5(a)).

Figure 1.6 Challenges for high-precision motion control by pneumatic actuator.

the system to track perfectly with the desired state trajectory. The effectiveness is verified by using a dc servo motor. This method is related to the minimum-time dead-beat control [37] and the idea has a connection to the finite-state control [31,32]. Secondly, this method is extended to systems with vibrations [53, 85] (see Fig. 1.9), in other words with stable zeros in continuous-time domain. This method is named as vibration suppression perfect tracking control (VSPTC). Ishihata *et al.* have proposed a discrete-time domain design method for the multirate feedforward control. Thirdly, the multirate feedforward control is extended to have a robustness by adaptive control [104] (see Fig. 1.10) or repetitive control scheme [105] (see Fig. 1.11). Multirate feedforward and its extension is applied to, for example, HDDs [53], large-scale high-precision stages [85, 106], atomic force microscopes [107], machine tools [13], optical drives [108], and robots [109].

However, when the plant has unstable zeros in continuous time domain, the desired state trajectory diverges. Chapter 2 extends the desired state trajectory generation method to apply systems with unstable zeros in the continuous-time domain (preactuation perfect tracking control: PPTC), which is a stable inversion method for unstable intrinsic and discretization zeros without approximation.

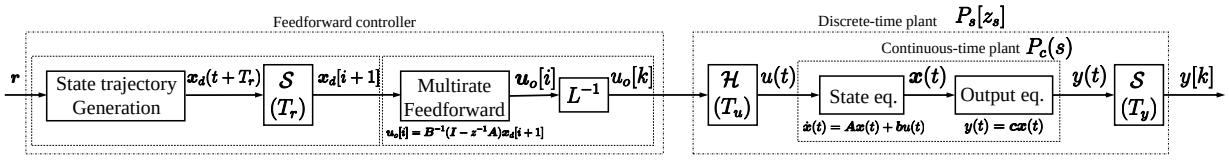

Figure 1.7 Simplified block diagram of the multirate feedforward (only feedforward path is shown). $\mathcal{S}$, $\mathcal{H}$, and L denote a sampler, holder, and lifting operator [110], respectively. z and z_s denote e^{sT_r} and e^{sT_u}, where $T_r = nT_u = nT_y$, respectively. Simply speaking, the block of the multirate feedforward is an inverse of the state equation of the plant and the block of the state trajectory generation is an inverse of the output equation. Additionally, due to the controllable canonical form realization, the continuous-time unstable zeros appear only in the output equation.

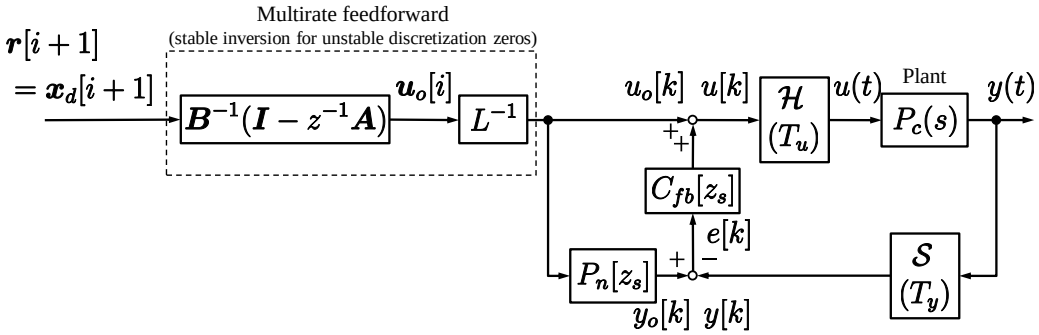

Figure 1.8 Rigid body perfect tracking control [103].

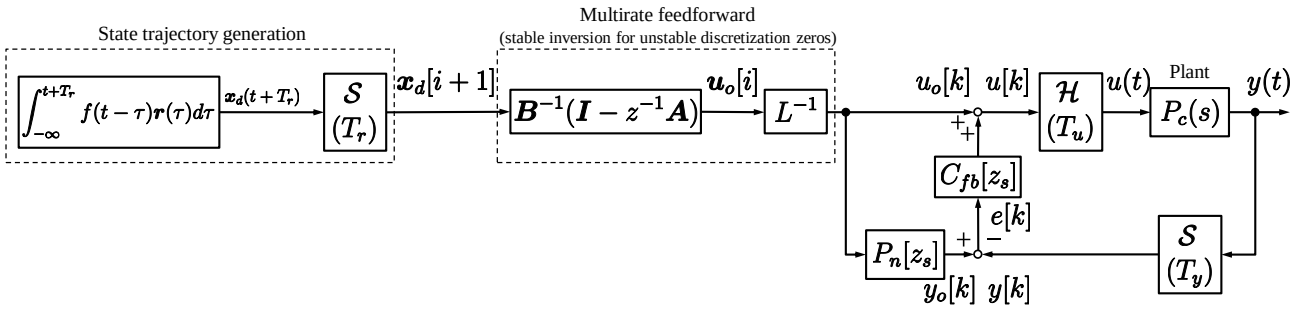

Figure 1.9 Vibration suppression perfect tracking control [111]

Additionally, Chapter 3 proposes a finite preactuation perfect tracking control (FPPTC) method, which realizes the perfect tracking after a finite preactuation. Chapter 4 proposes a minimum time preactuation considering the control input and plant output constraints. Chapter 5 proposes an optimal state trajectory generation method without preactuation.

1.4 Outline of the dissertation

The structure of this doctoral thesis is shown in Fig. 1.12.

In this thesis, in Part I, feedforward control methods to overcome the continuous-time unstable zeros are proposed. When the plant has unstable zeros in continuous-time domain, the desired state

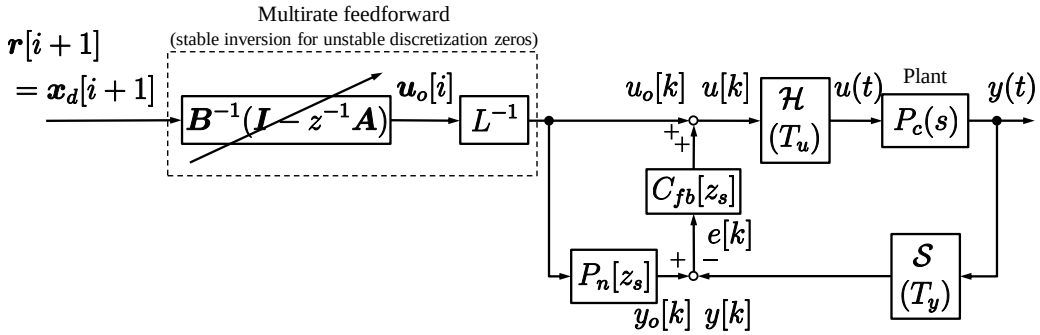

Figure 1.10 Multirate adaptive robust control (MARC) [104]

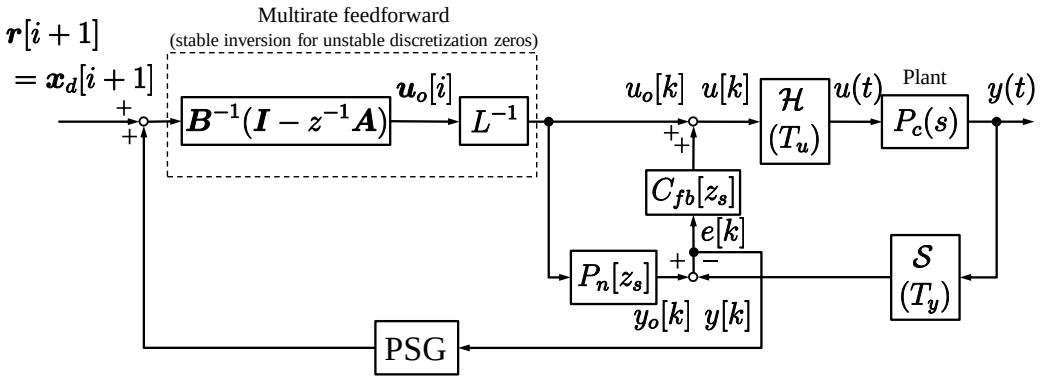

Figure 1.11 Repetitive perfect tracking control (RPTC) [13, 112]

trajectory diverges and the standard multirate feedforward control [103] cannot be applied.

Chapter 2 extends the desired state trajectory generation method to apply systems with unstable zeros in the continuous-time domain (preactuation perfect tracking control: PPTC), which is a stable inversion method for unstable intrinsic and discretization zeros without approximation. Stable inversion for unstable intrinsic zeros is performed by state variable trajectory generation by time axis reversal and imaginary axis flipping. The proposed method can be applied to any reference trajectory as long as the $(n-1)$th derivative of the reference trajectory is available (where n denotes the order of the nominal plant). Then, stable inversion for unstable discretization zeros is performed by the multirate feedforward control [103]. The point is that the problem of unstable intrinsic zeros and discretization zeros are decoupled. The perfect tracking for all time domain, in theory, is possible by infinite time preactuation. According to the experimental results, the maximum error is reduced by 93 % and 43 % compared to ZPETC method (single-rate approximated model inversion, see Section 2.3.1) and CPMI method (continuous-time preactuated model inversion, see 2.3.2), respectively.

Chapter 3 proposes a state trajectory *regeneration* method by redundant order polynomial to match the state variable after the preactuation. Although this method abandons perfect tracking during preactuation, it guarantees perfect tracking after preactuation. Moreover, the tracking error during finite time preactuation is reduced by the regenerated state trajectory obtained by the optimized

redundant order polynomial. According to the experimental results, the maximum tracking error is reduced by 66 % and 34 % compared to TSA (Truncated series approximation method, see Section 3.3) method and truncated PPTC method, respectively.

Chapter 4 proposes a minimum time preactuation method with an optimized state trajectory considering control input and tracking error constraints. The proposed method generates an optimal state trajectory for a given reference and minimum time while explicitly considering the actuator, i.e. peak force, and stroke, i.e. maximum undershoot, limitations of the system. A multirate feedforward scheme is subsequently presented to obtain a discretized control input that perfectly tracks the designed optimal continuous state trajectory. In comparison to conventional finite preactuation methods in simulation, the proposed approach reaches an order of magnitude lower tracking error bounds.

Chapter 5 proposes an optimal state trajectory *regeneration* method without preactuation. The original state trajectory, which requires the infinite preactuation, is generated by PPTC method. Then we *regenerate* the state trajectory between the start and end time of the reference motion trajectory. This method is an extension of the method proposed in Chapter 4. In the method of Chapter 4, perfect tracking after preactuation is guaranteed by regenerating the state trajectory during preactuation, whereas this method guarantees only after the end of the reference motion. The state trajectory during the reference motion is optimized with respect to the control input and plant output constraints. A multirate feedforward scheme, which is a stable inversion for unstable discretization zeros, is subsequently presented to obtain a discretized control input that perfectly tracks the designed optimal continuous state trajectory.

Chapter 6 proposes a multirate feedforward based on modal form. Multirate feedforward control has been proposed to achieve perfect tracking for a plant with unstable discretization zeros. However, multirate feedforward control requires controllable canonical form and inversion of a controllability matrix, both of which are known as numerically ill-conditioned. Chapter 6 proposes a multirate feedforward control method based on modal form to address these problems. Moreover, the intersample behavior is improved compared to the conventional full order multirate feedforward. The effectiveness of the proposed method is validated through simulation results.

In Part II, tracking control methods for pneumatically actuated stage with time delay are proposed. The aim of this part is to replace the linear motors implemented on coarse stages with the pneumatic actuator. The benefits are lightweight, low price, and low heat generation. However, it has following disadvantages: nonlinearity, delay, and position-dependent resonances. These disadvantages limit the control performance. Because of these disadvantages, pneumatic actuators are not commonly used in precision motion control applications [102].

To compensate the input delay, Chapter 7 proposes a modified Smith predictor, which can be used for

an integrative system. The proposed method achieves maximum tracking error 135 μm and standard deviation of the tracking error 19.5 μm (see Fig. 7.12 and Tab. 7.3). The results are considered as very accurate because literature [113] states that the positioning accuracy of pneumatic actuated systems is $100 - 500$ μm at best.

To compensate the position dependent resonances, Chapter 8 proposes a wave equation model, taking into account the damping of the system. Wave equation model is composed of delay elements (internal delay) and a first-order filter. Using this model, a wave cancellation filter is proposed for canceling all the resonances and anti-resonances. This filter comprises delay elements and a first-order filter. Commonly, wave equation model and controller ignores the damping terms [114–116]. The damping considerations for the controller is important for a stability analysis in frequency domain. The proposed method can model the damping of the resonances and anti-resonances separately. The experimental results indicate that -19 dB, -23 dB, and -16 dB gain attenuations are achieved for the first, second, and third modes, respectively (see Fig. 8.14(d)).

Chapter 9 reviews the proposed PPTC, FPPTC, minimum time PPTC, Optimal state trajectory generation without preactuation, multirate feedforward based on modal form, modified Smith predictor, and wave cancellation filter. Chapter 9 states strategies for compensating unstable zeros and delays and concludes the contributions of the thesis.

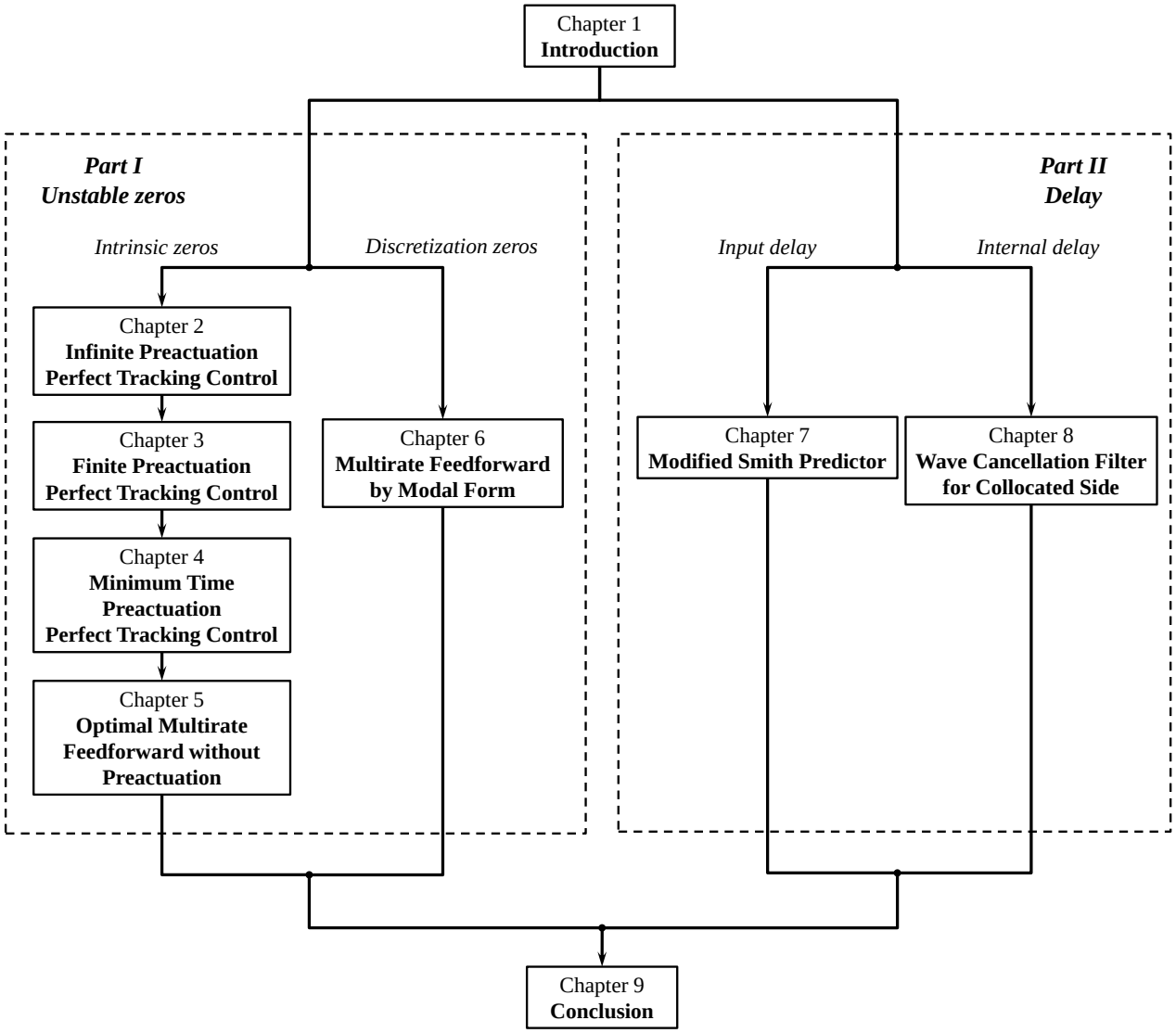

Figure 1.12 Structure of the thesis.

Part I

Trajectory Tracking Control for a High-Precision Stage with Continuous Time Unstable Zeros

Chapter 2

Infinite Preactuation Perfect Tracking Control by Multirate Feedforward and State Trajectory Generation based on Time Axis Reversal

Abstract

A plant with unstable zeros is known to be difficult to control because of the initial undershoot of its step response and the unstable poles in its inversion system. There are two reasons why a plant has unstable zeros in the discrete time domain: 1) non-collocation of actuators and sensors, 2) discretization by zero-order hold. Problem 2) has been solved by the perfect tracking control (PTC) method based on multirate feedforward control proposed by our research group. However, the conventional PTC method cannot achieve perfect tracking for a plant with continuous time unstable zeros generated by 1) due to divergence of the desired state trajectories. This chapter proposes a preactuation perfect tracking control (PPTC) method to solve problem 1) by a state trajectory generation based on a time axis reversal. This chapter verifies the effectiveness of PPTC by simulations and experiments in comparison with several single rate feedforward control methods. Additionally, this chapter clearly shows the role and importance of the multirate feedforward control by comparing a continuous-time domain approach with preactuation.

2.1 Introduction

Tracking control with zero gain and phase errors between the desired and output trajectories at every sampling point can be achieved, in theory, by model inversion (i.e. pole-zero cancellation). However,

a plant with unstable (i.e Non-Minimum Phase, NMP) zeros gives rise to an initial undershoot when stepped (Fig. 1.3) and highly oscillatory or unstable control trajectories when inverted [73, 74]. NMP zeros of discrete transfer functions can be classified as 1) intrinsic zeros proper to the plant dynamics (e.g. non-collocated placement of sensor and actuator) and 2) discretization zeros due to signal sampling (e.g. fast sampling rates) [117]. Note that, discretization zeros are unstable when the relative order of the continuous time plant is greater than two even without continuous-time unstable zeros [55].

Extensive research has been dedicated to the design of tracking control methods for systems with NMP zeros. Existing proposals can be classified as (i) approximate model-inversion methods and (ii) preactuated model inversion methods [118]. The straightforward way to implement an approximate inversion is to cancel stable poles and zeros while ignoring NMP zeros, i.e NPZI-method [30]. This approach exhibits both magnitude and phase errors, hence, zero-magnitude-error tracking control (ZMETC) [119] and zero-phase-error tracking control (ZPETC) [59] methods have been proposed and improved upon. Despite the stable control trajectory, NPZI, ZMETC, and ZPETC may not yield satisfactory tracking performance due to the approximations involved (depending on the system and performance specifications).

Preactuated model inversion can achieve perfect tracking with infinite preview (i.e. knowledge of future references) and preactuation (i.e. actuation applied a time-interval before the actual output of the system). Continuous-time domain stable inversion methods are proposed in [22, 70, 71, 120–122]. This chapter unifies these proposals as CPMI or continuous-time preactuated model-inverse methods. However, these approaches don't consider the effect of the zero-order hold. All mechatronic systems using digital control have zero order hold. There lays the key difference with the proposed preactuated multirate feedforward control. Alternatively, a discrete-time domain approach is proposed in [72], which compensates both intrinsic and discretization unstable zeros, simultaneously. This method can achieve perfect tracking at each sampling point, but could cause high oscillations in the inter-sampling behavior by direct cancellation of the discretization zeros [73, 74]. For high-precision motion systems such as wafer scanners and printing systems, preactuation methods are actively proposed and applied, focusing on iterative learning control and linear periodically time-varying (LPTV) systems [123, 124].

This chapter proposes a preactuation perfect tracking control (PPTC) method and experimentally validate its effectiveness. The PPTC method solves problems 1) and 2) separately, regardless of the desired trajectory given it is $n-1$ differentiable (where n denotes the order of the nominal plant). First, the unstable intrinsic zeros in the continuous time domain are offset through a state trajectory generation using a time-axis reversal. Then, the stable inversion of the discretization zeros is calculated through a multirate feedforward approach [103]. Additionally, this chapter thoroughly compares PPTC

with both approximate and preactuated model inversion methods. This chapter also shows that it is impossible to compensate for the zero-order hold delay by just shifting (previewing) the reference of CPMI method. The considered system has several intrinsic and discretization unstable zeros for which conventional approximate methods are unable to achieve perfect tracking. Note that, due to the presence of continuous time unstable zeros in the lower frequency range, it is difficult to design high-bandwidth feedback controllers. Simulation and experimental results show that the proposed method effectively reduces the tracking error.

2.2 Notations and definitions

The plant in continuous time domain is defined as $P_c(s)$. $P_s[z_s]$ denotes the discretized plant of $P_c(s)$ by the zero-order hold with sampling time T_u, where s denotes a complex variable for Laplace transform and $z_s = e^{sT_u}$.

A continuous-time transfer function of the nominal plant is

$$P_n(s) = \frac{B(s)}{A(s)}, \tag{2.1}$$

where $A(s)$ is nth order and $B(s)$ is mth order

$$\begin{aligned} A(s) &= \frac{s^n + a_{n-1}s^{n-1} \cdots + a_0}{b_0} \\ B(s) &= \frac{b_m s^m + b_{m-1}s^{m-1} + \cdots + b_0}{b_0}. \end{aligned} \tag{2.2}$$

Note that (2.1) is irreducible. The state space realization by controllable canonical form is

$$\dot{\boldsymbol{x}}(t) = \boldsymbol{A}_c\boldsymbol{x}(t) + \boldsymbol{b}_c u(t), y(t) = \boldsymbol{c}_c\boldsymbol{x}(t), \tag{2.3}$$

where

$$\begin{aligned} \boldsymbol{x}(t) &= \begin{bmatrix} x_1(t) & x_2(t) & \cdots & x_n(t) \end{bmatrix}^{\mathrm{T}}, \\ \boldsymbol{A}_c &= \begin{bmatrix} 0 & 1 & 0 & \cdots & 0 \\ 0 & 0 & 1 & \cdots & 0 \\ & & & \ddots & \\ -a_0 & -a_1 & -a_2 & \cdots & -a_{n-1} \end{bmatrix} \\ \boldsymbol{b}_c &= \begin{bmatrix} 0 & 0 & \cdots & b_0 \end{bmatrix}^{\mathrm{T}}, \\ \boldsymbol{c}_c &= \begin{bmatrix} 1 & \frac{b_1}{b_0} & \cdots & \frac{b_m}{b_0} & 0 & \cdots & 0 \end{bmatrix}. \end{aligned} \tag{2.4}$$

The discretized plant by a zero-order hold with sampling time T_u is defined as

$$\boldsymbol{x}[k+1] = \boldsymbol{A}_s\boldsymbol{x}[k] + \boldsymbol{b}_s u[k],\ \ y[k] = \boldsymbol{c}_s\boldsymbol{x}[k] \tag{2.5}$$

$$\boldsymbol{A}_s = e^{\boldsymbol{A}_c T_u},\ \ \boldsymbol{b}_s = \int_0^{T_u} e^{\boldsymbol{A}_c\tau}\boldsymbol{b}_c d\tau,\ \ \boldsymbol{c}_s = \boldsymbol{c}_c. \tag{2.6}$$

In the discrete transfer function, it is defined as

$$P_n[z_s] = \boldsymbol{c}_s(z_s\boldsymbol{I} - \boldsymbol{A}_s)^{-1}\boldsymbol{b}_s. \tag{2.7}$$

2.3 Single-rate model-inversion methods

2.3.1 Approximate model-inverse methods

When a nominal plant $P_n[z_s]$ discretized by zero-order hold has an unstable zero, the inversion system in the feedforward controller $P_n^{-1}[z_s]$ is unstable. To avoid this problem, several approximate model-inverse feedforward controllers $\tilde{P}_n^{-1}[z_s]$ are proposed in literature. A generalized block diagram is shown in Fig. 2.1 in which T_y and T_u denote the sampling and control periods, respectively. In this section, $T_y = T_u$ because only single-rate ($z_s = e^{T_u s}$) control methods are considered. The approximate approaches decompose the nominal plant in a stable $B^{\mathrm{st}}[z_s]$ and unstable part $B^{\mathrm{ust}}[z_s]$

$$P_n[z_s] = \frac{B[z_s]}{A[z_s]} = \frac{B^{\mathrm{st}}[z_s]B^{\mathrm{ust}}[z_s]}{A[z_s]} \tag{2.8}$$

$$B^{\mathrm{ust}}[z_s] = b_{un_u}z_s^{n_u} + b_{u(n_u-1)}z_s^{n_u-1} + \cdots + b_{u0}, \tag{2.9}$$

where n_u denotes the order of $B^{\mathrm{ust}}[z_s]$. The feedforward controller is then designed as

$$C_{ff}[z_s] = \tilde{P}_n^{-1}[z_s] = \frac{z_s^{-q}A[z_s]}{B^{\mathrm{st}}[z_s]\tilde{B}^{\mathrm{ust}}[z_s]}. \tag{2.10}$$

The difference between the three prominent methods (NPZI, ZPETC and ZMETC) is the design of the approximated unstable zeros $\tilde{B}^{\mathrm{ust}}[z_s]$ and q ($0 \le q \in \mathbb{Z}$). A comparison between the three methods is listed in Tab. 2.1. A Bode plot of tracking control performances of single-rate model-inversion methods is shown in Fig. 2.3, where a plant model shown in Fig. 2.17 is used for case study.

NPZI method [30]

NPZI method has the least computation load in the three methods. $\tilde{B}_u[z_s]$ is designed by

$$\tilde{B}^{\mathrm{ust}}[z_s] = B^{\mathrm{ust}}[z_s]|_{z_s=1} = B^{\mathrm{ust}}[1] \tag{2.11}$$

to compensate the DC term. q in (2.10) denotes the relative order of $A[z_s]$ and $B^{\mathrm{st}}[z_s]$.

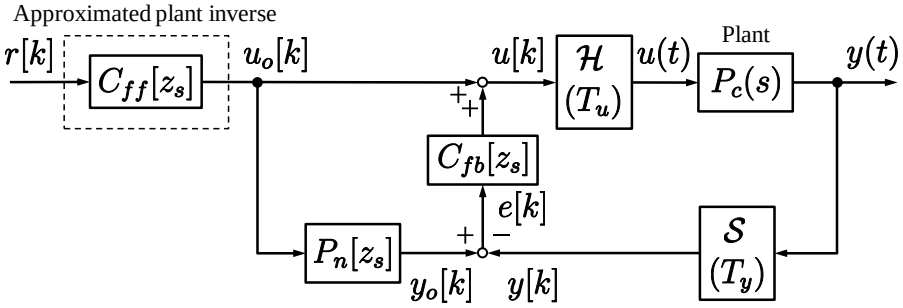

Figure 2.1 Approximated plant inverse feedforward control configuration ($C_{ff}[z_s] = \tilde{P}_n^{-1}[z_s]$). $\mathcal{H}$ and $\mathcal{S}$ denote a holder and a sampler, respectively.

Table 2.1 Comparison between NPZI, ZPETC, and ZMETC ([30]). $Y[z_s]$ and $R[z_s]$ denote $\mathcal{Z}$ transformed signal of $y(t)$ and $r(t)$ shown in Fig. 2.1 with sampling time T_u.

Method	$C_{ff}[z_s]$	$\dfrac{Y[z_s]}{R[z_s]}$	Note
NPZI	$\dfrac{z_s^{-q}A[z_s]}{B^{\mathrm{st}}[z_s]B^{\mathrm{ust}}[1]}$	$\dfrac{z_s^{-q}B^{\mathrm{ust}}[z_s]}{B^{\mathrm{ust}}[1]}$	low computation cost
ZPETC	$\dfrac{z_s^{-q}A[z_s]B_f^{\mathrm{ust}}[z_s]}{B^{\mathrm{st}}[z_s](B^{\mathrm{ust}}[1])^2}$	$\dfrac{z_s^{-q}B^{\mathrm{ust}}[z_s]B_f^{\mathrm{ust}}[z_s]}{(B^{\mathrm{ust}}[1])^2}$	$\mathrm{Im}\left(z_s^q\dfrac{Y[z_s]}{R[z_s]}\right) = 0$ (zero phase error)
ZMETC	$\dfrac{z_s^{-q}A[z_s]}{B^{\mathrm{st}}[z_s]B_f^{\mathrm{ust}}[z_s]}$	$\dfrac{z_s^{-q}B^{\mathrm{ust}}[z_s]}{B_f^{\mathrm{ust}}[z_s]}$	$\left\lvert\dfrac{Y[z_s]}{R[z_s]}\right\rvert = 1$ (zero magnitude error)

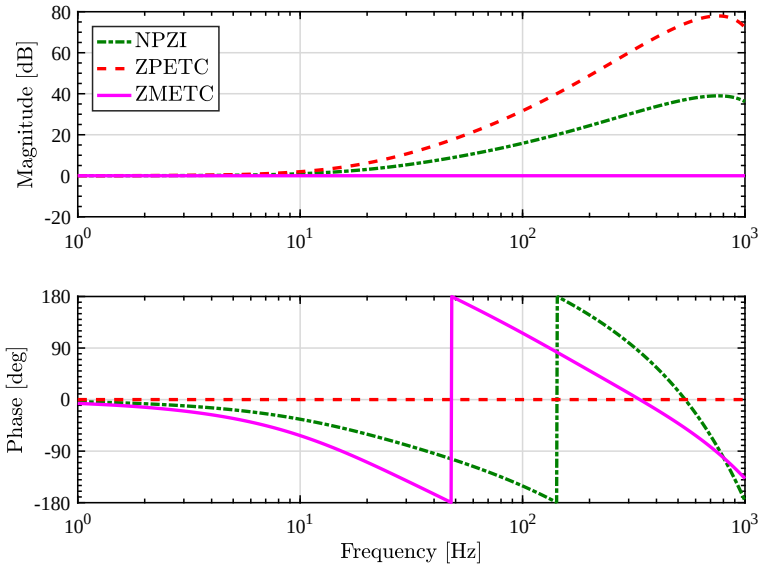

Figure 2.2 Example of tracking control performance of single-rate model-inversion methods $C_{ff}[z_s]P_s[z_s]z_s^{n_{pre}}$, where n_{pre} denotes the previewed number of samples for ZPETC. Plant shown in Fig. 2.17 is used for case study.

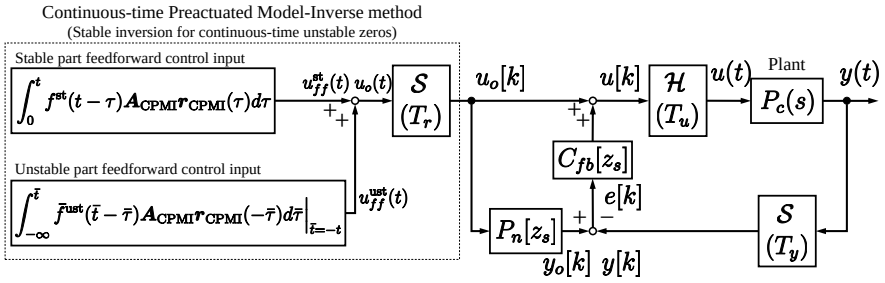

Figure 2.3 Continuous-time preactuated model-inverse method.

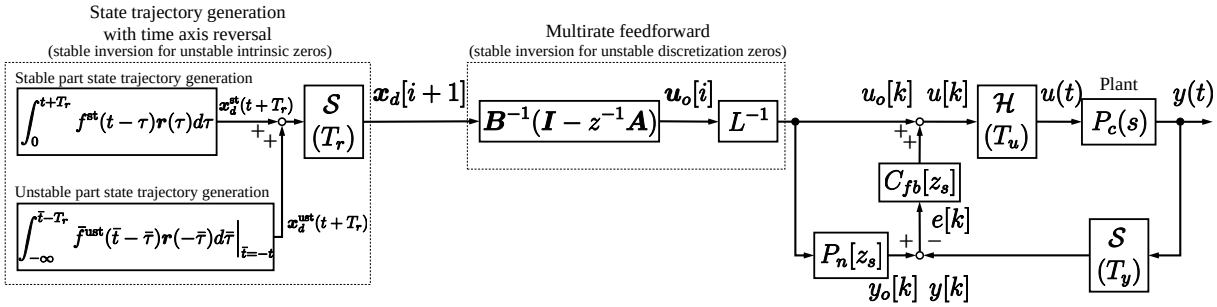

Figure 2.4 Multirate feedforward control with state trajectory generation based on time axis reversal [125]. $\mathcal{S}$, $\mathcal{H}$, and L denote a sampler, holder, and lifting operator [110], respectively. z and z_s denote e^{sT_r} and e^{sT_u}, where $T_r = nT_u$, respectively.

ZPETC method [59]

ZPETC method considers the dynamics of $B^{\mathrm{ust}}[z_s]$. $\tilde{B}^{\mathrm{ust}}[z_s]$ is designed by

$$\tilde{B}^{\mathrm{ust}}[z_s] = \frac{(B^{\mathrm{ust}}[z_s]|_{z_s=1})^2}{B_f^{\mathrm{ust}}[z_s]} = \frac{(B^{\mathrm{ust}}[1])^2}{B_f^{\mathrm{ust}}[z_s]} \tag{2.12}$$

to achieve zero-phase-error characteristics. q in (2.10) denotes the relative order of $A[z_s]B_f^{\mathrm{ust}}[z_s]$ and $B^{\mathrm{st}}[z_s]$. Here, $B_f^{\mathrm{ust}}[z_s]$ is defined by

$$B_f^{\mathrm{ust}}[z_s] = b_{u0}z_s^{n_u} + b_{u1}z_s^{n_u-1} + \cdots + b_{un_u}. \tag{2.13}$$

Under q samples previewed reference trajectory, the zero-phase error characteristics is achieved:

$$\mathrm{Im}\left\{\frac{y[k]}{r[k+q]}\right\} = \mathrm{Im}\left\{\frac{B^{\mathrm{ust}}(e^{-j\omega T_s})B^{\mathrm{ust}}(e^{j\omega T_s})}{(B^{\mathrm{ust}}[1])^2}\right\} = 0$$
$$0 \le \omega \le \pi/T_u \tag{2.14}$$

ZMETC method [119]

$\tilde{B}^{\mathrm{ust}}[z_s]$ is designed by

$$\tilde{B}^{\mathrm{ust}}[z_s] = B_u^f[z_s] \tag{2.15}$$

to achieve zero-magnitude-error characteristics. q in (2.10) denotes the relative order of $A[z_s]$ and $B^{\mathrm{st}}[z_s]B_f^{\mathrm{ust}}[z_s]$.

2.3.2 Continuous-time preactuated model-inverse methods

Several continuous-time preactuated model-inverse (CPMI) methods are proposed in [22,70,71,120–122]. However, these studies don't consider the existence of the zero-order hold in the digital control. The key difference between the CPMI methods and the proposed PPTC method is the zero-order hold consideration by multirate feedforward control. A block diagram of CPMI method is shown in Fig. 2.3.

Step 1: Stable-unstable decomposition

$B(s)^{-1}$ defined in (2.2) is decomposed into a stable part $F^{\mathrm{st}}(s)$ and an unstable part $F^{\mathrm{ust}}(s)$ as follows:

$$\begin{aligned} B(s)^{-1} &= \frac{b_0}{b_m s^m + b_{m-1}s^{m-1} + \cdots + b_0} \\ &= F^{\mathrm{st}}(s) + F^{\mathrm{ust}}(s), \end{aligned} \tag{2.16}$$

$$f^{\mathrm{st}}(t) = \bar{\mathcal{L}}^{-1}\left[F^{\mathrm{st}}(s)\right], \bar{f}^{\mathrm{ust}}(t) = \bar{\mathcal{L}}^{-1}\left[F^{\mathrm{ust}}(-s)\right]. \tag{2.17}$$

Note that $F^{\mathrm{ust}}(-s)$ is stable.

Step 2: Stable part feedforward control input

Stable part feedforward control input is calculated by a convolution between the reference $\boldsymbol{A}_{\mathrm{CPMI}}\boldsymbol{r}_{\mathrm{CPMI}}(t)$ and $f^{\mathrm{st}}(t)$.

$$u_{ff}^{\mathrm{st}}(t) = \int_{-\infty}^{t} f^{\mathrm{st}}(t-\tau)\boldsymbol{A}_{\mathrm{CPMI}}\boldsymbol{r}_{\mathrm{CPMI}}(\tau)d\tau, \tag{2.18}$$

where

$$\begin{aligned} \boldsymbol{A}_{\mathrm{CPMI}} &= \frac{1}{b_0}\begin{bmatrix} a_0 & a_1 & \cdots & a_{n-1} & 1 \end{bmatrix}, \\ \boldsymbol{r}_{\mathrm{CPMI}} &= \begin{bmatrix} 1 & \frac{d}{dt} & \cdots & \frac{d^n}{dt^n} \end{bmatrix}^{\mathrm{T}} r(t) \end{aligned} \tag{2.19}$$

(2.18) can be written as

$$u_{ff}^{\mathrm{st}}(t) = \int_{0}^{t} f^{\mathrm{st}}(t-\tau)\boldsymbol{A}_{\mathrm{CPMI}}\boldsymbol{r}_{\mathrm{CPMI}}(\tau)d\tau \tag{2.20}$$

assuming $\boldsymbol{r}_{\mathrm{CPMI}}(t) = \boldsymbol{0}$ when $t < 0$.

Step 3: Unstable part feedforward control input

Unstable part feedforward control input is calculated by 1) a convolution between the time axis reversed reference $\boldsymbol{A}_{\mathrm{CPMI}}\boldsymbol{r}_{\mathrm{CPMI}}(-\bar{\tau})$ and the stable signal $\bar{f}^{\mathrm{ust}}(\bar{t}-\bar{\tau})$ and 2) a time axis reversal. This procedure results in a infinity time preactuation for continuous-time unstable zeros compensation.

$$u_{ff}^{\mathrm{ust}}(t) = \int_{-\infty}^{\bar{t}} \bar{f}^{\mathrm{ust}}(\bar{t}-\bar{\tau})\boldsymbol{A}_{\mathrm{CPMI}}\boldsymbol{r}_{\mathrm{CPMI}}(-\bar{\tau})d\bar{\tau}\Big|_{\bar{t}=-t} \tag{2.21}$$

Step 4: Total feedforward control input

Total feedforward control input is calculated by a sum of the stable and the unstable part feedforward control input.

$$u_o(t) = u_{ff}^{\mathrm{st}}(t) + u_{ff}^{\mathrm{ust}}(t) \tag{2.22}$$

Then $u_{ff}(t)$ is sampled into $u_{ff}[k]$ by a zero-order hold, where $u_{ff}[k] = u_{ff}(kT_u), (k \in \mathbb{Z})$. No consideration of the zero-order hold causes a delay. This will be discussed in the section 2.6.6 and Fig. 2.22.

2.4 Preactuation perfect tracking control

This chapter proposes a preactuation perfect tracking control (PPTC) method to design a stable inversion feedforward controller for plants with unstable intrinsic and discretization zeros. This method solves the unstable zeros inversion problem in two steps. First, the stable inversion for the unstable intrinsic zeros is calculated using a time axis reversal in a continuous time domain. Next, the stable inversion for unstable discretization zeros are calculated using a multirate feedforward proposed by [103].

2.4.1 State trajectory $\boldsymbol{x}_d$ generation

This section generates the state trajectory $\boldsymbol{x}_d$ for the multirate feedforward (see Fig. 2.4). The state trajectory $\boldsymbol{x}_d$ is defined as

$$\boldsymbol{x}_d(t) = \begin{bmatrix} x_{1d}(t) & x_{2d}(t) & \cdots & x_{nd}(t) \end{bmatrix}^{\mathrm{T}} \tag{2.23}$$

Due to the controllable canonical form realization (see (2.4)),

$$\boldsymbol{x}_d(t) = \begin{bmatrix} x_{1d}(t) & \rho x_{1d}(t) & \cdots & \rho^{n-1}x_{1d}(t) \end{bmatrix}^{\mathrm{T}}, \tag{2.24}$$

where ρ denotes the Heaviside operator [37]

According to (2.3), to track the reference position trajectory $r(t)$, the desired state trajectory $\boldsymbol{x}_d(t)$ should satisfy

$$\begin{aligned} r(t) &= \boldsymbol{c}_c \boldsymbol{x}_d(t) \\ &= \begin{bmatrix} 1 & \frac{b_1}{b_0} & \cdots & \frac{b_m}{b_0} & 0 & \cdots & 0 \end{bmatrix} \begin{bmatrix} x_{1d}(t) \\ \rho x_{1d}(t) \\ \rho^2 x_{1d}(t) \\ \vdots \\ \rho^{n-1} x_{1d}(t) \end{bmatrix}. \end{aligned} \tag{2.25}$$

From (2.25) and (2.2), $\boldsymbol{x}_d(t)$ is obtained by

$$x_{1d}(t) = \frac{1}{B(\rho)} r(t) \tag{2.26}$$

Therefore, whole vector $\boldsymbol{x}_d(t)$ is obtained by

$$\boldsymbol{x}_d(t) = \frac{1}{B(\rho)} \boldsymbol{r}(t), \tag{2.27}$$

where

$$\begin{aligned} \boldsymbol{r}(t) &= \begin{bmatrix} r_1(t) & r_2(t) & \cdots & r_n(t) \end{bmatrix}^{\mathrm{T}} \\ &= \begin{bmatrix} 1 & \rho & \cdots & \rho^{n-1} \end{bmatrix}^{\mathrm{T}} r(t). \end{aligned} \tag{2.28}$$

However, (2.27) has unstable poles when the plant $P_n(s)$ has unstable zeros. To prevent the diversion of the state trajectory $\boldsymbol{x}_d(t)$, the stable-unstable decomposition and time axis reversal techniques are used.

Step 1: Stable-unstable decomposition

$B(s)^{-1}$ defined in (2.2) is decomposed into a stable part $F^{\mathrm{st}}(s)$ and an unstable part $F^{\mathrm{ust}}(s)$ as follows:

$$\begin{aligned} B(s)^{-1} &= \frac{b_0}{b_m s^m + b_{m-1} s^{m-1} + \cdots + b_0} \\ &= F^{\mathrm{st}}(s) + F^{\mathrm{ust}}(s), \end{aligned} \tag{2.29}$$

$$f^{\mathrm{st}}(t) = \bar{\mathcal{L}}^{-1}\left[F^{\mathrm{st}}(s)\right], \bar{f}^{\mathrm{ust}}(t) = \bar{\mathcal{L}}^{-1}\left[F^{\mathrm{ust}}(-s)\right]. \tag{2.30}$$

Note that $F^{\mathrm{ust}}(-s)$ is stable.

Step 2: Stable part state trajectory generation

The desired state trajectory $\boldsymbol{x}_d^{\mathrm{st}}(t)$ for the stable part is forwardly generated as follows.

$$\begin{aligned}\boldsymbol{x}_d^{\mathrm{st}}(t) &= \begin{bmatrix} x_{1d}^{\mathrm{st}}(t) & x_{2d}^{\mathrm{st}}(t) & \cdots & x_{nd}^{\mathrm{st}}(t) \end{bmatrix}^{\mathrm{T}} \\ &= \int_{-\infty}^{t} f^{\mathrm{st}}(t-\tau)\boldsymbol{r}(\tau)d\tau \end{aligned} \tag{2.31}$$

(2.32) can be written as

$$\boldsymbol{x}_d^{\mathrm{st}}(t) = \int_{0}^{t} f^{\mathrm{st}}(t-\tau)\boldsymbol{r}(\tau)d\tau \tag{2.32}$$

assuming $\boldsymbol{r}(t) = 0$ when $t < 0$.

Step 3: Unstable part state trajectory generation

The desired state trajectory $\boldsymbol{x}_d^{\mathrm{ust}}(t)$ for the unstable part is generated by

$$\begin{aligned}\boldsymbol{x}_d^{\mathrm{ust}}(t) &= \begin{bmatrix} x_{1d}^{\mathrm{ust}}(t) & x_{2d}^{\mathrm{ust}}(t) & \cdots & x_{nd}^{\mathrm{ust}}(t) \end{bmatrix}^{\mathrm{T}} \\ &= \int_{-\infty}^{\bar{t}} \bar{f}^{\mathrm{ust}}(\bar{t}-\bar{\tau})\boldsymbol{r}(-\bar{\tau})d\bar{\tau}\Big|_{\bar{t}=-t}. \end{aligned} \tag{2.33}$$

$\boldsymbol{x}_d^{\mathrm{ust}}(t)$ is calculated as follows. First, a convolution of the time reversed reference position trajectory $\boldsymbol{r}(-\bar{t})$ and the stable signal $\bar{f}^{\mathrm{ust}}(\bar{t})$ is calculated. Next, the time axis is reversed. The mathematical proof is provided in [126].

Step 4: State trajectory generation

The state trajectory $\boldsymbol{x}_d(t)$ is obtained by

$$\boldsymbol{x}_d(t) = \boldsymbol{x}_d^{\mathrm{st}}(t) + \boldsymbol{x}_d^{\mathrm{ust}}(t). \tag{2.34}$$

2.4.2 Feedforward input u_o generation from $\boldsymbol{x}_d$

The effect of unstable discretization zeros can be compensated by using the multirate feedforward control [103]. Fig. 2.4 shows that there are three time periods T_y, T_u, and T_r denoting the periods for $y(t)$, $u(t)$, and $r(t)$, respectively. These periods are set as $T_r = nT_u = nT_y$.

The multirate system of (2.5) is given as

$$\boldsymbol{x}[i+1] = \boldsymbol{A}\boldsymbol{x}[i] + \boldsymbol{B}\boldsymbol{u}[i], \;\; y[i] = \boldsymbol{c}\boldsymbol{x}[i], \tag{2.35}$$

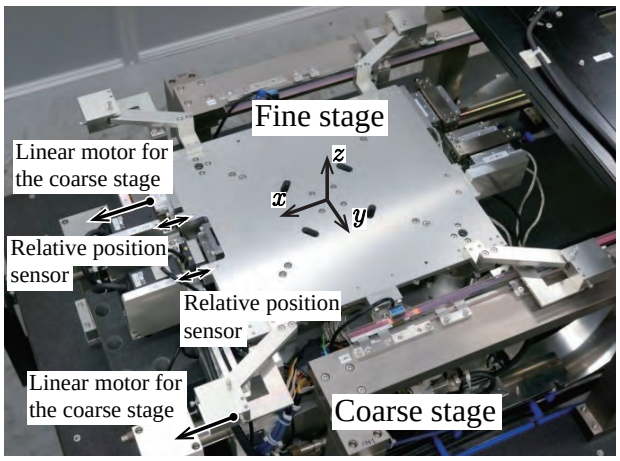

Figure 2.5 Photograph of the 6-DOF high-precision stage.

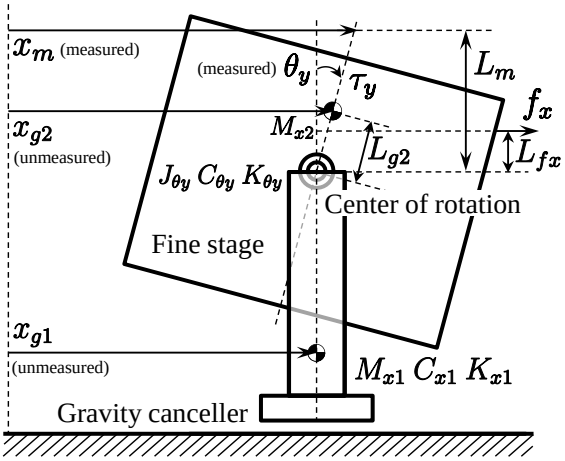

Figure 2.6 Fine stage model of the scanning motion x and the pitching motion θ_y.

where

$$\begin{aligned} &\boldsymbol{A} = \boldsymbol{A}_s^n,\ \ \boldsymbol{B} = \begin{bmatrix} \boldsymbol{A}_s^{n-1}\boldsymbol{b}_s & \boldsymbol{A}_s^{n-2}\boldsymbol{b}_s & \cdots & \boldsymbol{A}_s\boldsymbol{b}_s & \boldsymbol{b}_s \end{bmatrix} \\ &\boldsymbol{c} = \boldsymbol{c}_s,\ \ \boldsymbol{x}[i] = \boldsymbol{x}(iT_r) \end{aligned} \tag{2.36}$$

by calculating the state transition from $t = iT_r = kT_u$ to $t = (i+1)T_r = (k+n)T_u$. Here, the input vector $\boldsymbol{u}[i]$ is defined in the lifting form

$$\begin{aligned} \boldsymbol{u}[i] &= \begin{bmatrix} u_1[i] & u_2[i] & \cdots & u_n[i] \end{bmatrix}^{\mathrm{T}} \\ &= \begin{bmatrix} u(kT_u) & u((k+1)T_u) & \cdots & u((k+n-1)T_u) \end{bmatrix}^{\mathrm{T}}. \end{aligned} \tag{2.37}$$

According to (2.35), the feedforward input $\boldsymbol{u}_o[i]$ is obtained from the previewed state trajectory $\boldsymbol{x}_d[i+1]$ as follows:

$$\boldsymbol{u}_o[i] = \boldsymbol{B}^{-1}(\boldsymbol{I} - z^{-1}\boldsymbol{A})\boldsymbol{x}_d[i+1], \tag{2.38}$$

where $z = e^{sT_r}$.

2.5 Simulation study: 8 types of zeros locations

To investigate the relationship between the zeros locations, the generated state trajectory, and the control input, this section shows simulation results for 8 types of zeros locations. This section uses a setup shown in Fig. 2.5 and focuses on a translational motion and a pitching motion. The model shown in Fig. 2.6 considers the misalignment between the center of gravity, the center of rotation, the actuation point, and the measurement point.

This simulation deals with a model $\frac{x_m(s)}{f_x(s)}$. The derivation of the model is explained in Appendix A.

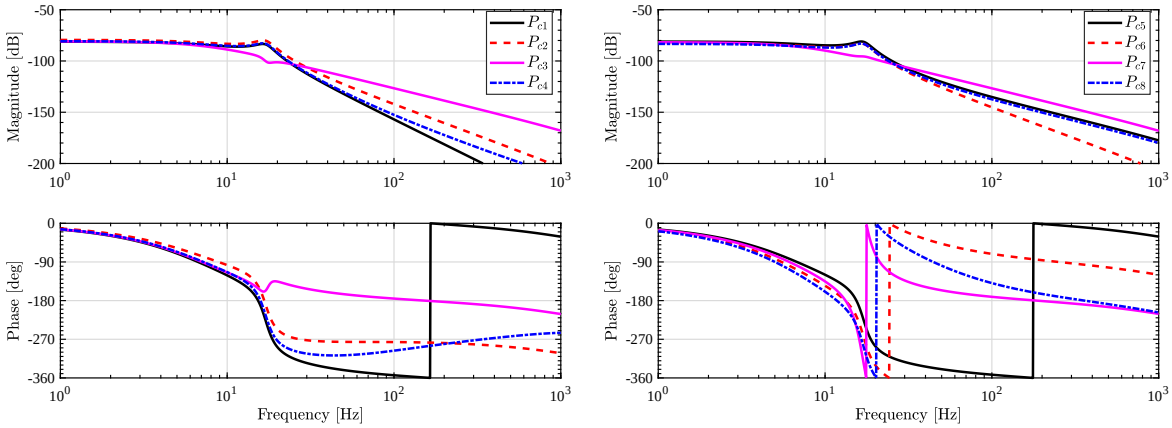

(a) $P_{c1}(s), P_{c2}(s), P_{c3}(s), P_{c4}(s)$. (b) $P_{c5}(s), P_{c6}(s), P_{c7}(s), P_{c8}(s)$.

Figure 2.7 Bode diagram of the simulation models.

We rewrite (A.15) as

$$P_c(s) = \frac{(b_2 s^2 + b_1 s + b_0)}{(s + 1.0 \times 10^4)(s^2 + 83s + 2100)(s^2 + 25s + 11000)} \tag{2.39}$$

$$\begin{cases} b_2 = 98000(L_{fx} - L_{g2})(L_m - L_{g2}) + 1400 L_{fx} L_m + 1900 \\ b_1 = L_{fx} L_m 8.0 \times 10^6 + 3.0 \times 10^4 \\ b_0 = L_{fx} L_m 2.0 \times 10^8 - 9.6 \times 10^5 + 2.2 \times 10^7 \\ L_{g2} = -0.051 \end{cases} \tag{2.40}$$

assuming a current controller model is a first-order with pole at $s = -10000$ rad/s. By changing the actuation height L_{fx} and the measurement point L_m, the location of zeros is changed according to (2.39). The Bode diagrams for 8 cases are shown in Fig. 2.7. Reference trajectory is designed as step trajectory interpolated by 15th order polynomial (see Fig. 2.8(a)). Step time is set as 0.05 s. Sampling time is set as $T_u = 400\ \mu$s

In the following section name, "in continuous time domain" is omitted.

Plant with no zeros (case1)

Taking $L_{fx} = 0.010$ m, and $L_m = -0.36$ m, (2.41) is obtained. Discretized transfer function by zero-order hold is shown in (2.42). The denominator polynomial (2.43) in discrete time is common to the all cases (case 1–8).

The simulation results are shown in Fig. 2.8. It is seen from Figs. 2.8(b) and 2.8(c) that, the three methods NPZI, ZPETC and ZMETC are affected by approximation of the unstable discretization zeros, resulting in tracking errors. Since there are no zeros, it can be seen that the state variable

trajectory $\boldsymbol{x}_d(t)$ shown in Figs. 2.8(e) and 2.8(f) coincides with the reference values of each dimension.

$$P_{c1}(s) = \frac{2.2 \times 10^7}{A(s)} \tag{2.41}$$

$$P_{s1}[z_s] = \frac{1.066 \times 10^{-12}(z_s + 15.29)(z_s + 1.470)(z_s + 0.2188)(z_s + 0.01472)}{A[z_s]} \tag{2.42}$$

$$A[z_s] = (z_s - 0.01832)(z_s^2 - 1.967z_s + 0.9677)(z_s^2 - 1.988z_s + 0.9902) \tag{2.43}$$

Plant with a stable zero (case2)

Taking $L_{fx} = -0.025\,\mathrm{m}$, and $L_m = -0.78\,\mathrm{m}$, (2.45) is obtained. The simulation results are shown in Fig. 2.9. Since there is a stable zero on the real axis in continuous time, as shown in Figs. 2.9(e) and 2.9(f), the state variable trajectory $\boldsymbol{x}_d$ is first-order lagged compared with the reference trajectory $\boldsymbol{r}(t)$. As a result, postactuation is performed as shown in Fig. 2.9(d).

$$P_{c2}(s) = \frac{1.9 \times 10^5(s + 140)}{A(s)} \tag{2.44}$$

$$P_{s2}[z_s] = \frac{1.058 \times 10^{-10}(z_s + 6.060)(z_s - 0.9449)(z_s + 0.5230)(z_s + 0.03172)}{A[z_s]} \tag{2.45}$$

Plant with two complex stable zeros (case3)

Taking $L_{fx} = 0.0020\,\mathrm{m}$, and $L_m = -0.051\,\mathrm{m}$, (2.47) is obtained. The simulation results are shown in Fig. 2.10. Since there are two complex stable zeros, as shown in Figs.2.10(e) and 2.10(f), the state variable trajectory $\boldsymbol{x}_d$ is second-order lagged compared with the reference trajectory $\boldsymbol{r}(t)$. As a result, oscillated postactuation is performed as shown in Fig. 2.10(d).

$$P_{c3}(s) = \frac{1900(s^2 + 16s + 12000)}{A(s)} \tag{2.46}$$

$$P_{s3}[z_s] = \frac{9.150 \times 10^{-9}(z_s + 1.899)(z_s + 0.07898)(z_s^2 - 1.992z_s + 0.9938)}{A[z_s]} \tag{2.47}$$

Plant with two real stable zeros (case4)

Taking $L_{fx} = -0.46\,\mathrm{m}$, and $L_m = -0.0050\,\mathrm{m}$, (2.49) is obtained. The simulation results are shown in Fig. 2.11. Since there is two stable zeros on the real axis in continuous time, as shown in Figs. 2.11(e) and 2.11(f), the state variable trajectory $\boldsymbol{x}_d$ is second-order lagged compared with the reference trajectory $\boldsymbol{r}(t)$. As a result, postactuation is performed as shown in Fig. 2.11(d).

$$P_{c4}(s) = \frac{8.6(s + 5100)(s + 520)}{A(s)} \tag{2.48}$$

$$P_{s4}[z_s] = \frac{7.047 \times 10^{-11}(z_s + 3.156)(z_s - 0.8112)(z_s - 0.1285)(z_s + 0.1629)}{A[z_s]} \tag{2.49}$$

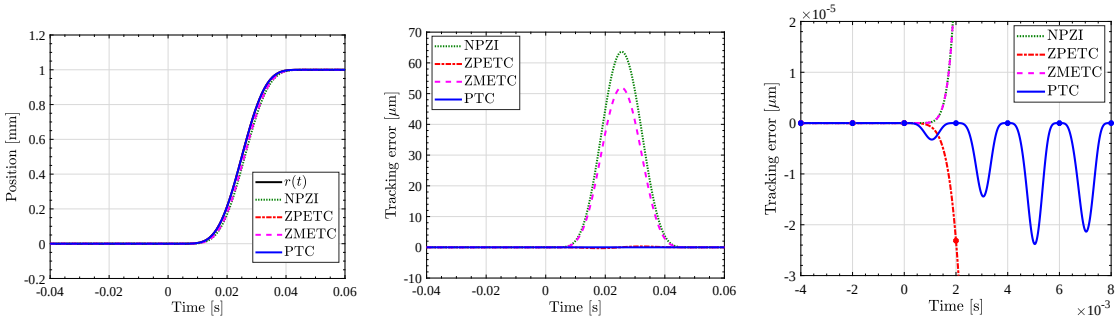

(a) Position. (b) Tracking error. (c) Tracking error (zoom).

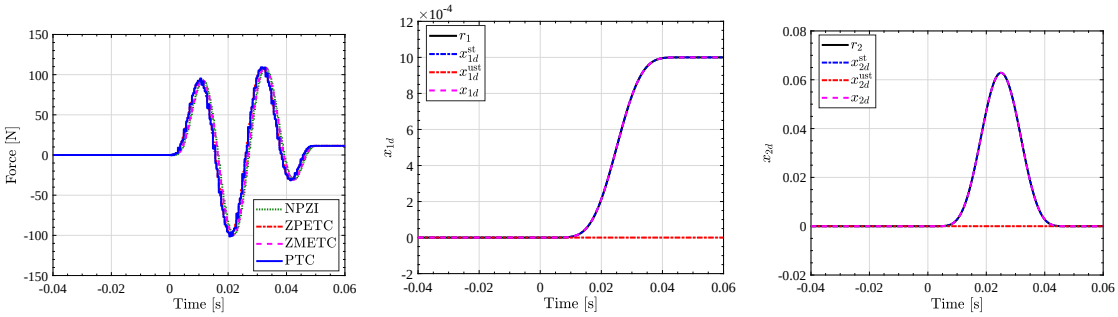

(d) Force. (e) $r_1(t), x_{1d}(t)$. (f) $r_2(t), x_{2d}(t)$.

Figure 2.8 Simulation results of the plant without zeros (case 1, $P_{c1}(s) = \dfrac{2.2 \times 10^7}{A(s)}$). Dots are illustrated by every nT_u in (c).

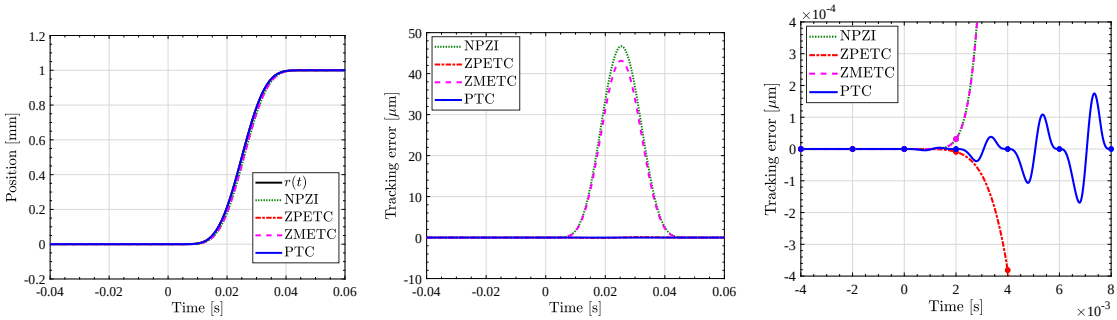

(a) Position. (b) Tracking error. (c) Tracking error (zoom).

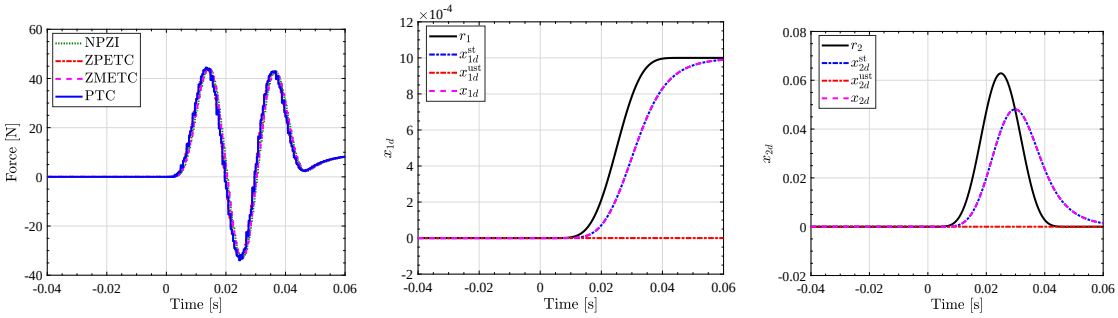

(d) Force. (e) $r_1(t), x_{1d}(t)$. (f) $r_2(t), x_{2d}(t)$.

Figure 2.9 Simulation results of the plant with one stable zero (case 2, $P_{c2}(s) = \dfrac{1.9 \times 10^5 (s + 140)}{A(s)}$). Dots are illustrated by every nT_u in (c).

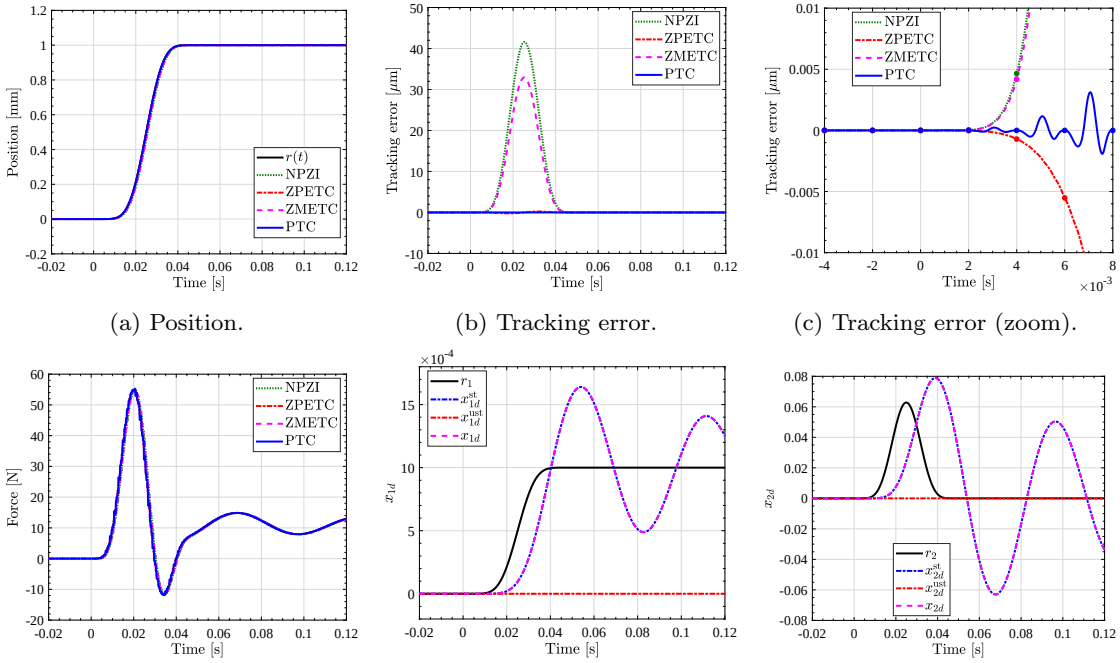

(a) Position. (b) Tracking error. (c) Tracking error (zoom).

(d) Force. (e) $r_1(t), x_{1d}(t)$. (f) $r_2(t), x_{2d}(t)$.

Figure 2.10 Simulation results of the plant with two complex stable zeros (case 3, $P_{c3}(s) = \dfrac{1900(s^2+16s+12000)}{A(s)}$). Dots are illustrated by every nT_u in (c).

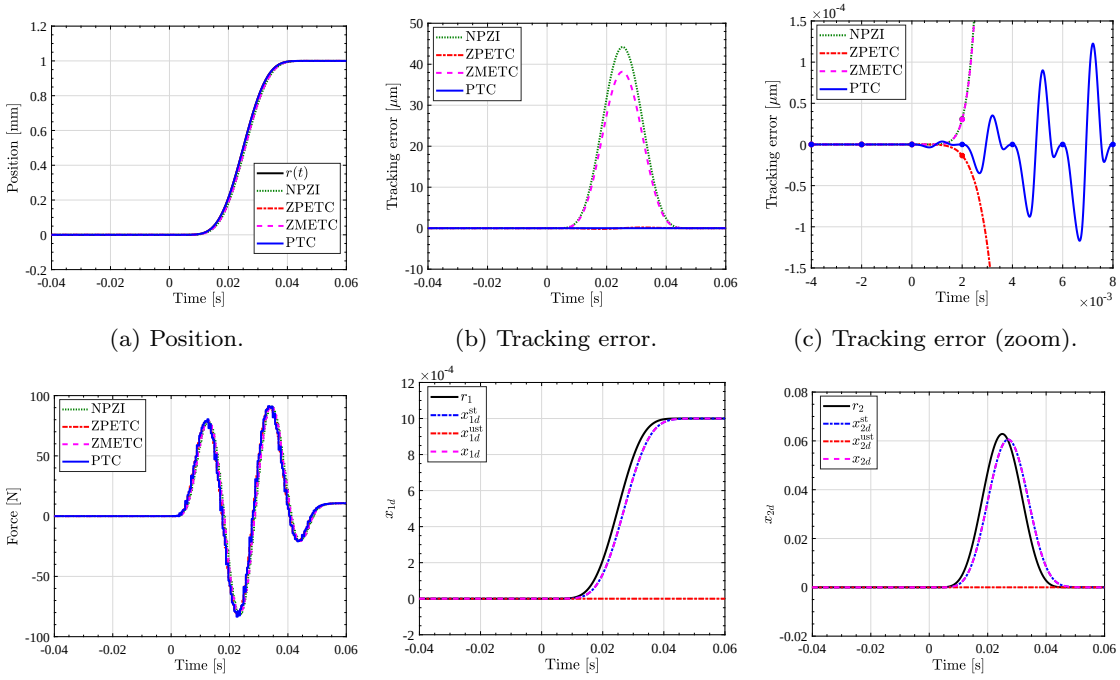

(a) Position. (b) Tracking error. (c) Tracking error (zoom).

(d) Force. (e) $r_1(t), x_{1d}(t)$. (f) $r_2(t), x_{2d}(t)$.

Figure 2.11 Simulation results of the plant with two stable real zeros (case 4, $P_{c4}(s) = \dfrac{8.6(s+5100)(s+520)}{A(s)}$). Dots are illustrated by every nT_u in (c).

Plant with a real stable zero and an unstable zero (case5)

Taking $L_{fx} = -0.50\,\mathrm{m}$, and $L_m = 0.0050\,\mathrm{m}$, (2.51) is obtained. The simulation results are shown in Fig. 2.12. As a result of an unstable zero on the real axis, $\boldsymbol{x}_d^{\mathrm{ust}}(t)$ has non-zero value in $0 < t$. Similarly, $\boldsymbol{x}_d^{\mathrm{st}}(t)$ varies in $0.02\ \mathrm{s} < t$ due to a stable zero on a real axis. Because of these effects, both preactuation and postactuation is performed as shown in Fig. 2.12(d). From Figs. 2.12(b) and 2.12(c), PPTC method achieves the perfect tracking not only in $0 \leq t$ but also in $t < 0$.

$$P_{c5}(s) = \frac{-620(s-200)(s+180)}{A(s)} \tag{2.50}$$

$$P_{s5}[z_s] = \frac{-3.049 \times 10^{-9}(z_s+1.892)(z_s-1.081)(z_s-0.9306)(z_s+0.07880)}{A[z_s]} \tag{2.51}$$

Plant with a real stable zero (case6)

Taking $L_{fx} = 0.13\,\mathrm{m}$, and $L_m = -0.15\,\mathrm{m}$, (2.53) is obtained. The simulation results are shown in Fig. 2.13. As a result of an unstable zero on the real axis, preactuation is performed as shown in Fig. 2.13(d).

$$P_{c6}(s) = \frac{-1.3 \times 10^{5}(s-140)}{A(s)} \tag{2.52}$$

$$P_{s6}[z_s] = \frac{-7.227 \times 10^{-11}(z_s+5.902)(z_s-1.058)(z_s+0.5101)(z_s+0.03114)}{A[z_s]} \tag{2.53}$$

Plant with two complex unstable zeros (case7)

Taking $L_{fx} = 0.20\,\mathrm{m}$, and $L_m = -0.051\,\mathrm{m}$, (2.55) is obtained. The simulation results are shown in Fig. 2.14. Since there are two complex unstable zeros, as shown in Fig. 2.14(d), oscillating preactuation waveform is generated.

$$P_{c7}(s) = \frac{1800(s^2-28s+11000)}{A(s)} \tag{2.54}$$

$$P_{s7}[z_s] = \frac{9.034 \times 10^{-9}(z_s+1.889)(z_s+0.07867)(z_s^2-2.010z_s+1.011)}{A[z_s]} \tag{2.55}$$

Plant with two real stable zero (case8)

Taking $L_{fx} = 0.30\,\mathrm{m}$, and $L_m = -0.090\,\mathrm{m}$, (2.57) is obtained. The simulation results are shown in Fig. 2.15. As a result of two unstable zeros on the real axis, preactuation is performed as shown in

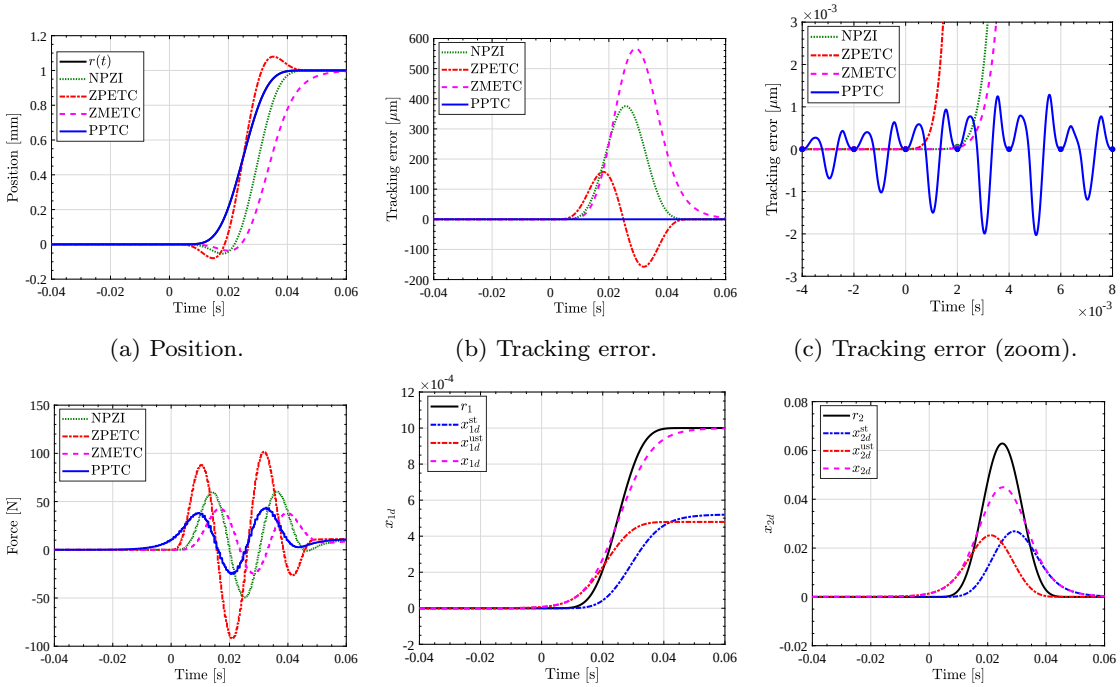

(a) Position. (b) Tracking error. (c) Tracking error (zoom).

(d) Force. (e) $r_1(t), x_{1d}(t)$. (f) $r_2(t), x_{2d}(t)$.

Figure 2.12 Simulation results of the plant with one stable zero and one unstable zero (case 5, $P_{c5}(s) = \dfrac{-620(s-200)(s+180)}{A(s)}$). Dots are illustrated by every nT_u in (c).

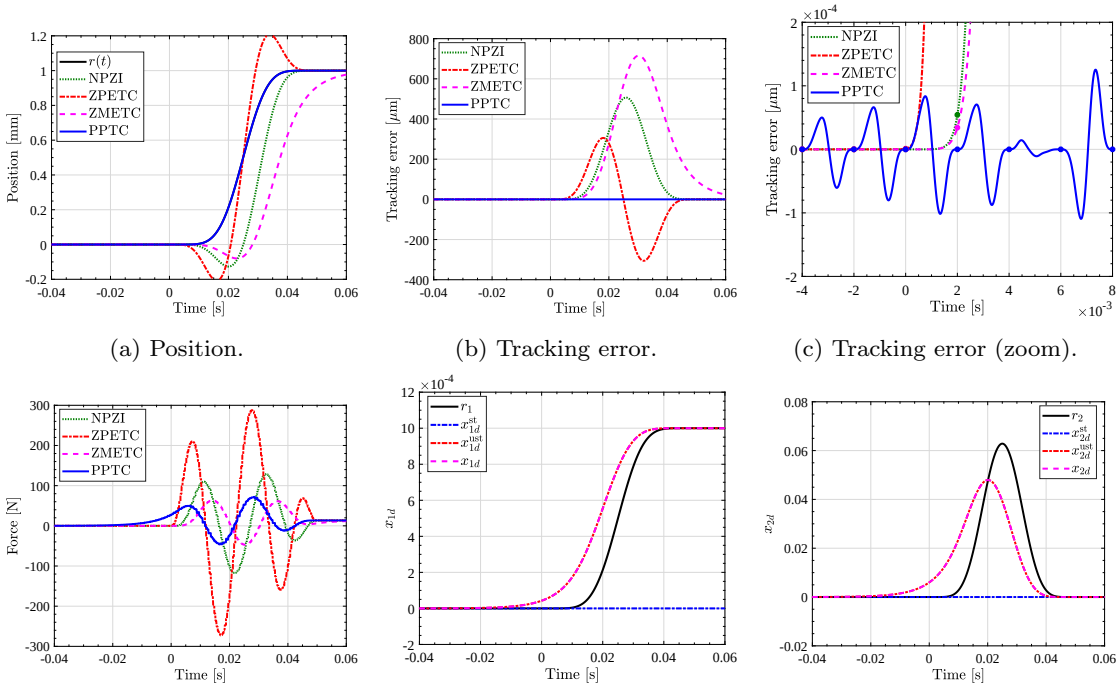

(a) Position. (b) Tracking error. (c) Tracking error (zoom).

(d) Force. (e) $r_1(t), x_{1d}(t)$. (f) $r_2(t), x_{2d}(t)$.

Figure 2.13 Simulation results of the plant with one unstable zero (case 6, $P_{c6}(s) = \dfrac{-1.299 \times 10^5 (s-140)}{A(s)}$). Dots are illustrated by every nT_u in (c).

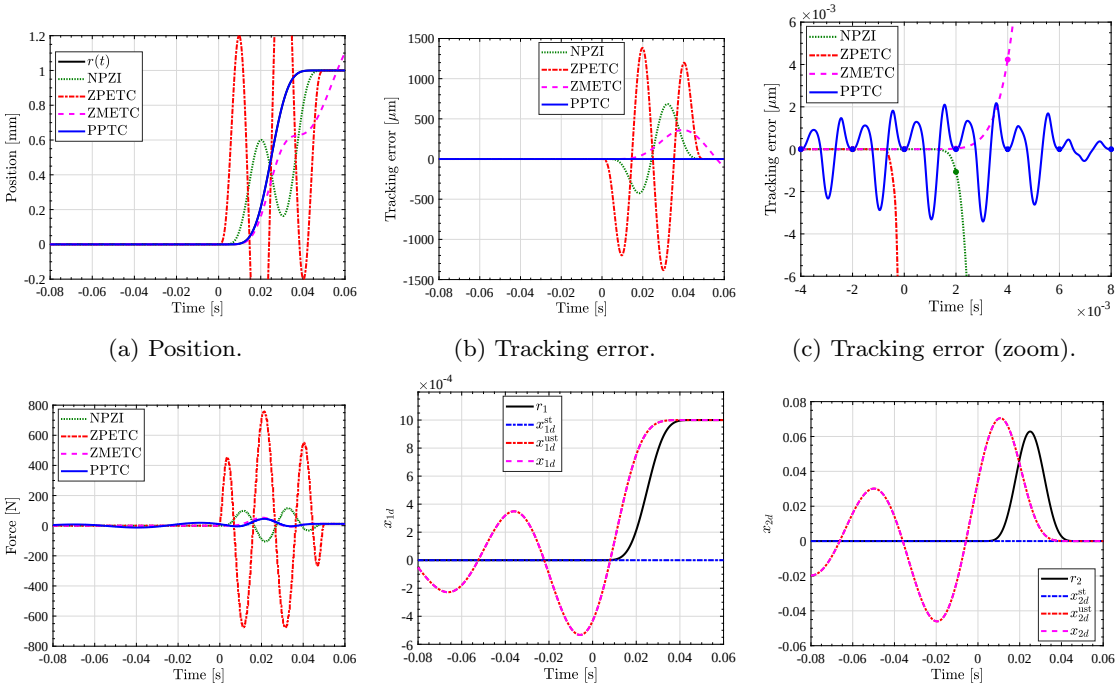

(a) Position. (b) Tracking error. (c) Tracking error (zoom).

(d) Force. (e) $r_1(t), x_{1d}(t)$. (f) $r_2(t), x_{2d}(t)$.

Figure 2.14 Simulation results of the plant with twp complex unstable zeros (case 7, $P_{c7}(s) = \dfrac{1800(s^2 - 28s + 11000)}{A(s)}$). Dots are illustrated by every nT_u in (c).

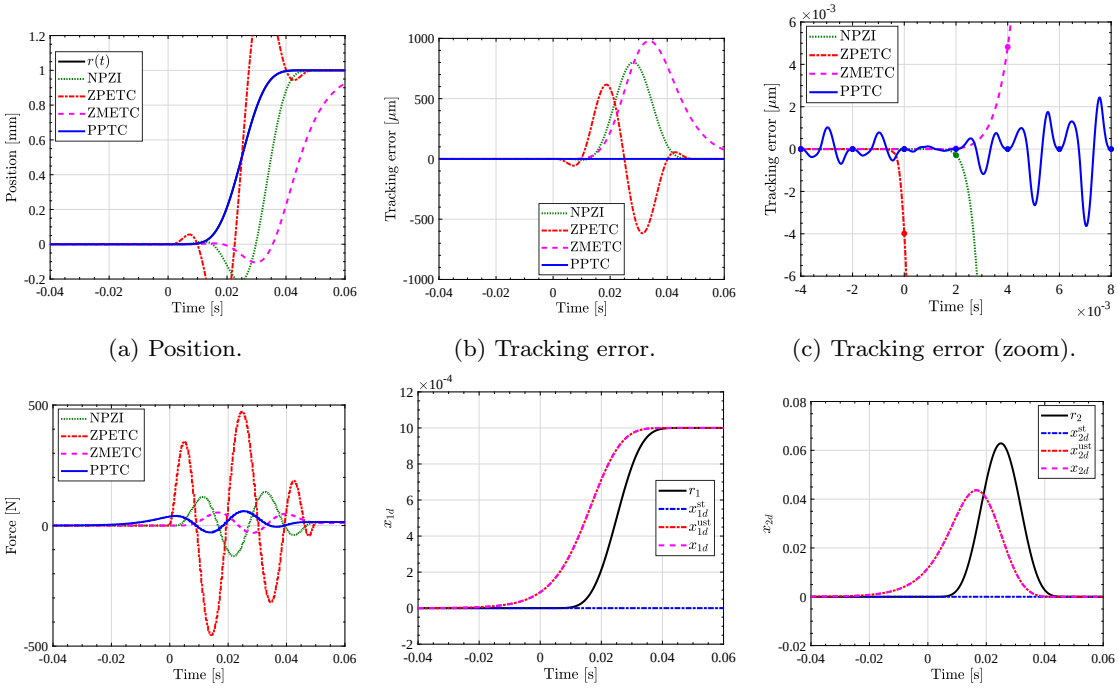

(a) Position. (b) Tracking error. (c) Tracking error (zoom).

(d) Force. (e) $r_1(t), x_{1d}(t)$. (f) $r_2(t), x_{2d}(t)$.

Figure 2.15 Simulation results of the plant with two real unstable zeros (case 8, $P_{c8}(s) = \dfrac{470(s - 250)(s - 140)}{A(s)}$). Dots are illustrated by every nT_u in (c).

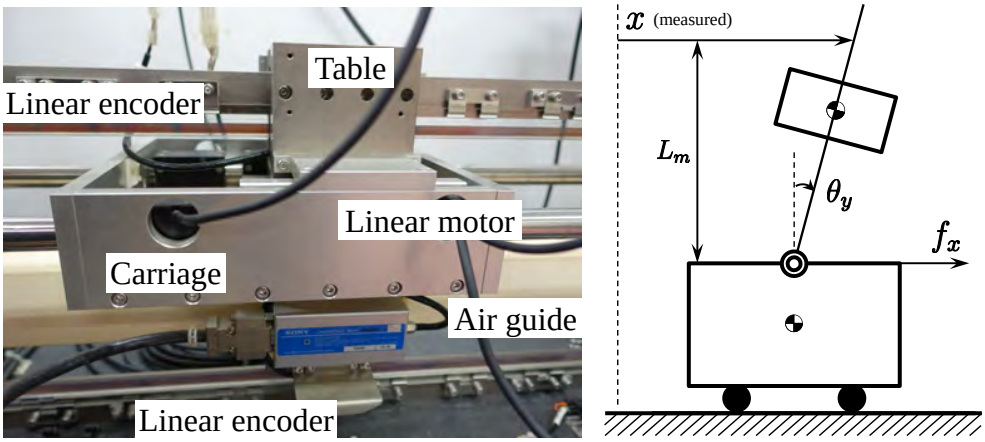

(a) High-precision positioning stage. (b) Model of (a).

Figure 2.16 Experimental high-precision positioning stage and its model [83, 84].

Fig. 2.15(d).

$$P_{c8}(s) = \frac{470(s-250)(s-140)}{A(s)} \tag{2.56}$$

$$P_{s8}[z_s] = \frac{2.213 \times 10^{-9}(z_s+1.807)(z_s-1.107)(z_s-1.058)(z_s+0.07617)}{A[z_s]} \tag{2.57}$$

Summary of simulation results

As described above, in all the cases 1 to 8, irrespective of the placement of zeros, the tracking error is zero in every period $T_r = nT_u = 2.00$ ms in the PTC and PPTC methods, showing that perfect tracking has been achieved. The following feedforward inputs are necessary to achieve perfect tracking.

1. Plant with no zeros in the continuous time plant

   Neither preactuation nor postactuation is required, and $T_r = nT_u$ preview is needed.

2. Plant with stable zeros in the continuous time plant

   Infinite time postactuation is required in addition to preview of $T_r = nT_u$.

3. Plant with unstable zeros in the continuous time plant

   Infinite time preactuation is required in addition to infinite time preview.

2.6 Experimental validation

2.6.1 Experimental setup

The considered experimental setup shown in Fig. 2.16 is an air-guided single degree-of-freedom flexible stage driven by a set of linear motors. The position of the table and the driven carriage are measured by two linear encoder with 1nm precision. By using interior or exterior division, we can

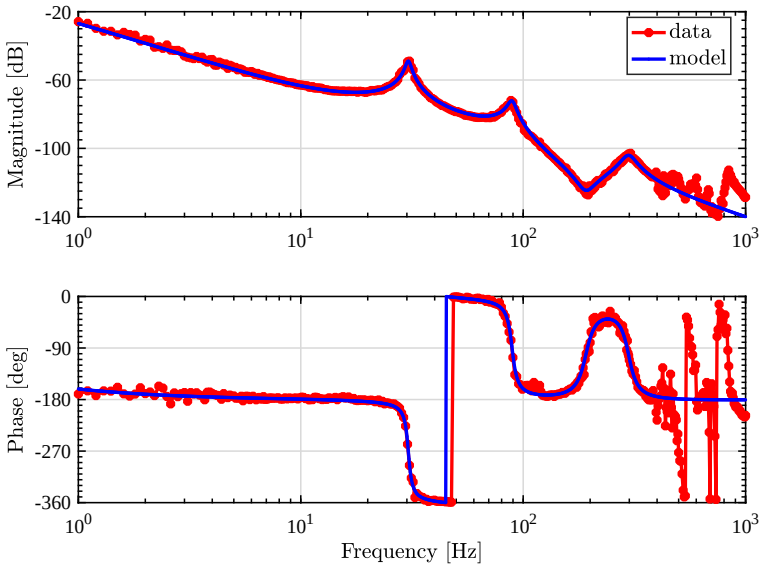

Figure 2.17 Measured frequency response and 8th order model for the high-precision stage shown in Fig. 2.16 ($L_m = 0.300$ m).

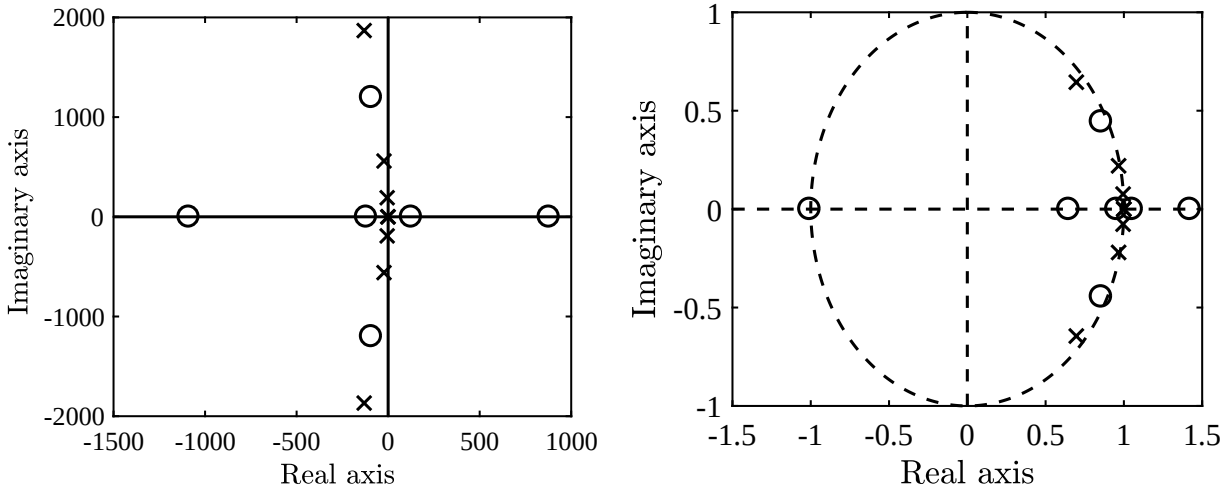

(a) P_c. (b) P_s.

Figure 2.18 Pole-zero map of identified model shown in Fig. 2.16.

measure any vertical imaginary position. In this chapter, the height of measurement point is set as $L_m = 0.300$ m by exterior division to have continuous time unstable zeros. The applied force, i.e. current, is measured through an inductive current sensor with a 25 A range and quantized with a 14-bit A/D converter, i.e 3.05 mA step.

2.6.2 System identification

The dominant system dynamics of the setup are modeled through frequency domain identification techniques, see [127]. First, the non-parametric frequency response is measured from open-loop experiments using periodic multisine excitations with quasi-logarithmic spacing to cover the wide frequency

band-of-interest. Subsequently, a 8th order parametric transfer function model $P_n(s)$ is estimated iteratively using a Levenberg-Marquardt method with a maximum likelihood criterion. Some additional weigthing is applied in the middle frequency range (10 to 400 Hz) to reflect the region in which high model accuracy is desired for feedforward design.

The measured frequency response and estimated 8th order model are shown in Fig. 2.17. The identified continuous time pole-zero map is shown in Fig. 2.18(a), in which $P_n(s)$ contains continuous time unstable zeros at $s = +126,\ +878$ and stable zeros at $s = -1090,\ -120, -92.7 \pm 1.20j$. Additionally, the pole-zero map of the discretized transfer function with $T_u = 400\ \mu$s is shown in Fig. 2.18(b), in which $P_s[z_s]$ contains both an additional stable and unstable discretized zero.

2.6.3 Conditions

The setup has a current controller as inner loop, which has 1 kHz bandwidth, with 12.5 kHz sampling and a position controller as outer loop with 2.5 kHz sampling. The position feedforward controllers are designed with $T_u = 400\ \mu$s sampling time. The position feedback controller is designed as a proportional-integral-derivative (PID) controller and a second order shaping filter. The feedback control performance is shown in Fig. 2.19, which shows that it is difficult to achieve high bandwidth for a plant with continuous time unstable zeros in the low frequency range. This indicates that the feedback controller cannot help the trajectory tracking performance. The block diagram shown in Fig. 2.1 is used for NPZI, ZPETC, and ZMETC methods. Note that in the configurations of Fig. 2.1 and 2.4, without modeling error or disturbances, the output of the feedback controller $C_{fb}[z_s]$ is zero.

The target trajectory is given as a 0.05 s step reference interpolated by a 15th order polynomial and is shown in i.e. Fig. 2.20(a).

2.6.4 Simulation results

Simulation results are shown in Fig. 2.20. Fig. 2.20(f) demonstrates that PPTC method can achieve perfect tracking without any undershoot or overshoot. In contrast, Fig. 2.20(a) and 2.20(e) show that the NPZI, ZMETC, and ZPETC controllers create undershoot and/or overshoot. The FB only case shows a slow response, which demonstrates that a plant with a slow continuous unstable zero cannot rely on a FB controller only for reference tracking. Fig. 2.21(g) shows that the CMPI method creates a similar current reference to PPTC with preactuation. However, due to the lack of considering the zero-order hold, the current reference is delayed compared to PPTC and it results in the tracking error shown in Fig. 2.20(f). Note that these simulations contain no modeling error and/or disturbances, hence, the FB current is zero for NPZI, ZPETC, ZMETC, CMPI and PPTC.

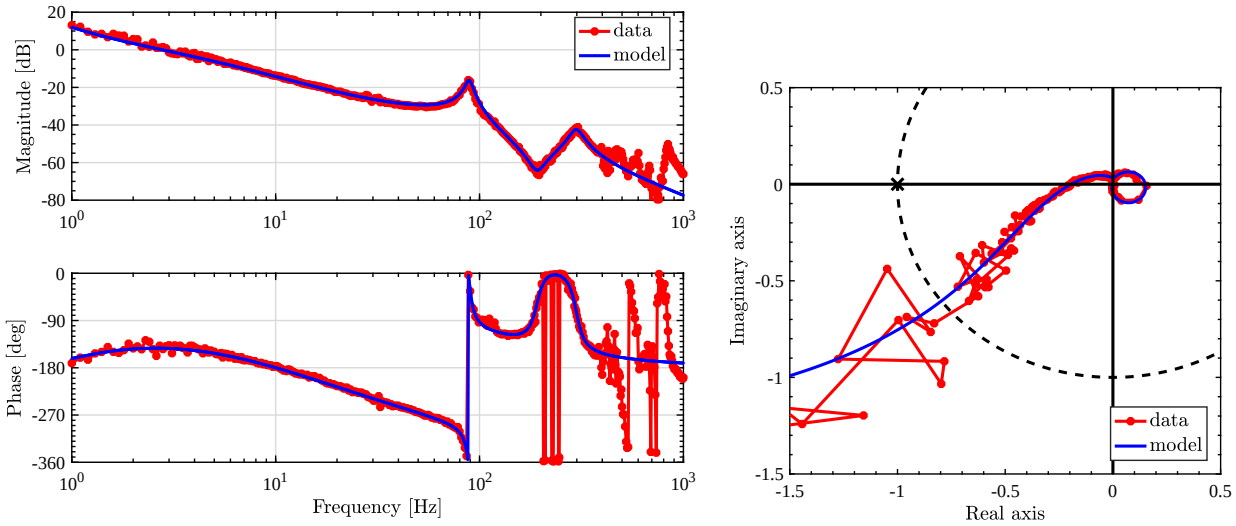

(a) Bode plot of the open loop system.

(b) Nyquist plot of the open loop system.

Figure 2.19 Feedback control performance. Feedback controller is designed as a PID controller and a second order shaping filter. Designed gain and phase margins are 14.2 dB (at 10 Hz) and 37.2 deg (2.8 Hz), respectively.

2.6.5 Experimental results

Because the infinity time preactuation is infeasible, the control input is applied from $t = -0.0428$ s to preactuate the system for the CMPI and PPTC methods. This time length is determined by the aforementioned current sensor resolution. This is 5.38 times longer than the time constant of the dominant unstable zero in continuous time domain. The effect regarding short time preactuation compared to the time constant of the unstable zeros is discussed in Chapter 3.

Experimental results are shown in Fig. 2.21. The trend in the experimental results are in good agreement with the simulations shown in Fig. 2.20. From Fig. 2.21(e) and 2.21(g), during preactuation, the output position has almost no motion. After preactuation, PPTC has almost no undershoot or overshoot. As summarized in Tab. 3.1, the proposed method is experimentally validated.

Fig. 2.21(d) and 2.21(h) show that, except the FB only case, the feedback current references are quite small compared to the feedforward current references. This is because the nominal output $y_o[k]$, which is calculated by the feedforward current reference $u_o[k]$ and the nominal plant $P_n[z_s]$, almost matches the actual output $y(t)$ due to the well identified nominal model.

2.6.6 Observation: comparison with CPMI and PPTC

As described above, the feedforward current reference is similar between the CPMI method and PPTC as shown in Fig. 2.20(g) and 2.21(g). The difference of the two methods is the zero-order hold consideration.

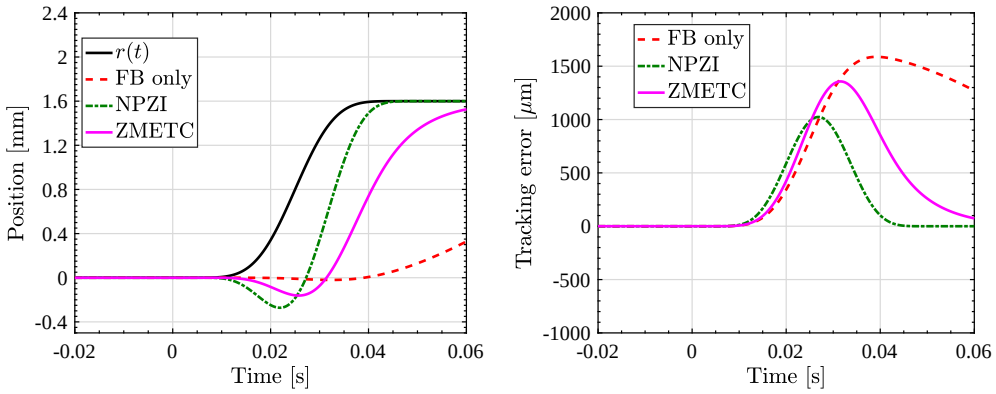

(a) Position.

(b) Tracking error.

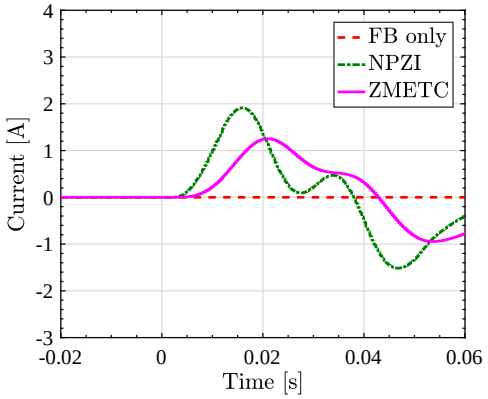

(c) FF current.

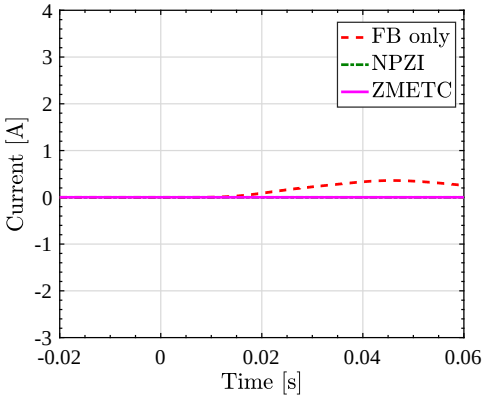

(d) FB current.

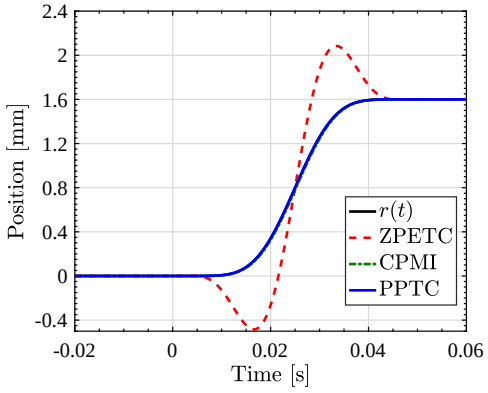

(e) Position.

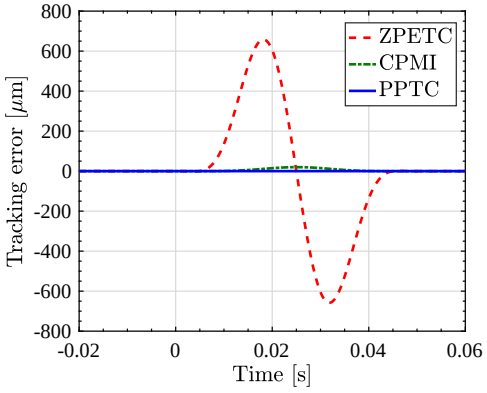

(f) Tracking error.

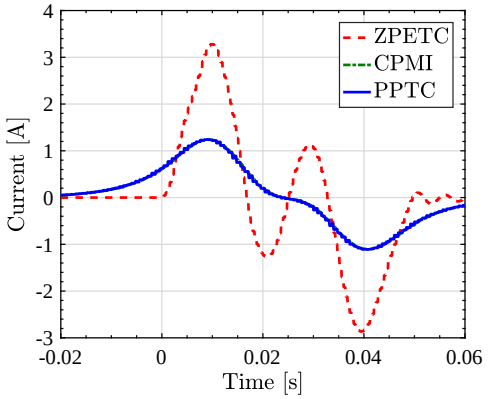

(g) FF current.

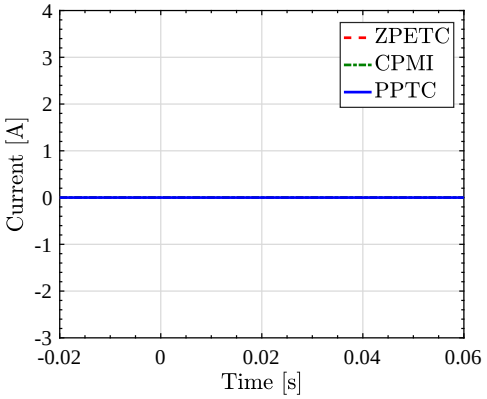

(h) FB current.

Figure 2.20 Simulation with 8th order model shown in Fig. 2.17. Note that in (c) and (f), FB current is zero for NPZI, ZPETC, ZMETC, CPMI, and PPTC due to no modeling error and disturbance assumption.

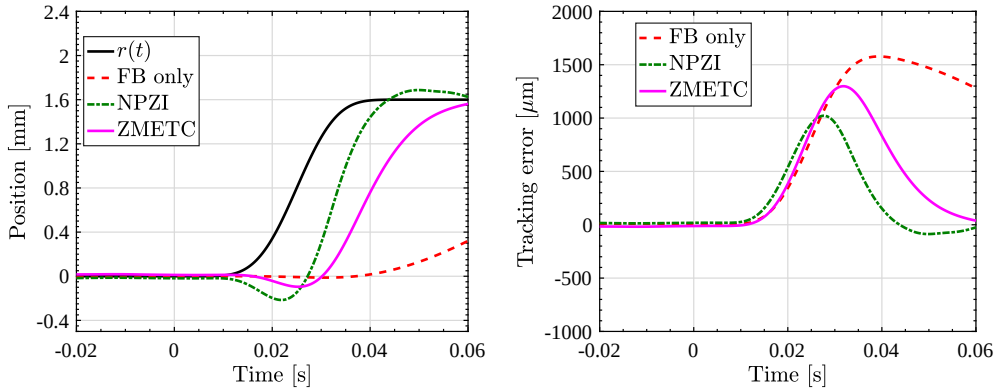

(a) Position.

(b) Tracking error.

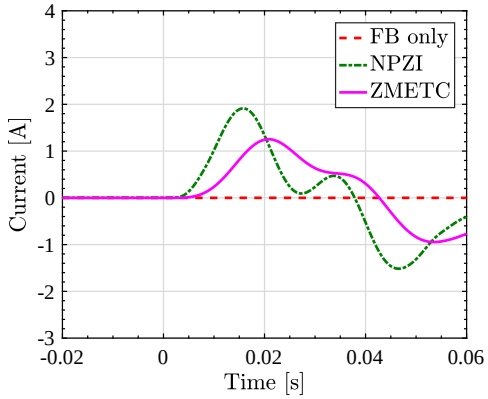

(c) FF current.

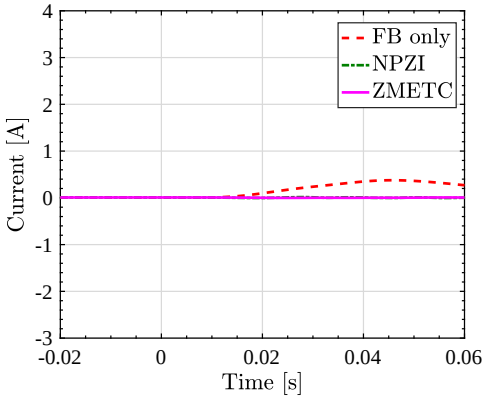

(d) FB current.

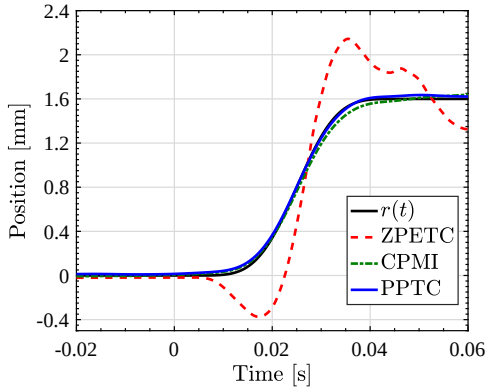

(e) Position.

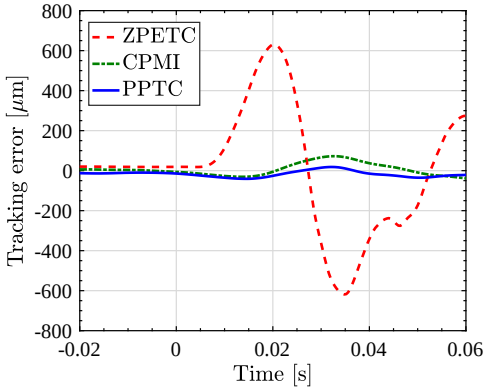

(f) Tracking error.

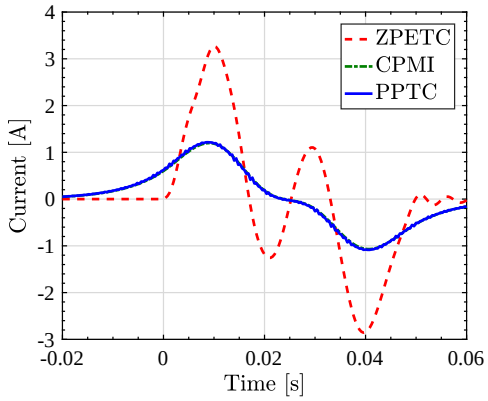

(g) FF current.

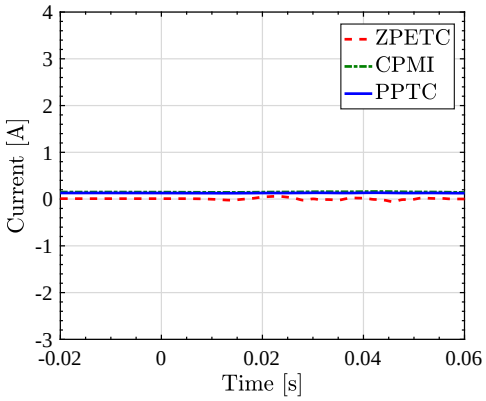

(h) FB current.

Figure 2.21 Experiment with the stage shown in Fig. 2.16. 8th order nominal model is used for feedforward controller design.

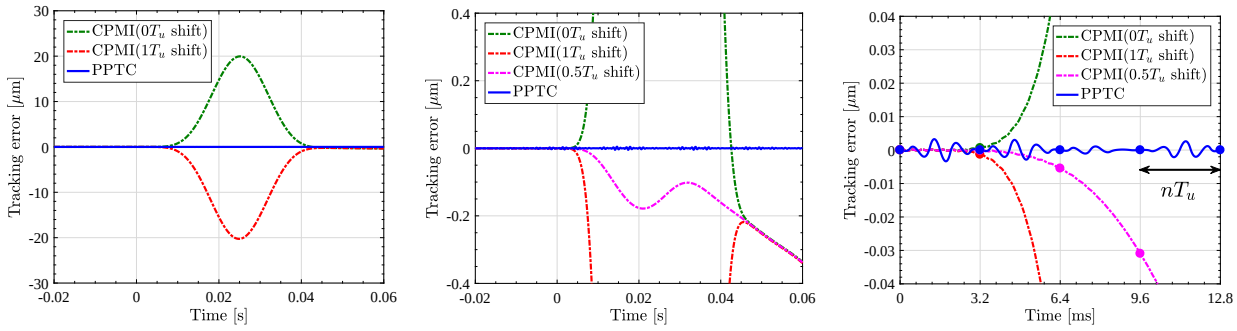

(a) Tracking error. (b) Tracking error (zoom). (c) Tracking error (zoom2).

Figure 2.22 Error comparison between PPTC and shifted CPMI method. Dots are illustrated by every $T_r = nT_u$ (simulation). It shows PPTC achieves the perfect tracking for $T_r = nT_u$ and it's not achievable by CPMI method.

Table 2.2 Maximum tracking error in μm.

	FB only	NPZI	ZMETC	ZPETC	CPMI	PPTC
Sim	1590	1020	1360	658	20.0	0.00491*
Exp	1580	1020	1300	631	72.3	41.1

* Intersample tracking error

Fig. 2.22 shows that tracking error comparison between PPTC and shifted CPMI methods. It shows that the zero-order hold delay cannot be compensated by just shifting the current reference even by a non-integer sample shift. This results clearly shows the importance of multirate feedforward control, which compensates for the zero-order hold delay. Fig. 2.22(c) shows that perfect tracking is achieved by PPTC method for every $T_r = nT_u$.

2.6.7 Discussion: Effect of a wrong feedback error calculation

This section shows the importance to calculate the nominal output $y_d[k]$ and use it for $e_d[k]$ calculation for the feedback controller. Correct block diagram is shown in Fig. 2.1. Important idea in

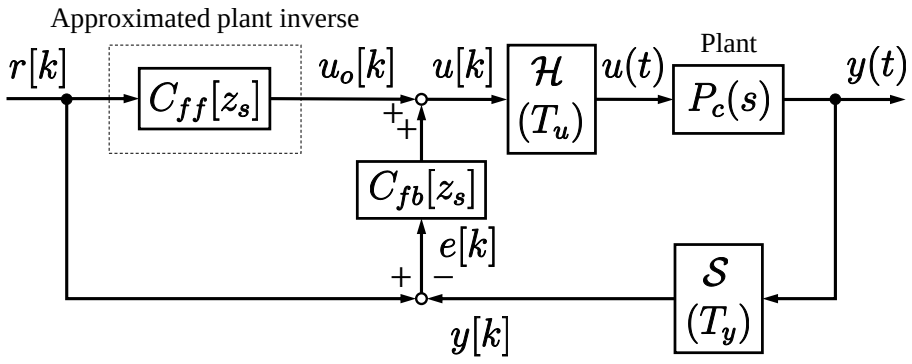

Figure 2.23 Wrong $e_d[k]$ calculation by $e_d[k] = r[k] - y[k]$ for approximated plant inversion methods.

two-degrees-of-freedom is to decouple $e_d[k]$ from $r[k]$ when there is no disturbance or modeling error [128]. Simulations are conducted by using a wrong configuration shown in Fig. 2.23. Comparing Fig. 2.20 and 2.24, the error is increased. Fig. 2.24(d) shows that the feedback controller is used for the reference tracking, which is undesired for two-degrees-of-freedom control.

2.7 Summary

In the discretized domain, there are two types of zeros: 1) the intrinsic zeros which have counterparts in the continuous time domain, 2) the discretization zeros generated by discretization by the zero-order hold. The proposed preactuation perfect tracking control (PPTC) method deals with problem 1) and 2) separately. On one hand, the unstable intrinsic zeros are compensated by the preactuation. On the other hand, the unstable discretization zeros are compensated by the multirate feedforward scheme with preview. Multirate feedforward controller generates the feedforward input which achieves perfect tracking for the designed state trajectory. The simulation results show that the zero-order hold delay cannot be compensated by just shifting the reference and underline the importance of multirate

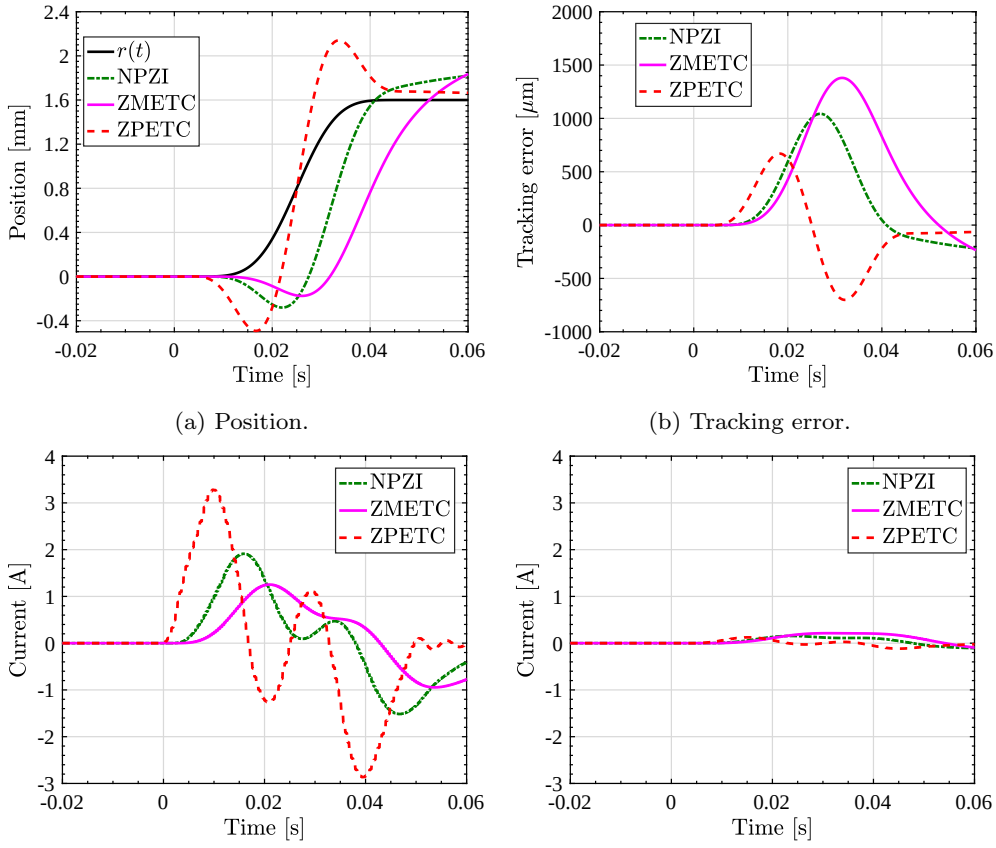

(a) Position.

(b) Tracking error.

(c) FF current.

(d) FB current.

Figure 2.24 Simulation with 8th order model shown in Fig. 2.17 using Fig. 2.23 configuration. Tracking performance is worse compared to Fig. 2.20 because the feedback controller with the low bandwidth is used for the reference tracking (see (d)).

feedforward.

This chapter experimentally validates the PPTC method using a high-precision stage with continuous time unstable zeros. Additionally, this system has a discretization zero. Due to a well identified 8th order model, the experimental results follow the simulations. The experimental result with PPTC strongly reduces the tracking error and achieves almost zero undershoot.

Chapter 3

Finite Preactuation Perfect Tracking Control based on State Trajectory Regeneration by using Redundant Order Polynomial

Abstract

A plant with unstable zeros is considered to be difficult to control because of initial undershoot of step response and unstable poles of its inversion system for a feedforward control. A plant has unstable zeros in discrete time domain because of following reasons: 1) non-collocation of actuators and sensors and 2) discretization by zero-order hold. Chapter 2 proposes a solution for these problems by using a multirate feedforward control with state trajectory generation based on time axis reversal. However, this method requires preactuation for negative infinite time. If we truncate the preactuation for a short time, the tracking error is not negligible. This chapter proposes a state trajectory *regeneration* method by redundant order polynomial to match the state variable after the preactuation. Although this method abandons perfect tracking during preactuation, it guarantees perfect tracking after preactuation. The validity of the proposed method is demonstrated through simulations and experiments.

3.1 Introduction

A plant with unstable zeros is known to be difficult to control because of unstable poles of its inversion system and initial undershoot of step response, as shown in Fig. 1.3. The zeros of the discretized transfer function can be classified as follows [129] [117]: 1) intrinsic zeros and 2) discretization zeros [55]. Intrinsic zeros correspond to zeros of the continuous time transfer function. The others are called discretization zeros. Discretization zeros are unstable when the relative order of the continuous time plant is greater than two even without continuous time unstable zeros [55].

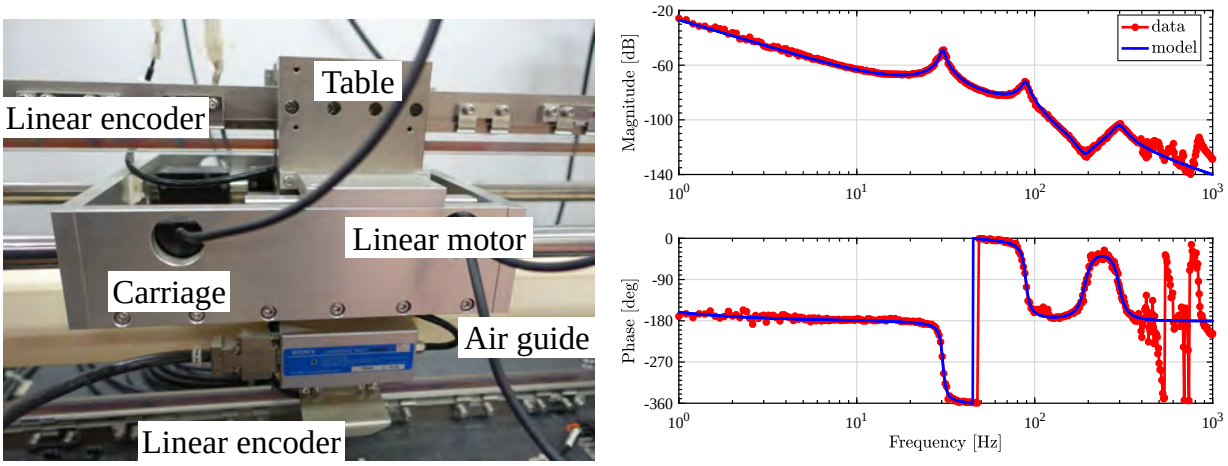

(a) High-precision positioning stage.

(b) Frequency response and its 8th order model.

Figure 3.1 High-precision positioning stage and its model (same as Fig. 2.16(a) and Fig. 2.17).

To design a stable feedforward controller for a plant with unstable zeros, approximated inversion-based feedforward controllers are proposed: for example, nonminimum-phase zeros ignore (NPZI) [30], zero-phase-error tracking controller (ZPETC) [59], and zero-magnitude-error tracking controller (ZMETC) [119]. These controllers handle aforementioned problems 1) and 2) simultaneously because they are designed using discretized transfer functions.

Compensation methods have been proposed for unstable intrinsic and discretization zeros through preactuation and preview [118] [72]. In addition, these methods compensate for intrinsic and discretization zeros simultaneously. A continuous time domain approach was proposed in [122]. This method ignores the zero order hold that all digital control systems have.

In Chapter 2, we propose a method to solve problems 1) and 2) separately. The unstable zeros in the continuous time transfer function are managed through a state trajectory generation based on time axis reversal and preactuation commands. This method can be applied for any reference trajectory, given its $n-1$ th derivative. Here, n denotes the order of the plant in the continuous time transfer function. Next, the plant discretization problem is solved through the multirate feedforward control [103]. However, this method requires preactuation of negative infinite time.

In this chapter, we proposes a finite time preactuation method based on state trajectory regeneration by using a redundant polynomial in the negative time domain. By using the state trajectory regeneration and the finite time preactuation with multirate feedforward, the initial state variables of the plant are matched with the desired initial state variables. As a result, the perfect tracking after preactuation is achieved. Although this method abandons perfect tracking for the reference trajectory r during the preactuation, it guarantees perfect tracking after the finite preactuation. The validity of the proposed method is demonstrated through simulations and experiments.

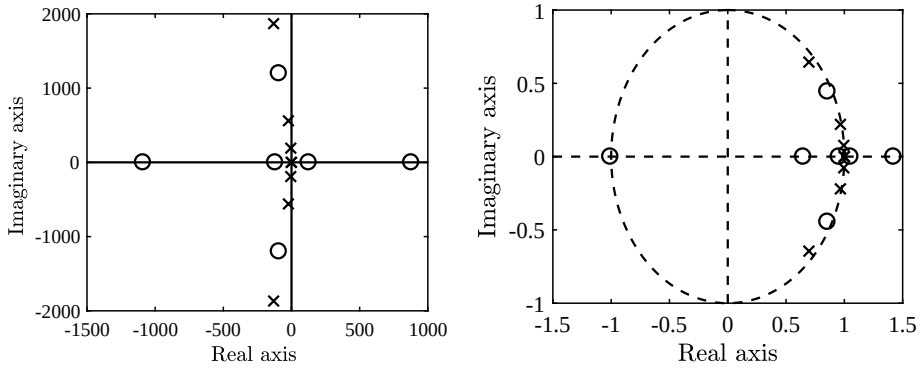

(a) P_c. (b) P_s.

Figure 3.2 Pole-zero map of identified model shown in Fig. 3.1(a) (same as Fig. 2.18).

3.2 Experimental setup

The considered experimental setup shown in Fig. 3.1(a) is an air-guided single degree-of-freedom flexible stage driven by a set of linear motors. The position feedforward controllers are designed with $T_u = 400\ \mu$s sampling time.

The dominant system dynamics of the setup are modeled through frequency domain identification techniques, see [127]. The measured frequency response and estimated 8th order model are shown in Fig. 3.1(b). The model has two unstable zeros in continuous time domain (see Fig. 3.2(a)) and the discretized model by the zero-order hold with $T_u = 400\ \mu$s has two unstable intrinsic zeros and an unstable discretization zero (see Fig. 3.2(b)).

3.3 Truncated series approximation method [130]

Truncated series approximation (TSA) method is proposed in [130]. This is a filter-based finite preactuation method. The approximated unstable zeros mode $\tilde{B}^{\text{ust}}[z_s]$ defined in (2.10) is

$$\frac{1}{\tilde{B}^{\text{ust}}[z_s]} = \frac{\Sigma_{k=0}^{m_T}\alpha_k z_s^k}{\tilde{B}^{\text{ust}}[1]\Sigma_{k=0}^{m_T}\alpha_k}, \tag{3.1}$$

where m_T is the order of the series approximation and the α_i is the coefficients derived from the Taylor series expansion [118, 130].

3.3.1 Deign results

Design results of the truncated series approximation are shown in Fig. 3.3(a). Here, τ denotes the time constant of the dominant unstable zero, which is $\tau = 0.00796$ s. It shows that the longer preactuation time (equivalently higher order approximation) achieves the better approximation.

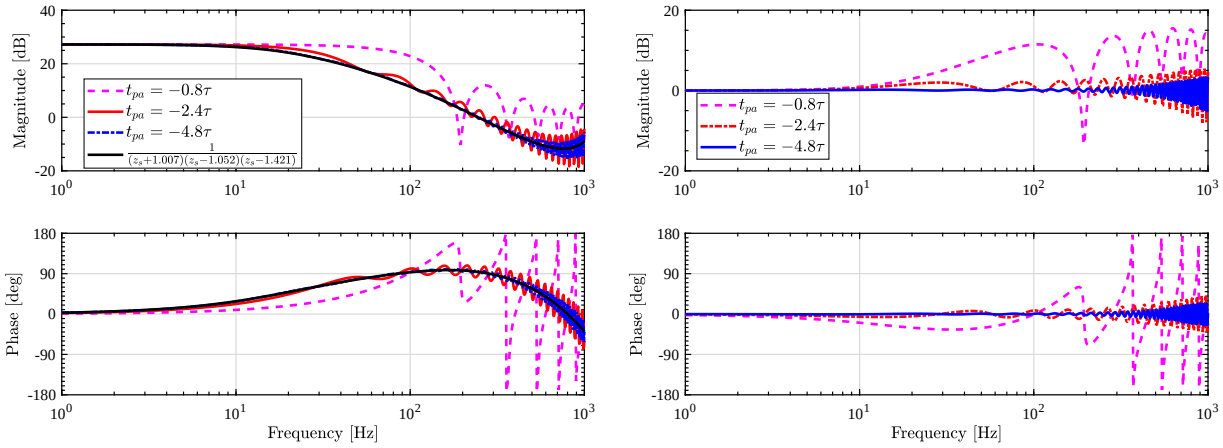

(a) Truncated series approximation. (b) r to y.

Figure 3.3 Bode diagram of TSA method.

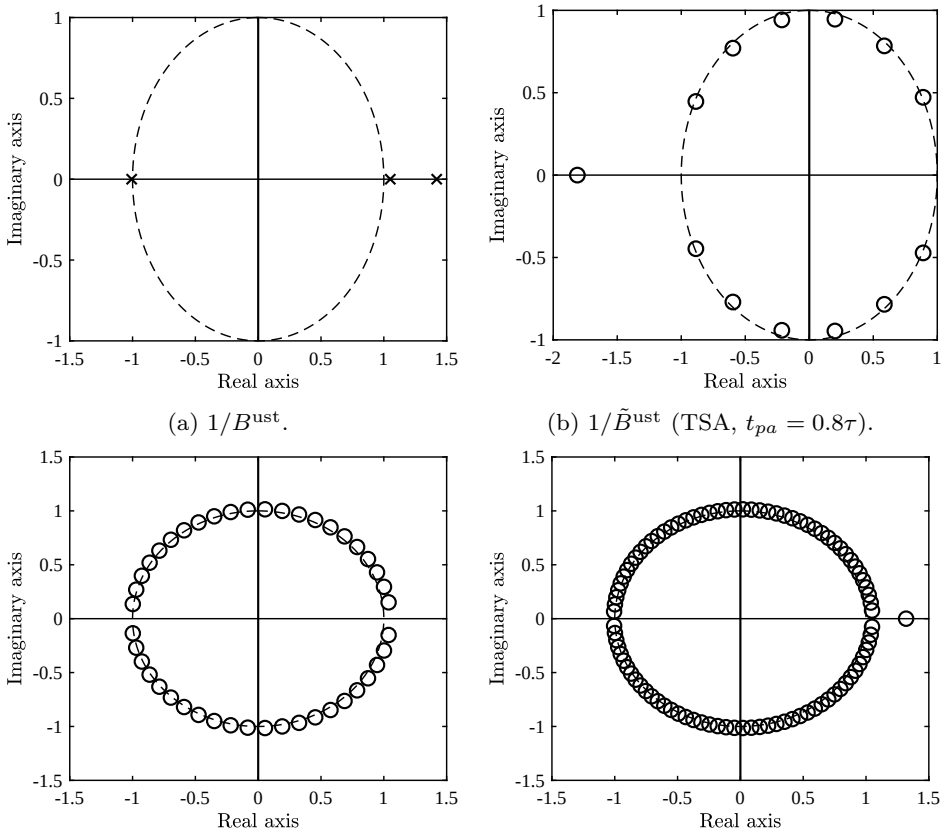

(a) $1/B^{\text{ust}}$. (b) $1/\tilde{B}^{\text{ust}}$ (TSA, $t_{pa} = 0.8\tau$).

(c) $1/\tilde{B}^{\text{ust}}$ (TSA, $t_{pa} = 2.4\tau$). Additional zero at $z_s = 21.3$ (d) $1/\tilde{B}^{\text{ust}}$ (TSA, $t_{pa} = 4.8\tau$).

Figure 3.4 Pole-zero map of TSA method.

Frequency responses of the reference r to the output y is shown in Fig. 3.3(b). Comparing with NPZI, ZPETC, and ZMETC shown in Fig. 2.2, the TSA method almost achieves zero-phase-error and zero-magnitude-error characteristics in the same time. Pole-zero maps of the approximation are shown in Fig. 3.4. The unstable poles (created from inversion of unstable zeros) shown in Fig. 3.4(a) are approximated as finite-impulse-response (FIR) filters.

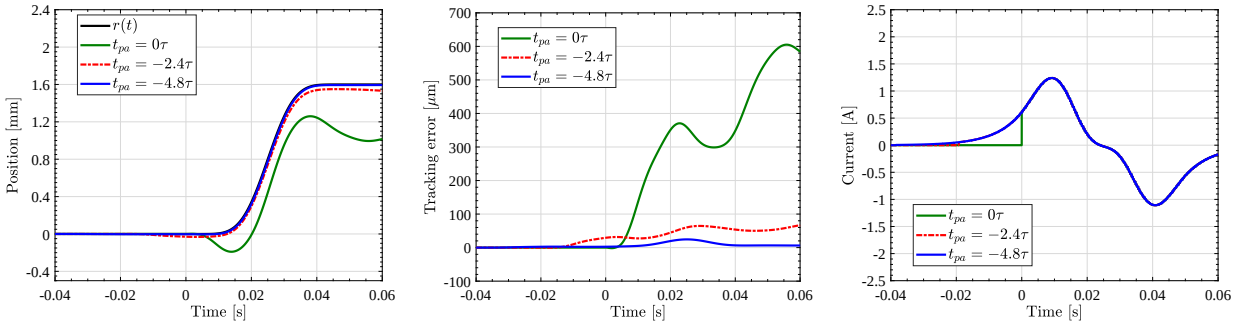

(a) Position. (b) Tracking error. (c) Current.

Figure 3.5 Truncation effect of CPMI method (see Section 2.3.2). $\tau = 0.00796$ s.

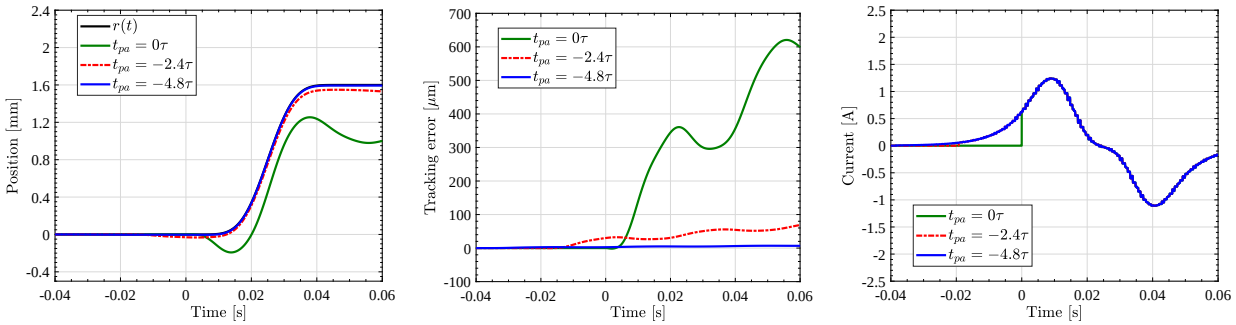

(a) Position. (b) Tracking error. (c) Current.

Figure 3.6 Truncation effect of PPTC method (see Section 2.4). $\tau = 0.00796$ s. Figs. 3.5(b) and 3.6(b) shows that the difference between the truncated between CPMI and PPTC methods becomes obvious when $t_{pa} = -4.8\tau$.

3.4 Preactuation truncation problem

The method introduced in Section 2.4 requires preactuation for $-\infty < t \leq 0$. In practice, infinite preactuation is infeasible. In this section, a simple preactuation truncation is considered.

$$u_o[k] = \begin{cases} 0 & (k < \frac{t_{pa}}{T_u}) \\ u_o[k] & (\text{otherwise}) \end{cases}, \tag{3.2}$$

where t_{pa} ($t_{pa} < 0$) denotes the length of the preactuation time.

However, this method cannot achieve a perfect tracking for not only $t_{pa} < t < 0$ but also $0 \leq t$ because the actual initial state variable $\boldsymbol{x}[0]$ does not match the initial state trajectory $\boldsymbol{x}_d[0]$.

The simulation results are shown in Figs. 3.5 and 3.6. Here, τ denotes the time constant of the dominant unstable zero, which is $\tau = 0.00796$ s. Fig. 3.6 shows the relationship between the preactuation time t_{pa} and the maximum error $||e||_\infty$. The difference between the truncated CPMI and PPTC is because the CPMI method ignores the zero-order hold effects (see 2.6.6). The tracking error of the truncated PPTC is exponentially reduced by longer preactuation ($||e||_\infty \simeq e^{0.94\frac{t_{pa}}{\tau} - 7.45}$).

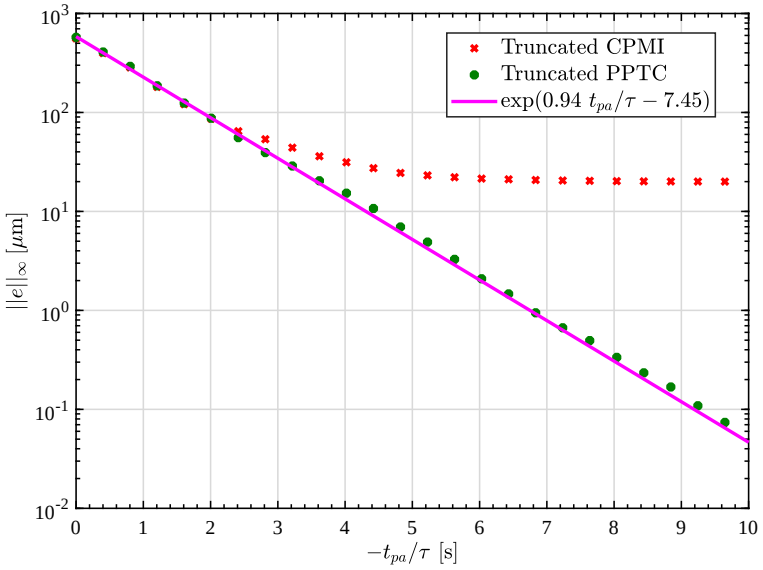

Figure 3.7 The relationship between the maximum tracking error and the preactuation time. Because the CPMI method ignores the zero-order hold, the tracking error of CPMI method does not decrease even with long preactuation.

3.5 Finite preactuation method by state trajectory regeneration

3.5.1 Original state trajectory $\boldsymbol{x}_d$ generation

First, the state trajectory for PPTC, which requires the infinity preactuation, is calculated by the method shown in Section 2.4.1. When the system has unstable zeros in the continuous-time domain, $\boldsymbol{x}_d(t)$ is non-zero for $t < 0$, assuming $\boldsymbol{r}(t) = 0$ when $t < 0$. This is because the unstable part state trajectory $\boldsymbol{x}_d^{\mathrm{ust}}(t)$ has a non-zero value in $t < 0$. Hence, to achieve perfect tracking, non-minimum phase systems require infinite preactuation [125].

A block diagram of the finite preactuation perfect tracking control (FPPTC) is shown in Fig. 3.9.

3.5.2 State trajectory regeneration

This section *regenerates* the state trajectory from a given $t = t_{pa}$ (< 0) to $t = 0$ in order to obtain a realistic *finite* preactuation as follows:

$$\boldsymbol{x}_d(t) = \begin{cases} \boldsymbol{0} & (t < t_{pa}) \\ \tilde{\boldsymbol{x}}_d(t) & (t_{pa} \leq t \leq 0) \\ \boldsymbol{x}_d^{\mathrm{st}}(t) + \boldsymbol{x}_d^{\mathrm{ust}}(t) & (0 < t) \end{cases}. \tag{3.3}$$

The idea and the block diagram are shown in Figs. 3.8 and 3.9. The regenerated state trajectory is defined as $\tilde{\boldsymbol{x}}_d(t)$. Although this method abandons perfect tracking for $t_{pa} < t < 0$, it achieves the

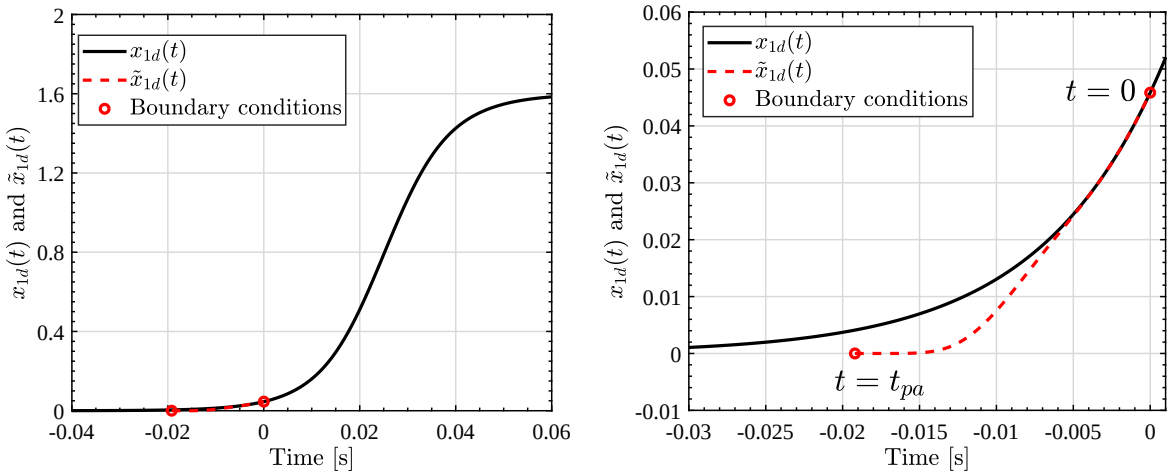

(a) $x_{1d}(t)$ and $\tilde{x}_{1d}(t)$. (b) Zoom of Fig. 3.8(a).

Figure 3.8 Idea of the state trajectory regeneration for $x_{1d}(t)$. When the plant has unstable zeros in continuous-time domain, $x_{1d}(t)$ has non-zero value in the negative infinite time. This method regenerates the state trajectory for a finite time $t_{pa} \leq t \leq 0$ as formulated in (3.3). $\tilde{\boldsymbol{x}}_d(t)$ is calculated from $\tilde{x}_{1d}(t)$ by (3.4).

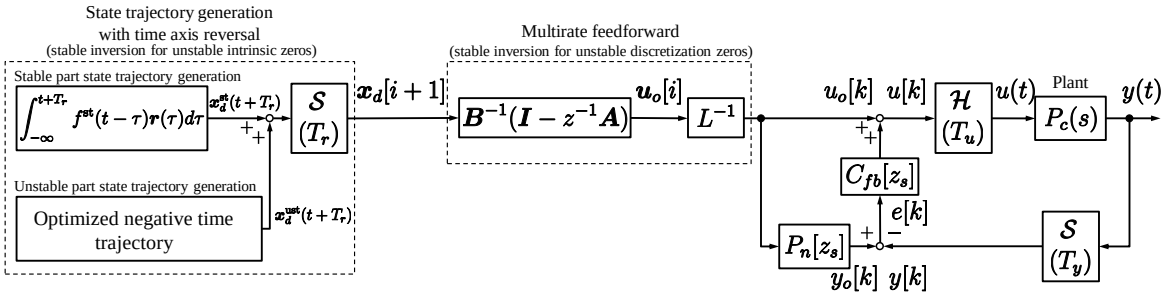

Figure 3.9 Finite preactuation perfect tracking control (FPPTC).

perfect tracking for $0 \leq t$ because it can match $\boldsymbol{x}_d(t)$ and $\boldsymbol{x}(t)$ by the multirate feedforward.

As defined in (2.4), the plant is realized through the controllable canonical form

$$\begin{aligned}\tilde{\boldsymbol{x}}_d(t) &= \begin{bmatrix}\tilde{x}_{1d}(t) & \tilde{x}_{2d}(t) & \cdots & \tilde{x}_{nd}(t)\end{bmatrix}^{\mathrm{T}}, \\ &= \begin{bmatrix}\tilde{x}_{1d}(t) & \frac{d}{dt}\tilde{x}_{1d}(t) & \cdots & \frac{d^{n-1}}{dt^{n-1}}\tilde{x}_{1d}(t)\end{bmatrix}^{\mathrm{T}},\end{aligned} \tag{3.4}$$

where n denotes the order of the plant.

We define $\tilde{x}_{1d}(t)$ as a n_tth order polynomial

$$\tilde{x}_{1d}(t) = \tilde{a}_0 + \tilde{a}_1 t + \tilde{a}_2 t^2 + \cdots + \tilde{a}_{n_t} t^{n_t}. \tag{3.5}$$

The coefficients $\tilde{a}_0, \tilde{a}_1, \tilde{a}_2, \cdots, \tilde{a}_{n_t}$ are defined as

$$\tilde{\boldsymbol{a}} = \begin{bmatrix}\tilde{a}_0 & \tilde{a}_1 & \cdots & \tilde{a}_{n_t}\end{bmatrix}. \tag{3.6}$$

From (3.4) and (3.5), the regenerated state trajectory $\tilde{\boldsymbol{x}}_d(t)$ is derived as the function of $\tilde{\boldsymbol{a}}$ and t.

$\tilde{\boldsymbol{x}}_d(t)$ should satisfy the two boundary conditions $\tilde{\boldsymbol{x}}_d(t_{pa}) = \boldsymbol{0}$ and $\tilde{\boldsymbol{x}}_d(0) = \boldsymbol{x}_d(0)$ to realize the finite

preactuation and perfect tracking after the preactuation. Hence, the minimum order of the polynomial is $2n-1$ because we have $2n$ elements in boundary conditions. We define the order of the redundancy of the trajectory n_r

$$n_r = n_t - (2n-1) \tag{3.7}$$

The desired output $y_d(t)$ is calculated by the output equation defined in (2.4),

$$y_d(t) = \boldsymbol{c}_d \tilde{\boldsymbol{x}}_d(t). \tag{3.8}$$

From the above, the tracking error e_d during the finite preactuation is

$$e_d(t) = r(t) - y_d(t) \tag{3.9}$$
$$= -y_d(t), \tag{3.10}$$

assuming $r(t) = 0$ when $t_{pa} \leq t < 0$. From the above, $y_d(t)$ and e_d are function of $\tilde{\boldsymbol{a}}$ and t.

An optimization problem is formulated as (3.11) and (3.12). We minimize the jerk of the output $y_d(t)$ to generate smooth control input. The minimum jerk trajectory has also advantage about less excitations for high-frequency unmodeled dynamics [20].

$$\underset{\tilde{\boldsymbol{a}}(\cdot)}{\text{minimize}} \quad J = \int_{t_{pa}}^{0} (\dddot{y}_d(t))^2 dt \tag{3.11}$$
$$\text{subject to} \quad \tilde{\boldsymbol{x}}_d(t_{pa}) = \boldsymbol{0}, \quad \tilde{\boldsymbol{x}}_d(0) = \boldsymbol{x}_d(0) \tag{3.12}$$

3.5.3 Feedforward input u_o generation from $\boldsymbol{x}_d$

The feedforward control input $\boldsymbol{u}_o$ is obtained by the multirate feedforward control as Section 2.4.2.

$$\boldsymbol{u}_o[i] = \boldsymbol{B}^{-1}(\boldsymbol{I} - z^{-1}\boldsymbol{A})\boldsymbol{x}_d[i+1], \tag{3.13}$$

where $z = e^{sT_r}$. The feedforward input $\boldsymbol{u}_o$ achieves the perfect state matching for $\boldsymbol{x}_d$ every nT_u.

3.6 Simulation

The model shown in Section 3.2 is used for the simulation. The target trajectory is given as a 0.05 s step reference interpolated by a 15th order polynomial and it is shown in e.g. Fig. 3.11(a). This is same as Section 2.6.

The relationship between the redundancy of the trajectory order n_r and the objective function (3.11) is shown in Fig. 3.13. In the following simulation and experimental results, n_r is set as 8 because the objective function is sufficiently small.

The simulation results of the TSA method and FPPTC are shown in Figs. 3.10 and 3.11. Longer

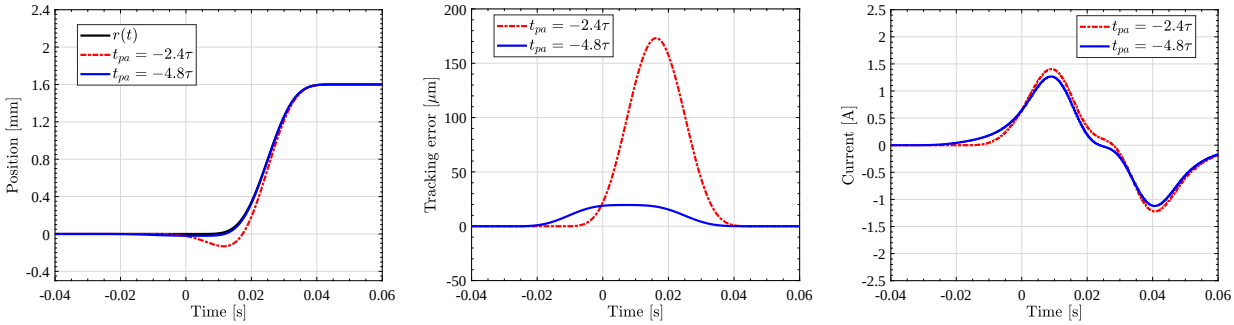

(a) Position. (b) Tracking error. (c) Current.

Figure 3.10 TSA method and t_{pa} tendency. $\tau = 0.00796$ s.

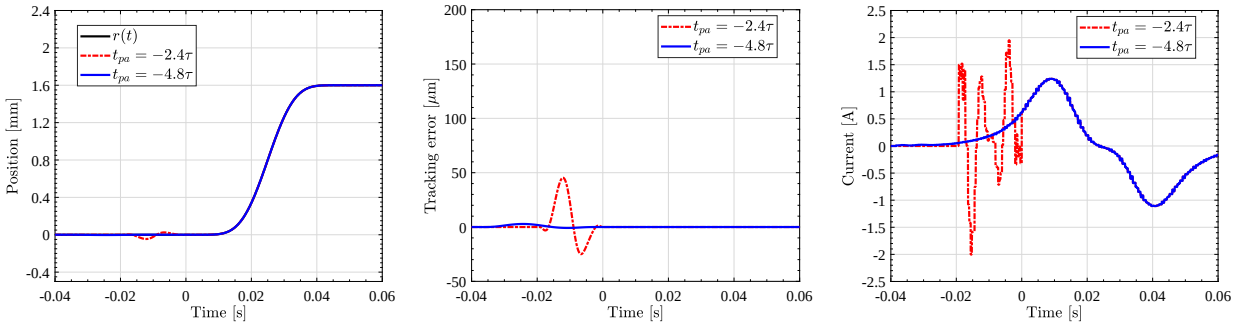

(a) Position. (b) Tracking error. (c) Current.

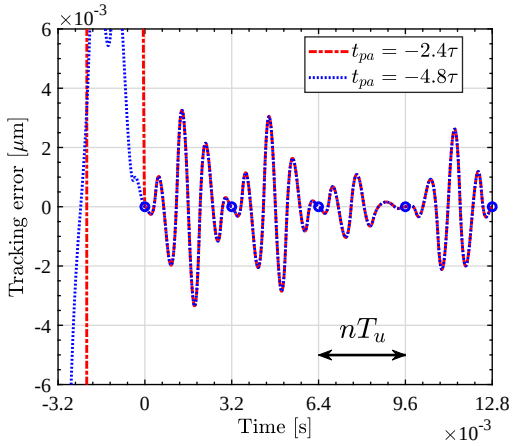

(d) Zoom of Fig. 3.11(b).

Figure 3.11 FPPTC method and t_{pa} tendency. $\tau = 0.00796$ s (simulation). Fig. 3.11(d) shows that FPPTC method achieves the perfect tracking for every $T_r = nT_u$ regardless of the preactuation time t_{pa}.

preactuation helps the smaller tracking error and smaller control input.

When the preactuation time t_{pa} is too short, FPPTC method generated an infeasible result. In this case, an optimal state trajectory generation without preactuation (see Chapter 5) is recommended. Comparing Figs. 3.10 and 3.11, FPPTC method achieves much smaller error for $t_{pa} = -2.4\tau$ and $t_{pa} = -4.8\tau$. Fig. 3.11(d) shows that FPPTC method achieves the perfect tracking for every $T_r = nT_u$ regardless of the preactuation time t_{pa}.

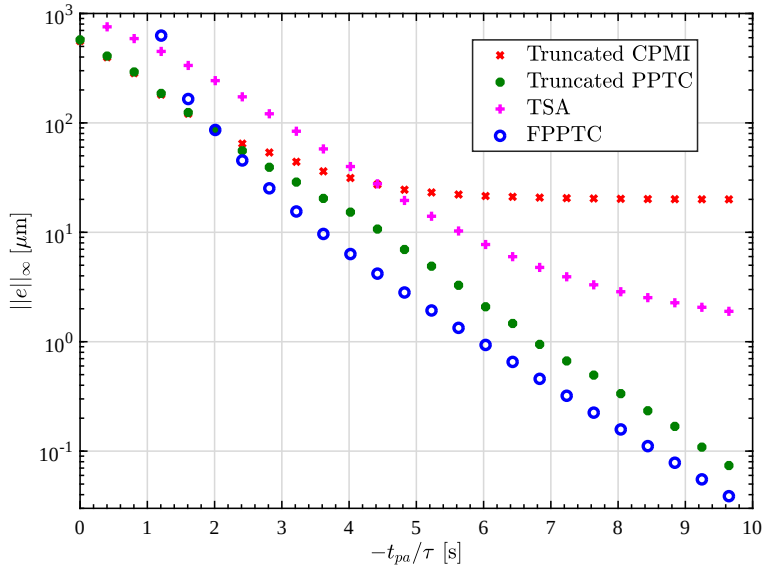

Figure 3.12 Relationship between the maximum tracking error and the preactuation time.

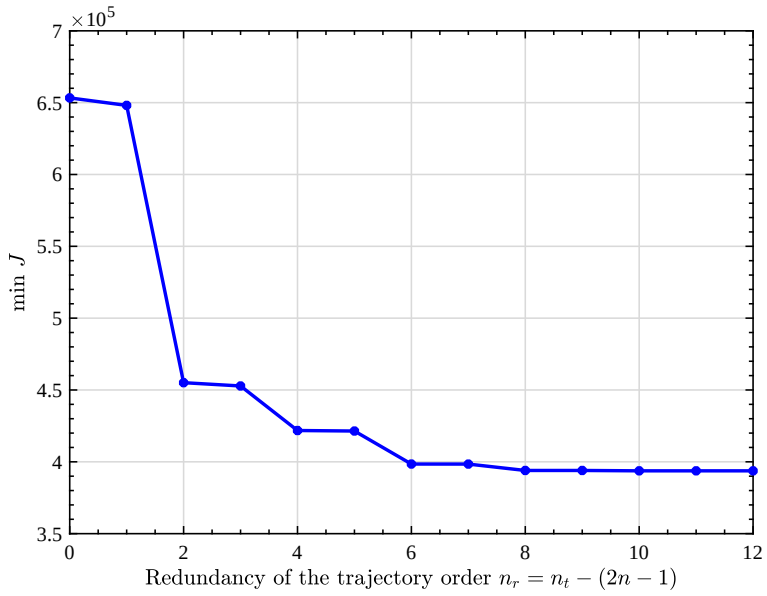

Figure 3.13 Relationship between the minimum value of J and the redundancy of the trajectory order n_r in (3.7) ($t_{pa} = -2.4\tau$).

3.7 Experimental validation

3.7.1 Conditions

The same feedback controller shown in Section 2.6 is used (see Fig. 2.19). Designed gain and phase margins are 14.2 dB (at 10 Hz) and 37.2 deg (2.8 Hz), respectively. The target trajectory is given as a 0.05 s step reference interpolated by a 15th order polynomial and is shown in Fig. 3.10(a).

Table 3.1 Maximum tracking error in μm ($0.04\,\mathrm{s} \leq t \leq 0.06\,\mathrm{s}$, $t_{pa} = -2.4\tau$).

	FB only	NPZI	ZMETC	ZPETC	Truncated PPTC	TSA	FPPTC
Sim	1590	1020	1360	658	68.9	173	45.4
Exp	1580	1020	1300	631	65.9	129	43.6

3.7.2 Simulation and experimental results

Simulation and experimental results are shown in Fig. 3.14–3.17. In all comparison, the experimental results well follows the simulation results. Figs. 3.14 and 3.15 show that TSA method achieves better performance compared to ZPETC and ZMETC methods. Despite the same preactuation time for TSA and FPPTC methods, FPPTC method achieves smaller tracking error than TSA method. Figs. 3.16 and 3.17 compare TSA, Truncated PPTC, and FPPTC methods for the same preactuation time $t_{pa} = -2.4\tau$.

3.8 Summary

In the discretized domain, a plant has two types of zeros: 1) intrinsic zeros, which have counterparts in the continuous time domain, and 2) discretization zeros generated through discretization. The feedforward control is thus difficult because of unstable pole(s) of its inversion system. According to Chapter 2, the unstable intrinsic and discretization zeros can be managed separately through the combination of multirate feedforward and state trajectory generation with time axis reversal. However, this method needs infinite time preactuation.

This chapter proposes a finite time preactuation method based on state trajectory regeneration using a redundant order polynomial. The proposed method can achieve perfect tracking after preactuation. Owing to the multirate feedforward and controllable canonical form realization, the proposed method can formulate the state trajectory during preactuation as a polynomial. The polynomial defined trajectory enables us to apply the optimization. The effectiveness of the proposed method is demonstrated through simulations and experiments.

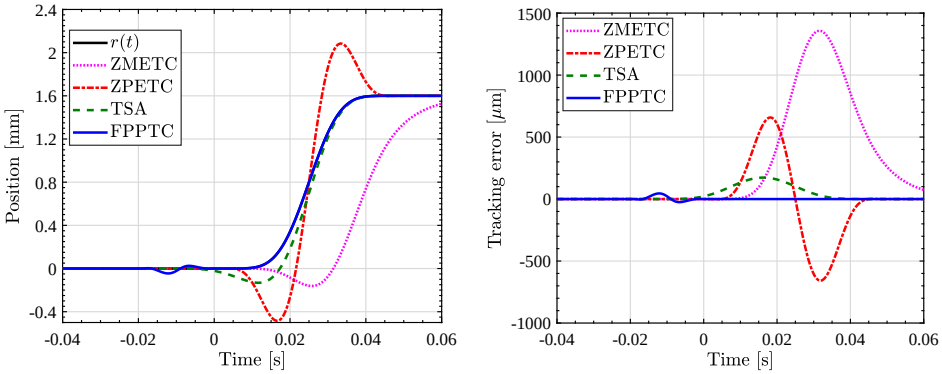

(a) Position.

(b) Tracking error.

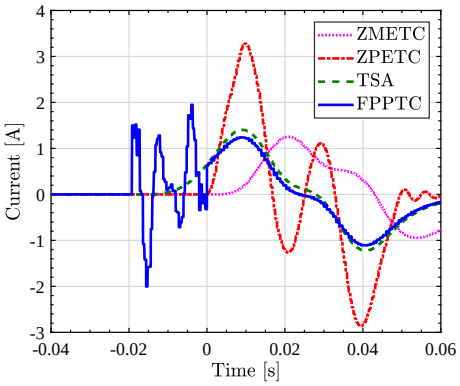

(c) FF Current.

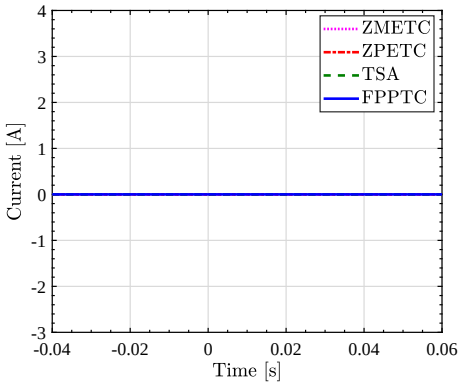

(d) FB Current.

Figure 3.14 Simulation results ($t_{pa} = -2.4\tau$ for TSA and FPPTC).

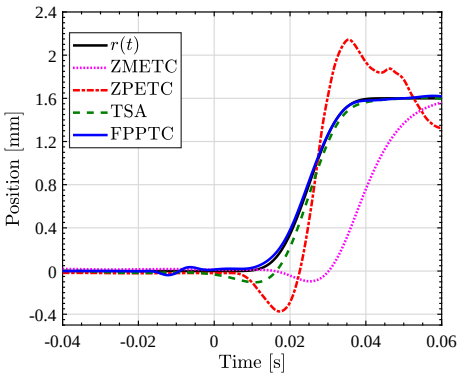

(a) Position.

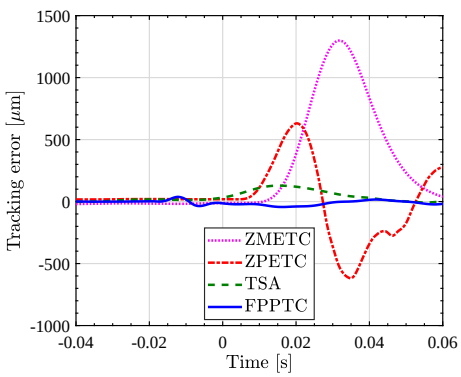

(b) Tracking error.

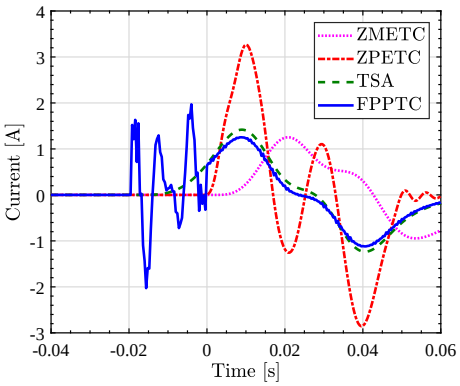

(c) FF Current.

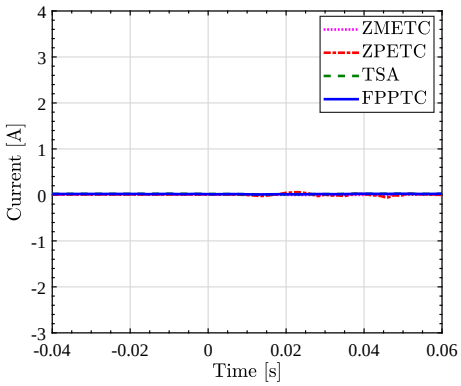

(d) FB Current.

Figure 3.15 Experimental results ($t_{pa} = -2.4\tau$ for TSA and FPPTC).

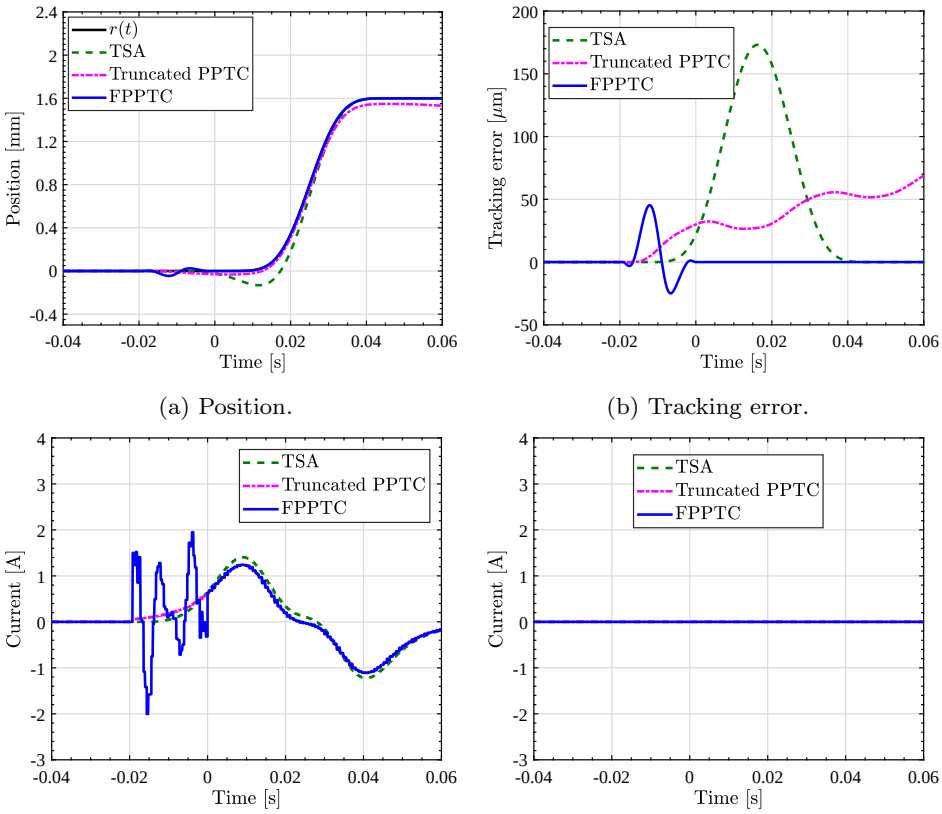

(a) Position. (b) Tracking error.

(c) FF Current. (d) FB Current.

Figure 3.16 Simulation results ($t_{pa} = -2.4\tau$ for TSA, Truncated PPTC, and FPPTC).

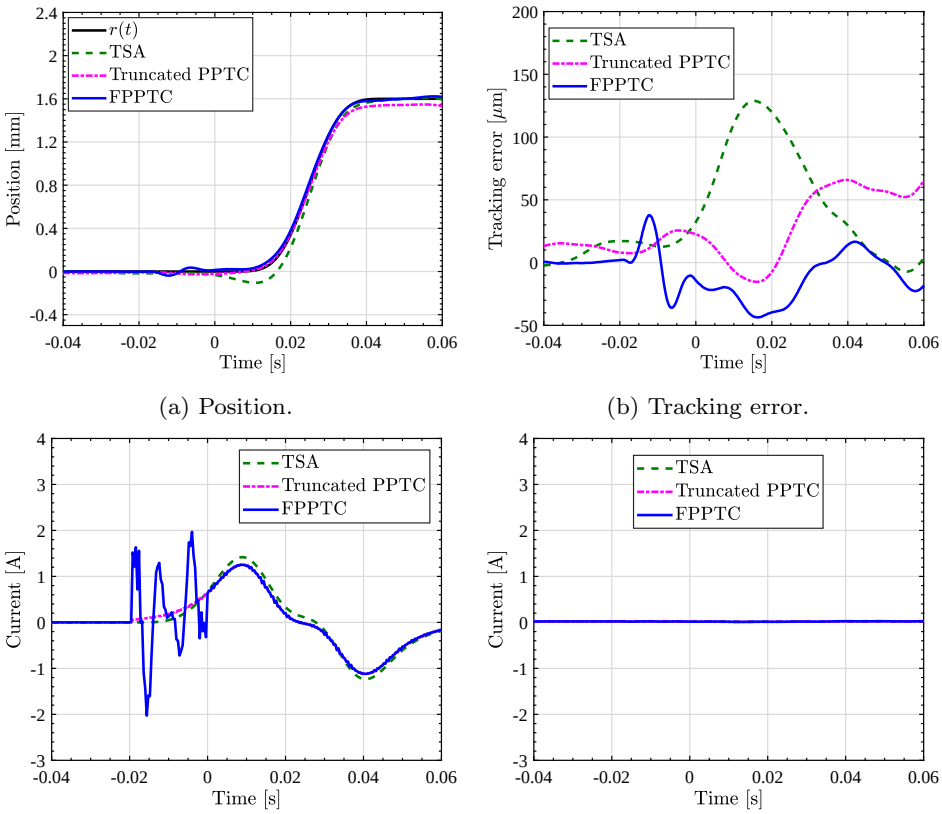

(a) Position. (b) Tracking error.

(c) FF Current. (d) FB Current.

Figure 3.17 Experimental results ($t_{pa} = -2.4\tau$ for TSA, Truncated PPTC, and FPPTC).

Chapter 4

Minimum Time Optimal Preactuation considering Control Input and Tracking Error Constraints

Abstract

To achieve perfect reference trajectory tracking, a plant with continuous time unstable zeros requires an *infinite* time preactuation. Albeit, this is practically infeasible, as typical high-precision motion systems target a short time *finite* preactuation. Truncating the control input to a short time preactuation leads to undesirable tracking errors. This chapter, thus, proposes a minimum time preactuation method with an optimized state trajectory considering control input and tracking error constraints. The proposed method generates an optimal state trajectory for a given reference and finite time while explicitly considering the actuator, i.e. peak force, and stroke, i.e. maximum undershoot, limitations of the system. A multirate feedforward scheme is subsequently presented to obtain a discretized control input that perfectly tracks the designed optimal continuous state trajectory. In comparison to conventional finite preactuation methods, the proposed approach reaches an order of magnitude lower tracking error bounds. Additionally, this finite time procedure attains, in contrast to conventional optimization approaches, through a multirate feedforward formulation, perfect tracking during the main motion after preactuation.

4.1 Introduction

Model-inverse feedforward control is an effective approach for trajectory tracking problems [20, 30]. Classic inversion provides, in theory, exact reference tracking, but leads to internal instability for systems with unstable zero(s), i.e. nonminimum phase (NMP) systems [131]. In discrete-time domain,

unstable zeros are classified as 1) intrinsic zeros proper to the plant dynamics (due to non-collocation of sensor and actuator) and 2) discretization zeros (due to fast signal sampling) [117]. Note that, discretization zeros are unstable when the relative order of the continuous time plant is greater than two, even without continuous-time unstable zeros [55].

Extensive research has been dedicated to feedforward control design of NMP systems and applied in a wide variety of applications, e.g. in scanning stages [1, 83], hard disk drives [53] and boost converters [54]. Existing approaches are typically analytical filter-based and can be categorized as either i) approximate model-inversion methods or ii) preactuated model-inversion methods. In the former case, the plant-model approximation results in an inherent trade-off between overshoot and setting time [30]. In the latter case, an exact continuous time model-inversion for 1) intrinsic zeros is obtain, albeit introducing tracking errors in the implementation by neglecting the 2) discretization zeros [70–72]. To address this problem, Chapter 2 proposes a preactuated perfect tracking control (PPTC) method, which solves problems 1) and 2) separately. On one hand, the continuous-time unstable zeros are stably inverted by preactuation, on the other hand the discretization zeros are stably inverted by a multirate feedforward approach [103]. Yet, this procedure requires, as former exact model-inversion methods, an *infinite* time preactuation. This is practically infeasible and may result in undesirably large tracking errors when simply truncating the control input (see Fig. 4.3).

A hybrid approach achieving finite time preactuation through a noncausal Taylor series approximation (TSA) is proposed in [130]. This method approximates the inverse of the unstable zeros by a finite order of the Taylor-series expansion, resulting in a finite preactuation. Alternatively, numerical optimization based approaches have been proposed (e.g. [132]) achieving finite-time preactuation, albeit at the cost of approximation errors during the main motion after preactuation.

This chapter improves the *infinite* time preactuation approach proposed in Chapter 2 by adding a constrained optimization step in order to achieve a *minimum* time preactuation while maintaining an exact inverse of the system during the main motion after preactuation. The procedure is based on the previously proposed two step framework: i) the generation of the desired state trajectory $\boldsymbol{x}_d(t)$ from the reference trajectory $\boldsymbol{r}(t)$ and its derivatives, and ii) the generation of the feedforward input $\boldsymbol{u}_o[i]$ from the discrete state trajectories $\boldsymbol{x}_d[i+1]$ through a multirate feedforward implementation [103]. However, this chapter extends step i) by generating an *optimal* state trajectory for a given reference and finite time while explicitly considering the actuator, i.e. peak force, and stroke, i.e. maximum undershoot, constraints of the system. The minimum feasible time is obtained by the bisection method. The effectiveness of this optimal control problem is demonstrated through simulations using a typical scanning stage model, whose dominant zero is unstable.

4.2 Minimum time finite preactuation perfect tracking control

The same notation shown in Section 2.2 is used.

4.2.1 Original state trajectory $\boldsymbol{x}_d$ generation

First, the state trajectory for PPTC, which requires the infinity preactuation, is calculated by the method shown in Section 2.4.1. When the system has unstable zeros in the continuous-time domain, $\boldsymbol{x}_d(t)$ is non-zero for $t < 0$, assuming $\boldsymbol{r}(t) = 0$ when $t < 0$. This is because the unstable part state trajectory $\boldsymbol{x}_d^{\mathrm{ust}}(t)$ has a non-zero value in $t < 0$. Hence, to achieve perfect tracking, nonminimum phase systems require infinite preactuation [125].

A block diagram of the finite preactuation perfect tracking control (FPPTC) is shown in Fig. 3.9.

4.2.2 State trajectory re-generation

Due to the stable inversion for the continuous time unstable zeros, $\boldsymbol{x}_d(t)$ is non-zero for $t < 0$, assuming $\boldsymbol{r}(t) = 0$ when $t < 0$. Hence, to achieve perfect tracking, nonminimum phase systems require infinite preactuation [125].

This section *regenerates* the state trajectory from a given $t = t_{pa}$ (< 0) to $t = 0$ in order to obtain a realistic *finite* preactuation as follows:

$$\boldsymbol{x}_d(t) = \begin{cases} \boldsymbol{0} & (t < t_{pa}) \\ \tilde{\boldsymbol{x}}_d(t) & (t_{pa} \le t \le 0) \\ \boldsymbol{x}_d^{\mathrm{st}}(t) + \boldsymbol{x}_d^{\mathrm{ust}}(t) & (0 < t) \end{cases}, \tag{4.1}$$

where $\tilde{\boldsymbol{x}}_d(t)$ denotes the regenerated state trajectory. The regenerated state trajectory is defined by a piecewise polynomial.

Problem setting

Two constrained optimization problems are proposed for the state reference regeneration.

- Minimum tracking error

  A semi-infinite optimization for preactuation tracking error is formalized here as

$$\underset{\boldsymbol{x}(\cdot)}{\text{minimize}} \quad \|e_d(t)\|_p = \|r(t) - y_d(t)\|_p, \quad p = 1, 2, \infty \tag{4.2}$$

$$\underset{\forall t \in [t_{pa}, 0]}{\text{subject to}} \quad \tilde{\boldsymbol{x}}_d(t_{pa}) = \boldsymbol{0}, \quad \tilde{\boldsymbol{x}}_d(0) = \boldsymbol{x}_d(0) \tag{4.3}$$

$$y_{min} \le y[k] \le y_{max}, \quad u_{min} \le u[k] \le u_{max} \tag{4.4}$$

The tracking error $e_d(t)$ is minimized over $t_{pa} \leq t \leq 0$ taking into account both the physical constraints of the stage, e.g. stroke y_{min}, y_{max} and actuator, e.g. peak current u_{min}, u_{max}. Although this method abandons perfect tracking over $t_{pa} < t < 0$, it guarantees perfect tracking for $0 \leq t$ by constraining the re-generated state trajectory $\tilde{\boldsymbol{x}}_d(t)$ at $t = 0$ to match the desired state trajectory $\boldsymbol{x}_d(t)$ calculated using (2.34).

Despite the good tracking achieved through this formulation given a certain t_{pa}, the resulting constrained feedforward output is impeded by a high jerk.

- Minimum jerk input

  A second semi-infinite optimization problem for preactuation feedforward input is formalized here as

$$\begin{aligned} \underset{\boldsymbol{x}(\cdot)}{\text{minimize}} \quad & \|\dot{\boldsymbol{u}}_{reg}\|_\infty \\ \underset{\forall t \in [t_{pa},0]}{\text{subject to}} \quad & \tilde{\boldsymbol{x}}_d(t_{pa}) = \mathbf{0}, \quad \tilde{\boldsymbol{x}}_d(0) = \boldsymbol{x}_d(0) \\ & e_{min} \leq e_d[k] \leq e_{max}, \quad u_{min} \leq u[k] \leq u_{max} \end{aligned} \tag{4.5}$$

  $\boldsymbol{u}_{reg}$ is the control input during the finite preactuation obtained by (4.8).

  The objective of this setting is to balance the control performance (i.e. maximum error) and the smoothness of the control input.

Problem formulation

Eq. (4.2) and (4.5) are optimal control problems where one is interested in finding the input $\boldsymbol{u}_{reg}$ that brings the system from an initial state $\tilde{\boldsymbol{x}}_d(t_{pa}) = \mathbf{0}$ to a final state $\boldsymbol{x}_d(0)$ and that minimizes a performance criterion while obeying state and input constraints. The difficulty of solving these states optimal control problem is the need for numerically costly integration. Albeit, this is avoided in the multi-rate feedforward formulation used here, the plant is realized through the controllable canonical form

$$\begin{aligned} \tilde{\boldsymbol{x}}_d(t) &= \begin{bmatrix} \tilde{x}_{1d}(t) & \tilde{x}_{2d}(t) & \cdots & \tilde{x}_{nd}(t) \end{bmatrix}^{\mathrm{T}}, \\ \tilde{x}_{qd}(t) &= \rho^{q-1}\tilde{x}_{1d}(t), \quad q = 2, 3, \cdots, n, \end{aligned} \tag{4.6}$$

where $\tilde{x}_{1d}(t)$ is a piecewise polynomial defined in $t_{pa} \leq t \leq 0$. The desired output $y_d(t)$ is then defined as a linear function of $\tilde{x}_{1d}(t)$

$$\begin{aligned} y_d(t) &= \boldsymbol{c}_c \tilde{\boldsymbol{x}}_d(t) \\ &= \boldsymbol{c}_c \begin{bmatrix} \tilde{x}_{1d}(t) & \rho\tilde{x}_{1d}(t) & \dots & \rho^{n-1}\tilde{x}_{1d}(t) \end{bmatrix}^{\mathrm{T}} \end{aligned} \tag{4.7}$$

Hence, simplifying the evaluation of the tracking error during preactuation in (4.2) to a linear function of the state vector $\tilde{\boldsymbol{x}}_d(t)$. To evaluate the control input during preactuation in (4.5), the multirate feedforward control shown in (4.12) is applied [*1].

4.2.3 Multirate feedforward control

This subsection applies multirate feedforward control [103] as Section 2.4.2 to generate the feedforward input $\boldsymbol{u}_o$, which can achieve the perfect tracking for every nT_u, from $\boldsymbol{x}_d(t)$.

Fig. 3.9 shows that there are three time periods T_y, T_u, and T_r denoting the periods for $y(t)$, $u(t)$, and $r(t)$, respectively. These periods are set as $T_r = nT_u = nT_y$. The multirate system of (2.5) is given as

$$\boldsymbol{x}[i+1] = \boldsymbol{A}\boldsymbol{x}[i] + \boldsymbol{B}\boldsymbol{u}_o[i],\ \ y[i] = \boldsymbol{c}\boldsymbol{x}[i], \tag{4.9}$$

where

$$\begin{aligned} &\boldsymbol{A} = \boldsymbol{A}_s^n,\ \ \boldsymbol{B} = \begin{bmatrix} \boldsymbol{A}_s^{n-1}\boldsymbol{b}_s & \boldsymbol{A}_s^{n-2}\boldsymbol{b}_s & \cdots & \boldsymbol{A}_s\boldsymbol{b}_s & \boldsymbol{b}_s \end{bmatrix} \\ &\boldsymbol{c} = \boldsymbol{c}_s,\ \ \boldsymbol{x}[i] = \boldsymbol{x}(iT_r) \end{aligned} \tag{4.10}$$

by calculating the state transition from $t = iT_r = kT_u$ to $t = (i+1)T_r = (k+n)T_u$. Here, the input vector $\boldsymbol{u}[i]$ is defined in the lifting form

$$\begin{aligned} \boldsymbol{u}[i] &= \begin{bmatrix} u_1[i] & u_2[i] & \cdots & u_n[i] \end{bmatrix}^{\mathrm{T}} \\ &= \begin{bmatrix} u(kT_u) & u((k+1)T_u) & \cdots & u((k+n-1)T_u) \end{bmatrix}^{\mathrm{T}}. \end{aligned} \tag{4.11}$$

According to (4.9), the feedforward output $\boldsymbol{u}_o[i]$ is obtained from the previewed state trajectory $\boldsymbol{x}_d[i+1]$ as follows:

$$\boldsymbol{u}_o[i] = \boldsymbol{B}^{-1}(\boldsymbol{I} - z^{-1}\boldsymbol{A})\boldsymbol{x}_d[i+1], \tag{4.12}$$

where $z = e^{sT_r}$. The feedforward input $\boldsymbol{u}_o$ achieves the perfect state matching for $\boldsymbol{x}_d$ every nT_u.

[*1] Defining the preactuation sample as $k_{tp} = ni_{tp}$ with $i_{tp} = \mathrm{floor}(t_{pa}/nT_u)$. The FF input during the finite preactuation is calculated by

$$\begin{aligned} \boldsymbol{u}_{reg} &= \begin{bmatrix} \boldsymbol{u}^{\mathrm{T}}[i_{tp}] & \boldsymbol{u}^{\mathrm{T}}[i_{tp}+1] & \cdots & \boldsymbol{u}^{\mathrm{T}}[-1] \end{bmatrix}^{\mathrm{T}} \\ &= \begin{bmatrix} \boldsymbol{B}^{-1}\boldsymbol{A}\tilde{\boldsymbol{x}}[k_{tp}] + \boldsymbol{B}^{-1}\tilde{\boldsymbol{x}}[k_{tp}+n] \\ \boldsymbol{B}^{-1}\boldsymbol{A}\tilde{\boldsymbol{x}}[k_{tp}+n] + \boldsymbol{B}^{-1}\tilde{\boldsymbol{x}}[k_{tp}+2n] \\ \vdots \\ \boldsymbol{B}^{-1}\boldsymbol{A}\tilde{\boldsymbol{x}}[-n] + \boldsymbol{B}^{-1}\tilde{\boldsymbol{x}}[0] \end{bmatrix}. \end{aligned} \tag{4.8}$$

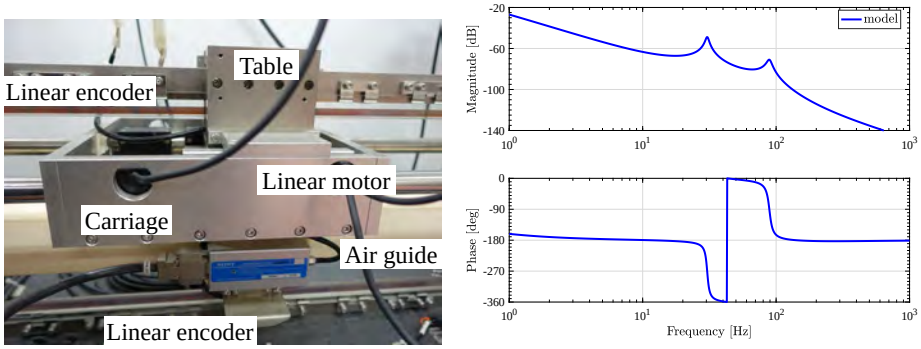

(a) High-precision positioning stage. (b) 6th order model of Fig. 4.1(a).

Figure 4.1 Experimental high-precision positioning stage and its model [83, 84].

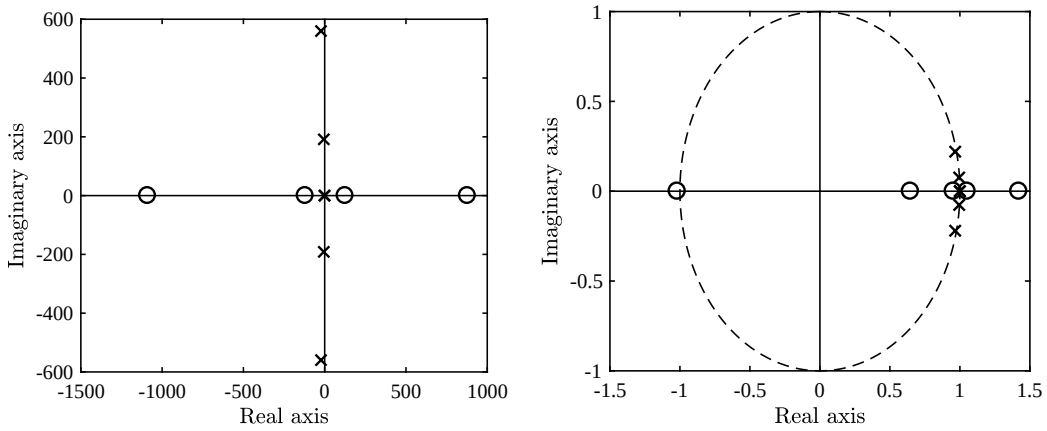

(a) P_c. (b) P_s.

Figure 4.2 Pole-zero map of identified model shown in Fig. 4.1.

4.2.4 Search minimum preactuation time

The minimum preactuation time considering constraints is searched by the bisection method. This section implements a dual-loop optimization, in which an unconstrained upper loop relaxes the given finite time constraint for the inner semi-infinite optimization and checks feasibility, i.e. it iterates as long as the inner loop doesn't converge.

- Step 1

  Set a initial preactuation time $t_{pa} = t_l$ and check the feasibility. Set a initial upper bound (infeasible preactuation time) $t_u = 0$.

- Step 2

  Set a new test preactuation time $t_{pa} = \frac{t_u + t_l}{2}$.

- Step 3

  Apply optimization in Section 4.2.2 and check the feasibility.

  – If it is feasible

Set $t_l = t_{pa}$.

– If it is infeasible

Set $t_u = t_{pa}$.

- Step 4

Iteratively preform step 2 and 3 until $t_u - t_l < T_r$.

4.3 Simulation

4.3.1 Plant model and simulation condition

The simulations in this chapter are based on the experimentally obtained model of the setup shown in Fig. 4.1. This stage can be modeled by a 6^{th} order plant shown in Figs. 4.1(b) and 4.2, which has two unstable zeros in continuous time domain. Additionally, this model has a discretization unstable zero in $P_s[z_s]$.

4.3.2 Parametrized B-spline implementation

Multirate feedforward is a sampled based approach, hence, the optimization function is limited to the short sampling time T_u. In order to guarantee constraint satisfaction in continuous time domain the optimization problem is defined in terms of B-spline coefficients. The state vector $\tilde{\boldsymbol{x}}_d(t)$ $(t_{pa} \leq t \leq 0)$ is defined as a B-spline of degree $p > n$ [22] as

$$\tilde{x}_{1d}(t) = \sum_{j=0}^{m} \boldsymbol{p}_j B_j^p(t) \tag{4.13}$$

where $\boldsymbol{p}_j$, $j = 0, ..., m$ are the coefficient or control points. Let $\boldsymbol{\kappa} = [\kappa_0, ..., \kappa_{n_{knot}}]$ be a given knot vector, extended to add flexibility to the optimization problem [133]. The j-th B-spline basis function is chosen of degree $m > n$ to guarantee n-order differentiable state trajectories.

The degree of the B-spline is set as 20 and the number of the free knots is set as 3.

4.3.3 Fixed preactuation time perfect tracking control: Comparison with TSA method and truncated PPTC method

Fig. 4.3 shows the comparison between the truncated PPTC, TSA, and the proposed method with $\|e_d\|_\infty$ minimization. Preactuation time t_{pa} is fixed as -3.3τ. Simply truncating the control input in the PPTC method to the given preactuation time, accumulates considerable error and requires low-bandwidth feedback action. As seen in Fig. 4.3(a), the stage doesn't reach the desired end-position

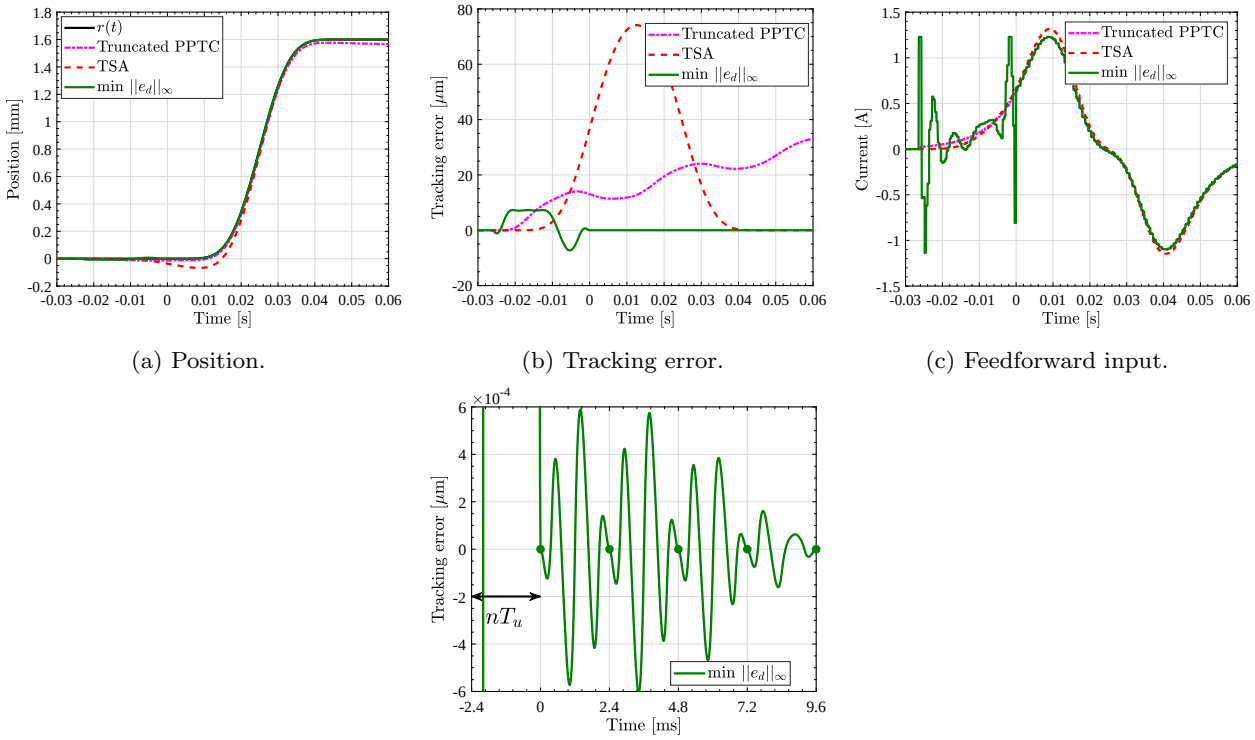

(a) Position.

(b) Tracking error.

(c) Feedforward input.

(d) Zoom of Fig. 4.3(b).

Figure 4.3 Comparison between TSA, truncated PPTC and proposed method (min $||e_d||_\infty$). $t_{pa} = -3.3\tau = -0.0264$ s is fixed for the three methods. Proposed method achieves the perfect tracking is achieved after preactuation ($0 < t$).

$r = 1.6$ mm in the given time window.

The control input constraints are set as $u_{max} = 1.23$ A and $u_{min} = -u_{max}$, which are the maximum/minimum control input of PPTC shown in Fig. 2.20(g). Fig. 4.3(c) shows that the feedforward input of the FPPTC method effectively respects those imposed constraints. Fig. 4.3(b) then shows that the tracking performance of FPPTC (min. $||e_d||_\infty$) exceeds that of both TSA and truncated PPTC for the same preactuation time t_{pa}. Fig. 4.4 finally shows the regenerated state trajectory of the FPPTC method for $t_{pa} \leq t \leq 0$, which satisfy the imposed boundary conditions.

4.3.4 Fixed preactuation time perfect tracking control: Objective function comparison

This section shows the tendency difference of the choice of the objective function under the fixed preactuation time. Preactuation time t_{pa} is fixed as -3.3τ. The control input constraints are set as $u_{max} = 1.23$ A and $u_{min} = -u_{max}$, which are the maximum/minimum control input of PPTC shown in Fig. 2.20(g).

Fig. 4.5 compares the minimization of $||e_d||_1$, $||e_d||_2$, $||e_d||_\infty$. The generated feedforward input shown in Fig. 4.7 contains high-frequency contents. It may excite unmodeled plant dynamics.

To balance the control performance (i.e. maximum error) and the smoothness of the control input,

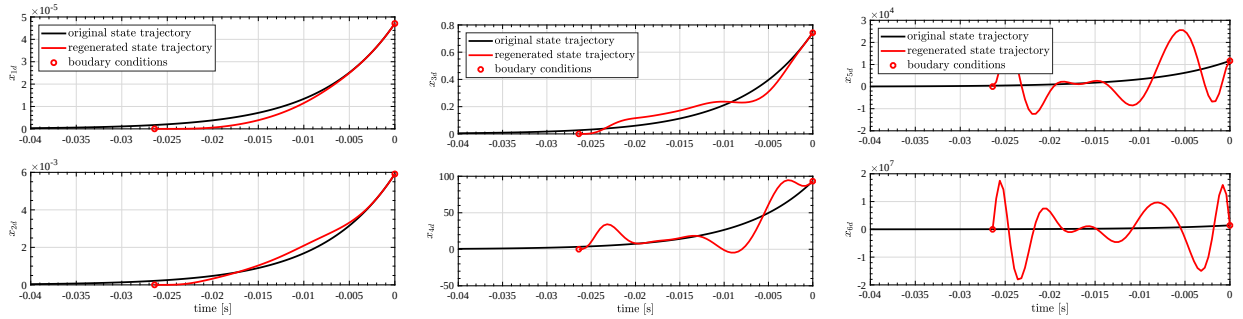

(a) x_{1d}, x_{2d}. (b) x_{3d}, x_{4d}. (c) x_{5d}, x_{6d}.

Figure 4.4 State trajectory of proposed method in Fig. 4.3.

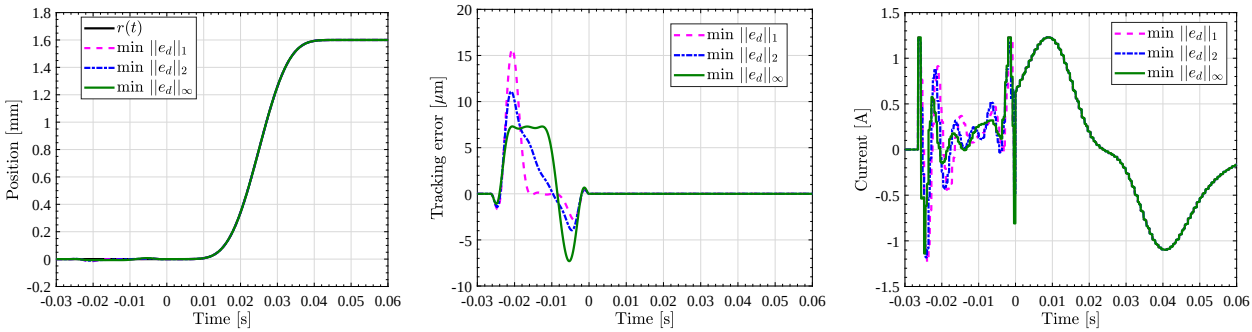

(a) Position. (b) Tracking error. (c) Feedforward input.

Figure 4.5 Comparison between objective functions (min $||e_d||_1$, $||e_d||_2$, $||e_d||_\infty$). $t_{pa} = -3.3\tau = -0.0264$ s is fixed for the three methods.

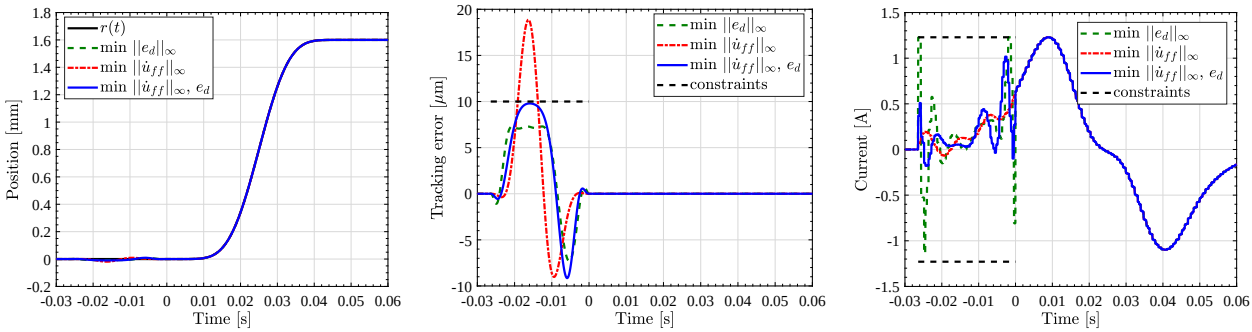

(a) Position. (b) Tracking error. (c) Feedforward input.

Figure 4.6 Comparison between objective functions (min $||e_d||_\infty$, $||\dot{u}_{ff}||_\infty$, $||\dot{u}_{ff}||_\infty$ with e_d constraints).

the derivatives of the control input is set as an objective function. "$||\dot{u}_{ff}||_\infty$" denotes the condition defined in (4.5), which has constraints for the state variables and maximum/minimum control input. It generates smooth control input but the tracking error become larger. "$||\dot{u}_{ff}||_\infty, e_d$" denotes the condition defined in (4.5), which has constraints for the state variables, maximum/minimum control input, and the maximum undershoot value e_{max}.

As shown in Fig. 4.7, an expected trade-off exists between the amount of high-frequency contents and the maximum tracking error. The optimal variant of the proposed approach is, thus, more a question of the user's preferences and application objectives.

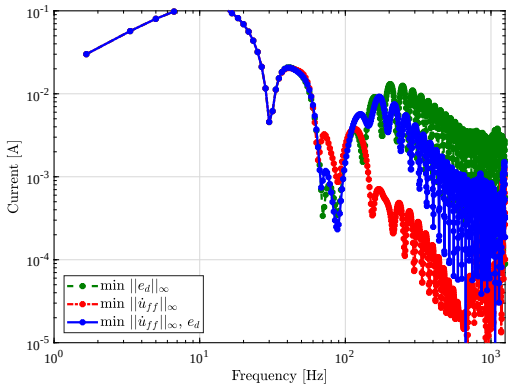

Figure 4.7 Frequency spectrum comparison between objective functions.

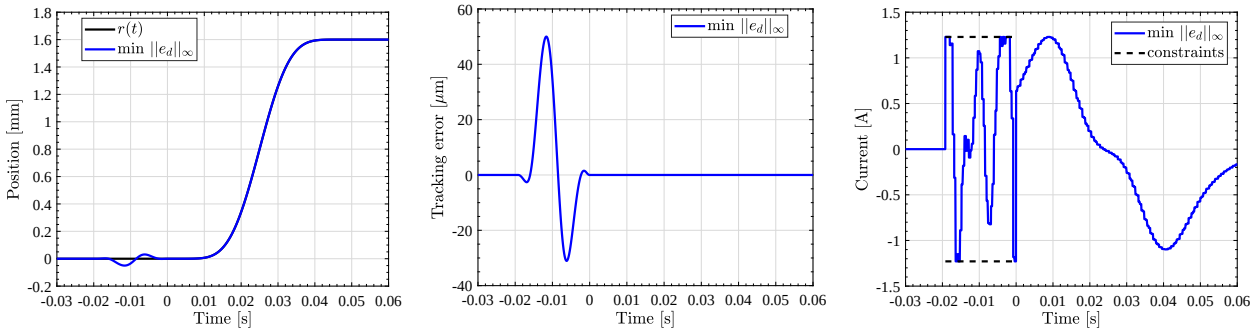

(a) Position. (b) Tracking error. (c) Feedforward input.

Figure 4.8 Minimum time preactuation perfect tracking control considering control input constraints. $t_{pa} = -2.41\tau = -0.192\,\text{s}$.

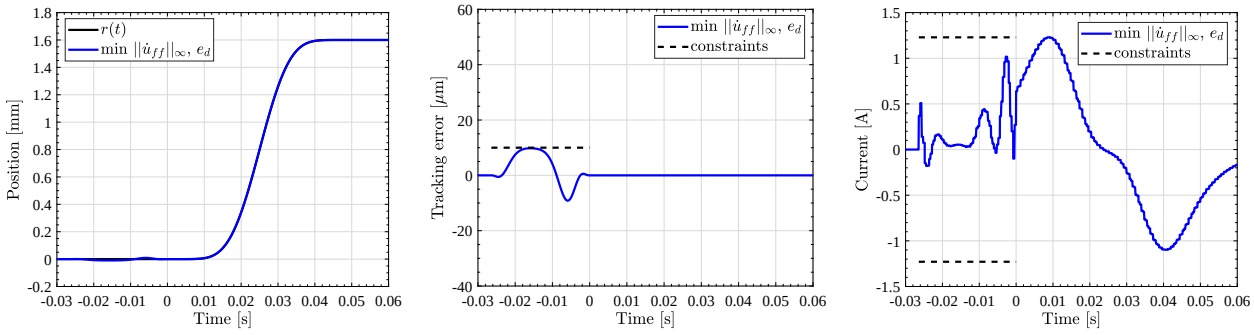

(a) Position. (b) Tracking error. (c) Feedforward input.

Figure 4.9 Minimum time preactuation perfect tracking control considering control input constraints. $t_{pa} = -3.32\tau = -0.264\,\text{s}$.

Please note that, independent of the optimization formulation chosen, the presented method achieves, in contrast to conventional finite preactuation approaches, perfect tracking after preactuation, i.e. for $t > 0$ (see Fig. 4.3(d)).

4.3.5 Minimum time preactuation perfect tracking control

Control input constraints

Simulation result of the minimum time preactuation perfect tracking control with control input constraints is shown in Fig. 4.8. The control input constraints are set as $u_{max} = 1.23$ A and $u_{min} = -u_{max}$, which are the maximum/minimum control input of PPTC shown in Fig. 2.20(g). The feasible minimum preactuation time is $t_{pa} = -2.41\tau = -0.192$ s. The perfect tracking is achieved after preactuation ($0 < t$).

Control input and maximum error constraints

Simulation result of the minimum time preactuation perfect tracking control with control input constraints and the maximum error is shown in Fig. 4.9. The control input constraints are set as $u_{max} = 1.23$ A and $u_{min} = -u_{max}$, which are the maximum/minimum control input of PPTC shown in Fig. 2.20(g). The maximum error constraint (equivalently maximum value of undershoot) is set as $e_{max} = 10\,\mu$m. The feasible minimum preactuation time is $t_{pa} = -3.32\tau = -0.264$ s. Due to the maximum error constraint, the minimum feasible preactuation time is longer than the result shown in section 4.3.5. The perfect tracking is achieved after preactuation ($0 < t$).

4.4 Summary

This chapter proposes a *minimum* time preactuation method for nonminimum phase systems through an optimization approach explicitly considering both control input and tracking error constraints. Previously proposed exact model-inversion methods, achieve perfect tracking, in theory, for systems with unstable zeros, albeit at the cost of an *infinite* preactuation. Input truncation or model approximation both lead to undesirable tracking errors, hence, the authors propose an optimal control formulation to *regenerate* the state trajectories in a minimum feasible time while imposing system constraints. A multirate feedforward scheme is subsequently presented to obtain a discretized control input that perfectly tracks the designed optimal continuous state trajectory.

In comparison to conventional finite preactuation methods such as the TSA method, the proposed approach reaches an order of magnitude lower tracking error bounds. Additionally, this finite time procedure attains, in contrast to conventional optimization approaches, through a multirate feedforward formulation, perfect tracking during the main motion after preactuation.

Chapter 5

Optimal State Trajectory Regeneration for Multirate Feedforward: No Preactuation Approach

Abstract

To achieve perfect reference trajectory tracking, a plant with continuous time unstable zeros requires an *infinite* time preactuation. However, this is practically infeasible. Preactuation as short as possible is desirable for high-precision motion systems. This chapter, thus, proposes an optimal state trajectory *regeneration* method without preactuation. The original state trajectory, which requires the infinite preactuation, is generated by PPTC method (see Chapter 2). Then we *regenerate* the state trajectory between the start and end time of the reference motion trajectory. This method is an extension of the method proposed in Chapter 4. In the method of Chapter 4, perfect tracking after preactuation is guaranteed by regenerating the state trajectory during preactuation, whereas this method guarantees only after the end of the reference motion. The state trajectory during the reference motion is optimized with respect to the control input and plant output constraints. A multirate feedforward scheme, which is a stable inversion for unstable discretization zeros, is subsequently presented to obtain a discretized control input that perfectly tracks the designed optimal continuous state trajectory.

5.1 Introduction

Model-inverse feedforward control is effective for reference tracking [20, 30]. It is well known that when the sensors and actuators are non-collocated, the plant zero(s) of continuous time can be unstable [131]. System with continuous-time unstable zeros are, for instance, scanning stages [1, 83], hard disk drives [53], boost converters [54]. In discrete-time domain, there are two types of zeros: 1) intrinsic

zeros proper to the plant dynamics and 2) discretization zeros due to signal sampling [117]. Note that discretization zeros are unstable when the relative order of the continuous time plant is greater than two, even without continuous-time unstable zeros [55].

The preactuation perfect tracking control (PPTC) method proposed in Chapter 2 solves problems 1) and 2) separately. Continuous-time unstable zeros are stably inverted by preactuation and discretization zeros are also stably inverted by a multirate feedforward technique [103]. To make exact inverse, we need infinity time preactuation [72,118], which is infeasible. When the preactuation time is sufficiently long compared to the time constant of unstable zeros τ, the truncation effect is negligible. However, when the truncate all the preactuation, the significant tracking error arises (see $t_{pa} = 0$ in Figs. 3.6 and 3.7).

PPTC method consists of two steps: i) the desired state trajectory $\boldsymbol{x}_d(t)$ generation from the reference trajectory with its derivatives $\boldsymbol{r}(t)$, and ii) the feedforward input $\boldsymbol{u}_o[i]$ generation from $\boldsymbol{x}_d[i+1]$ by the multirate feedforward [103]. When the system has unstable zeros in the continuous-time domain, step i) requires non-causal filtering. Step ii) can generate the the feedforward input $\boldsymbol{u}_o[i]$ from arbitrary state trajectory $\boldsymbol{x}_d[i]$.

This Chapter modifies step i) to regenerate the state trajectory during the step motion, taking into account constraints. Constraints include maximum/minimum feedforward input and the amount of undershoot. The effectiveness is shown by simulation using a scanning stage model, whose dominant zero is unstable.

This method is an extension of the method proposed in Chapter 4. In the method of Chapter 4, perfect tracking after preactuation is guaranteed by regenerating the state trajectory during preactuation, whereas this method guarantees only after the end of the reference motion. The state trajectory during the reference motion is optimized with respect to the control input and plant output constraints. References [134, 135] deal with similar scenario considering constraints. These methods are continuous-time approach for nonlinear systems. In contrast, the proposed method designs the exact inverse of the zero-order-hold (see Section 2.6.6).

5.2 Optimal state trajectory generation for multirate feedforward

The same notation shown in section 2.2 is used.

5.2.1 Original state trajectory $\boldsymbol{x}_d$ generation

First, the state trajectory for PPTC, which requires the infinity preactuation, is calculated by the method shown in 2.4.1. When the system has unstable zeros in the continuous-time domain, $\boldsymbol{x}_d(t)$ is

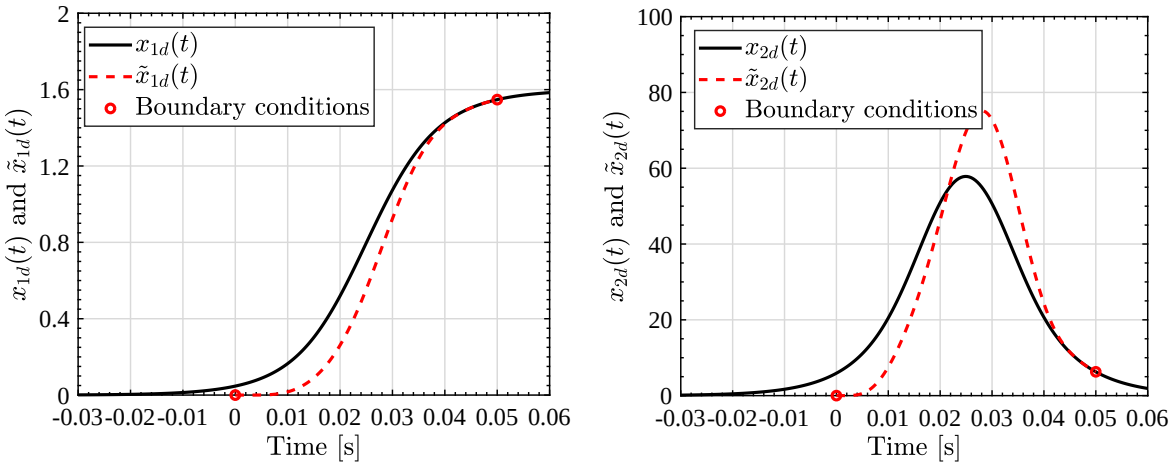

(a) $x_{1d}(t)$ and $\tilde{x}_{1d}(t)$. (b) $x_{2d}(t)$ and $\tilde{x}_{2d}(t)$.

Figure 5.1 Idea of the optimal state trajectory regeneration without preactuation. In contrast to the FPPTC method shown in Fig. 3.8, this method regenerates the state trajectory for a finite time $0 \leq t \leq t_{\mathrm{traj}}$. $\tilde{\boldsymbol{x}}_d(t)$ is calculated from $\tilde{x}_{1d}(t)$ by (3.4).

non-zero for $t < 0$, assuming $\boldsymbol{r}(t) = 0$ when $t < 0$. This is because the unstable part state trajectory $\boldsymbol{x}_d^{\mathrm{ust}}(t)$ has a non-zero value in $t < 0$. Hence, to achieve perfect tracking, nonminimum phase systems require infinite preactuation [125].

5.2.2 State trajectory re-generation

This section *regenerates* the state trajectory from a given $t = 0$ to $t = t_{\mathrm{traj}}$ to achieve the optimal performance without preactuation as shown in Fig. 5.1. t_{traj} denotes the given reference trajectory end time. We regenerate the state trajectory as follows:

$$\boldsymbol{x}_d(t) = \begin{cases} \boldsymbol{0} & (t < 0) \\ \tilde{\boldsymbol{x}}_d(t) & (0 \leq t \leq t_{\mathrm{traj}}) \\ \boldsymbol{x}_d^{\mathrm{st}}(t) & (t_{\mathrm{traj}} < t) \end{cases}, \tag{5.1}$$

where $\tilde{\boldsymbol{x}}_d(t)$ denotes the regenerated state trajectory. Note that $\boldsymbol{x}_d^{\mathrm{ust}}(t) = 0$ when $t_{\mathrm{traj}} < t$.

Problem setting

Two constrained optimization problems are proposed for the state reference regeneration.

- Minimum tracking error

A semi-infinite optimization for preactuation tracking error is formalized here as

$$\underset{\boldsymbol{x}(\cdot)}{\text{minimize}} \quad \|e_d(t)\|_p = \|r(t) - y_d(t)\|_p, \quad p = 1, 2, \infty \tag{5.2}$$

$$\underset{\forall t \in [0, t_{\text{traj}}]}{\text{subject to}} \quad \tilde{\boldsymbol{x}}_d(0) = \mathbf{0}, \quad \tilde{\boldsymbol{x}}_d(t_{\text{traj}}) = \boldsymbol{x}_d(t_{\text{traj}}) \tag{5.3}$$

$$y_{min} \leq y[k] \leq y_{max}, \quad u_{min} \leq u[k] \leq u_{max} \tag{5.4}$$

The tracking error $e_d(t)$ is minimized over $0 \leq t \leq t_{\text{traj}}$ taking into account both the physical constraints of the stage, e.g. stroke y_{min}, y_{max} and actuator, e.g. peak current u_{min}, u_{max}. Although this method abandons perfect tracking over $0 < t < t_{\text{traj}}$, it guarantees perfect tracking during postactuation ($t_{\text{traj}} \leq t$) by constraining that the re-generated state trajectory $\tilde{\boldsymbol{x}}_d(t)$ at $t = t_{\text{traj}}$ matches the desired state trajectory $\boldsymbol{x}_d(t)$ calculated using (2.34).

Despite the good tracking achieved through this formulation, the resulting constrained feedforward output is impeded by a high jerk.

- Minimum jerk input

  A second semi-infinite optimization problem for preactuation feedforward input is formalized here as

$$\underset{\boldsymbol{x}(\cdot)}{\text{minimize}} \quad \|\dot{\boldsymbol{u}}_{reg}\|_\infty \tag{5.5}$$

$$\underset{\forall t \in [0, t_{\text{traj}}]}{\text{subject to}} \quad \tilde{\boldsymbol{x}}_d(0) = \mathbf{0}, \quad \tilde{\boldsymbol{x}}_d(t_{\text{traj}}) = \boldsymbol{x}_d(t_{\text{traj}}) \tag{5.6}$$

$$e_{min} \leq e_d[k] \leq e_{max}, \quad u_{min} \leq u[k] \leq u_{max} \tag{5.7}$$

  $\boldsymbol{u}_{reg}$ is the control input during the finite preactuation obtained by (5.10).

  The objective of this setting is to balance the control performance (i.e. maximum error) and the smoothness of the control input.

Problem formulation

Eq. (5.2) and (5.5) are optimal control problems where one is interested in finding the input $\boldsymbol{u}_{reg}$ that brings the system from an initial state $\tilde{\boldsymbol{x}}_d(0) = \mathbf{0}$ to a final state $\boldsymbol{x}_d(t_{\text{traj}})$ at the end of the trajectory and that minimizes a performance criterion (5.2) and (5.5) while obeying state and input constraints. The difficulty of solving these states optimal control problem is the need for numerically costly integration. Albeit, this is avoided in the multi-rate feedforward formulation used here, the plant is realized through the controllable canonical form

$$\begin{aligned} \tilde{\boldsymbol{x}}_d(t) &= \begin{bmatrix} \tilde{x}_{1d}(t) & \tilde{x}_{2d}(t) & \cdots & \tilde{x}_{nd}(t) \end{bmatrix}^{\mathrm{T}}, \\ \tilde{x}_{qd}(t) &= \rho^{q-1} \tilde{x}_{1d}(t), \quad q = 2, 3, \cdots, n, \end{aligned} \tag{5.8}$$

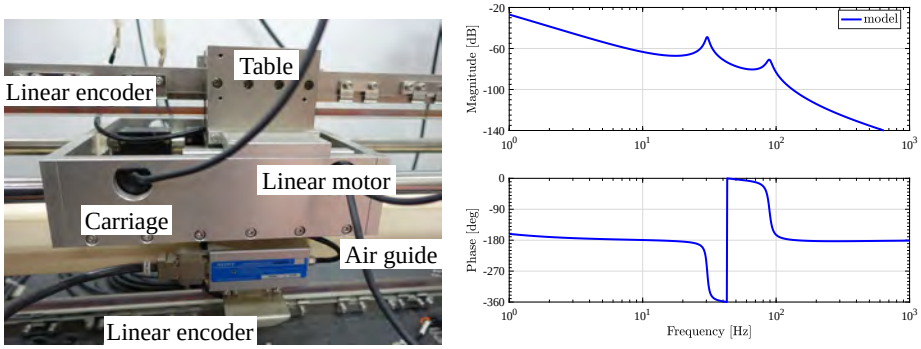

(a) High-precision positioning stage. (b) 6th order model of Fig. 5.2(a).

Figure 5.2 Experimental high-precision positioning stage and its model [83, 84].

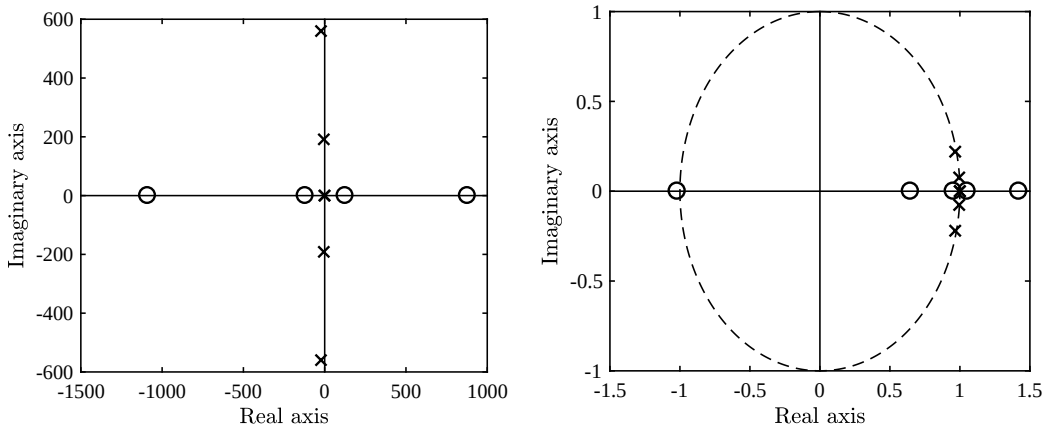

(a) P_c. (b) P_s.

Figure 5.3 Pole-zero map of identified model shown in Fig. 5.2.

where $\tilde{x}_{1d}(t)$ is a piecewise polynomial defined in $0 \leq t \leq t_{\text{traj}}$. The desired output $y_d(t)$ is, hence, defined as a linear function of $\tilde{x}_{1d}(t)$

$$\begin{aligned} y_d(t) &= \boldsymbol{c}_c \tilde{\boldsymbol{x}}_d(t) \\ &= \boldsymbol{c}_c \begin{bmatrix} \tilde{x}_{1d}(t) & \rho \tilde{x}_{1d}(t) & \dots & \rho^{n-1} \tilde{x}_{1d}(t) \end{bmatrix}^{\mathrm{T}} \end{aligned} \tag{5.9}$$

Hence, the desired output $y_d(t)$ can be evaluated by (5.2). To evaluate the control input during preactuation in (5.5), the multirate feedforward control shown in (2.38) is applied.

5.2.3 Feedforward input u_o generation from $\boldsymbol{x}_d$

The feedforward control input $\boldsymbol{u}_o$ is obtained by the multirate feedforward control as Section 2.4.2.

$$\boldsymbol{u}_o[i] = \boldsymbol{B}^{-1}(\boldsymbol{I} - z^{-1}\boldsymbol{A})\boldsymbol{x}_d[i+1], \tag{5.10}$$

where $z = e^{sT_r}$. The feedforward input $\boldsymbol{u}_o$ achieves the perfect state matching for $\boldsymbol{x}_d$ every nT_u.

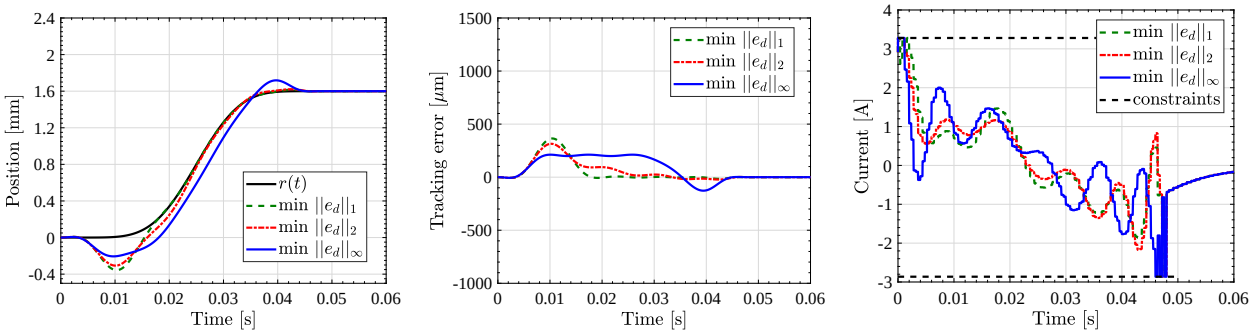

(a) Position. (b) Tracking error. (c) Feedforward input.

Figure 5.4 Comparison between objective functions (min $||e_d||_1$, $||e_d||_2$, $||e_d||_\infty$).

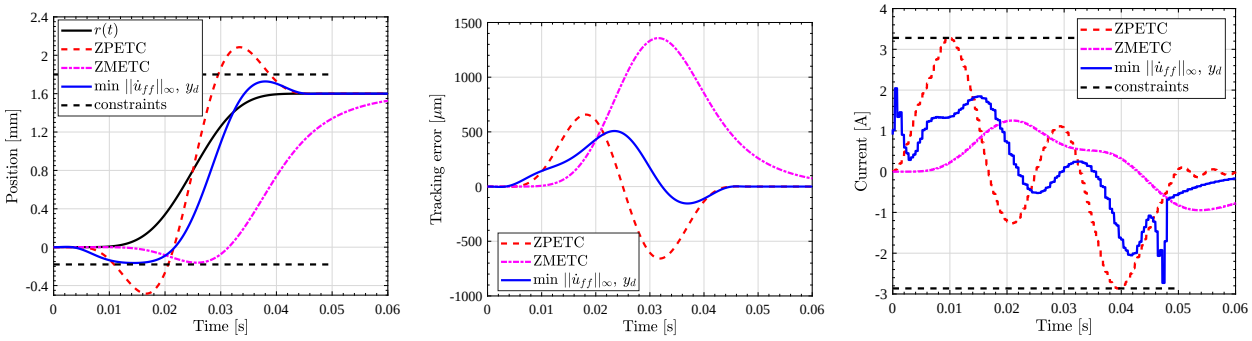

(a) Position. (b) Tracking error. (c) Feedforward input.

Figure 5.5 Comparison between ZPETC, ZMETC, and proposed method. $||\dot{u}_{ff}||_\infty$ denotes the condition defined in (5.5), which has equality constraints for the state variables and maximum/minimum control input.

5.3 Simulation

5.3.1 Plant model and simulation condition

Simulations of this chapter assume a experimental setup shown in Fig. 5.2. This stage can be modeled by 6th order model shown in Fig. 5.2(b) and 5.3, which has two unstable zeros in continuous time domain. Additionally, this model has a discretization unstable zero in $P_s[z_s]$.

5.3.2 Parametrized B-spline implementation

Multirate feedforward is a sampled based approach, hence, the optimization function is limited to the short sampling time T_u. In order to guarantee constraint satisfaction in continuous time domain the optimization problem is defined in terms of B-spline coefficients. The state vector $\tilde{\boldsymbol{x}}_d(t)$ $(0 \leq t \leq t_{\text{traj}})$ is defined as a B-spline of degree $p > n$ [22] as

$$\tilde{x}_{1d}(t) = \sum_{j=0}^{m} \boldsymbol{p}_j B_j^p(t) \tag{5.11}$$

where $\boldsymbol{p}_j$, $j = 0, ..., m$ are the coefficient or control points. Let $\boldsymbol{\kappa} = [\kappa_0, ..., \kappa_{n_{knot}}]$ be a given knot vector, extended to add flexibility to the optimization problem [133]. The j-th B-spline basis function is chosen of degree $m > n$ to guarantee n-order differentiable state trajectories.

The degree of the B-spline is set as 20 and the number of the free knots is set as 3.

5.4 Simulation results

The control input constraints are set as maximum/minimum current of the ZPETC method.

Fig. 5.4 compares the minimization of $||e_d||_1$, $||e_d||_2$, $||e_d||_\infty$. The generated feedforward input shown in Fig. 5.4(c) contains high-frequency contents.

To balance the control performance (i.e. maximum error) and the smoothness of the control input, the derivatives of the control input is set as an objective function. $||\dot{u}_{ff}||_\infty, y_d$ denotes the condition defined in (5.5), which has constraints for the state variables, maximum/minimum control input, and the output y_d. The proposed method achieves the smaller tracking error than ZPETC and smaller undershoot than ZMETC.

5.5 Summary

This chapter proposes a *optimal* state trajectory generation method for nonminimum phase systems through an optimization approach explicitly considering both control input and tracking error constraints. It regenerates the state trajectory from $t = 0$ to $t = t_{\text{traj}}$. Therefore, it optimize the state trajectory during the main motion without preactuation. Previously proposed exact model-inversion methods, achieve perfect tracking, in theory, for systems with unstable zeros, albeit at the cost of an *infinite* preactuation. Input truncation or model approximation both lead to undesirable tracking errors, hence, the authors propose an optimal control formulation to *regenerate* the state trajectories during main motion while imposing system constraints. A multirate feedforward scheme is subsequently presented to obtain a discretized control input that perfectly tracks the designed optimal continuous state trajectory. In comparison to conventional single-rate model-inversion methods, the proposed method achieves the smaller tracking error than ZPETC and smaller undershoot than ZMETC in same time.

Chapter 6

Multirate Feedforward Control based on Modal Form

Abstract

Multirate feedforward control has been proposed to achieve perfect tracking for a plant with unstable discretization zeros. However, multirate feedforward control requires controllable canonical form and inversion of a controllability matrix, both of which are known as numerically ill-conditioned. This chapter proposes a multirate feedforward control method based on modal form to address these problems. Moreover, the intersample behavior is improved compared to the conventional full order multirate feedforward. The effectiveness of the proposed method is validated through simulation results.

6.1 Introduction

Model-inverse feedforward control is effective for reference tracking [20, 30]. Typically, controllers are implemented in a discrete time domain [37]. Zeros in the discrete time domain are classified as 1) intrinsic zeros proper to the plant dynamics and 2) discretization zeros due to signal sampling [117]. Note that discretization zeros are unstable when the relative order of the continuous time plant is greater than two, even without continuous-time unstable zeros [55]. When a plant has unstable zeros, perfect tracking defined in [59] is impossible by a single-rate control scheme because of the unstable poles of its inversion system. Therefore, there has been extensive research into approximate model-inverse feedforward control techniques such as the nonminimum-phase zeros ignore (NPZI) method [30], zero-phase-error tracking controller (ZPETC) method [59], and zero-magnitude-error tracking controller (ZMETC) method [119].

To address the unstable discretization zeros problem, we have proposed a multirate feedforward

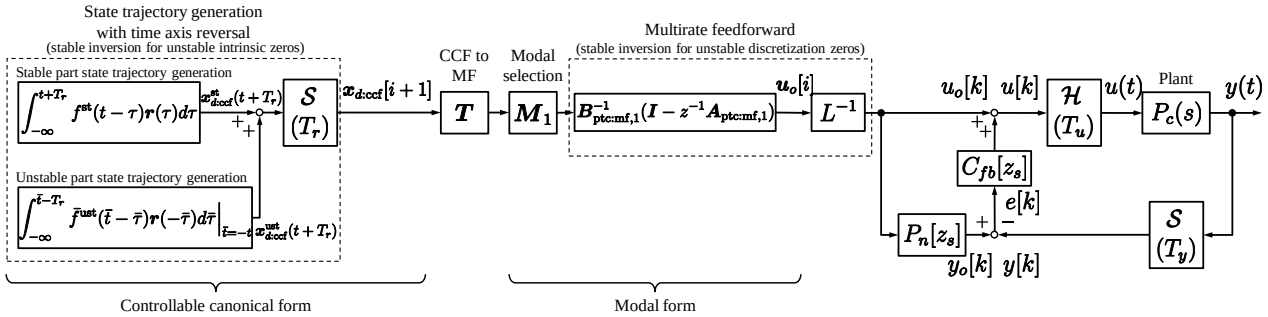

Figure 6.1 Multirate feedfoward based on modal form. $\mathcal{S}$, $\mathcal{H}$, and L denote a sampler, holder, and lifting operator [110], respectively. z and z_s denote e^{sT_r} and e^{sT_u}, respectively. Note that $T_r = nT_u$.

control [103] to design stable inverse for unstable discretization zero(s) [55], which is generated by a zero-order-hold. This method generates a feedforward control input, which enables the system to track perfectly with the desired state trajectory for every nT_u, where n and T_u denote the nominal plant order and the sampling period, respectively. Conventional multirate feedforward control has several issues concerning a high-order plant: i) long time (nT_u) for perfect tracking and ii) low numerical stability due to inversion of controllability matrix with matrix size ($n \times n$). The controllability matrix is numerically ill-conditioned for a high-order plant [136].

Modeling accuracy is essential for the tracking performance for the model-based methods. It is well known that time nT_u is needed to achieve zero-error at sampling points for a minimum-time dead-beat control [37]. The same restriction exists in a multirate feedforward control [103]. This means that a higher order plant requires a longer time to achieve perfect tracking for state variables.

The proposal of this chapter, multirate feedforward based on modal form, consists of the following steps.

1. State trajectory generation by controllable canonical form
2. Similarity transformation to modal form

   Modes are separated by every second order to have real coefficients.
3. Mode extraction
4. Multirate feedforward control for extracted second order mode

Using this procedure, the proposed method has the following advantages regardless of the plant order n:

- Perfect state matching for arbitrary two states for every two samples ($2T_u$)

  Intersample tracking error is reduced compared to the conventional full order multirate feedforward.

- Controllability matrix with size of (2×2) for multirate feedforward

6.2 Multirate feedforward based on modal form

Block diagram of the proposed method is shown in Fig. 6.1.

6.2.1 Plant definition

A nominal plant in a continuous time domain is defined as

$$\begin{cases} P_c(s) = \dfrac{B(s)}{A(s)} = \dfrac{b_m s^m + b_{m-1}s^{m-1} + \cdots + b_0}{s^n + a_{n-1}s^{n-1} \cdots + a_0} \\ A(s) = \dfrac{s^n + a_{n-1}s^{n-1} \cdots + a_0}{b_0} \\ B(s) = \dfrac{b_m s^m + b_{m-1}s^{m-1} + \cdots + b_0}{b_0} \end{cases}, \tag{6.1}$$

where (6.1) is an irreducible fraction.

6.2.2 State trajectory $\boldsymbol{x}_{d:\mathrm{ccf}}(t)$ generation by controllable canonical form

The state and output equations of (6.1) realized by the controllable canonical form are

$$\dot{\boldsymbol{x}}_{\mathrm{ccf}}(t) = \boldsymbol{A}_{c:\mathrm{ccf}}\boldsymbol{x}_{\mathrm{ccf}}(t) + \boldsymbol{b}_{c:\mathrm{ccf}}u(t),\ y(t) = \boldsymbol{c}_{c:\mathrm{ccf}}\boldsymbol{x}_{\mathrm{ccf}}(t), \tag{6.2}$$

where

$$\begin{cases} \boldsymbol{x}_{\mathrm{ccf}} := \begin{bmatrix} x_{1:\mathrm{ccf}}(t) \\ x_{2:\mathrm{ccf}}(t) \\ \vdots \\ x_{n:\mathrm{ccf}}(t) \end{bmatrix}, \boldsymbol{A}_{c:\mathrm{ccf}} := \begin{bmatrix} 0 & 1 & 0 & \cdots & 0 \\ 0 & 0 & 1 & \cdots & 0 \\ & & & \ddots & \\ -a_0 & -a_1 & -a_2 & \cdots & -a_{n-1} \end{bmatrix}. \\ \boldsymbol{b}_{c:\mathrm{ccf}} := \begin{bmatrix} 0 & 0 & \cdots & b_0 \end{bmatrix}^{\mathrm{T}} \\ \boldsymbol{c}_{c:\mathrm{ccf}} := \begin{bmatrix} 1 & \frac{b_1}{b_0} & \cdots & \frac{b_m}{b_0} & 0 & \cdots & 0 \end{bmatrix} \end{cases} \tag{6.3}$$

The subscript 'ccf' means the controllable canonical form realization. n and $m(< n)$ denote the orders of $A(s)$ and $B(s)$, respectively. The discretized plant by a zero-order hold with sampling time T_u is defined as

$$\begin{aligned} \boldsymbol{x}_{\mathrm{ccf}}[k+1] &= \boldsymbol{A}_{s:\mathrm{ccf}}\boldsymbol{x}_{\mathrm{ccf}}[k] + \boldsymbol{b}_{s:\mathrm{ccf}}u[k], \\ y[k] &= \boldsymbol{c}_{s:\mathrm{ccf}}\boldsymbol{x}_{\mathrm{ccf}}[k], \end{aligned} \tag{6.4}$$

where

$$\boldsymbol{A}_{s:\mathrm{ccf}} := e^{\boldsymbol{A}_{c:\mathrm{ccf}}T_u},\ \boldsymbol{b}_{s:\mathrm{ccf}} := \int_0^{T_u} e^{\boldsymbol{A}_{c:\mathrm{ccf}}\tau}\boldsymbol{b}_{c:\mathrm{ccf}}d\tau,\ \boldsymbol{c}_{s:\mathrm{ccf}} := \boldsymbol{c}_{c:\mathrm{ccf}}. \tag{6.5}$$

According to the output equation shown in (6.2), the desired state trajectory $\boldsymbol{x}_{d:\mathrm{ccf}}(t)$ by the controllable canonical form realization should satisfy

$$r(t) = \boldsymbol{c}_{c:\mathrm{ccf}}\boldsymbol{x}_{d:\mathrm{ccf}}(t) \tag{6.6}$$

to track the plant output $y(t)$ for the reference $r(t)$. (6.6) is expressed as

$$r(t) = \begin{bmatrix} 1 & \frac{b_1}{b_0} & \cdots & \frac{b_m}{b_0} & 0 & \cdots & 0 \end{bmatrix} \begin{bmatrix} x_{1:\mathrm{ccf}}(t) \\ \rho x_{1:\mathrm{ccf}}(t) \\ \rho^2 x_{1:\mathrm{ccf}}(t) \\ \vdots \\ \rho^{n-1} x_{1:\mathrm{ccf}}(t) \end{bmatrix} \tag{6.7}$$

considering the controllable canonical form realization (6.3), where ρ denotes the Heaviside operator [37]. From (6.1) and (6.7), $x_{1:\mathrm{ccf}}(t)$ is obtained by

$$x_{1:\mathrm{ccf}}(t) = \frac{1}{B(\rho)}r(t) \tag{6.8}$$

Therefore, whole vector $\boldsymbol{x}_{d:\mathrm{ccf}}(t)$ is obtained by

$$\boldsymbol{x}_{d:\mathrm{ccf}}(t) = \frac{1}{B(\rho)}\boldsymbol{r}(t), \tag{6.9}$$

where $\boldsymbol{r}(t)$ denotes the reference trajectory and its derivatives:

$$\begin{aligned} \boldsymbol{r}(t) &:= \begin{bmatrix} r_1(t) & r_2(t) & \cdots & r_n(t) \end{bmatrix}^{\mathrm{T}} \\ &:= \begin{bmatrix} 1 & \rho & \cdots & \rho^{n-1} \end{bmatrix}^{\mathrm{T}} r(t). \end{aligned} \tag{6.10}$$

Equation (6.9) is calculated by following convolution

$$\begin{aligned} \boldsymbol{x}_{d:\mathrm{ccf}}(t) &= \int_{-\infty}^{t} f(t-\tau)\boldsymbol{r}(\tau)d\tau \\ &= \int_0^t f(t-\tau)\boldsymbol{r}(\tau)d\tau \end{aligned} \tag{6.11}$$

assuming $\boldsymbol{r}(t) = \boldsymbol{0}$ when $t < 0$. Here $f(t) = \bar{\mathcal{L}}^{-1}\left[\frac{1}{B(s)}\right]$, where $\bar{\mathcal{L}}^{-1}$ denotes the inverse of one-sided Laplace transform.

When the continuous time plant has unstable zeros, a stable inversion technique (see Chapter 2) is used to obtain a bounded state trajectory.

6.2.3 Similarity transformation to modal form

The plant defined in (6.1) is decomposed by second-order modes.

$$P_c(s) = \sum_{m_d=1}^{n_m-1} \frac{b_{m_d,1}s + b_{m_d,0}}{s^2 + a_{m_d,1}s + a_{m_d,0}} + O(s), \tag{6.12}$$

where m_d and n_m denote mode number and number of modes, respectively. Here we assume the maximum pole multiplicity is two since a mechanical system is considered. Note that $b_{m_d,1}$, $b_{m_d,0}$, $a_{m_d,1}$, and $a_{m_d,0}$ are real numbers for all m_d. When n is an even number, $n_m = n/2$ otherwise $n_m = (n+1)/2$.

$$\begin{cases} O(s) = \dfrac{b_{n_m,0}}{s + a_{n_m,0}} \quad (\text{if } n \text{ is an odd number}) \\ O(s) = \dfrac{b_{n_m,1}s + b_{n_m,0}}{s^2 + a_{n_m,1}s + a_{n_m,0}} \quad (\text{if } n \text{ is an even number}) \end{cases} \tag{6.13}$$

(6.14) is realized by the modal form from (6.12). Each mode is realized by the second-order controllable canonical form.

$$\begin{aligned} \dot{\boldsymbol{x}}_{\mathrm{mf}}(t) &= \boldsymbol{A}_{c:\mathrm{mf}}\boldsymbol{x}_{\mathrm{mf}}(t) + \boldsymbol{b}_{c:\mathrm{mf}}u(t), \\ y(t) &= \boldsymbol{c}_{c:\mathrm{mf}}\boldsymbol{x}_{\mathrm{mf}}(t), \end{aligned} \tag{6.14}$$

where

$$\begin{cases} \boldsymbol{x}_{\mathrm{mf}}(t) := \begin{bmatrix} x_{1:\mathrm{mf}}(t) & x_{2:\mathrm{mf}}(t) & \cdots & x_{n:\mathrm{mf}}(t) \end{bmatrix}^{\mathrm{T}} \\ \boldsymbol{A}_{c:\mathrm{mf}} := \mathrm{diag}\{\boldsymbol{A}_{c:\mathrm{mf},1}, \boldsymbol{A}_{c:\mathrm{mf},2}, \cdots, \boldsymbol{A}_{c:\mathrm{mf},m_d}, \cdots \boldsymbol{A}_{c:\mathrm{mf},n_m}\} \\ \boldsymbol{b}_{c:\mathrm{mf}} := [\boldsymbol{b}_{c:\mathrm{mf},1}^{\mathrm{T}}, \boldsymbol{b}_{c:\mathrm{mf},2}^{\mathrm{T}}, \cdots, \boldsymbol{b}_{c:\mathrm{mf},m_d}^{\mathrm{T}}, \cdots, \boldsymbol{b}_{c:\mathrm{mf},n_m}^{\mathrm{T}}] \\ \boldsymbol{c}_{c:\mathrm{mf}} := [\boldsymbol{c}_{c:\mathrm{mf},1}, \boldsymbol{c}_{c:\mathrm{mf},2}, \cdots, \boldsymbol{c}_{c:\mathrm{mf},m_d}, \cdots, \boldsymbol{c}_{c:\mathrm{mf},n_m}] \\ \boldsymbol{A}_{c:\mathrm{mf},m_d} := \begin{bmatrix} 0 & 1 \\ -a_{m_d,0} & -a_{m_d,1} \end{bmatrix}, \boldsymbol{b}_{c:\mathrm{mf},m_d} := \begin{bmatrix} 0 \\ b_{m_d,0} \end{bmatrix} \\ \boldsymbol{c}_{c:\mathrm{mf},m_d} := \begin{bmatrix} 1 & \dfrac{b_{m_d,1}}{b_{m_d,0}} \end{bmatrix} \end{cases} \tag{6.15}$$

The subscript 'mf' means the modal form realization. The transformation matrix to the controllable canonical form [37] is

$$\boldsymbol{T} = \boldsymbol{U}_c\boldsymbol{W}, \tag{6.16}$$

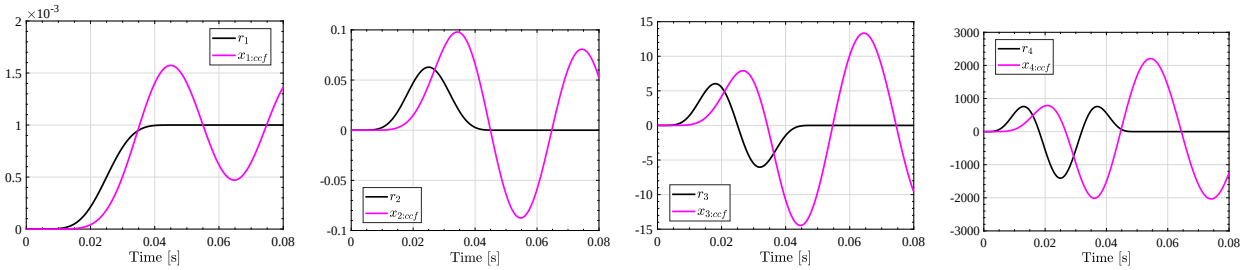

(a) $x_{1:\mathrm{ccf}}$. (b) $x_{2:\mathrm{ccf}}$. (c) $x_{3:\mathrm{ccf}}$. (d) $x_{4:\mathrm{ccf}}$.

Figure 6.2 State trajectory realized by controllable canonical form obtained from (6.11).

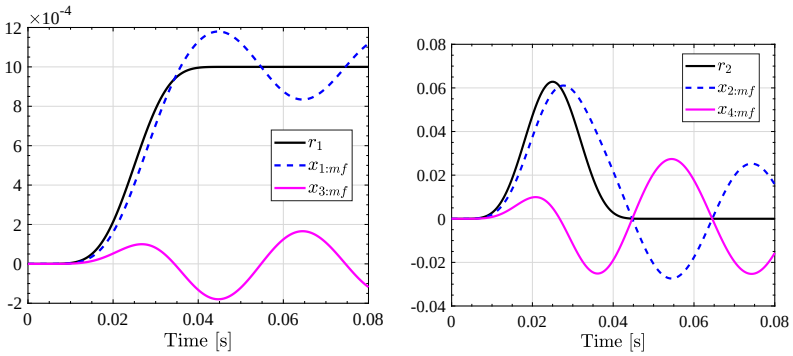

(a) $x_{1:\mathrm{mf}}(t)$ and $x_{3:\mathrm{mf}}(t)$. (b) $x_{2:\mathrm{mf}}(t)$ and $x_{4:\mathrm{mf}}(t)$.

Figure 6.3 State trajectory realized by modal form obtained from (6.16). Note that the first element of $\boldsymbol{c}_{c:\mathrm{mf}}$ is normalized as 1 for visualization.

where

$$\boldsymbol{U}_c := \begin{bmatrix} \boldsymbol{b}_{c:\mathrm{mf}} & \boldsymbol{A}_{c:\mathrm{mf}}\boldsymbol{b}_{c:\mathrm{mf}} & \cdots & \boldsymbol{A}_{c:\mathrm{mf}}^{(n_m-1)}\boldsymbol{b}_{c:\mathrm{mf}} \end{bmatrix} \tag{6.17}$$

$$\boldsymbol{W} := \begin{bmatrix} a_1 & \cdots & a_{n-1} & 1 \\ \vdots & \iddots & \iddots & \\ a_{n-1} & 1 & & \\ 1 & & & \boldsymbol{O} \end{bmatrix}. \tag{6.18}$$

From the above, the state trajectory by the modal form $\boldsymbol{x}_{d:\mathrm{mf}}(t)$ is obtained by

$$\boldsymbol{x}_{d:\mathrm{mf}}(t) = \boldsymbol{T}\boldsymbol{x}_{d:\mathrm{ccf}}(t). \tag{6.19}$$

$\boldsymbol{x}_{d:\mathrm{mf}}(t)$ satisfies

$$r(t) = \boldsymbol{c}_{c:\mathrm{mf}}\boldsymbol{x}_{d:\mathrm{mf}}(t), \tag{6.20}$$

because $\boldsymbol{c}_{c:\mathrm{ccf}} = \boldsymbol{c}_{c:\mathrm{mf}}\boldsymbol{T}$ [37].

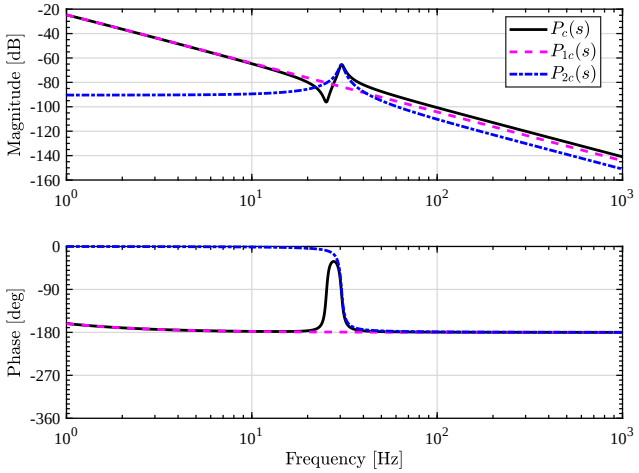

Figure 6.4 Bode diagram of (6.30)

6.2.4 Feedforward control input generation

Owing to the modal form realization shown in (6.14) and (6.15), there is no coupling between modes. Therefore, arbitrarily chosen jth mode consideration is sufficient to generate feedforward control input. As an example, the desired state trajectory of the first mode is extracted as (6.21) by (6.22)

$$\begin{bmatrix} x_{1d:\mathrm{mf}}(t) \\ x_{2d:\mathrm{mf}}(t) \end{bmatrix} = \boldsymbol{M}_1 \boldsymbol{x}_{d:\mathrm{mf}}(t) \tag{6.21}$$

$$\boldsymbol{M}_1 = \begin{bmatrix} \boldsymbol{I}_{(2,2)} & \boldsymbol{O}_{(2,n-2)} \end{bmatrix}, \tag{6.22}$$

where $\boldsymbol{O}$ and $\boldsymbol{I}$ denote the empty and identity matrix, respectively. The subscripts denote the sizes of the matrices.

The state equation for the first mode is

$$\begin{bmatrix} \dot{x}_{1:\mathrm{mf}}(t) \\ \dot{x}_{2:\mathrm{mf}}(t) \end{bmatrix} = \boldsymbol{A}_{c:\mathrm{mf},1} \begin{bmatrix} x_{1:\mathrm{mf}}(t) \\ x_{2:\mathrm{mf}}(t) \end{bmatrix} + \boldsymbol{b}_{c:\mathrm{mf},1} u(t). \tag{6.23}$$

(6.23) is discretized by sampling period T_u and (6.24) is obtained.

$$\begin{bmatrix} \dot{x}_{1:\mathrm{mf}}[k] \\ \dot{x}_{2:\mathrm{mf}}[k] \end{bmatrix} = \boldsymbol{A}_{s:\mathrm{mf},1} \begin{bmatrix} x_{1:\mathrm{mf}}[k] \\ x_{2:\mathrm{mf}}[k] \end{bmatrix} + \boldsymbol{b}_{s:\mathrm{mf},1} u[k], \tag{6.24}$$

where

$$\boldsymbol{A}_{s:\mathrm{mf}} := e^{\boldsymbol{A}_{c:\mathrm{mf}} T_u}, \ \boldsymbol{b}_{s:\mathrm{mf}} := \int_0^{T_u} e^{\boldsymbol{A}_{c:\mathrm{mf}} \tau} \boldsymbol{b}_{c:\mathrm{mf}} d\tau. \tag{6.25}$$

The multirate system with input multiplicity two of (6.24) is

$$\begin{bmatrix} \dot{x}_{1:\mathrm{mf}}[i+1] \\ \dot{x}_{2:\mathrm{mf}}[i+1] \end{bmatrix} = \boldsymbol{A}_{\mathrm{mrff:mf},1} \begin{bmatrix} x_{1:\mathrm{mf}}[i] \\ x_{2:\mathrm{mf}}[i] \end{bmatrix} + \boldsymbol{B}_{\mathrm{mrff:mf},1}\boldsymbol{u}[i], \tag{6.26}$$

where

$$\begin{aligned} \boldsymbol{A}_{\mathrm{mrff:mf},1} &:= \boldsymbol{A}_{s:\mathrm{mf},1}^2, \ \boldsymbol{B}_{\mathrm{mrff:mf},1} := \begin{bmatrix} \boldsymbol{A}_{s:\mathrm{mf},1}\boldsymbol{b}_{s:\mathrm{mf},1} & \boldsymbol{b}_{s:\mathrm{mf},1} \end{bmatrix}, \\ \boldsymbol{x}[i] &:= \boldsymbol{x}(i2T_u). \end{aligned} \tag{6.27}$$

(6.26) is obtained by calculating the state transition from $t = iT_r = kT_u$ to $t = (i+1)T_r = (k+2)T_u$. Here, the input vector $\boldsymbol{u}_o[i]$ is defined in the lifting form

$$\begin{aligned} \boldsymbol{u}_o[i] &:= \begin{bmatrix} u_1[i] & u_2[i] \end{bmatrix}^{\mathrm{T}} \\ &:= \begin{bmatrix} u(kT_u) & u((k+1)T_u) \end{bmatrix}^{\mathrm{T}}. \end{aligned} \tag{6.28}$$

According to (6.26), the feedforward input $\boldsymbol{u}_o[i]$ is obtained from the previewed state trajectory $\boldsymbol{x}_{d:\mathrm{mf}}[i+1]$ as follows:

$$\boldsymbol{u}_o[i] = \boldsymbol{B}_{\mathrm{mrff:mf},1}^{-1}(\boldsymbol{I} - z^{-1}\boldsymbol{A}_{\mathrm{mrff:mf},1}) \begin{bmatrix} x_{1d:\mathrm{mf}}[i+1] \\ x_{2d:\mathrm{mf}}[i+1] \end{bmatrix}, \tag{6.29}$$

where z denotes e^{s2T_u}. The feedforward input $\boldsymbol{u}_o[i]$ enables us to achieve the perfect state matching for every $2T_u$ for the selected modes. Note that this method does not ensure the perfect state matching for the rest modes, however, it can achieve reasonable tracking because the desired state trajectory is generated considering the other modes in (6.19). The short period of the state matching for the selected modes contributes the smaller intersample tracking error compared to the conventional full order multirate feedforward [103], which ensures the full state matching for every nT_u.

6.3 Simulation

6.3.1 Plant definition

In the following, the forth-order plant is considered. A Bode diagram is illustrated in Fig. 6.4.

$$\begin{aligned} P_c(s) &= \frac{3.5321(s^2 + 8.142s + 2.518 \times 10^4)}{s(s + 2.101)(s^2 + 10.89s + 3.665 \times 10^4)} \\ &= \frac{3.532s^2 + 28.76s + 8.894 \times 10^4}{s^4 + 12.99s^3 + 3.667 \times 10^4 s^2 + 7.699 \times 10^4 s} \end{aligned} \tag{6.30}$$

6.3.2 State trajectory $\boldsymbol{x}_{d:\mathrm{ccf}}(t)$ generation by controllable canonical form

(6.30) is realized by the controllable canonical form:

$$\begin{aligned}\dot{\boldsymbol{x}}_{\mathrm{ccf}}(t) =& \begin{bmatrix} 0 & 1 & 0 & 0 \\ 0 & 0 & 1 & 0 \\ 0 & 0 & 0 & 1 \\ 0 & -7.699\times10^4 & -3.667\times10^4 & -12.99 \end{bmatrix} \boldsymbol{x}_{\mathrm{ccf}}(t) + \\ & \begin{bmatrix} 0 \\ 0 \\ 0 \\ 8.894\times10^4 \end{bmatrix} u(t) \\ =& \boldsymbol{A}_{c:\mathrm{ccf}}\boldsymbol{x}_{\mathrm{ccf}}(t) + \boldsymbol{b}_{c:\mathrm{ccf}}u(t) \end{aligned} \tag{6.31}$$

$$\begin{aligned} y =& \begin{bmatrix} 1 & 0.0003233 & 3.971\times10^{-5} & 0 \end{bmatrix} \boldsymbol{x}_{\mathrm{ccf}}(t) \\ =& \boldsymbol{c}_{\mathrm{ccf}}\boldsymbol{x}_{\mathrm{ccf}}(t). \end{aligned} \tag{6.32}$$

The state trajectory $\boldsymbol{x}_{d:\mathrm{ccf}}(t)$ is generated by 6.2.2 and Fig. 6.2 is obtained.

6.3.3 Similarity transformation to the modal form

(6.33) is obtained from (6.30).

$$P_c(s) = P_{1c}(s) + P_{2c}(s) \tag{6.33}$$

$$P_{1c}(s) := \frac{2.427}{s^2 + 2.101s} \tag{6.34}$$

$$P_{2c}(s) := \frac{1.105}{s^2 + 10.89s + 3.665\times10^4} \tag{6.35}$$

(6.33) is realized by the modal form:

$$\begin{aligned} \dot{\boldsymbol{x}}_{\mathrm{mf}}(t) &= \boldsymbol{A}_{c:\mathrm{mf}}\boldsymbol{x}_{\mathrm{mf}}(t) + \boldsymbol{b}_{c:\mathrm{mf}}u(t), \\ y(t) &= \boldsymbol{c}_{c:\mathrm{mf}}\boldsymbol{x}_{\mathrm{mf}}(t), \end{aligned} \tag{6.36}$$

where

$$
\begin{aligned}
\boldsymbol{A}_{c:\mathrm{mf}} &:= \begin{bmatrix} \boldsymbol{A}_{c:\mathrm{mf},1} & \boldsymbol{O} \\ \boldsymbol{O} & \boldsymbol{A}_{c:\mathrm{mf},2} \end{bmatrix}, \\
\boldsymbol{A}_{c:\mathrm{mf},1} &:= \begin{bmatrix} 0 & 1 \\ 0 & -2.101 \end{bmatrix}, \boldsymbol{A}_{c:\mathrm{mf},2} := \begin{bmatrix} 0 & 1 \\ -3.665 \times 10^4 & -10.89 \end{bmatrix}, \\
\boldsymbol{b}_{c:\mathrm{mf}} &:= \begin{bmatrix} \boldsymbol{b}_{c:\mathrm{mf},1} \\ \boldsymbol{b}_{c:\mathrm{mf},2} \end{bmatrix}, \ \boldsymbol{c}_{c:\mathrm{mf}} := \begin{bmatrix} \boldsymbol{c}_{c:\mathrm{mf},1} & \boldsymbol{c}_{c:\mathrm{mf},2} \end{bmatrix} \\
\boldsymbol{b}_{c:\mathrm{mf},1} &:= \begin{bmatrix} 0 & 2.427 \end{bmatrix}^{\mathrm{T}}, \boldsymbol{b}_{c:\mathrm{mf},2} := \begin{bmatrix} 0 & 1.105 \end{bmatrix}^{\mathrm{T}} \\
\boldsymbol{c}_{c:\mathrm{mf},1} &:= \begin{bmatrix} 1 & 0 \end{bmatrix}, \ \boldsymbol{c}_{c:\mathrm{mf},2} := \begin{bmatrix} 1 & 0 \end{bmatrix}.
\end{aligned} \tag{6.37}
$$

$\boldsymbol{U}_c$ and $\boldsymbol{W}$ in (6.16) are

$$
\boldsymbol{U}_c = \begin{bmatrix} \boldsymbol{b}_{c:\mathrm{mf}} & \boldsymbol{A}_{c:\mathrm{mf}}\boldsymbol{b}_{c:\mathrm{mf}} & \boldsymbol{A}_{c:\mathrm{mf}}^2\boldsymbol{b}_{c:\mathrm{mf}} & \boldsymbol{A}_{c:\mathrm{mf}}^3\boldsymbol{b}_{c:\mathrm{mf}} \end{bmatrix} \tag{6.38}
$$

$$
\boldsymbol{W} = \begin{bmatrix} 76993 & 36673 & 13 & 1 \\ 36673 & 13 & 1 & 0 \\ 13 & 1 & 0 & 0 \\ 1 & 0 & 0 & 0 \end{bmatrix}. \tag{6.39}
$$

The state trajectory $\boldsymbol{x}_{d:\mathrm{mf}}(t)$ obtained by (6.19) is shown in Fig. 6.3.

6.3.4 Feedforward control input generation

We discretize the first mode (6.34) by sampling period $T_u = 400\,\mu$s and the multirate feedforward (6.29) in the second order is obtained as

$$
\begin{aligned}
\boldsymbol{A}_{\mathrm{mrff:mf},1} &:= \begin{bmatrix} 1.00 & 7.99 \times 10^{-4} \\ 0 & 0.998 \end{bmatrix}, \\
\boldsymbol{B}_{\mathrm{mrff:mf},1} &:= \begin{bmatrix} 5.82 \times 10^{-7} & 1.94 \times 10^{-7} \\ 9.69 \times 10^{-4} & 9.70 \times 10^{-4} \end{bmatrix}
\end{aligned} \tag{6.40}
$$

6.3.5 Simulation results

We compare the three methods for the simulation for the fourth order plant shown in Fig. 6.4 and (6.30). Simulation results are shown in Fig. 6.5 and Tab. 6.1. The proposed method ('MRFF(MF)') achieves smaller intersample error and on sample error (every T_u). Tab. 6.2 shows the condition number of the discrete controllability matrix. The inversion of it is needed for the multirate feedforward calculation in (6.29) and (6.42). The full order multirate feedforward ('MRFF(CCF)') have a high-

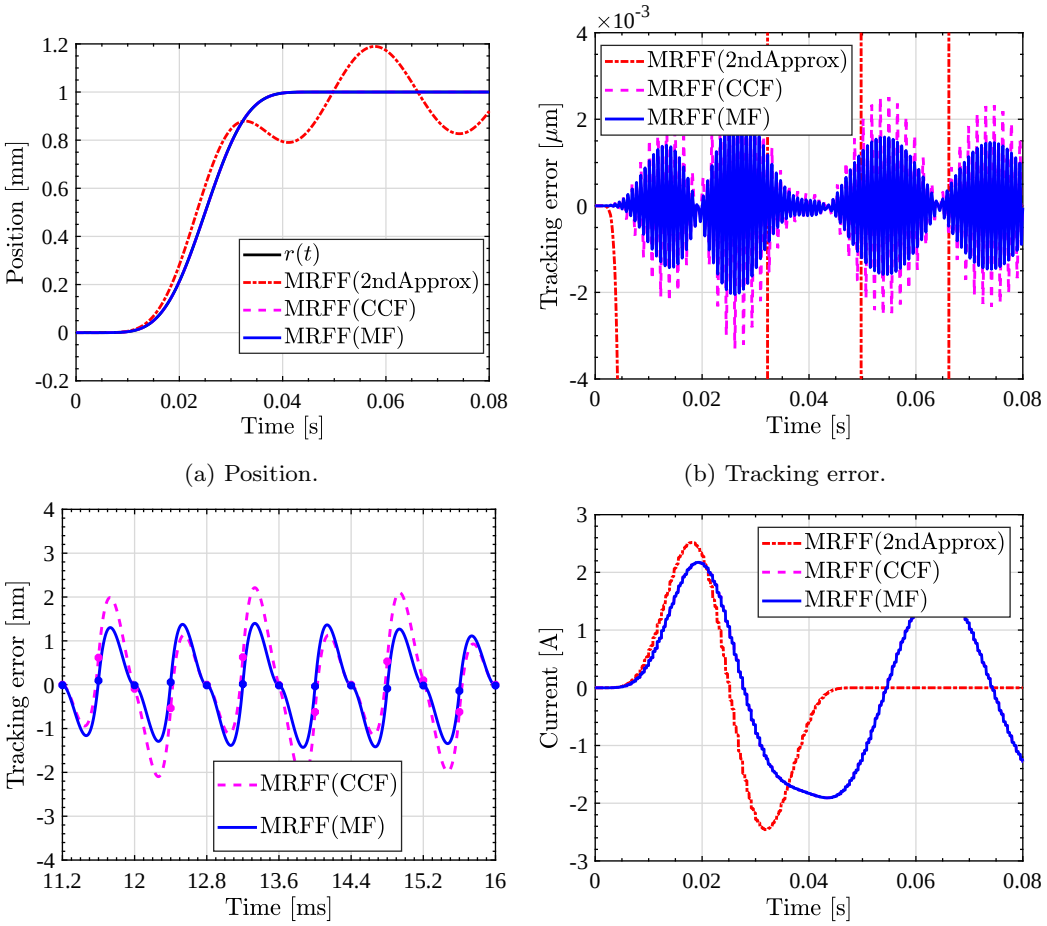

(a) Position.

(b) Tracking error.

(c) Tracking error(zoom).

(d) Feedfoward input.

Figure 6.5 Simulation results. Note that grids of (c) are every $2T_u$. Dots are illustrated for every T_u. (c) shows that the proposed method has less intersampling error.

condition number. It is assumed that condition number will be much worse with a higher order nominal plant. The proposed method based on the modal form can keep the condition number low and it is numerically more reliable.

Second order approximated multirate feedforward

This method approximates the nominal plant as the second order $P_{1c}(s)$ in (6.34) and the approximated model is used for multirate feedforward [103]. 'MRFF(2ndApprox)' in Fig. 6.5 indicates this method. The state and output equations are

$$\dot{\boldsymbol{x}}(t) = \begin{bmatrix} 0 & 1 \\ 0 & -2.101 \end{bmatrix} \boldsymbol{x}(t) + \begin{bmatrix} 0 \\ 2.427 \end{bmatrix} u(t), \quad y(t) = \begin{bmatrix} 1 & 0 \end{bmatrix} \boldsymbol{x}(t). \tag{6.41}$$

Note that the equation for multirate feedforward shown in (6.29) is as same as the proposed method based on modal form (6.40). However, the given state trajectory by (6.7) is $\boldsymbol{x}(t) = [r(t) \ \ \rho r(t)]^{\mathrm{T}}$ and it is different from the proposed method because the proposed method generates the desired state

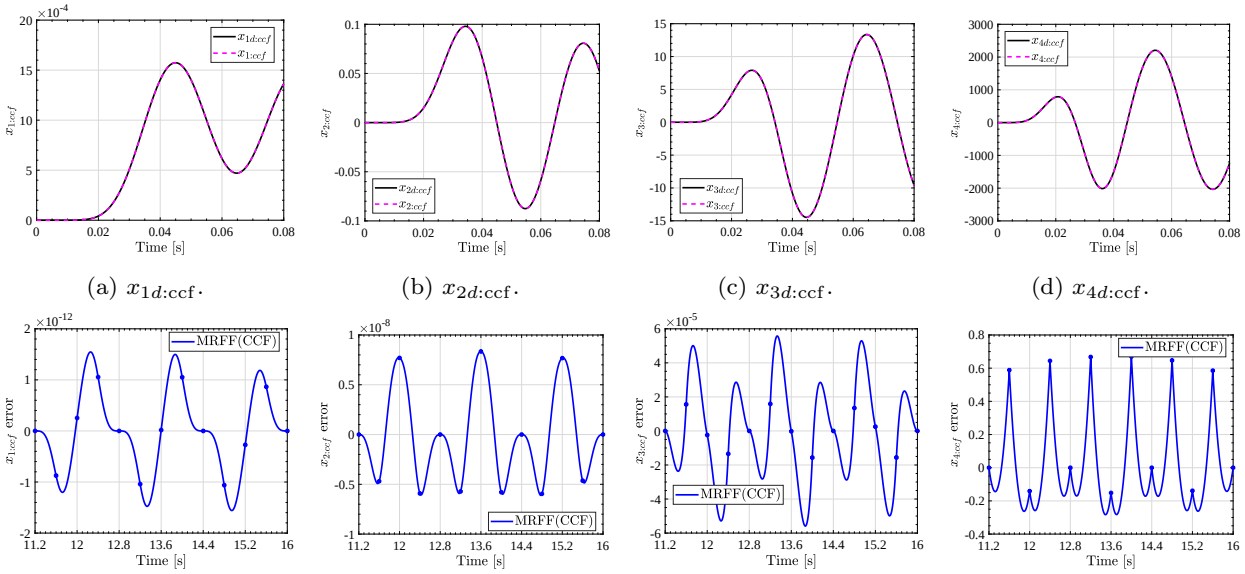

(a) $x_{1d:\mathrm{ccf}}$. (b) $x_{2d:\mathrm{ccf}}$. (c) $x_{3d:\mathrm{ccf}}$. (d) $x_{4d:\mathrm{ccf}}$.

(e) $x_{1d:\mathrm{ccf}}$ error. (f) $x_{2d:\mathrm{ccf}}$ error. (g) $x_{3d:\mathrm{ccf}}$ error. (h) $x_{4d:\mathrm{ccf}}$ error.

Figure 6.6 Simulation results of the full order multirate feedforward [103]. Dots are illustrated for every T_u. The perfect state matching for every $4T_u$ is achieved and the output error $r(t)-y(t)$ is exactly zero for every $4T_u$.

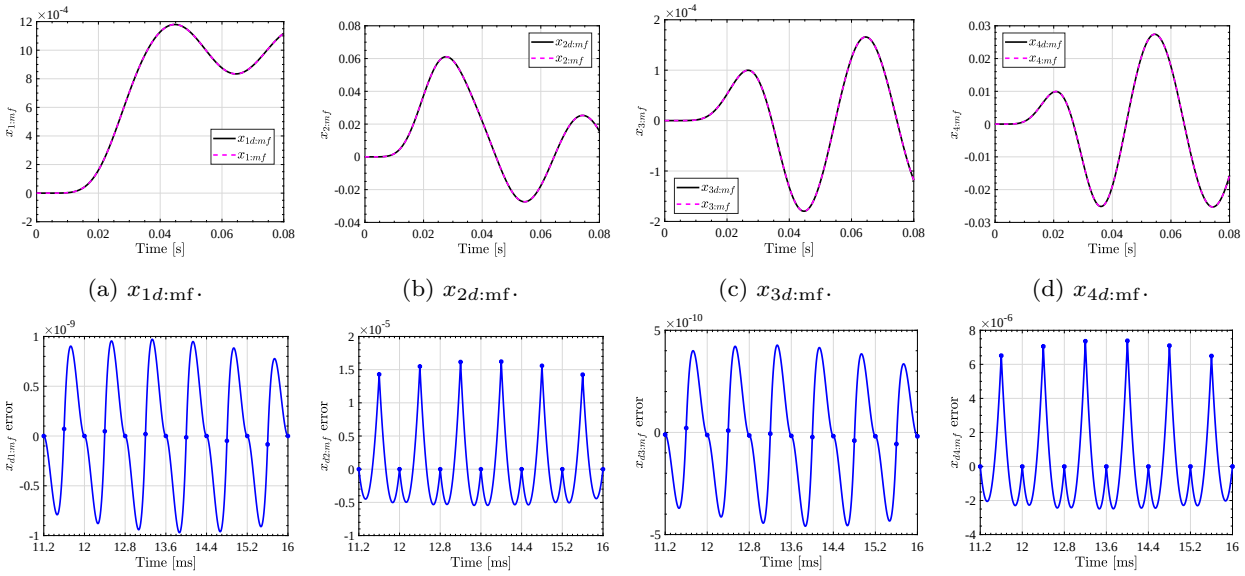

(a) $x_{1d:\mathrm{mf}}$. (b) $x_{2d:\mathrm{mf}}$. (c) $x_{3d:\mathrm{mf}}$. (d) $x_{4d:\mathrm{mf}}$.

(e) $x_{1d:\mathrm{mf}}$ error. (f) $x_{2d:\mathrm{mf}}$ error. (g) $x_{3d:\mathrm{mf}}$ error. (h) $x_{4d:\mathrm{mf}}$ error.

Figure 6.7 Simulation results of the proposed multirate feedforward based on modal form. Dots are illustrated for every T_u. From (a) to (d), a good state tracking is achieved. (e) and (f) shows that the state matching for $x_{1d:mf}$ and $x_{2d:mf}$ is achieved for every $2T_u$. Perfect state matching is not achieved for $x_{3d:mf}$ and $x_{4d:mf}$ (it's clear on (g)). Although the state mismatch on sample contributes the output error $r(t)-y(t)$, Fig. 6.5 shows that it is negligibly small on sample and the benefit on small intersample error remains.

Table 6.1 Maximum tracking error for Fig. 6.5

	Sampling points (every T_u)	Sampling points (every $4T_u$)*	Intersample
MRFF(2ndApprox)	208 μm	208 μm	208 μm
MRFF(CCF)	0.937 nm	1.88×10^{-4} nm	331 nm
MRFF(MF)	0.299 nm	7.03×10^{-2} nm	214 nm

* $T_r = nT_u = 4T_u$ for MRFF(CFF).

Table 6.2 Condition number of the controllability matrix

	Condition number
MRFF(2ndApprox)	5.00×10^3
MRFF(CCF)	1.36×10^{11}
MRFF(MF)	5.00×10^3

trajectory considering the other modes by (6.19).

Fig. 6.5(a) shows that this method cannot track the reference $r(t)$ at all because the state trajectory is generated ignoring the resonance mode $P_{2c}(s)$.

Full order multirate feedforward

This method used the full order model (6.30) for the multirate feedforward [103]. 'MRFF(CCF)' in Fig. 6.5 indicates this method.

$$\boldsymbol{u}_o[i] = \boldsymbol{B}_{\text{mrff:ccf}}^{-1}(\boldsymbol{I} - z^{-1}\boldsymbol{A}_{\text{mrff:ccf}})\boldsymbol{x}_{d\text{:ccf}}[i+1], \tag{6.42}$$

$$\boldsymbol{A}_{\text{mrff:ccf}} := \boldsymbol{A}_{s\text{:ccf}}^4, \quad \boldsymbol{x}[i] := \boldsymbol{x}(i4T_u) \tag{6.43}$$

$$\boldsymbol{B}_{\text{mrff:ccf}} := \begin{bmatrix} \boldsymbol{A}_{s\text{:ccf}}^3\boldsymbol{b}_{s\text{:ccf}} & \boldsymbol{A}_{s\text{:ccf}}^2\boldsymbol{b}_{s\text{:ccf}} & \boldsymbol{A}_{s\text{:ccf}}\boldsymbol{b}_{s\text{:ccf}} & \boldsymbol{b}_{s\text{:ccf}} \end{bmatrix} \tag{6.44}$$

Fig. 6.5(c) indicates that the perfect tracking is achieved for every $4T_u$ because the order of multirate feedforward is four. Fig. 6.6 shows that the perfect state matching for all the states for every $4T_u$ is achieved.

Multirate feedforward based on modal form

The procedure shown in Section 6.3.2–6.3.4 is applied. 'MRFF(CCF)' in Fig. 6.5 indicates this method.

Fig. 6.5(b) shows that the intersample tracking error is smaller than the conventional full order multirate feedforward. Fig. 6.7(e) and 6.7(f) show that the perfect state matching is achieved for every $2T_u$ and good state tracking is achieved the rest states (Fig. 6.7(c) and 6.7(d)). Although Fig. 6.7(g) and 6.7(h) show that the perfect state matching is not achieved for every $2T_u$, Fig. 6.5(c) shows that the effect to the output error $r(t) - y(t)$ is negligibly small on sample and the benefit on small

intersample error remains.

6.4 Conclusion

Multirate feedforward has been proposed to design stable inversion for a plant with unstable discretization zeros. However, the multirate feedforward control method based on the controllable canonical form has several issues for a high-order plant: i) long time (nT_u) for perfect tracking and ii) low numerical stability due to inversion of controllability matrix with matrix size ($n \times n$).

This chapter proposes a multirate feedforward control method based on the modal form to relax their problems. The proposed method has the following four steps: 1) state trajectory generation by controllable canonical form, 2) similarity transformation to modal form, 3) mode extraction, and 4) multirate feedforward control for the extracted second-order mode. The proposed method has the following advantages regardless of the plant order: i) perfect state matching for the selected mode for every $2T_u$ and ii) size of the controllability matrix for multirate feedforward. The simulation results validate these advantages and show better intersample error owing to the shorter period for the state matching.

Part II

Tracking Control Method for Pneumatically Actuated Stage with Time Delay

Chapter 7

Trajectory Tracking Control for Pneumatically Actuated Scan Stage with Time Delay Compensation

Abstract

A pneumatic actuator has several advantages such as low heat generation, high weight/power ratio, and low cost. However, it has several disadvantages such as time delays and nonlinearities. Because pressure and position feedback band- widths are limited by time delay, it is difficult to implement a pneumatic actuator for a scan stage. To enable this, this chapter proposes to use a modified Smith predictor and implements it for an experimental scan stage. The effectiveness of the proposed control system is validated by frequency and time domain characterization experiments.

7.1 Introduction

High-precision stages are important machinery in the semiconductor and flat panel display manufacturing processes [1, 85]. To achieve high integration and reduce the cost of manufacturing for electronic devices, faster and more precise positioning by larger stages are required. High speed positioning requires more massive actuators, increasing the moving mass combined with the larger stage. As a result, the heat generated by electromagnetic actuators is increased. Heat is a serious concern because it affects not only the proprieties of the mechanical system but also those of the actuation and measurement systems [82, 97]. Another problem accompanying a larger and more massive stage is reduced resonant frequencies. Due to this problem, it is difficult to design a high bandwidth feedback controller. Hence, conventional scan stages inherently face a trade-off between throughput and positioning accuracy [43].

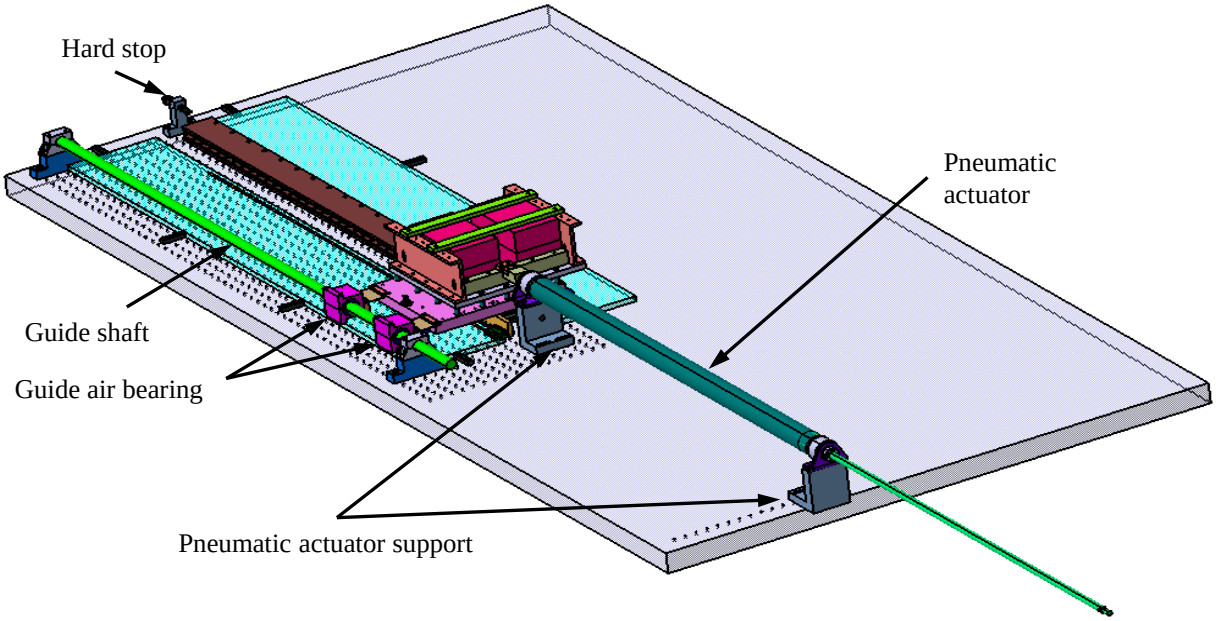

(a) Oblique view.

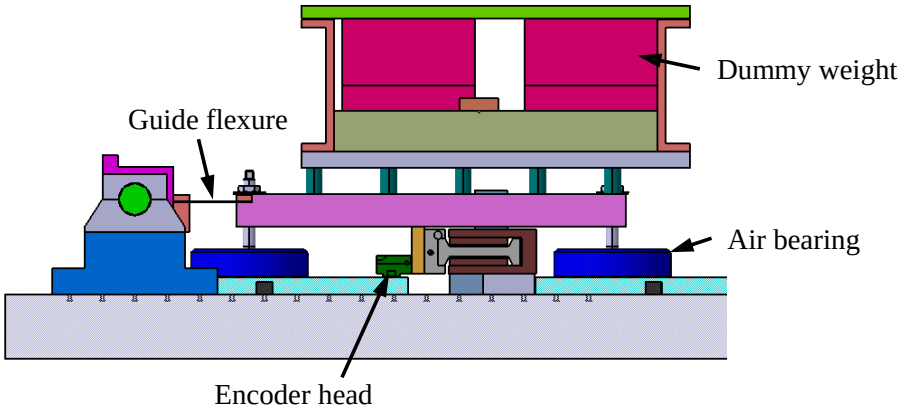

(b) Side view.

Figure 7.1 Schematics of the pneumatic actuated scan stage.

To relax the trade-off, a contactless dual stage structure which has a short stroke fine stage and a long stroke coarse stage is commonly used [2, 79]. This structure allows a slightly lighter fine stage and reduces disturbance from the coarse stage. However, the weight reduction of the ne stage is limited by the required maximum acceleration of the fine stage actuator determined by the setpoint trajectory. To address this issue, our group has proposed a catapult stage [34, 95, 96] which allows both contact and separation between the fine and coarse stages. The fine stage of the catapult stage is lighter and simpler compared to the conventional dual stage because the fine stage actuation is not necessary in the acceleration and deceleration regions in the scanning motion.

This chapter considers replacing the linear motor in the coarse stage with a pneumatic actuator for a lighter and simpler stage. This pneumatically-actuated coarse stage can be used in the catapult configuration to create a new-generation lightweight dual stage that generates little heat and demonstrates high positioning accuracy. A pneumatic actuator has advantages compared to a linear motor:

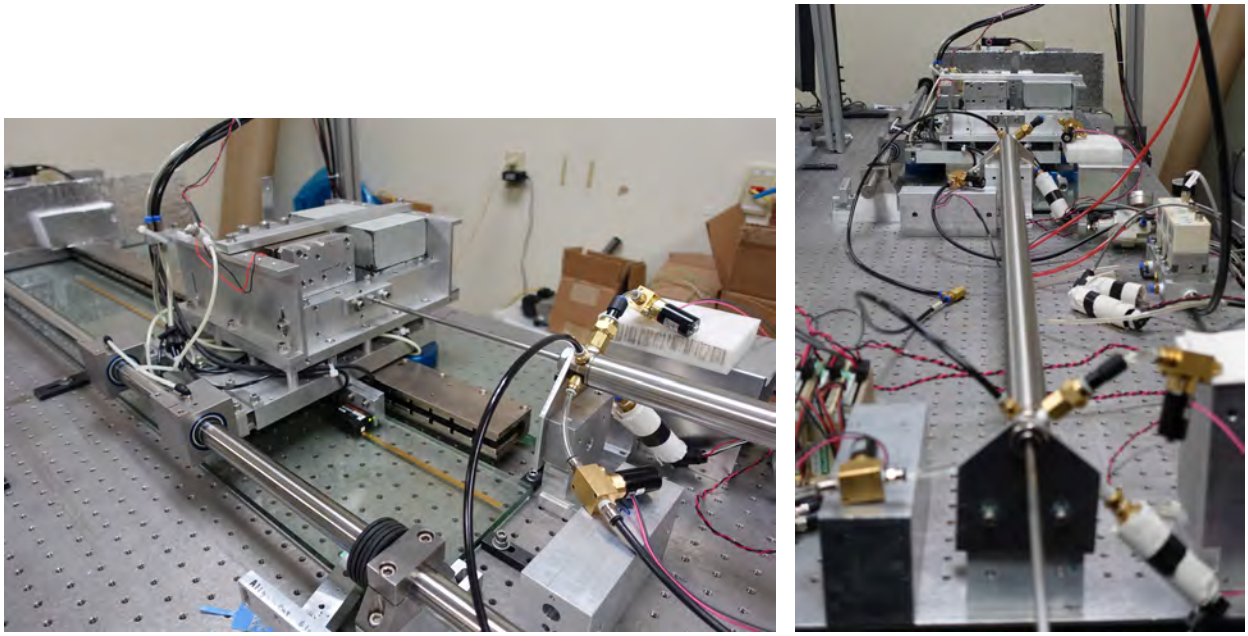

(a) Oblique view. (b) Side view.

Figure 7.2 Photograph of the pneumatic actuated scan stage.

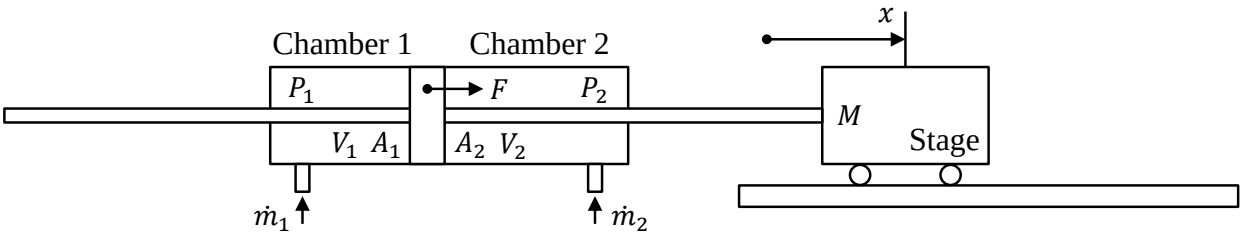

Figure 7.3 Model of the pneumatic actuated scan stage.

1) low heat generation [97], 2) high power-weight ratio [98], and 3) low cost [98]. Disadvantages include 1) time delay [99] and 2) nonlinear dynamics [100, 101] due to air dynamics and servo valves. Because of these disadvantages, pneumatic actuators are not commonly used in precision motion control applications [102]. This chapter focuses on the time delay problem which limits feedback control bandwidth. Various methods have been studied to address time delay: 1) Smith predictor [137] and its modifications [138,139], 2) Internal Model Control (IMC) [140], and 3) communication disturbance observer [88]. This chapter applies a modied Smith predictor to a trajectory tracking control problem.

Control methods for pneumatic actuators have been studied [141] including PID control [142], iterative learning control [143], and sliding mode control [144]. The control system proposed in this chapter has an inner pressure feedback loop with a modified Smith predictor for each chamber, and an outer position feedback loop. Each inner loop also has a pressure-derivative feedforward calculated by a jerk reference of the stage to improve pressure tracking control performance.

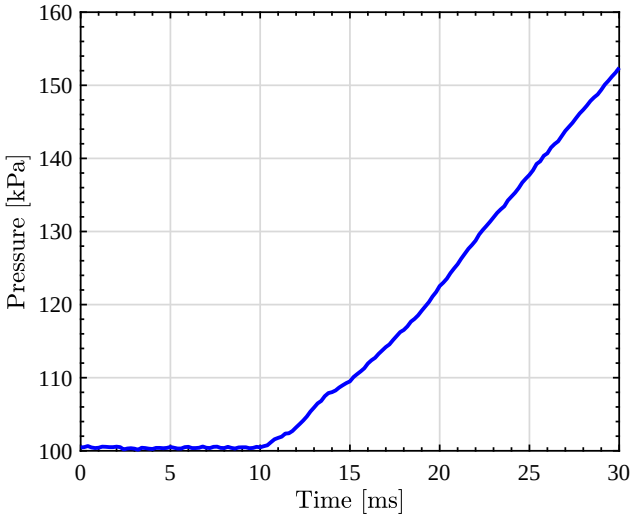

Figure 7.4 Step response of the chamber 1. There is a delay from u_1^{ref} to P_{1m}.

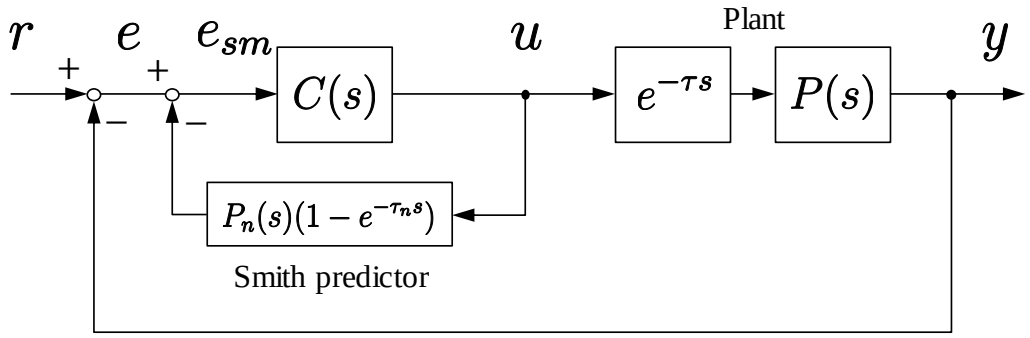

Figure 7.5 Block diagram of the Smith predictor.

7.2 Experimental setup

Schematics and photographs of our experimental setup are shown in Figs. 7.1 and 7.2. This stage is designed as a miniaturized single axis (x) coarse stage actuated by a pneumatic cylinder. The coarse stage is supported by air pads to reduce friction. As illustrated in Fig. 7.3, the cylinder has two chambers. Each chamber has a pressure sensor, a high-pressure poppet valve and an ambient poppet valve. The supply air of the high-pressure side is 4×10^5 Pa. The position of the stage is measured by a linear encoder.

One of the problems of this pneumatically actuated stage is time delay. Fig. 7.4 shows a step response from a valve voltage reference to the measured pressure in Chamber 1. There is a delay of about 10 ms. This delay is not negligible to achieve high feedback bandwidths for the pressure and position feedback loops.

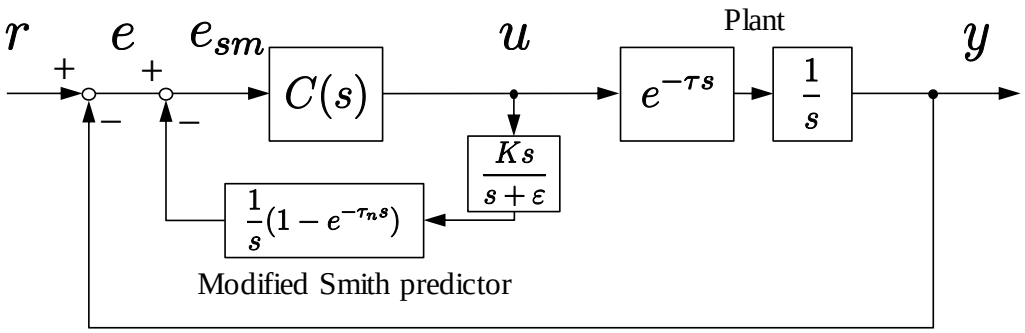

Figure 7.6 Block diagram of the modified Smith predictor.

7.3 Time delay compensation by modified Smith predictor

7.3.1 Smith predictor

This subsection introduces the Smith predictor [137]. Here, a plant with input delay $P(s)e^{-\tau s}$ is assumed. Without the Smith predictor, the tracking control performance is

$$\frac{y(s)}{r(s)} = \frac{C(s)P(s)e^{-\tau s}}{1 + C(s)P(s)e^{-\tau s}}. \tag{7.1}$$

The denominator of (7.1) has a delay element undermining feedback stability. With the Smith predictor shown in Fig. 7.5, the tracking control performance becomes

$$\frac{y(s)}{r(s)} = \frac{C(s)P(s)e^{-\tau s}}{1 + C(s)P(s)} \tag{7.2}$$

when $P_n(s) = P(s)$ and $\tau_n = \tau$. Because the denominator of (7.2) does not have a delay element, the feedback controller $C(s)$ can be designed as a system without delay.

7.3.2 Modified Smith predictor and its analysis

The Smith predictor cannot be used for an unstable system or an integrating system with a constant disturbance [139]. To address this issue, this chapter proposes a modied Smith predictor with a high pass lter (HPF) illustrated in Fig. 7.6 for the integrating system. Fig. 7.6 has three tuning parameters: a cut off frequency of the HPF ε, a gain K, and a nominal delay τ_n. Nyquist diagrams calculated from a measured frequency response of the pressure feedback control are shown in Fig. 7.7. Proportional integral (PI) controller with 14 Hz nominal bandwidth is used for the pressure feedback.

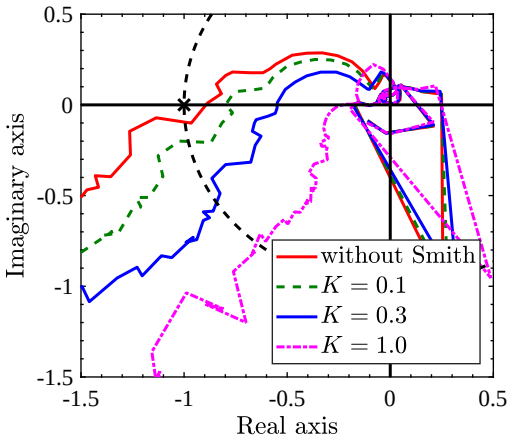

(a) K dependency. $\tau_n = 10\,\text{ms}, \varepsilon = 1 \times 2\pi$.

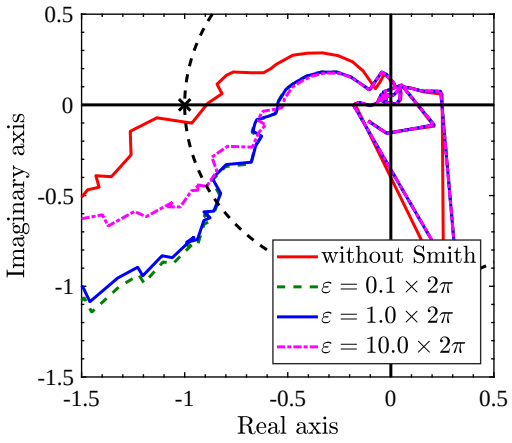

(b) ε dependency. $K = 0.3, \tau_n = 10\,\text{ms}$.

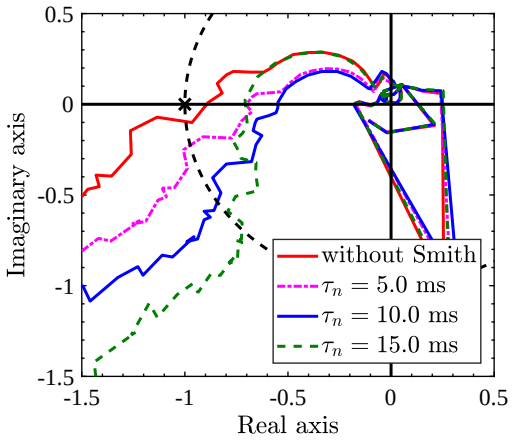

(c) τ_n dependency. $K = 0.3, \varepsilon = 1 \times 2\pi$.

Figure 7.7 Nyquist diagram of the pressure control.

7.4 Modeling

The model of the pneumatically actuated stage is illustrated in Fig. 7.3. A block diagram of the overall control system is shown in Fig. 7.8. The ideal gas equation is

$$P_i(t)V_i(t) = m_i(t)RT_i, \tag{7.3}$$

where P_i, V_i, m_i, R, T_i denotes chamber pressure, chamber volume, mass of the gas, ideal gas constant, temperature for each chambers, respectively. Chamber temperature T_i is assumed to be a constant. Subscript i represents the chamber number. By time differentiation of (7.3),

$$\dot{P}_i(t)V_i(t) + P_i(t)\dot{V}_i(t) = \dot{m}_i(t)RT_i \tag{7.4}$$

is obtained. From (7.4), $\dot{P}_i$ is modeled as

$$\dot{P}_i(t) = \frac{-P_i(t)\dot{V}_i(t) + \dot{m}_i(t)RT_i}{V_i(t)}. \tag{7.5}$$

Nonlinear model NL from valve commands $u_{i,in}, u_{i,out}$ to $\dot{m}_i$ shown in Fig. 7.8 is obtained by polynomial fitting of experimental data [100, 145].

Equation of motion of the stage is

$$\begin{aligned} f(t) &= P_1(t)A - P_2(t)A \\ &= M\ddot{x}(t), \end{aligned} \tag{7.6}$$

where f, A, M, and x denotes force from the pneumatic cylinder, pressurized area, mass of the stage, and position of the stage, respectively.

7.5 Control system of the pneumatically actuated stage

The control system of the pneumatic actuation stage is shown in Fig. 7.8. As an inner loop, a pressure feedback is implemented for each chamber. As an outer loop, a position feedback is implemented for stage position by using a linear encoder.

7.5.1 Position control

$C_{fb}^{x}(s)$ is implemented as an outer loop position feedback controller. The relationship between the output of position feedback f^{ref} and pressure commands P_1^{ref}, P_2^{ref} is

$$P_1^{ref}(t) = P^{set} + \frac{f^{ref}(t)}{2A}, \;\; P_2^{ref}(t) = P^{set} - \frac{f^{ref}(t)}{2A}, \tag{7.7}$$

where P^{set} denotes the set pressure for each chamber. In this case, P^{set} is set as 2.0×10^5 Pa. $C_{fb}^{x}(s)$ is designed by a series connection of a PI controller, a phase lead filter, and notch filters.

7.5.2 Pressure control

Pressure feedback controllers C_{fb}^{P1}, C_{fb}^{P2} are designed as a series connection of a PI controller, a phase lead filter, and notch filters.

The reference of the derivative of the gas mass is obtained as follows:

$$\dot{m}_i^{ref}(t) = \frac{\dot{P}_i^{ref}(t)V_i(t) + P_i(t)\dot{V}_i(t)}{RT_i}. \tag{7.8}$$

Inverse model NL^{-1} from $\dot{m}_i^{ref}$ to $u_{i,in}^{ref}, u_{i,out}^{ref}$ is calculated by the inverse of the polynomial obtained in section 7.4.

Feedforward commands $\dot{P}_{1,ff}^{ref}, \dot{P}_{2,ff}^{ref}$ are obtained by the differentiations of (7.6) and (7.7):

$$\dot{P}_{1,ff}^{ref}(t) = \frac{M\dddot{x}^{ref}(t)}{2A}, \;\; \dot{P}_{2,ff}^{ref}(t) = -\frac{M\dddot{x}^{ref}(t)}{2A}. \tag{7.9}$$

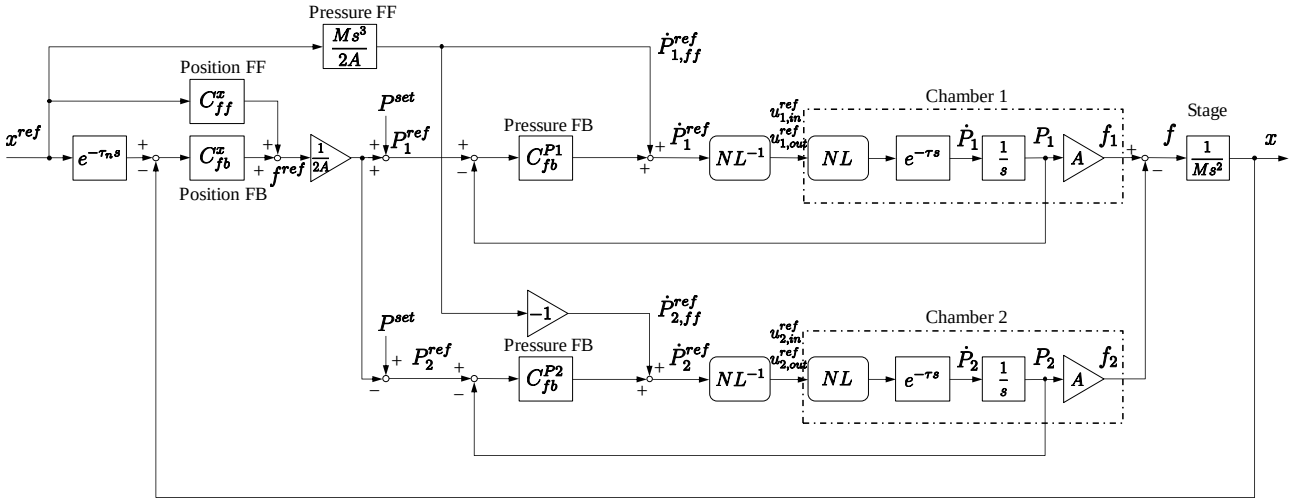

Figure 7.8 Block diagram of the conventional control system.

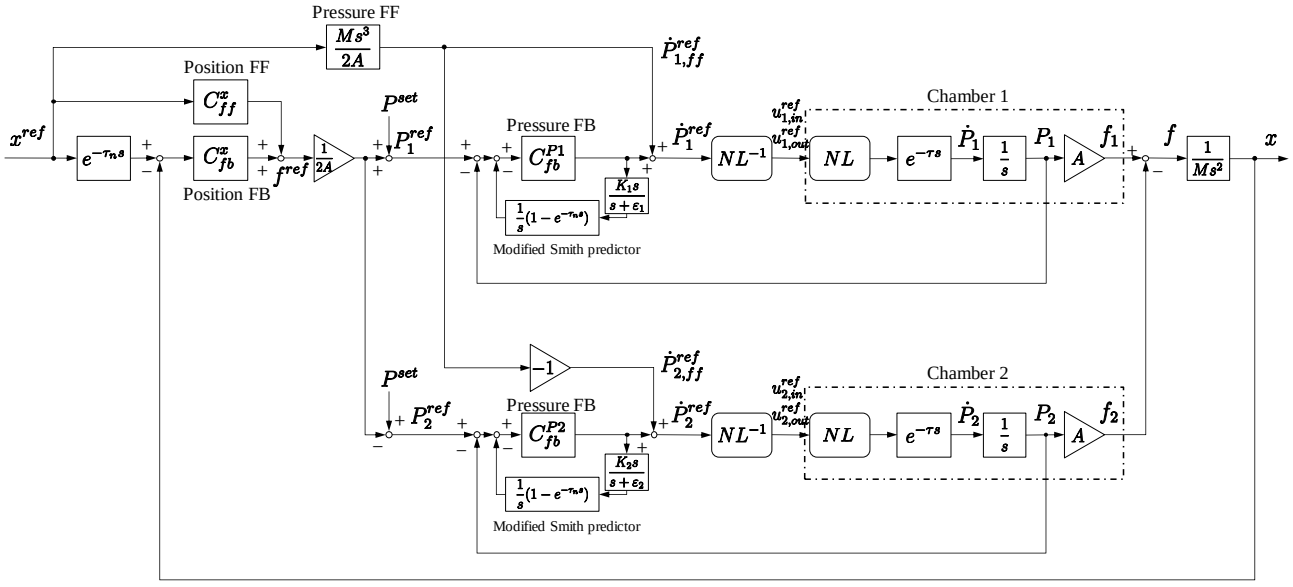

Figure 7.9 Block diagram of the proposed control system.

7.6 Experimental results

7.6.1 Pressure feedback

We performed experiments in three cases: Case1 (Conv), Case2 (Prop) and Case3 (Prop2). The conditions are listed in Tab. 7.1 and 7.2. The experiments are performed by the block diagrams shown in Fig. 7.8 and Fig. 7.9, respectively. Pressure feedback control performance is shown in Fig. 7.10 and Tab. 7.1. In Case 1 (Conv), C_{fb}^{P1}, C_{fb}^{P2} are designed to have about 35 degree phase margin without the modified Smith predictor. In Case 2 (Prop), C_{fb}^{P1}, C_{fb}^{P2} are redesigned to have about phase margin of 35 degrees with the modified Smith predictor. The parameters of the modified Smith predictor are set as $\tau_n = 10\,\mathrm{ms}$, $K_1 = 0.3$, $K_2 = 0.4$, and $\varepsilon = 1 \times 2\pi\,\mathrm{rad/s}$.

Fig. 7.10 shows a frequency response from the force command for the pneumatic cylinder f^{ref} to estimated force generated by the pneumatic cylinder $\hat{f}$. $\frac{\hat{f}(j\omega)}{f^{ref}(j\omega)}$ is calculated by

$$\frac{\hat{f}(j\omega)}{f^{ref}(j\omega)} = \frac{P_1(j\omega)A - P_2(j\omega)A}{f^{ref}(j\omega)}. \tag{7.10}$$

In Tab. 7.1, the bandwidth is defined as the -90 degree crossover of $\frac{\hat{f}(j\omega)}{f^{ref}(j\omega)}$. From Fig. 7.10 and Tab. 7.1, the pressure feedback bandwidth is improved from 9.4 Hz to 31 Hz regardless of similar phase margin.

7.6.2 Position feedback

Frequency response of the position feedback is shown in Fig. 7.11 and Tab. 7.2. In Case 1 (Conv), the phase margin of position feedback is 22 degree. In Case 2 (Prop), the phase margin of position feedback is 53 degree because the inner loop pressure feedback is improved. In Case 3 (Prop2), the outer loop position feedback controller C_{fb}^{x} is redesigned. The position feedback bandwidth is improved from 5.3 Hz to 11 Hz although the gain and phase margins increase.

Time responses are shown in Fig. 7.12. In this experiment, a scan trajectory is given as a reference shown in Fig. 7.12(a). Tracking performances are shown in Fig. 7.12(d) and Tab. 7.3. In Case 3 (Prop2), the maximum tracking error is improved from 507.7 μm to 135.3 μm because of its high bandwidth feedback controller.

7.7 Summary

This chapter investigated a pneumatic actuator for a scan stage to replace a linear motor. A pneumatic actuator has advantages such as low heat generation, high power-weight ratio, and low

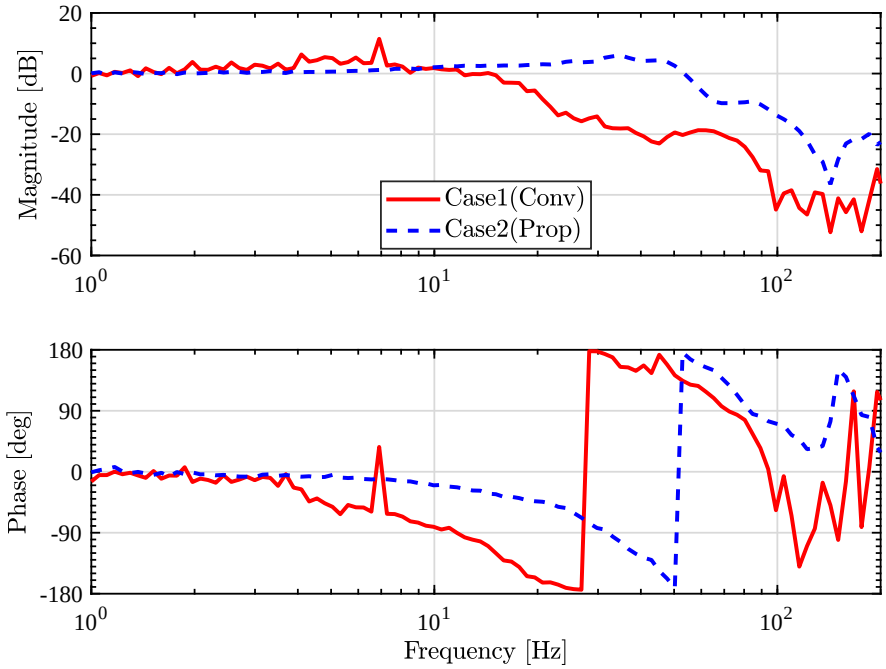

Figure 7.10 Pressure feedback control performance $\frac{\hat{f}(j\omega)}{f^{ref}(j\omega)}$ calculated by (7.10). By applying the modified Smith predictor, the feedback bandwidth is improved as listed in Tab. 7.1.

Table 7.1 Pressure feedback control performance by Fig. 7.10.

	Case1 (Conv)	Case2 (Prop)
Pressure FB	low gain	high gain + MSP*
Gain margin	13dB (32Hz)	6.4dB (62Hz)
Phase margin	35deg (6.9Hz)	35deg (27Hz)
Bandwidth	9.4Hz	31Hz

*Modified Smith predictor

Table 7.2 Position feedback control performance by Fig. 7.11.

	Case1 (Conv)	Case2 (Prop)	Case3 (Prop2)
Pressure FB	low gain	high gain + MSP*	same as case 2
Position FB	low gain	same as case 1	high gain
Gain margin (Position FB)	7.0 dB (9 Hz)	17 dB (30 Hz)	9.6 dB (30 Hz)
Phase margin (Position FB)	22 deg (5.9 Hz)	53 deg (3.2 Hz)	26 deg (10 Hz)
Bandwidth (Position FB)	5.3 Hz	7.7 Hz	11 Hz

*Modified Smith predictor

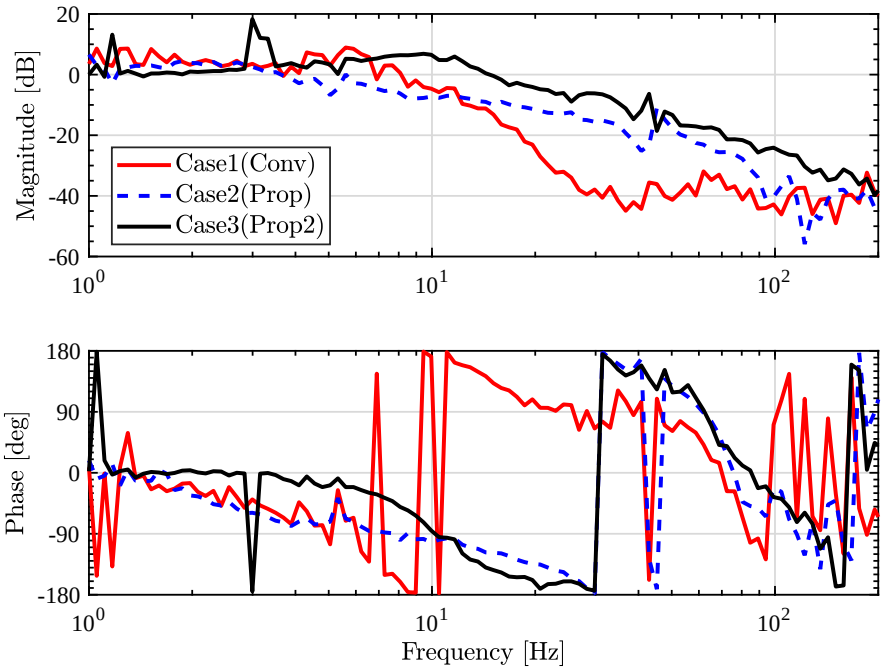

Figure 7.11 Position control performance $\frac{x(j\omega)}{x^{ref}(j\omega)}$. Position feedback bandwidth is improved as listed in Tab. 7.2.

Table 7.3 Scan motion experimental results by Fig. 7.12.

	Case1 (Conv)	Case2 (Prop)	Case3 (Prop2)
Maximum tracking error	508 μm	418 μm	135 μm
Standard deviation of the tracking error	114 μm	94.0 μm	19.5 μm

cost. On the other hand, it has disadvantages such as time delay and nonlinearity. Due to the time delay problem, it is difficult to implement a high bandwidth feedback controller.

The proposed control system has a pressure feedback inner loop for each chamber and a position feedback outer loop. The nominal plant of the inner loop is an integrator. The standard Smith predictor cannot be used in a system with an integrator. Therefore, this chapter proposes a modified Smith predictor and implements it for an experimental scan stage.

The proposed control system with the modified Smith predictor in the inner loops can achieve high bandwidths for the inner loops and outer loop. The proposed method achieves maximum tracking error 135 μm and standard deviation of the tracking error 19.5 μm. The results are considered as very accurate because literature [113] states that the positioning accuracy of pneumatic actuated systems is $100 - 500$ μm at best.

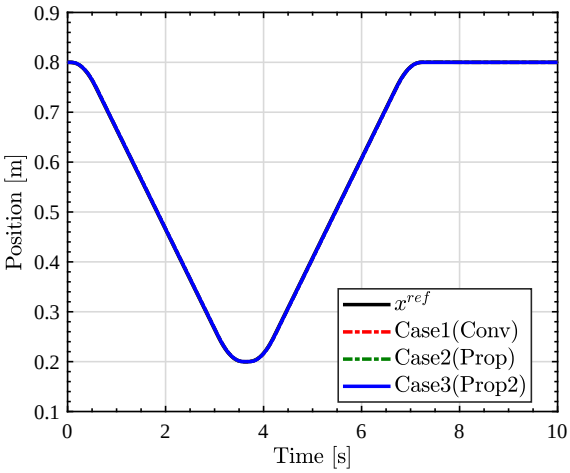

(a) Stage position x_m.

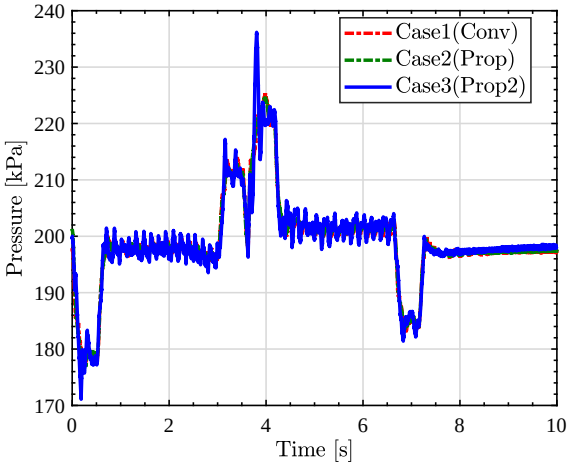

(b) Chamber 1 pressure P_1.

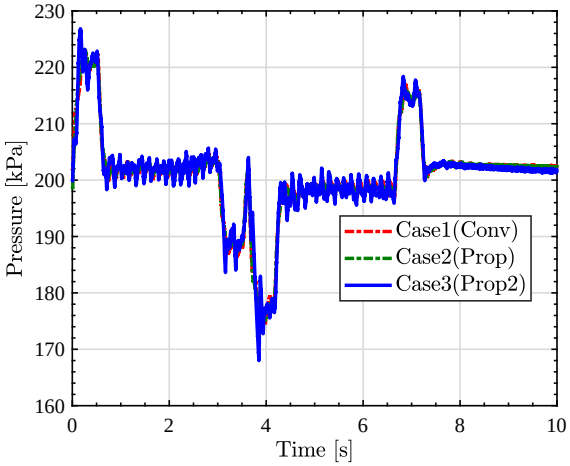

(c) Chamber 2 pressure P_2.

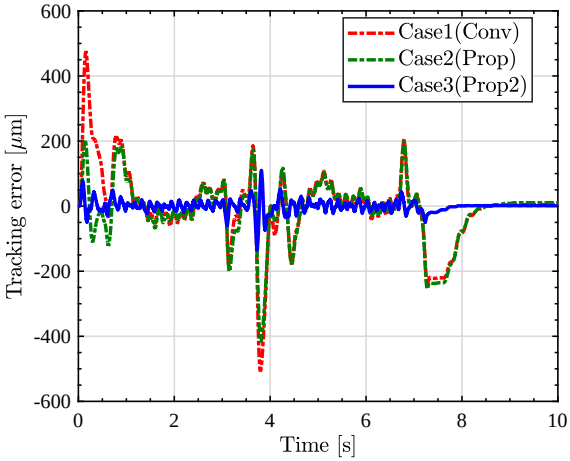

(d) Stage position tracking error.

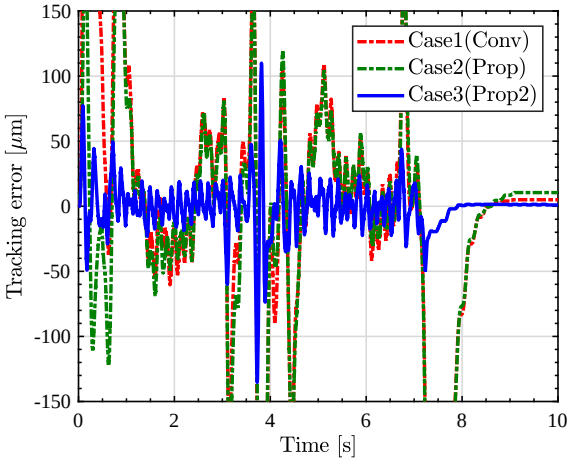

(e) Stage position tracking error (zoom).

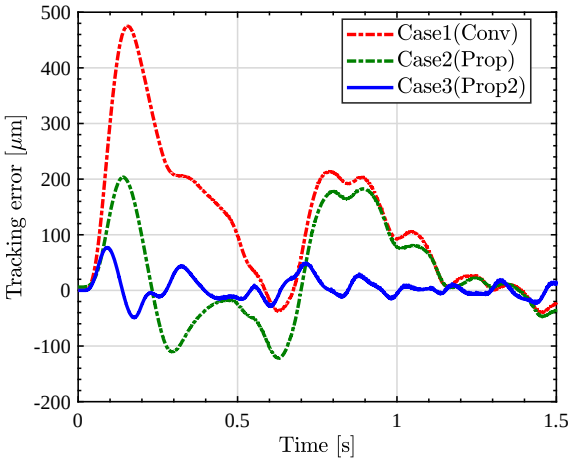

(f) Stage position tracking error (zoom2).

Figure 7.12 Scan motion experimental results. The tracking error is drastically reduced by the proposed method (Case3).

Chapter 8

Acoustic Wave Equation Based Modeling and Collocated Side Vibration Cancellation for Pneumatic Cylinder

Abstract

A pneumatic actuator has several advantages such as low heat generation, a high power-to-weight ratio, and low costs; however, it also has disadvantages such as time delays, nonlinearities, and position-dependent multiple pressure resonances. In this study, we propose a wave equation-based model, which can fit the position-dependent pressure resonances based on delay elements, taking into account the damping. Using this model, a wave cancellation filter is proposed for canceling all the resonances and anti-resonances. The effectiveness of both the model and the filter were verified through experiments.

8.1 Introduction

A high-precision stage is an important type of apparatus used in semiconductor and flat panel display manufacturing processes [1, 85]. Faster and more precise positioning using a large stage is required to achieve high integration and reduce the cost of manufacturing electronic devices [2, 3]. A dual stage structure with a short stroke fine stage and long stroke coarse stage is used widely to satisfy these two requirements [1]. Linear motors or ball screws are normally used for the coarse stages, but the electric motors become larger and heavier due to the high acceleration and larger stage demands, thereby increasing the generation of heat [146]. Variations in temperature have severe effects on the measurement system and lens apparatus [97, 147], and thus precise temperature control [147] is problematic.

The aim of the present study is to replace the linear motor/ball screw implemented in the coarse

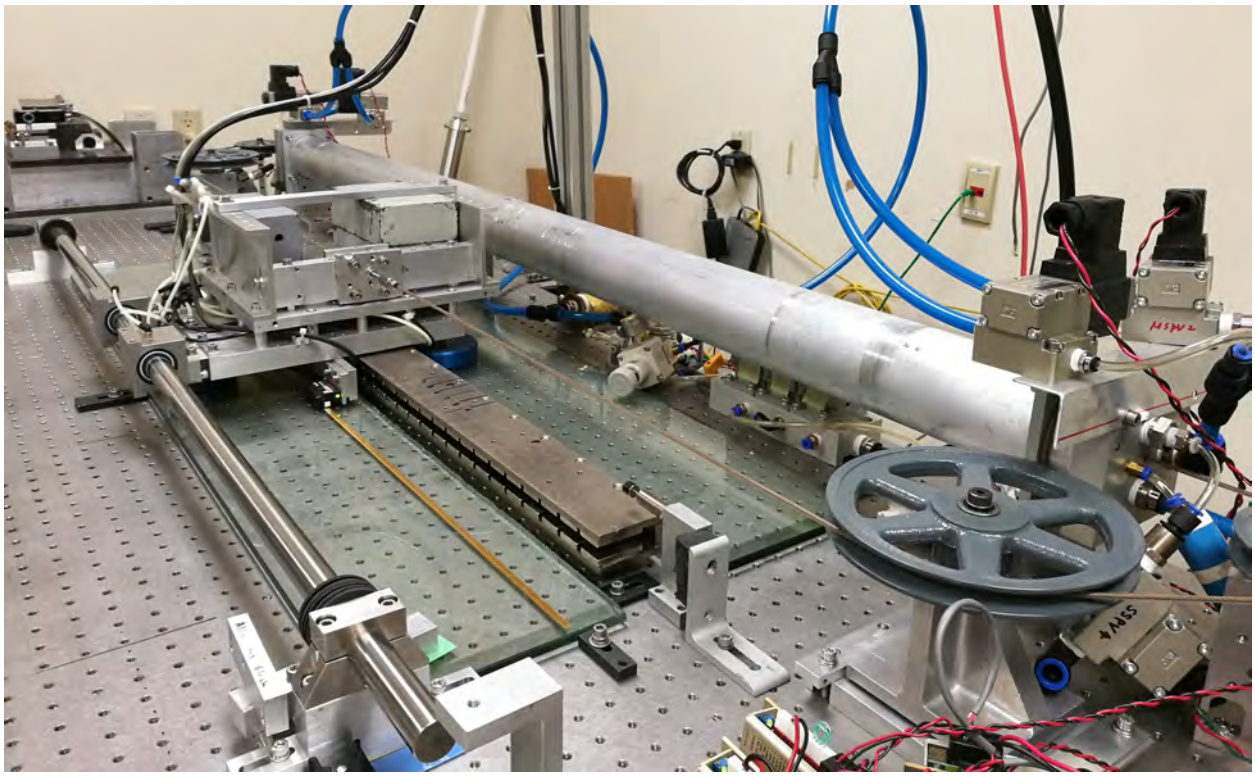

Figure 8.1 Pneumatically actuated stage.

stage with a pneumatic actuator. A pneumatic actuator has the following advantages compared with a linear motor: 1) low heat generation [97]; 2) high power-to-weight ratio [98]; and 3) low cost [98]; but its disadvantages also include: 1) a time delay [99]; 2) nonlinear dynamics [100,101,148] due to air dynamics and servo valves; and 3) position-dependent resonances. To address the time delay problem, we previously proposed a modified Smith predictor and applied it to a pneumatically actuated scan stage to achieve high-bandwidth pressure feedback [89]. However, both the delay and resonances limit the pressure feedback bandwidth. The resonances are functions of the chamber length, valve position, and pressure sensor position. Moreover, the resonances have multiple modes with a high peak in the frequency domain.

In this study, we propose a modeling method for a pneumatic cylinder based on acoustic wave equation. This model fits the frequency response with multiple resonances based on delay elements, taking into account the damping effect of the system. We also propose a wave cancellation filter to cancel multiple modes and shape it as a single integrator. This filter comprises delay elements and a first-order filter.

Wave equation based modeling for valve-cylinder connecting tube with open-end condition is studied in [148]. However, the damping term is ignored when the boundary condition is given. In contrast, we make a model for a cylinder not for a tube with fixed-end condition and damping is considered not only for modeling step but also plant shaping step for resonance cancellation. Vibration suppression control

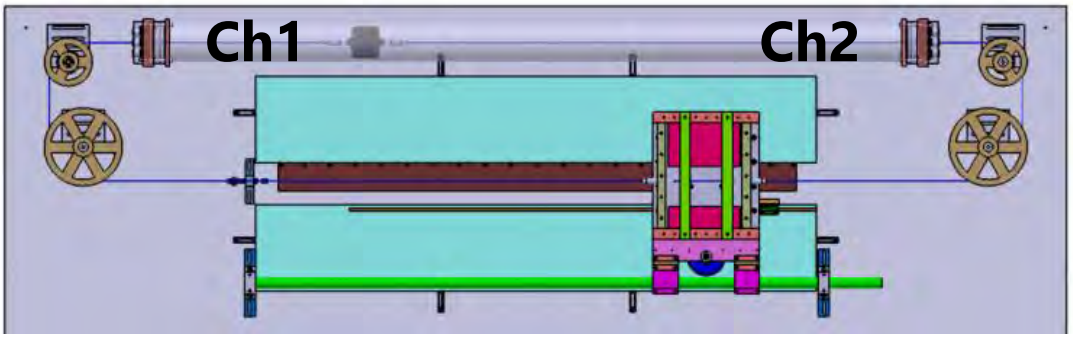

(a) Beginning of scan motion.

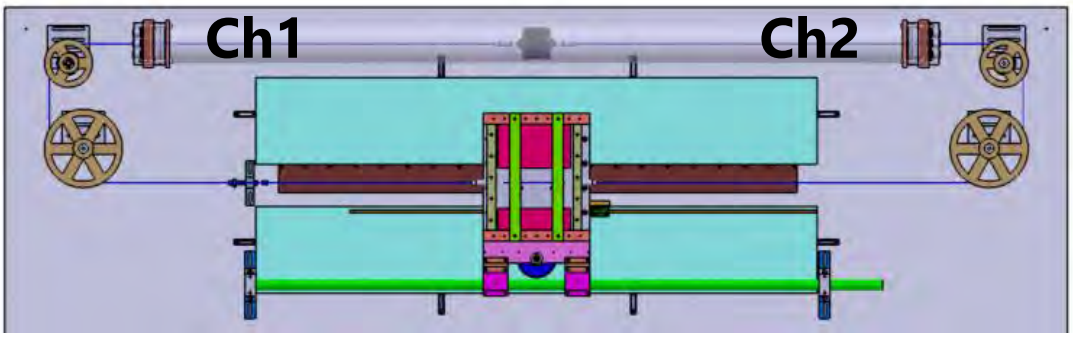

(b) Constant velocity region.

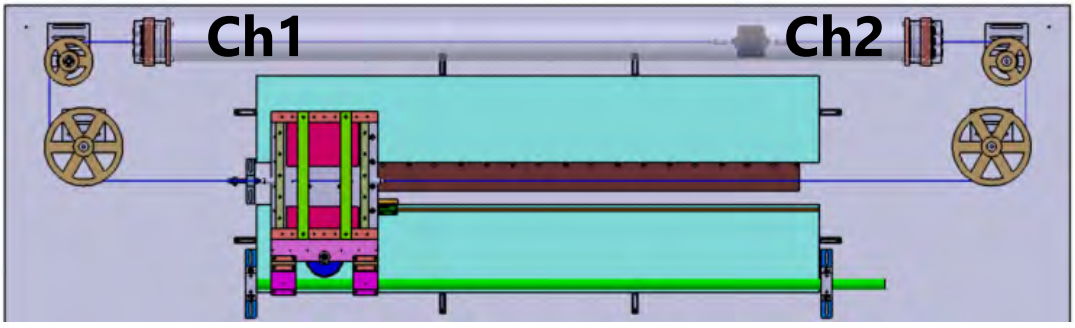

(c) End of scan motion.

Figure 8.2 Relationship between the stage position and chamber length during scan motion. Ch1 and Ch2 denote the chamber 1 and 2, respectively.

for pneumatic vibration isolator is studied in [99]. This method suppresses only the first resonance mode by relative velocity feedback

Wave equation-based resonance canceling has been proposed for elastic beams [149–152]. Unlike the wave compensator proposed in previous studies [151, 152], the proposed wave cancellation filter is implemented between the plant and feedback controller in the same manner as notch filters. Moreover, methods proposed in [151,152] do not consider the damping of the system. The damping considerations for a model and a controller are important for a stability analysis in frequency domain. The proposed method can model the damping of the resonances and anti-resonances separately.

Fig. 8.1 shows a pneumatically actuated stage. In a scanning motion, which is required in fabrication processes for electronic devices, the chamber length is varied as shown in Fig. 8.2. To verify the position

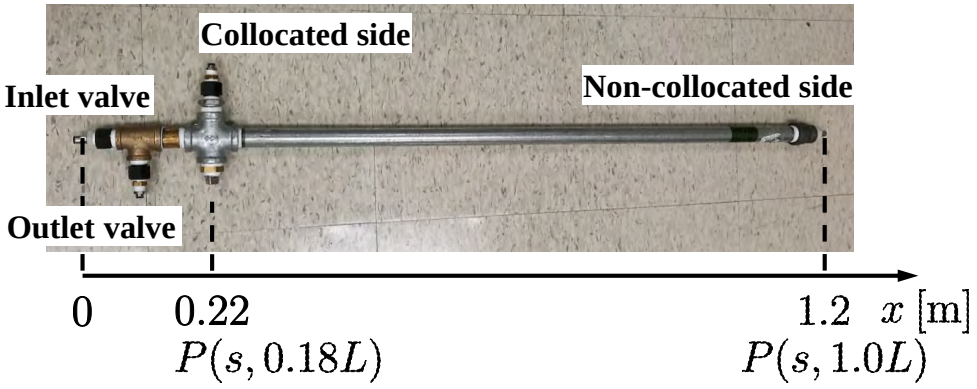

(a) $L = 1.2$ m.

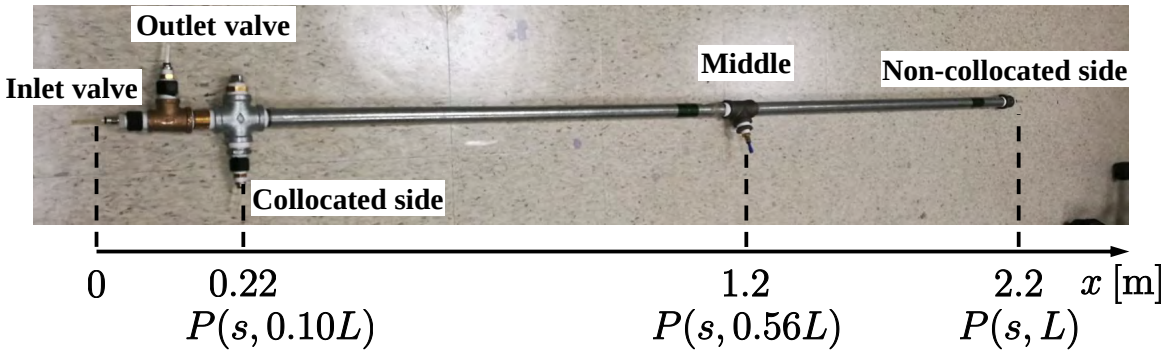

(b) $L = 2.2$ m.

Figure 8.3 The two lengths chambers.

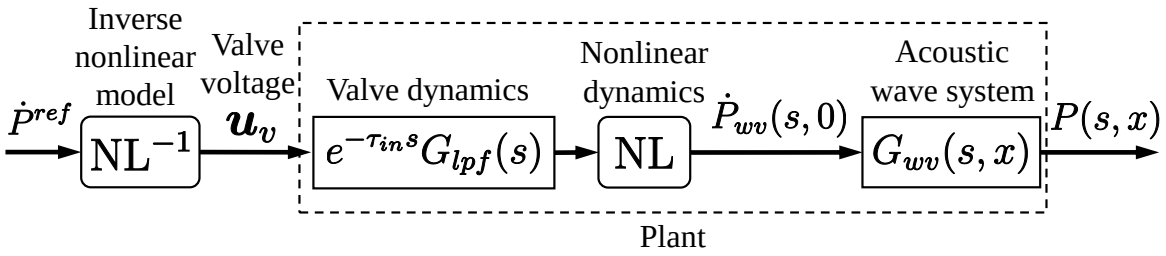

Figure 8.4 Plant model for a single chamber.

dependency, two simple closed chambers were prepared, as shown in Fig. 8.3. The two chambers had lengths of 1.2 m and 2.2 m, respectively. The proposed model and control method were validated through experiments.

8.2 Experimental setup

The experimental setups are shown in Fig. 8.3. This chamber had inlet and outlet poppet vales on one end. The inlet valve was connected to a high-pressure source (400kPa) and the outlet valve was connected to the ambient air. Pressure sensors were implemented on the valve side, the other side of the chamber, and the middle of the chamber. Two chambers with different lengths were prepared to investigate the chamber length and sensor position dependency.

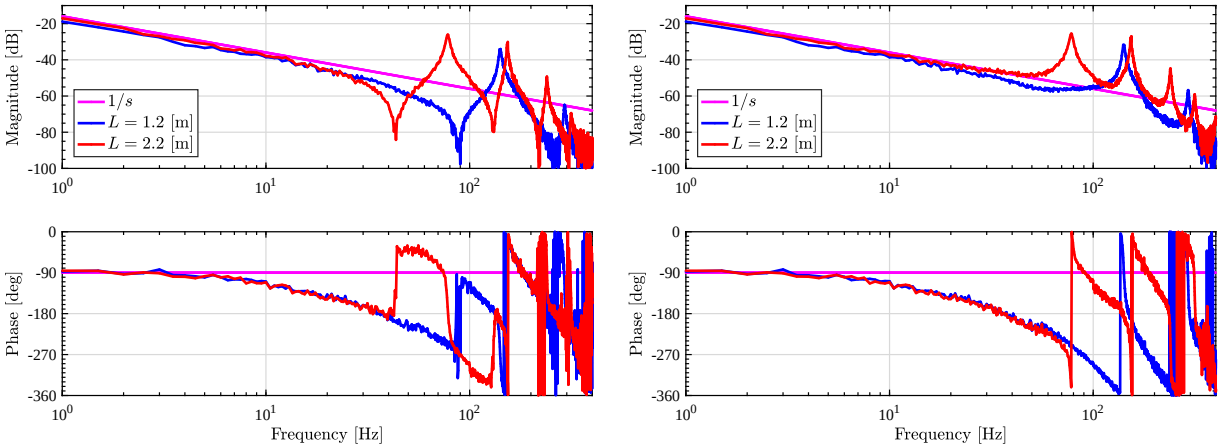

(a) $x = 0.22\,\mathrm{m}$ (collocated side). (b) $x = 1.0L$ (non-collocated side).

Figure 8.5 Chamber length dependency of $\dfrac{P(s,x)}{\dot{P}^{ref}(s)}$.

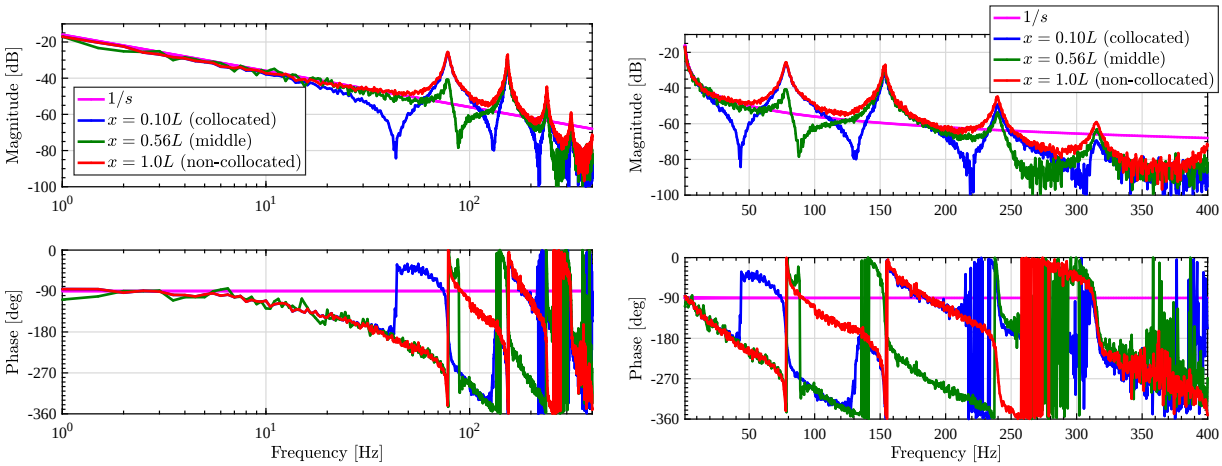

(a) Logarithmic frequency plot. (b) Linear frequency plot.

Figure 8.6 Sensor position dependency of $\dfrac{P(s,x)}{\dot{P}^{ref}(s)}$, $(L = 2.2\,\mathrm{m})$.

Table 8.1 List of symbols

Symbols	Definition	Value	Unit
ρ	density		$\mathrm{kg/m^3}$
p	pressure		Pa
v	flow speed		m/s
γ	heat capacity ratio	1.402	-
c_0	speed of sound		m/s
R	ideal gas constant	287.1	$\mathrm{J/(kg \cdot K)}$
T	temperature (Kelvin)		K
x	pressure sensor position		m

8.3 Modeling

Plant model for single chamber is shown in Fig. 8.4. NL denotes nonlinear dynamics of the valve and air flow equation [97,153,154]. To compensate the nonlinearity by nonlinear inversion, the relationship between the inlet and outlet valve voltages ($\boldsymbol{u}_v$), mass flow rate, and chamber pressure is modeled by a polynomial [100]. Dead-zone compensation is also used for the valve nonlinearity between the valve voltages ($\boldsymbol{u}_v$) and size of orifice areas. The frequency responses of the systems in Fig. 8.3 are shown in Figs. 8.5 and 8.6 which both illustrate the chamber length dependency and sensor position dependency, respectively.

8.3.1 Basic equations [155]

The variables are listed in Tab. 8.1. A one-dimensional wave, constant cross-sectional area, isentropic change, and non-static flow are assumed. The basic equations are as follows.

- Equation of continuity

$$\frac{\partial \rho}{\partial t} + \rho \frac{\partial v}{\partial x} + v \frac{\partial \rho}{\partial x} = 0 \tag{8.1}$$

- Euler's equation of motion

$$\frac{\partial v}{\partial t} + v \frac{\partial v}{\partial x} = -\frac{1}{\rho} \frac{\partial p}{\partial x} \tag{8.2}$$

- Equation of isentropic change

$$\frac{p}{\rho^{\gamma}} = \text{const} \tag{8.3}$$

- Ideal gas low

$$p = \rho R T \tag{8.4}$$

8.3.2 Acoustic wave equation [155]

A small perturbation is assumed as follows.

$$p = p_0 + p', \;\; \rho = \rho_0 + \rho', \;\; v = 0 + v' \tag{8.5}$$

By substituting (8.5) into (8.1) and (8.2), and ignoring the second order small terms, the following equations are obtained.

$$\frac{\partial \rho'}{\partial t} + \rho_0 \frac{\partial v'}{\partial x} = 0 \tag{8.6}$$

$$\frac{\partial v'}{\partial t} + \frac{1}{\rho_0} \frac{\partial p'}{\partial x} = 0 \tag{8.7}$$

The Taylor expansion of p is

$$p = p_0 + A\left(\frac{\rho - \rho_0}{\rho}\right) + \frac{1}{2}B\left(\frac{\rho - \rho_0}{\rho}\right)^2 + \cdots, \tag{8.8}$$

where

$$A \equiv \rho_0 \left(\frac{\partial p}{\partial \rho}\right)_{\rho=\rho_0} = \rho_0 c_0^2, \;\; B \equiv \rho^2 \left(\frac{\partial^2 p}{\partial \rho^2}\right)_{\rho=\rho_0}. \tag{8.9}$$

(8.8) is approximated as

$$p' \simeq p - p_0 = A\left(\frac{\rho - \rho_0}{\rho}\right) = c_0^2 \rho'. \tag{8.10}$$

From (8.7) and (8.10), we obtain

$$\frac{\partial v'}{\partial t} + \frac{c_0^2}{\rho_0} \frac{\partial \rho'}{\partial x} = 0. \tag{8.11}$$

From (8.6) and (8.11), the following wave equations are obtained.

$$\frac{\partial^2 v'}{\partial t^2} - c_0^2 \frac{\partial^2 v'}{\partial x^2} = 0 \tag{8.12}$$

$$\frac{\partial^2 \rho'}{\partial t^2} - c_0^2 \frac{\partial^2 \rho'}{\partial x^2} = 0 \tag{8.13}$$

$$\frac{\partial^2 p'}{\partial t^2} - c_0^2 \frac{\partial^2 p'}{\partial x^2} = 0 \tag{8.14}$$

8.3.3 Transfer function

From the following, $'$ is omitted for p', v', ρ' in the small perturbation condition. The boundary conditions are given by (8.15) by considering a fixed end condition [150] and a dimensional analysis,

$$c_o^2 \frac{\partial p(t,x)}{\partial x}\bigg|_{x=0} = -u(t), \;\; \frac{\partial p(t,x)}{\partial x}\bigg|_{x=L} = 0, \tag{8.15}$$

where the control input $u(t)$ is $L\frac{\partial^2 p_{wv}(t,0)}{\partial t^2}$. $p_{wv}(t,0)$ denotes the pressure wave created by the inlet and outlet valves located at $x = 0$. The Laplace transform of (8.14) is

$$a^2 s^2 P(s,x) = \frac{\partial^2 P(s,x)}{\partial x^2}, \tag{8.16}$$

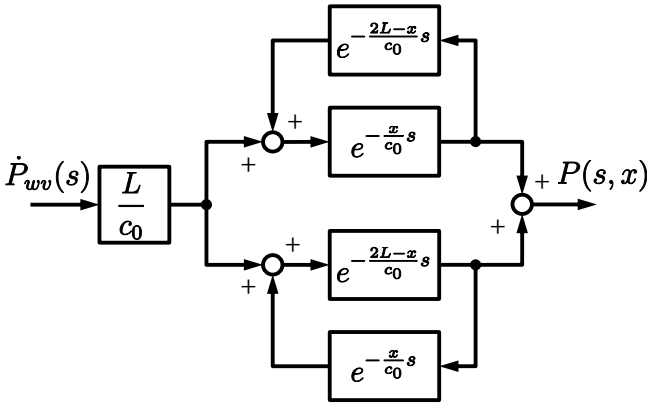

Figure 8.7 Block diagram interpretation of (8.22).

where a denotes $\frac{1}{c_0}$. From (8.15) and (8.16), we obtain

$$\frac{\partial P(s,0)}{\partial x} = -a^2 U(s), \quad \frac{\partial P(s,L)}{\partial x} = 0. \tag{8.17}$$

The general solution is given by

$$P(s,x) = C_1 \cosh(axs) + C_2 \sinh(axs). \tag{8.18}$$

By partial differentiation of (8.18) with respect to x, the following equation is obtained.

$$\frac{\partial P(s,x)}{\partial x} = C_1 sa \sinh(axs) + C_2 sa \cosh(axs) \tag{8.19}$$

According to (8.19) and (8.17), integral constants are obtained by

$$C_1 = \frac{a}{s}\frac{\cosh(aLs)}{\sinh(aLs)}U(s), \quad C_2 = -\frac{a}{s}U(s). \tag{8.20}$$

The transfer function from $U(s)$ to $P(s,x)$ is

$$\begin{aligned}\frac{P(s,x)}{U(s)} &= \frac{a}{s}\frac{\cosh(aLs)}{\sinh(aLs)}\cosh(axs) - \frac{a}{s}\sinh(axs) \\ &= \frac{a}{s}\frac{\cosh(aLs)\cosh(axs) - \sinh(aLs)\sinh(axs)}{\sinh(aLs)} \\ &= \frac{a}{s}\frac{\cosh[as(L-x)]}{\sinh(aLs)}.\end{aligned} \tag{8.21}$$

From the above, the acoustic wave system is derived.

$$\frac{P(s,x)}{\dot{P}_{wv}(s)} = \frac{L}{c_0}\frac{e^{-\frac{x}{c_0}s} + e^{-\frac{2L-x}{c_0}s}}{1 - e^{-\frac{2L}{c_0}s}}. \tag{8.22}$$

Block diagram interpretation of (8.22) is shown in Fig. 8.7. According to (8.22), the transfer functions from the valve input to the valve side end ($x = 0$) pressure and the other side end ($x = L$) pressure

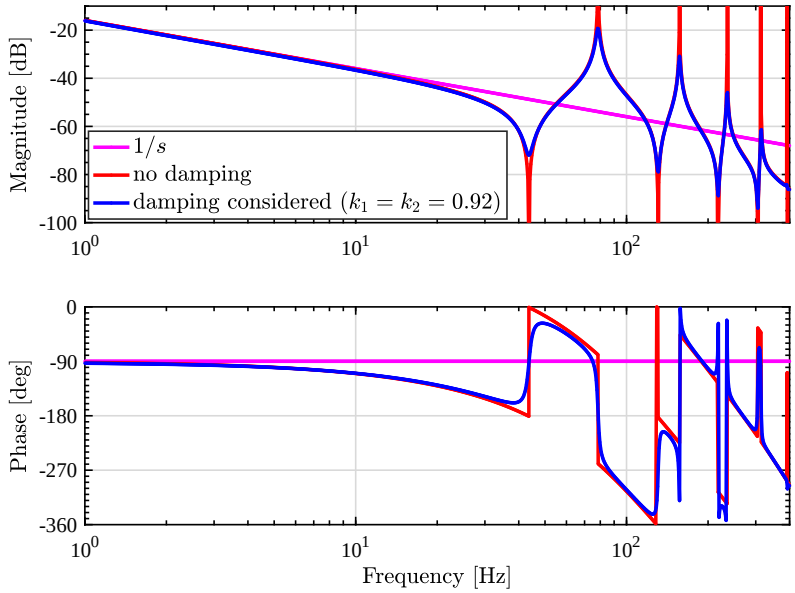

Figure 8.8 Effect of damping ($x = 0.10L$).

Table 8.2 Parameters for fitting and wave cancellation filter design.

Symbols	Definition	Value	Unit
c_0	speed of sound	343.4	m/s
L	chamber length	2.2	m
k_1, k_2	damping coefficient	0.92, 0.92	-
τ_{in}	input delay	1.8	ms
ζ_1, ζ_2	damping coefficient of the valve dynamics	0.70, 0.70	-
ω_1, ω_2	cutoff frequency of the valve dynamics	90, 170	Hz

are given as

$$\frac{P(s,0)}{\dot{P}_{wv}(s)} = \frac{L}{c_0}\frac{1+e^{-\frac{2Ls}{c_0}}}{1-e^{-\frac{2Ls}{c_0}}}, \tag{8.23}$$

$$\frac{P(s,L)}{\dot{P}_{wv}(s)} = \frac{L}{c_0}\frac{2e^{-\frac{Ls}{c_0}}}{1-e^{-\frac{2Ls}{c_0}}}. \tag{8.24}$$

8.3.4 Modified acoustic wave equation considering damping

The model defined in (8.22) does not take into account the damping, so the gain becomes 0 at anti-resonances and $+\infty$ at resonances. However, the measured frequency responses shown in Figs. 8.5 and 8.6 indicate that the system experiences damping. Thus, damping coefficients $0 < k_1 < 1$, $0 < k_2 < 1$

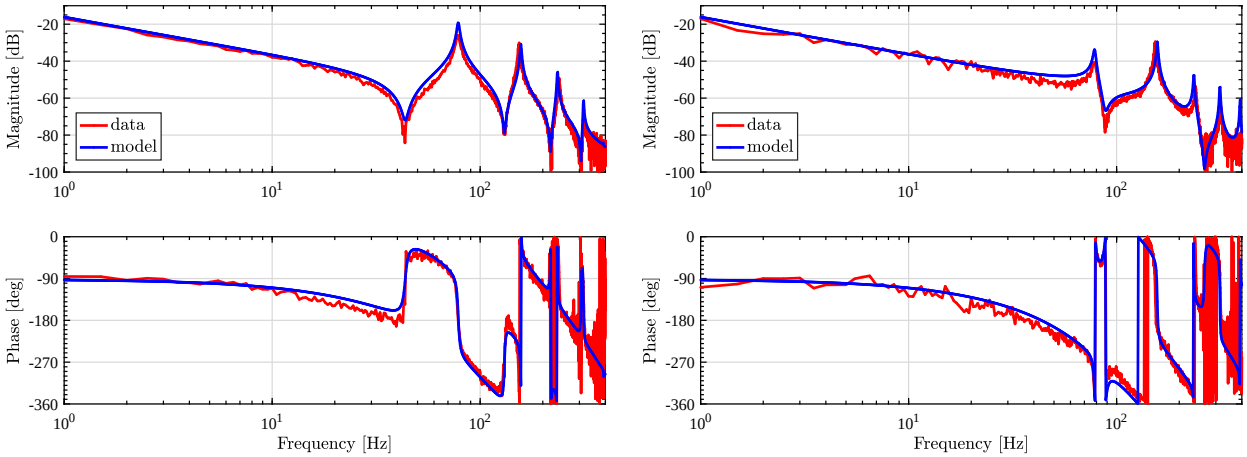

(a) $x = 0.10L$. (b) $x = 0.56L$.

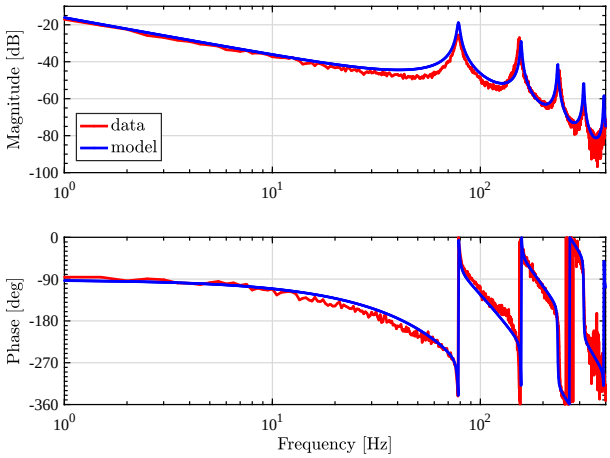

(c) $x = 1.0L$.

Figure 8.9 Fitted by (8.30) and Tab. 8.2.

are introduced to model this phenomenon.

$$G_{wv}(s,x) = \frac{P(s,x)}{\dot{P}_{wv}(s)} = \frac{2L}{c_0}\frac{k_1}{1+k_2}\frac{s+\frac{1-k_1}{k_1}\frac{c_0}{2L}}{s}\frac{e^{-\frac{xs}{c_0}}(1+k_2e^{-\frac{2(L-x)s}{c_0}})}{1-k_1e^{-\frac{2Ls}{c_0}}} \tag{8.25}$$

The coefficients are determined to be a single integrator in a low frequency range, considering that the measured frequency response shown in Figs. 8.5 and 8.6 well matches a single integrator blow 3 Hz. Note that

$$\lim_{s\to 0} sG_{wv}(s,x) = 1. \tag{8.26}$$

The effect of damping is shown in Fig. 8.8. From (8.25), the valve side end ($x = 0$) and the other side end ($x = L$) transfer functions are modeled by

$$G_{wv}(s,0) = \frac{P(s,0)}{\dot{P}_{wv}(s)} = \frac{2L}{c_0}\frac{k_1}{1+k_2}\frac{s+\frac{1-k_1}{k_1}\frac{c_0}{2L}}{s}\frac{1+k_2 e^{-\frac{2Ls}{c_0}}}{1-k_1 e^{-\frac{2Ls}{c_0}}} \tag{8.27}$$

$$G_{wv}(s,L) = \frac{P(s,L)}{\dot{P}_{wv}(s)} = \frac{2L}{c_0}\frac{k_1}{1+k_2}\frac{s+\frac{1-k_1}{k_1}\frac{c_0}{2L}}{s}\frac{e^{-\frac{Ls}{c_0}}(1+k_2)}{1-k_1 e^{-\frac{2Ls}{c_0}}}. \tag{8.28}$$

8.3.5 Valve model

Poppet valves are used in this setup. The valve dynamics are modeled by a fourth order low pass filter and input delay

$$G_{lpf}(s)e^{-\tau_{in}s} = \frac{\omega_1^2}{s^2+2\zeta_1\omega_1 s+\omega_1^2}\frac{\omega_2^2}{s^2+2\zeta_2\omega_2 s+\omega_2^2}e^{-\tau_{in}s} \tag{8.29}$$

Considering the valve dynamics, the transfer function from $\dot{P}^{ref}(s)$ to pressure $P(s,x)$ in Fig. 8.4 is obtained assuming perfect nonlinearity compensation.

$$\frac{P(s,x)}{\dot{P}^{ref}(s)} = G_{wv}(s,x)G_{lpf}(s)e^{-\tau_{in}s} \tag{8.30}$$

The fitting results by (8.30) and parameters in Tab. 8.2 are shown in Fig. 8.9. The position-dependent multiple resonances are modeled well by the single equation.

8.4 Proposed wave cancellation filter

8.4.1 Case ignoring damping

Figs. 8.5, 8.6, and (8.23) indicate that the plant model should have an integrator in a low frequency range. By the first-order Taylor expansion of (8.23), we obtain (8.31).

$$\begin{aligned}\frac{P(s,0)}{\dot{P}^{ref}(s)} &= \frac{L}{c_0}\frac{1+e^{-\frac{2Ls}{c_0}}}{1-e^{-\frac{2Ls}{c_0}}} \\ &\simeq \frac{1}{s}-\frac{L}{c_0} \\ &\simeq \frac{1}{s}\end{aligned} \tag{8.31}$$

To cancel the all resonances and anti-resonances, the integrator and the rest are separated as follows

$$\frac{P(s,0)}{\dot{P}^{ref}(s)} = \frac{1}{s}\frac{Ls(1+e^{-\frac{2Ls}{c_0}})}{c_0(1-e^{-\frac{2Ls}{c_0}})}. \tag{8.32}$$

The wave cancellation filter C_{wcf} for $(x = 0)$ is obtained by inversion of the resonant modes as follows

$$C_{wcf}(s,0) = \frac{c_0(1 - e^{-\frac{2Ls}{c_0}})}{Ls(1 + e^{-\frac{2Ls}{c_0}})}. \tag{8.33}$$

8.4.2 Case considering damping

The generalized wave cancellation filter is obtained using the same procedure employed in subsection 8.4.1 for (8.25) as follows.

$$C_{wcf}(s,x) = \frac{c_0}{2L}\frac{1+k_2}{k_1}\frac{1}{s + \frac{1-k_1}{k_1}\frac{c_0}{2L}}\frac{1 - k_1 e^{-\frac{2Ls}{c_0}}}{1 + k_2 e^{-\frac{2(L-x)s}{c_0}}} \tag{8.34}$$

The shaping result obtained by (8.34) is shown in Fig. 8.14. Fig. 8.14(a) indicates that the proposed wave cancellation filter has gain peaks at the anti-resonances and gain attenuation at the resonances. Fig. 8.14(b) shows shaping results by simulation using model expressed in (8.25), which indicates that the anti-resonances and resonances are all canceled. Fig. 8.14(c) shows the simulation results by the measured frequency response data shown in Fig. 8.9(a). The resonances and anti-resonances are well canceled due to a good model matching. Fig. 8.14(d) shows the experimental results, which indicate that -19 dB, -23 dB, and -16 dB gain attenuations are achieved for the first, second, and third modes, respectively. This performance is not as good as the simulation results shown in Figs. 8.14(b) and 8.14(c). This difference may be due to the non-canceled nonlinearity of the valves and air dynamics shown in Fig. 8.4.

8.4.3 Parameter dependency observations

Equations (8.25) and (8.34) have four parameters assuming the speed of sound is constant. Parameter dependencies are shown in Figs. 8.10–8.13. Fig. 8.10 indicates the wave cancellation filter automatically changes the resonance and anti-resonance frequencies according to the chamber length L. Fig. 8.11 shows that the frequencies for anti-resonance canceling of the wave cancellation filter $C_{wcf}(s,x)$ are automatically changed according to the pressure sensor position (x). Fig. 8.12(b) and 8.13(b) show that k_1 and k_2 change the strength of the resonance and anti-resonance canceling, respectively.

8.5 Experiments

A block diagram is shown in Fig. 8.15. A proportional-integral (PI) and phase-lead controller are used for feedback. The pressure reference is the first-order delayed step. α denotes the pole of the

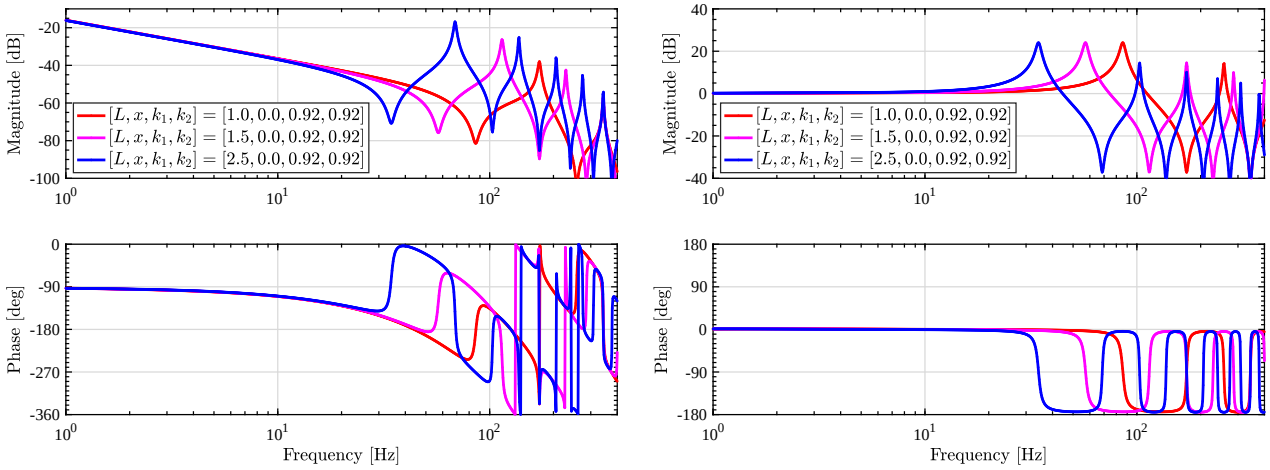

(a) $G_{wv}(s, x)G_{lpf}(s)e^{-\tau_{in}s}$. (b) $C_{wcf}(s, x)$.

Figure 8.10 Chamber length (L) dependency.

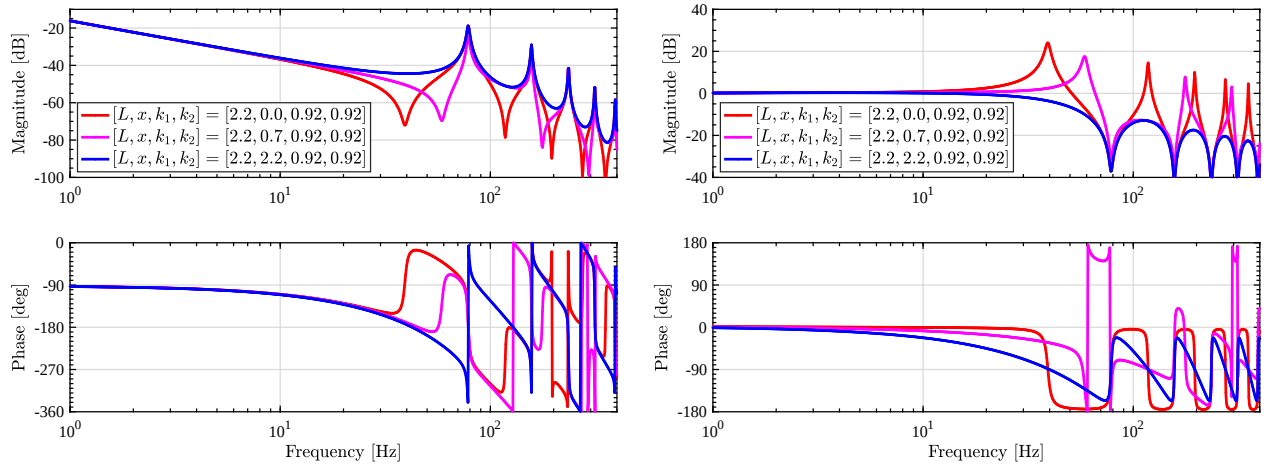

(a) $G_{wv}(s, x)G_{lpf}(s)e^{-\tau_{in}s}$. (b) $C_{wcf}(s, x)$.

Figure 8.11 Pressure sensor position (x) dependency.

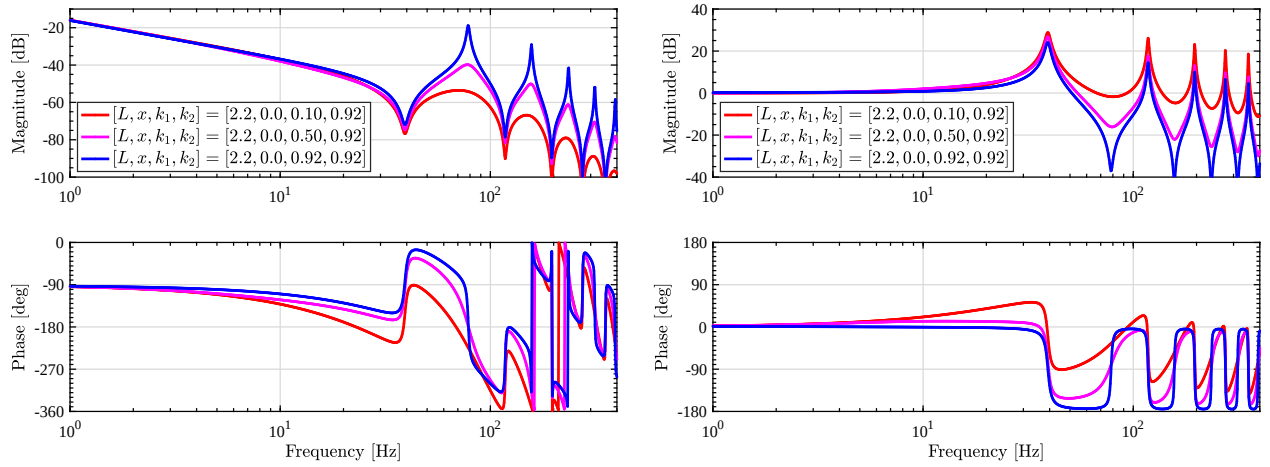

(a) $G_{wv}(s, x)G_{lpf}(s)e^{-\tau_{in}s}$. (b) $C_{wcf}(s, x)$.

Figure 8.12 k_1 dependency.

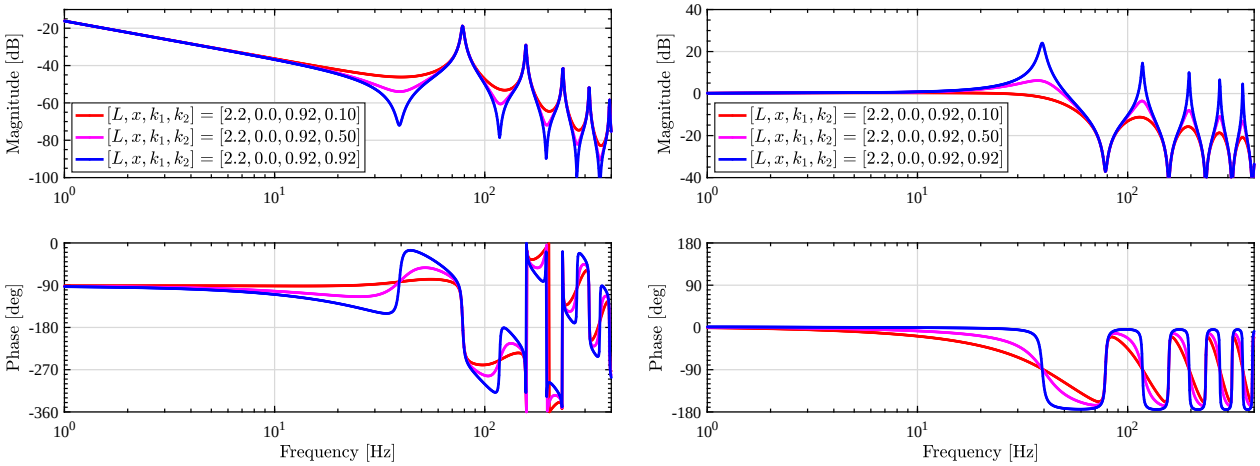

(a) $G_{wv}(s, x)G_{lpf}(s)e^{-\tau_{in}s}$. (b) $C_{wcf}(s, x)$.

Figure 8.13 k_2 dependency.

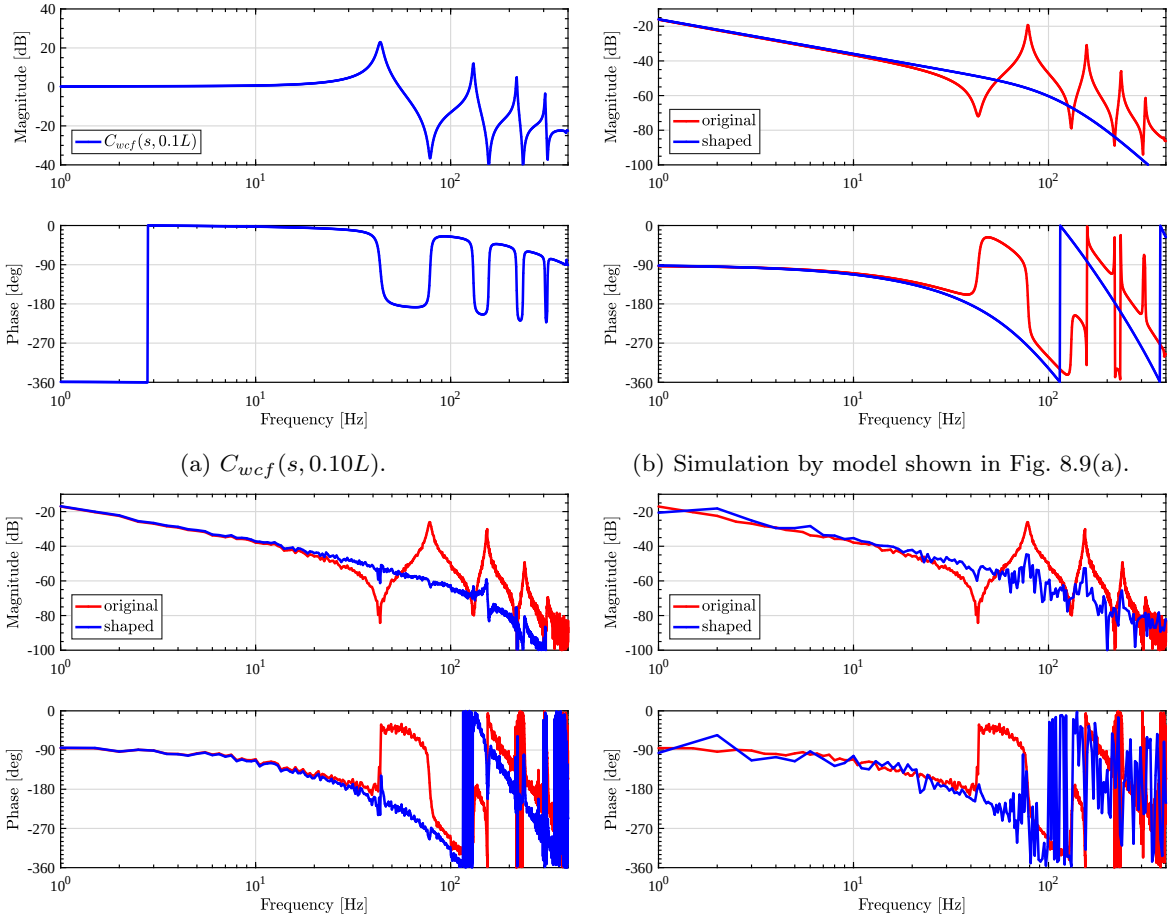

(a) $C_{wcf}(s, 0.10L)$. (b) Simulation by model shown in Fig. 8.9(a).

(c) Simulation by frequency response data shown in Fig. 8.9(a). (d) Experiment.

Figure 8.14 Shaped results obtained by (8.34).

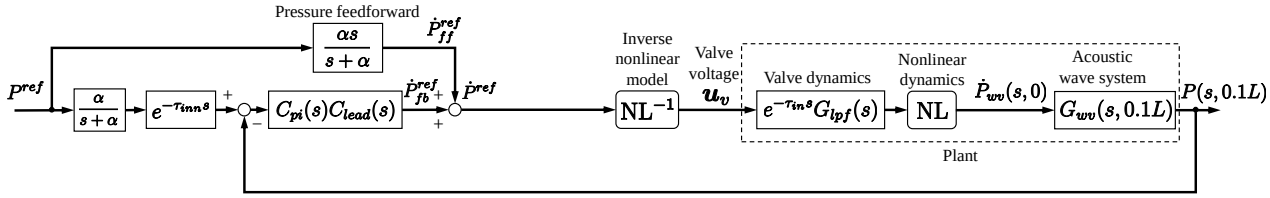

(a) Without wave cancellation filter.

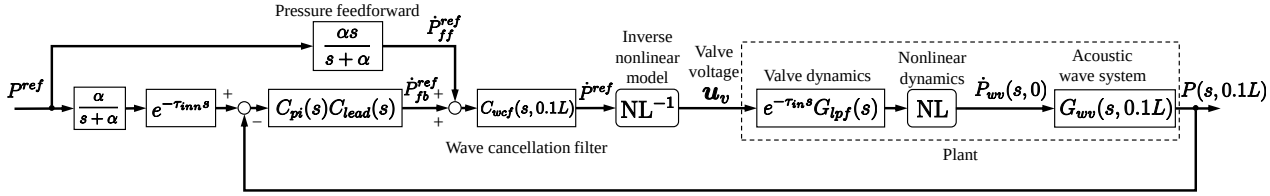

(b) With wave cancellation filter.

Figure 8.15 Block diagram with pressure feedforward.

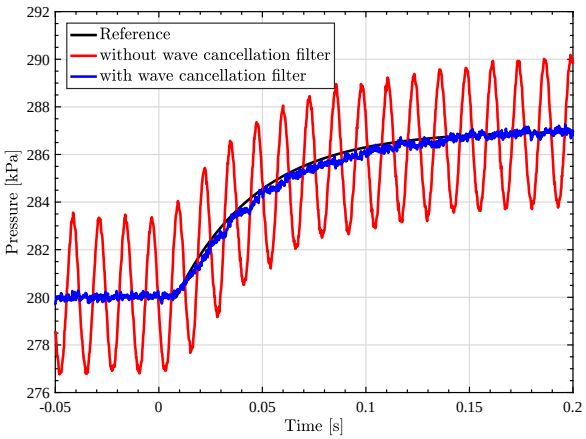

(a) Pressure responses.

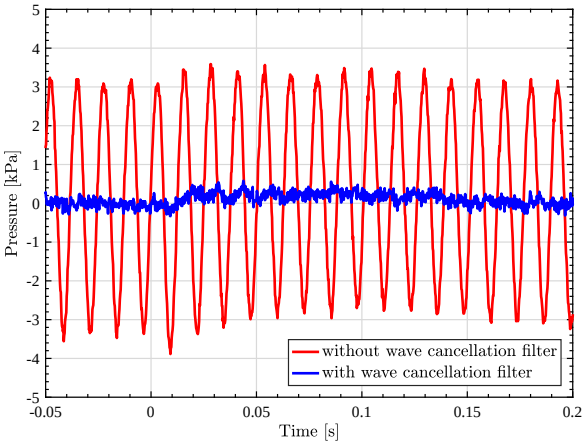

(b) Pressure tracking error.

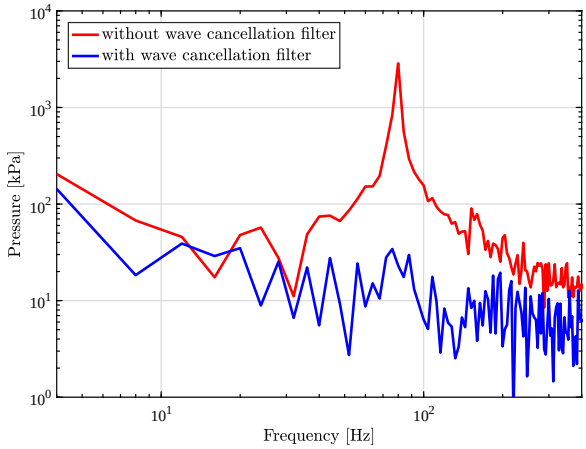

(c) Frequency analysis for (b).

Figure 8.16 Step response experiments.

low-pass filter used for trajectory generation. $\frac{1}{s}$ is used as a nominal model of the pressure feedforward controller.

The step response is shown in Fig. 8.16. The pressure vibration is canceled well with the wave cancellation filter. Fig. 8.16(c) shows the frequency analysis of Fig. 8.16(b), where up to the fourth mode is observed without the wave cancellation filter. This demonstrates that the proposed wave cancellation filter attenuates multiple modes with a single filter. The pressure closed loop performance is shown in Fig. 8.17. Without the wave cancellation filter C_{wcf}, a higher bandwidth is difficult to achieve due to the high-gain peak.

Fig. 8.18 shows the effect of the pressure feedforward. Wave cancellation filter is used in both cases. The shaping of the plant by wave cancellation filter means that the simple model $P_n(s) = \frac{1}{s}$ can be used for the nominal model as the feedforward controller.

8.6 Summary

High-bandwidth pressure control for a pneumatic cylinder is difficult because of position-dependent multiple resonances and anti-resonances. In this study, we modeled these phenomena based on a acoustic wave equation, taking into account the damping. It contains delay elements and it can fit multiple modes. According to the proposed model, we proposed a wave cancellation filter to cancel the multiple position-dependent modes. Theoretically, this filter can shape the position-dependent plant as a single integrator. The effectiveness of the proposed method was verified by experiments.

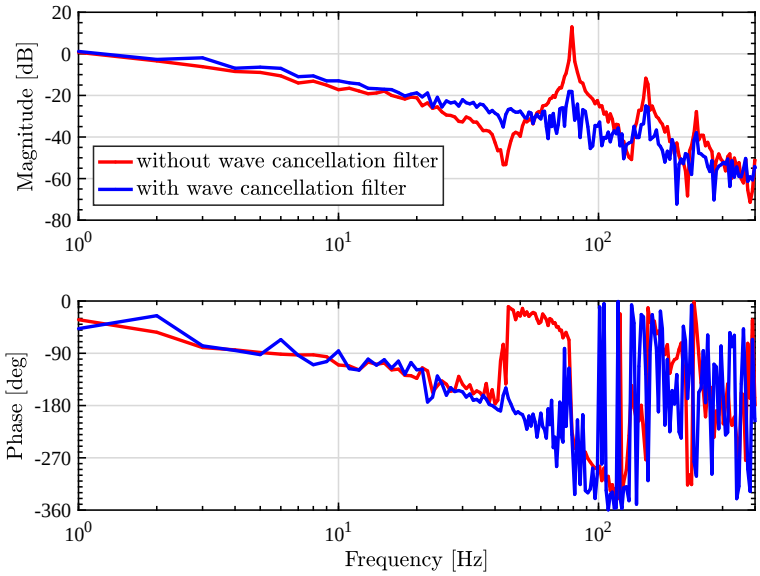

Figure 8.17 Pressure closed loop $\frac{P(s,0.1L)}{P^{ref}(s)}$.

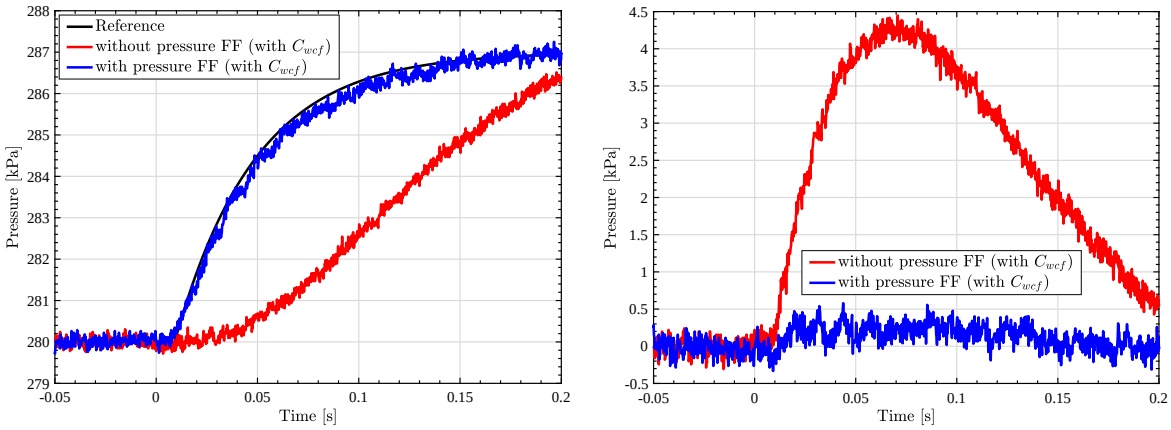

(a) Pressure responses. (b) Pressure tracking error.

Figure 8.18 Effect of pressure feedforward.

Chapter 9

Conclusion

In this dissertation, a framework of high-precision motion control method for nonminimum phase systems was presented. Nonminimum phase systems are notoriously difficult to control from both sides of feedback and feedforward. Nonminimum phase systems are classified as 1) systems with unstable zeros and 2) systems with time delay.

In Part I, feedforward control methods for systems with unstable zeros are investigated. Feedforward controller for reference tracking is commonly designed by the feedforward plant-injection (FFPI) or feedforward closed-loop-injection (FFCLI) architectures. In both cases, the inversion system with unstable zeros has unstable poles and it is infeasible to implement. The core idea of the Part I is to compensate the unstable zeros separately, depending on the type of zeros. Zeros of discrete transfer functions are classified as i) intrinsic zeros proper to the plant dynamics and ii) discretization zeros due to signal sampling. The intrinsic zeros are compensated through the state trajectory generation by time axis reversal. Discretization zeros are unstable when the relative order of the continuous time plant is greater than two even without continuous-time unstable zeros. The discretization zeros are stably inverted by the multirate feedforward control.

The tracking control performance is summarized in Tabs. 9.1–9.3 and Figs. 9.1 and 9.2. Strategies for compensating unstable intrinsic zeros and discretization zeros with trajectory preview are as follows:

- Infinite (sufficiently long) time preactuation is possible
  (Truncated) preactuation perfect tracking control (PPTC) proposed in Chapter 2 is recommended. “Sufficiently long time” means enough long time compared to the time constant of unstable zeros. This method generates smooth and natural control input compared to FPPTC method. The truncation effect is shown in Figs. 3.6 and 3.7. The truncation effect decays exponentially by longer preactuation. These figures show the need of zero-order-hold consideration and compensation by the multirate feedforward. According to the experimental results shown

in Section 2.6, the maximum error is reduced by 93 % and 43 % compared to ZPETC method and CPMI method, respectively.

- Finite time preactuation is possible

  Finite preactuation perfect tracking control (FPPTC) method proposed in Chapter 3 is recommended. FPPTC method *regenerates* a state trajectory by redundant order polynomial to match the state variable after the preactuation. Although this method abandons perfect tracking during preactuation, it guarantees perfect tracking after preactuation regardless the preactuation time (see Fig. 9.2). According to the experimental results, the maximum tracking error is reduced by 66 % and 34 % compared to TSA method and truncated PPTC method, respectively (see Section 3.7).

- Minimum time preactuation is desired

  Minimum time preactuation perfect tracking control proposed in Chapter 4 is recommended. It generates an optimal state trajectory for a given reference and minimum feasible time while explicitly considering the actuator, i.e. peak force, and stroke, i.e. maximum undershoot, limitations of the system. A multirate feedforward scheme is subsequently presented to obtain a discretized control input that perfectly tracks the designed optimal continuous state trajectory. In comparison to conventional finite preactuation methods in simulation, the proposed approach reaches an order of magnitude lower tracking error bounds (see Section 4.3).

- Preactuation is not implementable

  Optimal state trajectory generation method without preactuation proposed in Chapter 5 is recommended. The original state trajectory, which requires the infinite preactuation, is generated by PPTC method. Then we *regenerate* the state trajectory between the start and end time of the reference motion trajectory. This method is an extension of the method proposed in Chapter 4. In the method of Chapter 4, perfect tracking after preactuation is guaranteed by regenerating the state trajectory during preactuation, whereas this method guarantees only after the end of the reference motion. The state trajectory during the reference motion is optimized with respect to the control input and plant output constraints. A multirate feedforward scheme, which is a stable inversion for unstable discretization zeros, is subsequently presented to obtain a discretized control input that perfectly tracks the designed optimal continuous state trajectory. Without preactuation, it achieves smaller undershoot than ZMETC and smaller tracking error than ZPETC (see Section 5.4).

Table 9.1 Comparison between infinite time preactuation methods in simulation. Model shown in Fig. 4.1 is used for the benchmark.

Methods	Max error	Preview time	Preactuation time	Perfect tracking period	Reference
CPMI	20.0 μm	Infinite	Infinite	No PTC achieved	[70] (see Section 2.3.2)
PPTC	0.00491* μm	Infinite	Infinite	Every nT_u for all time	Chapter 2

* Intersample tracking error

Table 9.2 Comparison between finite time preactuation methods in simulation. Model shown in Fig. 4.1 is used for the benchmark.

Methods	Max error	Preview time	Preactuation time	Perfect tracking period	Reference
Truncated CPMI	21.6 μm ($t_{pa} = -6\tau$)	Infinite	Finite	No PTC achieved	(see Section 3.4)
Truncated PPTC	2.22 μm ($t_{pa} = -6\tau$)	Infinite	Finite	No PTC achieved	(see Section 3.4)
TSA	5.49 μm ($t_{pa} = -6\tau$)	Finite	Finite	Every T_u for $t_{\text{traj}} \leq t$	[130] (see Section 3.3)
FPPTC	0.359 μm ($t_{pa} = -6\tau$)	Infinite	Finite	Every nT_u for $0 \leq t$	Chapter 3
Minimum time PPTC	48.9 μm ($t_{pa} = -2.4\tau$)	Infinite	Finite	Every nT_u for $0 \leq t$	Chapter 4

Table 9.3 Comparison between no preactuation methods in simulation. Model shown in Fig. 4.1 is used for the benchmark.

Methods	Max error	Preview time	Preactuation time	Perfect tracking period	Reference
NPZI	1024 μm	0	0	Every T_u for $t_{\text{traj}} \leq t$	[30] (Section 2.3.1)
ZMETC	1360 μm	0	0	No PTC achieved	[119] (Section 2.3.1)
ZPETC	767 μm or 658* μm	0 or Finite*	0 or Finite*	Every T_u for $t_{\text{traj}} \leq t$	[59] (Section 2.3.1)
Opt MRFF	212 μm	Infinite	0	Every nT_u for $t_{\text{traj}} \leq t$	Chapter 5

* with a few samples of preview and preactuation to achieve zero-phase-error

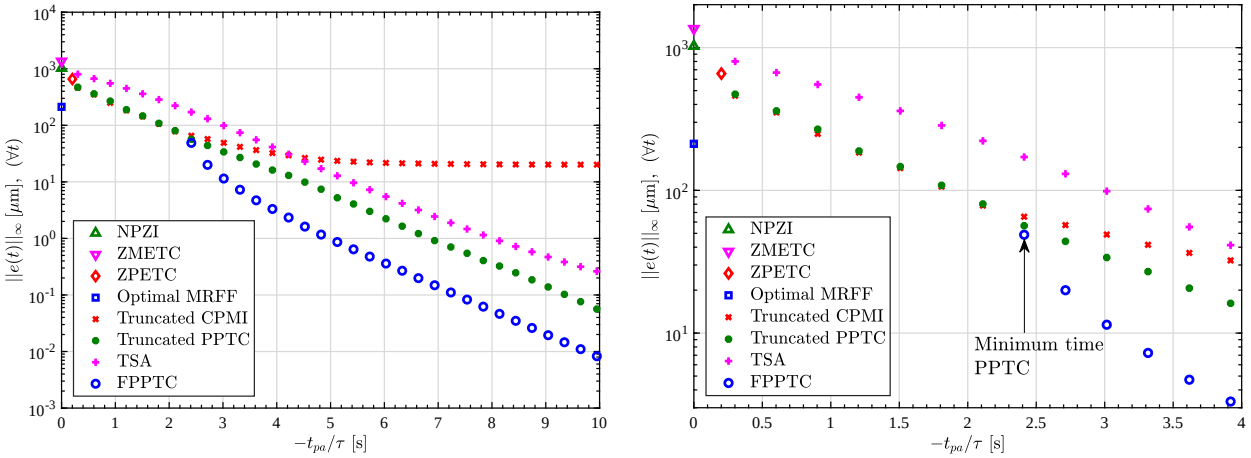

(a) $-t_{pa}/\tau$ v.s. $||e||_\infty$.

(b) Magnified figure of (a).

Figure 9.1 Relationship between the maximum tracking error $||e(t)||_\infty, (\forall t)$ and the preactuation time. 6th order plant shown in Fig. 4.1 is used for this comparison. Corresponding sections are i) NPZI, ZMETC, and ZPETC (Section 2.3.1), ii) Optimal MRFF (Chapter 5), iii) Truncated CPMI (Section 2.3.2), iv) Truncated PPTC (Chapter 2), v) TSA (Section 3.3), and vi) FPPTC (Chapter 3 and 4). As for FPPTC, the implementation shown in Section 4.2 is applied.

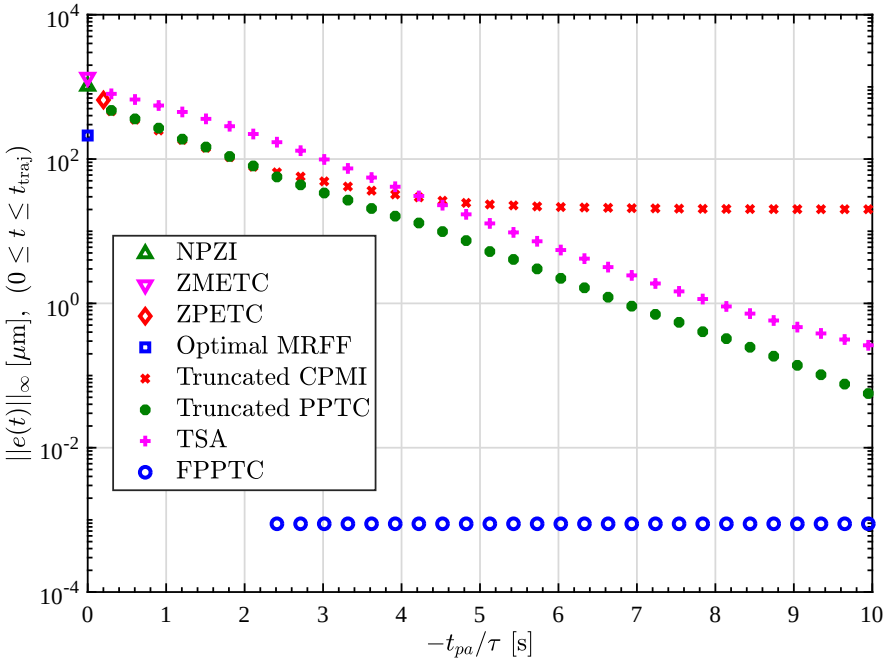

Figure 9.2 Relationship between the maximum tracking error and the preactuation time during the step motion. FPPTC achieves the perfect tracking for every T_r after preactuation. After the preactuation, the waveform of FPPTC is same regardless of the preactuation time (see Fig. 3.11(d)). The value of $||e(t)||_\infty, (0 \leq t \leq t_{\mathrm{traj}})$ in FPPTC is intersample tracking error.

For a high-order identified nominal model, multirate feedforward based on modal form proposed in Chapter 6 is recommended. Multirate feedforward control has been proposed to achieve perfect tracking for a plant with unstable discretization zeros. However, multirate feedforward control requires controllable canonical form and inversion of a controllability matrix, both of which are known as numerically ill-conditioned. Chapter 6 proposed a multirate feedforward control method based on modal form to address these problems. Moreover, the intersample behavior is improved compared to the conventional full order multirate feedforward. The effectiveness of the proposed method is validated through simulation results.

In Part II, tracking control methods for pneumatically actuated stage with input delay and internal delay were proposed. The aim of this part is to replace the linear motors implemented on coarse stages with the pneumatic actuator. The benefits are lightweight, low price, and low heat generation. However, it has following disadvantages: nonlinearity, delay, and position-dependent resonances. These disadvantages limit the control performance. Because of these disadvantages, pneumatic actuators are not commonly used in precision motion control applications [102].

Chapter 7 proposed one type of a modified Smith predictor, which can apply integrative system. The proposed method achieves maximum tracking error 135 μm and standard deviation of the tracking error 19.5 μm (see Fig. 7.12 and Tab. 7.3). The results are considered as very accurate because literature [113] states that the positioning accuracy of pneumatic actuated systems is $100 - 500$ μm at best. This method can be applied not only pneumatic actuator only but also system with bilateral teleoperation and chemical plants and so on.

Chapter 8 proposed a wave equation-based model, which can fit the position-dependent pressure resonances based on delay elements, taking into account the damping. Wave equation model is composed of delay elements (internal delay) and a first-order filter. Using this model, a wave cancellation filter is proposed for canceling all the resonances and anti-resonances. This filter comprises delay elements and a first-order filter. Note that, commonly, wave equation model and controller ignores the damping terms. The damping considerations for the controller is important for a stability analysis in frequency domain. The proposed method can model the damping of the resonances and anti-resonances separately. The experimental results indicate that -19 dB, -23 dB, and -16 dB gain attenuations are achieved for the first, second, and third modes, respectively (see Fig. 8.14(d)).

As a conclusion, this dissertation succeeded to present strategies to control the nonminimum phase systems, which are difficult to control. The use of expensive and heavy linear motors has become a bottleneck for the control of the large-scale positioning stage. However, the use of inexpensive pneumatic actuator was conventionally avoided because of its input delays and internal delays. The internal delay caused by wave equation brings position dependent resonances. By applying proposed

method, it becomes easier to control the large-scale positioning stage by the pneumatic actuator. Generally, the mechanical structure is rigorously designed so as not to have unstable zeros and delays to the extent possible. When unstable zeros were inevitable, perfect tracking was abandoned because of the approximated inverse system. The effectivenesses of all the proposed methods are demonstrated by simulations and experiments dealing with high-precision positioning stages with nonminimum phase characteristics. This thesis concludes that, with the proposed methods, the constraints on the design of the mechanical structure are relaxed in the applications and new options are presented.

Appendix A

Derivation of model (2.39)

This appendix formulates a model for a high-precision positioning stage shown in Figs. 2.5 and A.1. This stage consists of a coarse stage with a long stroke and a fine stage with a short stroke. This is a typical design for high-precision mechatronics such as scanning states [1, 156] and HDDs [157, 158].

A.1 Structure of the stage

To achieve high control performance, a contactless fine stage is desirable because this structure can remarkably reduce friction. This structure, however, needs gravity compensation. For this purpose, air bearing systems or magnetic levitation systems are often used [159] [160]. Although magnetic levitation systems have advantages of vacuum compatibility, they also have a disadvantage of generating heat and difficulty of controlling stages compared to air bearing systems. The heat generated by coils could change characteristics of actuators and sensors, and lead to degrade positioning resolution [82]. On the other hand, due to simple structure, air bearing systems are lightweight and cost-effective compared to magnetic levitation systems. Because of these reasons, this stage has a 6-DOF air bearing called gravity canceller [78]. The picture and schematic of the gravity canceller are shown in Fig. A.3. The gravity canceller compensates for the gravitational force experienced by the fine stage and supports its 6-DOF without friction. The gravity canceller is composed of three parts: the air gyro, the planar air bearing and the air bearing actuator that supports the $(\theta_x, \theta_y, \theta_z)$, (x, y) and (z)-directional motion, respectively. As shown in Fig. A.3, the air gyro is shaped like a hemisphere. The fine stage slides on the hemispheric surface of the air gyro with an air gap of a few micrometers. In this thesis, the center of the hemisphere is called the CoR. In other words, the radius of the curvature of the air gyro determines the height of the CoR.

A drawback of this structure is a kinetically fixed CoR. The CoG, CoR, the actuation point, and the measurement point are not always at the same points. This causes the coupling between the

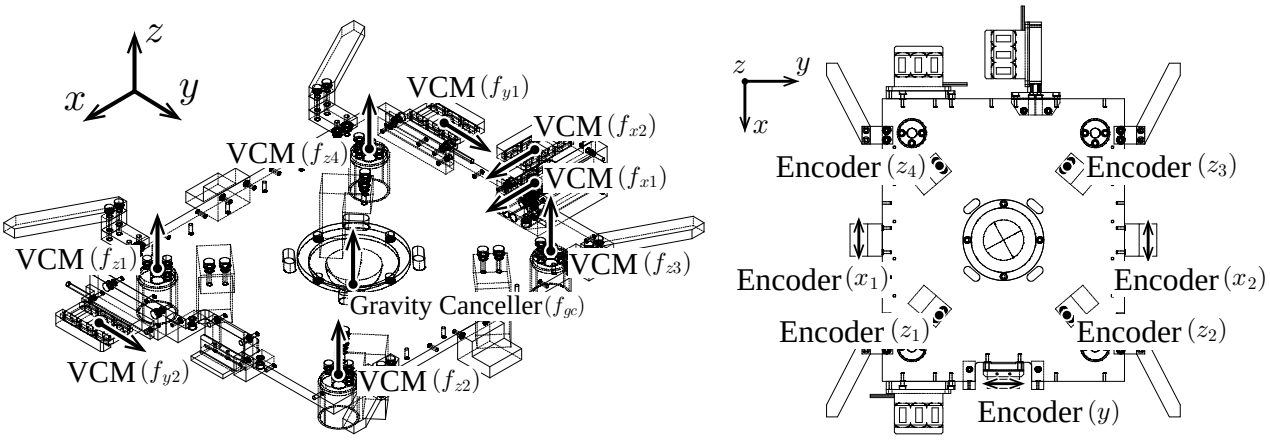

(a) Actuator arrangement of the fine stage. (b) Sensor arrangement of the fine stage.

Figure A.1 Structure of the fine stage.

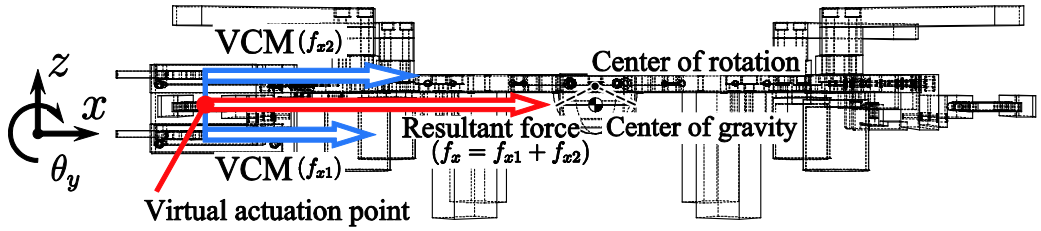

Figure A.2 Side view of the fine stage. By changing the thrust distribution ratio, the height of the virtual actuation point can be determined arbitrarily.

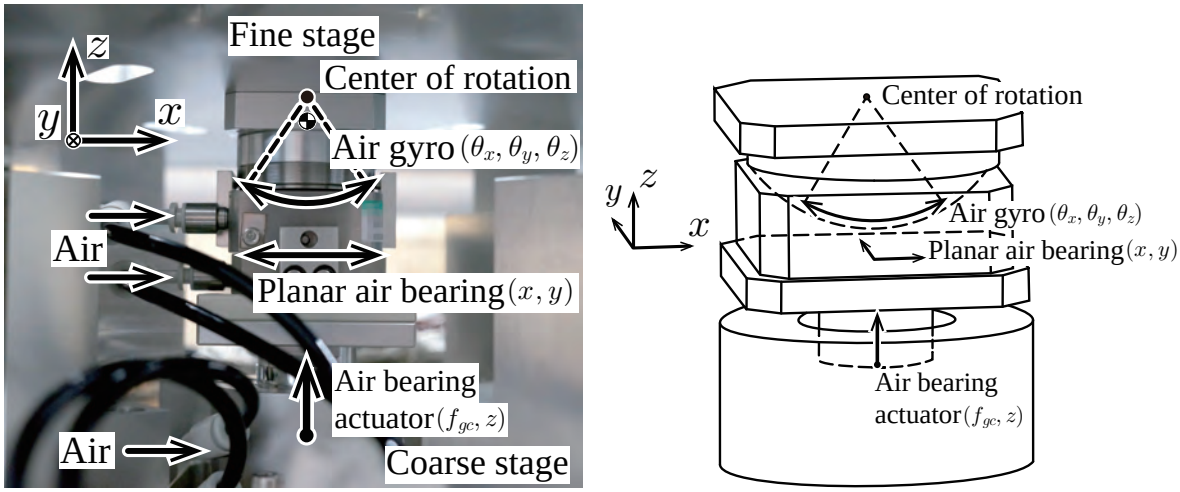

(a) Actuator arrangement of the fine stage. (b) Sensor arrangement of the fine stage.

Figure A.3 Structure of the fine stage.

translational motion and rotational motion (i.e. x and θ_y). We have investigated this phenomena and proposes decoupling methods using multiple actuators [51, 79, 161].

The actuator and sensor arrangement of the fine stage is shown in Fig. A.1. As shown in Fig. A.2 and Fig. A.1(a), the fine stage has two voice coil motors (VCMs) in the x direction. By using thrust distribution, the height of the actuation point can be changed arbitrarily.

Table A.1 Model parameters.

Symbol	Meaning	Value
x_m	Measured position of the fine stage	–
x_{g1}	Position of the CoG of the planar air bearing and the air gyro	–
x_{g2}	Position of the CoG of the fine stage	–
θ_y	Measured attitude angle of the fine stage	–
f_x	Input force of the fine stage in the x direction	–
τ_y	Input torque of the fine stage in the θ_y direction	–
M_{x1}	Mass of the planar air bearing and the air gyro	0.077 kg
C_{x1}	Viscosity coefficient in the x_{g1} motion	430 N/(m/s)
K_{x1}	Spring coefficient in the x_{g1} motion	11000 N/m
M_{x2}	Mass of the fine stage	5.3 kg
$J_{\theta y}$	Moment of inertia of the fine stage	0.10 kgm^2
$C_{\theta y}$	Viscosity coefficient of the fine stage in the θ_y motion	1.6 Nm/(rad/s)
$K_{\theta y}$	Spring coefficient of the fine stage in the θ_y motion	1200 Nm/rad
L_m	Distance between the measurement point of x_m and the CoR	-0.028 m
L_{g2}	Distance between the CoR and the CoG of the fine stage	-0.051 m
L_{fx}	Distance between the CoR of the fine stage and the actuation point	changeable

A.2 Model derivation

A.2.1 Lagrange's equations

The definitions of symbols are shown in Tab. A.1. In this section, Lagrange's equations are formulated on the basis of the model shown in Fig. 2.6 and Tab. A.1. First, the relationship between x_{g1}, x_{g2}, and θ_y is expressed by

$$x_{g2} = x_{g1} + L_{g2}\sin(\theta_y), \tag{A.1}$$
$$\dot{x}_{g2} = \dot{x}_{g1} + L_{g2}\cos(\theta_y)\dot{\theta}_y. \tag{A.2}$$

The kinetic energy T, the potential energy U, the dissipation function B, and the work W are defined as follows:

$$T = \frac{1}{2}M_{x1}\dot{x}_{g1}^2 + \frac{1}{2}M_{x2}\dot{x}_{g2}^2 + \frac{1}{2}J_{\theta y}\dot{\theta}_y^2, \tag{A.3}$$
$$U = \frac{1}{2}K_{x1}x_{g1}^2 + \frac{1}{2}K_{\theta y}\theta_y^2 + L_{g2}M_{x2}g\cos(\theta_y), \tag{A.4}$$
$$B = \frac{1}{2}C_{x1}\dot{x}_{g1}^2 + \frac{1}{2}C_{\theta y}\dot{\theta}_y^2, \tag{A.5}$$
$$W = f_x\left[x_{g1} + L_{fx}\sin(\theta_y)\right] + \tau_y\theta_y. \tag{A.6}$$

According to (A.3) and (A.4), the Lagrangian $L = T - U$ is given by

$$L = \frac{1}{2}M_{x1}\dot{x}_{g1}^2 + \frac{1}{2}M_{x2}\left[\dot{x}_{g1} + L_{g2}\cos(\theta_y)\dot{\theta}_y\right]^2 + \frac{1}{2}J_{\theta y}\dot{\theta}_y^2 - \frac{1}{2}K_{x1}x_{g1}^2 - \frac{1}{2}K_{\theta y}\theta_y^2 - L_{g2}M_{x2}g\cos(\theta_y). \tag{A.7}$$

Lagrange's equations are given by

$$\frac{d}{dt}\left(\frac{\partial L}{\partial \dot{q}_i}\right) - \frac{\partial L}{\partial q_i} + \frac{\partial B}{\partial \dot{q}_i} = \frac{\partial W}{\partial q_i} \ (i = 1, 2), \tag{A.8}$$

where q_1 and q_2 denote the generalized coordinates, $q_1 = x_{g1}$ and $q_2 = \theta_y$, respectively. Finally, according to (A.1)–(A.8), the following equations (A.9) and (A.10) are obtained:

$$\ddot{x}_{g1}(M_{x1} + M_{x2}) + C_{x1}\dot{x}_{g1} + K_{x1}x_{g1} + M_{x2}L_{g2}\left[\cos(\theta_y)\ddot{\theta}_y - \sin(\theta_y)\dot{\theta}_y^2\right] = f_x, \tag{A.9}$$

$$M_{x2}L_{g2}\left[\ddot{x}_{g1}\cos(\theta_y) - g\sin(\theta_y) + L_{g2}\ddot{\theta}_y\cos^2(\theta_y) - L_{g2}\dot{\theta}_y^2\sin(\theta_y)\cos(\theta_y)\right] + J_{\theta y}\ddot{\theta}_y + C_{\theta y}\dot{\theta}_y + K_{\theta y}\theta_y = \tau_y + f_x L_{fx}\cos(\theta_y). \tag{A.10}$$

A.2.2 Linearization

Assuming $\cos(\theta_y) \simeq 1, \sin(\theta_y) \simeq \theta_y$, $\dot{\theta}_y^2 \simeq 0$, (A.9) and (A.10) are linearized as follows:

$$(M_{x1} + M_{x2})\ddot{x}_{g1} + C_{x1}\dot{x}_{g1} + K_{x1}x_{g1} + M_{x2}L_{g2}\ddot{\theta}_y = f_x, \tag{A.11}$$

$$(M_{x2}L_{g2}^2 + J_{\theta y})\ddot{\theta}_y + C_{\theta y}\dot{\theta}_y + K_{\theta y}\theta_y + M_{x2}L_{g2}(\ddot{x}_{g1} - g\theta_y) = \tau_y + f_x L_{fx}. \tag{A.12}$$

A.2.3 Transformation to measurable coordinate

The generalized coordinate x_{g1} cannot be measured. Thus, x_{g1} is converted to x_m by

$$\frac{x_m(s)}{f_x(s)} = \frac{x_{g1}(s)}{f_x(s)} + L_m\frac{\theta_y(s)}{f_x(s)}, \tag{A.13}$$

$$\frac{x_m(s)}{\tau_y(s)} = \frac{x_{g1}(s)}{\tau_y(s)} + L_m\frac{\theta_y(s)}{\tau_y(s)}. \tag{A.14}$$

A.2.4 Transfer functions

According to (A.11)–(A.14), transfer functions (A.15)–(A.19) are obtained.

$$\frac{x_m(s)}{f_x(s)}=\frac{[J_{\theta y}+L_{fx}L_mM_{x1}-(L_{fx}-L_{g2})(L_{g2}-L_m)M_{x2}]s^2+(C_{\theta y}+L_{fx}L_mC_{x1})s+K_{\theta y}+L_{fx}L_mK_{x1}-L_{g2}M_{x2}g}{D(s)} \tag{A.15}$$

$$\frac{\theta_y(s)}{f_x(s)}=\frac{[L_{fx}M_{x1}+(L_{fx}-L_{g2})M_{x2}]s^2+L_{fx}C_{x1}s+L_{fx}K_{x1}}{D(s)} \tag{A.16}$$

$$\frac{x_m(s)}{\tau_y(s)}=\frac{[L_mM_{x1}+(L_m-L_{g2})M_{x2}]s^2+L_mC_{x1}s+L_mK_{x1}}{D(s)} \tag{A.17}$$

$$\frac{\theta_y(s)}{\tau_y(s)}=\frac{(M_{x1}+M_{x2})s^2+C_{x1}s+K_{x1}}{D(s)} \tag{A.18}$$

$$\begin{aligned}D(s)=&[(M_{x1}+M_{x2})J_{\theta y}+M_{x1}M_{x2}L_{g2}^2]s^4+[(M_{x1}+M_{x2})C_{\theta y}+(J_{\theta y}+M_{x2}L_{g2}^2)C_{x1}]s^3+\\&[(J_{\theta y}+M_{x2}L_{g2}^2)K_{x1}+(M_{x1}+M_{x2})(K_{\theta y}-M_{x2}L_{g2}g)+C_{\theta y}C_{x1}]s^2+\\&[C_{\theta y}K_{x1}+C_{x1}(K_{\theta y}-L_{g2}M_{x2}g)]s+K_{x1}(K_{\theta y}-L_{g2}M_{x2}g)\end{aligned} \tag{A.19}$$

References

[1] Butler, H.: Position Control in Lithographic Equipment, *IEEE Control Systems Magazine*, Vol. 31, No. 5, pp. 28–47 (2011).

[2] Heertjes, M. F.: Variable Gains in Motion Control of Wafer Scanners, *IEEJ Journal of Industry Applications*, Vol. 5, No. 2, pp. 90–100 (2016).

[3] Oomen, T.: Advanced Motion Control for Next-Generation Precision Mechatronics: Challenges for Control, Identification, and Learning, in *SAMCON2017* (2017).

[4] 佐伯和明：制御屋と呼ばれたい, システム/制御/情報： システム制御情報学会誌, Vol. 52, No. 12, pp. 463–466 (2008).

[5] 八木澤悠太, 平田光男, 鈴木雅康, 圓山智史：FPD 露光装置の軸間干渉を考慮した制御系設計, in *MoViC2015*, No. 15, pp. 178–181 (2015).

[6] Atsumi, T., Nakamura, S., Odai, M., Naniwa, I. and Nosaki, S.: Experimental Evaluation of Triple-Stage-Actuator System with Thermal Actuator for Hard Disk Drives, *Journal of Advanced Mechanical Design, Systems, and Manufacturing*, Vol. 7, No. 4, pp. 722–735 (2013).

[7] Heertjes, M. and Leenknegt, G.: Switching control in blu-ray disk drives, *Mechatronics*, Vol. 20, No. 4, pp. 453–463 (2010).

[8] Ohashi, T., Yoshida, K., Ohishi, K. and Miyazaki, T.: Single-rate two-dimensional feedforward control system for optical disk systems in consideration of the phase delay, *Japanese Journal of Applied Physics*, Vol. 54, No. 9S (2015).

[9] Merry, R., Uyanik, M., Molengraft, van de R., Koops, R., Veghel, van M. and Steinbuch, M.: Identification, control and hysteresis compensation of A 3 DOF metrological AFM, *Asian Journal of Control*, Vol. 11, No. 2, pp. 130–143 (2009).

[10] Shiraishi, T. and Fujimoto, H.: High-speed atomic force microscope by surface topography observer, *Japanese Journal of Applied Physics*, Vol. 51, No. 2 PART 1 (2012).

[11] Bolder, J., Zundert, van J., Koekebakker, S. and Oomen, T.: Enhancing Flatbed Printer Accuracy and Throughput: Optimal Rational Feedforward Controller Tuning via Iterative Learning Control, *IEEE Transactions on Industrial Electronics*, Vol. 64, No. 5, pp. 4207–4216 (2017).

[12] Blanken, L., Boeren, F., Bruijnen, D. and Oomen, T.: Batch-to-Batch Rational Feedforward

Control : From Iterative Learning to Identification Approaches, With Application to a Wafer Stage, *IEEE/ASME Transactions on Mechatronics*, Vol. 22, No. 2, pp. 826–837 (2017).

[13] Fujimoto, H. and Takemura, T.: High-precision control of ball-screw-driven stage based on repetitive control using n-times learning filter, *IEEE Transactions on Industrial Electronics*, Vol. 61, No. 7, pp. 3694–3703 (2014).

[14] Zhu, H. and Fujimoto, H.: Mechanical Deformation Analysis and High-Precision Control for Ball-Screw-Driven Stages, *IEEE/ASME Transactions on Mechatronics*, Vol. 20, No. 2, pp. 956–966 (2015).

[15] Hirata, M. and Ueno, F.: Final-State Control Using a Time-Symmetric Polynomial Input, *IEEE Transactions on Control Systems Technology*, Vol. 20, No. 2, pp. 395–401 (2012).

[16] 姿勢制御研究委員会：人工衛星の力学と制御ハンドブック―基礎理論から応用技術まで―, 培風館 (2007).

[17] 安藤慎悟, 鹿山透：産業用ロボットマニピュレーション：アクチュエータ・制御編, 計測と制御, Vol. 56, No. 10, pp. 770–775 (2017).

[18] 竹内一生：包装機械と精密サーボ技術, 電気学会誌, Vol. 137, No. 1, pp. 27–30 (2017).

[19] 置田肇, 黒澤良一, 島田明, 新誠一, 津村幸治, 真鍋舜治, 山口高司, 渡邊亮, 平田光男：実用から見たモーションコントロールの本音と期待, 計測と制御, Vol. 39, No. 10, pp. 667–676 (2000).

[20] Yamaguchi, T., Hirata, M. and Pang, J. C. K.: *High-speed precision motion control* (2011).

[21] Mizoshita, Y., Hasegawa, S. and Takaishi, K.: Vibration minimized access control for disk drives, *IEEE Transactions on Magnetics*, Vol. 32, No. 3, pp. 1793–1798 (1996).

[22] Biagiotti, L. and Melchiorri, C.: *Trajectory Planning for Automatic Machines and Robots* (2008).

[23] Singer, N. C. and Seering, W. P.: Preshaping Command Inputs to Reduce System Vibration, *Journal of Dynamic Systems, Measurement, and Control*, Vol. 112, No. 1, pp. 76–82 (1990).

[24] Singh, T. and Singhose, W.: Input shaping/time delay control of maneuvering flexible structures, in *American Control Conference*, pp. 1717–1731 (2002).

[25] Boeren, F., Bruijnen, D., Dijk, van N. and Oomen, T.: Joint input shaping and feedforward for point-to-point motion: Automated tuning for an industrial nanopositioning system, *Mechatronics*, Vol. 24, No. 6, pp. 572–581 (2014).

[26] Gilbert, E. G. and Tan, K. T.: Linear systems with state and control constraints: The theory and application of maximal output admissible sets, *IEEE Transactions on Automatic Control*, Vol. 36, No. 9, pp. 1008–1020 (1991).

[27] Kolmanovsky, I., Garone, E. and Di Cairano, S.: Reference and command governors: A tutorial on their theory and automotive applications, in *American Control Conference*, pp. 226–241 (2014).

[28] Ohta, Y. and Masubuchi, I.: On the implementation of reference governor, in *40th Annual Conference of IEEE Industrial Electronics Society*, pp. 215–220 (2014).

[29] Yazaki, Y. and Fujimoto, H.: Sudden Disturbance Suppression Control Considering Constraints for High-Precision Stage Using Reference Governor, in *American Control Conference*, pp. 6195–6200 (2016).

[30] Butterworth, J. A., Pao, L. Y. and Abramovitch, D. Y.: Analysis and comparison of three discrete-time feedforward model-inverse control techniques for nonminimum-phase systems, *Mechatronics*, Vol. 22, No. 5, pp. 577–587 (2012).

[31] Totani, T. and Nishimura, H.: Final-state control using compensation input, *Transactions of the Society of Instrument and Control Engineers*, Vol. 30, No. C, pp. 253–260 (1994).

[32] Hirata, M. and Ueno, F.: Final-State Control Using Polynomial and Time-Series Data, *IEEE Transactions on Magnetics*, Vol. 47, No. 7, pp. 1944–1950 (2011).

[33] Hirata, M., Hasegawa, T. and Nonami, K.: Seek control of hard disk drives based on final-state control taking account of the frequency components and the magnitude of control input, in *7th International Workshop on Advanced Motion Control*, Vol. 47, pp. 40–45, IEEE (2011).

[34] Yazaki, Y., Fujimoto, H., Sakata, K., Hara, A. and Saiki, K.: Settling time shortening method using final state control for high-precision stage with decouplable structure of fine and coarse parts, in *40th Annual Conference of the IEEE Industrial Electronics Society*, pp. 2859–2865 (2014).

[35] Yazaki, Y. and Fujimoto, H.: Generation Method of Admissible Sets for Mode Switching Control Using Final-State Control with Thrust Limitation, in *IEEE International Conference on Mechatronics*, pp. 228–233 (2015).

[36] Doyle, J., Francis, B. and Tannenbaum, A.: *Feedback control: Theory and design* (1990).

[37] Goodwin, G. C., Graebe, S. F. and Salgado, M. E.: *Control System Design* (2000).

[38] Skogestad, S. and Postlethwaite, I.: *Multivariable feedback control: analysis and design*, Wiley (2005).

[39] Kobayashi, M., Nakagawa, S. and Nakamura, S.: A phase-stabilized servo controller for dual-stage actuators in hard disk drives, *IEEE Transactions on Magnetics*, Vol. 39, No. 2 I, pp. 844–850 (2003).

[40] 兼松正人, 藤本博志：HDD ベンチマーク問題における位相安定化補償器及びゲイン安定化補償器の GKYP 設計法, 電気学会論文誌 D 産業応用部門誌, Vol. 137, No. 4, pp. 342–349 (2017).

[41] Heertjes, M. F. and Nijmeijer, H.: Self-tuning of a switching controller for scanning motion systems, *Mechatronics*, Vol. 22, No. 3, pp. 310–319 (2012).

[42] Oomen, T., Herpen, van R., Quist, S., Wal, van de M., Bosgra, O. and Steinbuch, M.: Connecting

System Identification and Robust Control for Next-Generation Motion Control of a Wafer Stage, *IEEE Transactions on Control Systems Technology*, Vol. 22, No. 1, pp. 102–118 (2014).

[43] Sakata, K., Asaumi, H., Hirachi, K., Saiki, K. and Fujimoto, H.: Self Resonance Cancellation Techniques for a Two-Mass System and Its Application to a Large-Scale Stage, *IEEJ Journal of Industry Applications*, Vol. 3, No. 6, pp. 455–462 (2014).

[44] 山田翔太, 藤本博志, 堀洋一：高分解能エンコーダの適用による駆動側情報を用いない 2 慣性系の制振制御法, 電気学会論文誌D（産業応用部門誌）, Vol. 135, No. 3, pp. 212–219 (2015).

[45] 高橋正人, 涌井伸二, 牧野内進：アクチュエータの多点配置によるアクティブ除振装置の広帯域化, 日本機械学會論文集. C 編, Vol. 76, No. 763, pp. 550–556 (2010).

[46] Van Herpen, R., Oomen, T., Kikken, E., Van De Wal, M., Aangenent, W. and Steinbuch, M.: Exploiting additional actuators and sensors for nano-positioning robust motion control, *Mechatronics*, Vol. 24, No. 6, pp. 619–631 (2014).

[47] 大日方五郎：構造系と制御系の同時最適設計問題, 計測と制御, Vol. 36, No. 4, pp. 254–261 (1997).

[48] 原辰次, 山浦弘：磁気ヘッド位置決め機構系と制御系の統合化設計, 計測と制御, Vol. 41, No. 6, pp. 406–411 (2002).

[49] Atsumi, T., Arisaka, T., Shimizu, T. and Yamaguchi, T.: Vibration Servo Control Design for Mechanical Resonant Modes of a Hard-Disk-Drive Actuator, *JSME International Journal Series C*, Vol. 46, No. 3, pp. 819–827 (2003).

[50] Steinbuch, M.: Design and Control of High Tech Systems, in *IEEE International Conference on Mechatronics*, pp. 13–17 (2013).

[51] Ohnishi, W., Fujimoto, H., Sakata, K., Suzuki, K. and Saiki, K.: Integrated Design of Mechanism and Control for High-Precision Stages by the Interaction Index in the Direct Nyquist Array Method, in *American Control Conference*, pp. 2825–2830 (2015).

[52] Hoagg, J. and Bernstein, D.: Nonminimum-phase zeros - much to do about nothing - classical control - revisited part II, *IEEE Control Systems*, Vol. 27, No. 3, pp. 45–57 (2007).

[53] Fujimoto, H., Fukushima, K. and Nakagawa, S.: Vibration suppression short-span seeking of HDD with multirate feedforward control, in *American Control Conference*, pp. 582–587 (2006).

[54] Erickson, R. W. and Maksimovic, D.: *Fundamentals of Power Electronics*, Springer (2011).

[55] Åström, K., Hagander, P. and Sternby, J.: Zeros of sampled systems, *Automatica*, Vol. 20, No. 1, pp. 31–38 (1984).

[56] Dubeau, F. and Savoie, J.: On the roots of orthogonal polynomials and Euler-Frobenius polynomials, *Journal of Mathematical Analysis and Applications*, Vol. 196, No. 1, pp. 84–98 (1995).

[57] Weller, S. R., Moran, W., Ninness, B. and Pollington, A. D.: Sampling zeros and the Euler-Frobenius polynomials, *IEEE Transactions on Automatic Control*, Vol. 46, No. 2, pp. 340–343

(2001).

[58] Sogo, T.: Inversion of sampled-data system approximates the continuous-time counterpart in a noncausal framework, *Automatica*, Vol. 44, No. 3, pp. 823–829 (2008).

[59] Tomizuka, M.: Zero phase error tracking algorithm for digital control, *Journal of Dynamic Systems, Measurement, and Control*, Vol. 109, pp. 65–68 (1987).

[60] Oriolo, G., Luca, A. D. and Vendittelli, M.: WMR control via dynamic feedback linearization: design, implementation, and experimental validation, *IEEE Transactions on Control Systems Technology*, Vol. 10, No. 6, pp. 835–852 (2002).

[61] Stengel, R.: *Flight Dynamics*, Princeton University Press (2004).

[62] Hori-Fujimoto Lab, The University of Tokyo. http://hflab.k.u-tokyo.ac.jp/index.html.

[63] Qiu, L. and Davison, E. J.: Performance limitations of non-minimum phase systems in the servomechanism problem, *Automatica*, Vol. 29, No. 2, pp. 337–349 (1993).

[64] Freudenberg, J. S. and Looze, D. P.: Right Half Plane Poles and Zeros and Design Tradeoffs in Feedback Systems, *IEEE Transactions on Automatic Control*, Vol. 30, No. 6, pp. 555–565 (1985).

[65] 原辰次：制御系における零点 [VI] 制御系の特性と零点, 計測と制御, Vol. 29, No. 9, pp. 830–838 (1990).

[66] 松尾孝美：制御系における零点 [IV] 零点と応答波形, 計測と制御, Vol. 29, No. 6, pp. 543–550 (1990).

[67] 乗松立木, 伊藤正美：零非正則制御系について, 電氣學會雜誌, Vol. 81, No. 871, pp. 566–575 (1961).

[68] Mita, T. and Yoshida, H.: Undershooting phenomenon and its control in linear multivariable servomechanisms, *IEEE Transactions on Automatic Control*, Vol. 26, No. 2, pp. 402–407 (1981).

[69] Butterworth, J. A., Pao, L. Y. and Abramovitch, D. Y.: A discrete-time single-parameter combined feedforward/feedback adaptive-delay algorithm with applications to piezo-based raster tracking, *IEEE Transactions on Control Systems Technology*, Vol. 20, No. 2, pp. 416–423 (2012).

[70] Devasia, S., Chen, D. and Paden, B.: Nonlinear inversion-based output tracking, *IEEE Transactions on Automatic Control*, Vol. 41, No. 7, pp. 930–942 (1996).

[71] Hunt, L., Meyer, G. and Su, R.: Noncausal inverses for linear systems, *IEEE Transactions on Automatic Control*, Vol. 41, No. 4, pp. 608–611 (1996).

[72] Marconi, L., Marro, G. and Melchiorri, C.: A solution technique for almost perfect tracking of non-minimum-phase, discrete-time linear systems, *International Journal of Control*, Vol. 74, No. 5, pp. 496–506 (2001).

[73] Moore, K. L., Bhattacharyya, S. P. and Dahleh, M.: Capabilities and limitations of multirate control schemes, *Automatica*, Vol. 29, No. 4, pp. 941–951 (1993).

[74] Sogo, T. and Joo, M.: Design of Compensators to Relocate Sampling Zeros of Digital Control Systems for DC Motors, *SICE Journal of Control, Measurement, and System Integration*, Vol. 5, No. 5, pp. 283–289 (2012).

[75] Ozawa, S.: The Current Lithography Technologies of the LCD Exposure System, *IEICE Trans. C*, Vol. J84-C, No. 12, pp. 1227–1231 (2001).

[76] Yang, P., Alamo, B. and Andeen, G.: Control design for a 6 DOF e-beam lithography stage, in *American Control Conference*, Vol. 3, pp. 2255–2260 (2001).

[77] Sakata, K., Fujimoto, H., Hara, A. and Saiki, K.: Design fabrication of high-precision stage and ultrahigh-speed nanoscale positioning, in *American Control Conference*, pp. 2254–2259 (2009).

[78] Ohnishi, W., Fujimoto, H., Sakata, K., Suzuki, K. and Saiki, K.: Design and Control of 6-DOF High-Precision Scan Stage with Gravity Canceller, in *American Control Conference*, pp. 997–1002 (2014).

[79] Ohnishi, W., Fujimoto, H., Sakata, K., Suzuki, K. and Saiki, K.: Decoupling Control Method for High-Precision Stages using Multiple Actuators considering the Misalignment among the Actuation Point, Center of Gravity, and Center of Rotation, *IEEJ Journal of Industry Applications*, Vol. 5, No. 2, pp. 141–147 (2016).

[80] Binnard, M.: Planar motor with linear coil arrays, *United States Patent*, No. US6452292 (2002).

[81] Rovers, J. M. M., Jansen, J. W., Compter, J. C. and Lomonova, E. a.: Analysis method of the dynamic force and torque distribution in the magnet array of a commutated magnetically levitated planar actuator, *IEEE Transactions on Industrial Electronics*, Vol. 59, No. 5, pp. 2157–2166 (2012).

[82] Choi, Y. and Gweon, D.: A high-precision dual-servo stage using halbach linear active magnetic bearings, *IEEE/ASME Transactions on Mechatronics*, Vol. 16, No. 5, pp. 925–931 (2011).

[83] Hara, A., Saiki, K., Sakata, K. and Fujimoto, H.: Basic examination on simultaneous optimization of mechanism and control for high precision single axis stage and experimental verification, in *34th Annual Conference of IEEE Industrial Electronics*, pp. 2509–2514 (2008).

[84] Shiraishi, T. and Fujimoto, H.: Trajectory tracking control method based on zero-phase minimum-phase factorization for nonminimum-phase continuous-time system, in *International Workshop on Advanced Motion Control*, pp. 1–6 (2012).

[85] Saiki, K., Hara, A., Sakata, K. and Fujimoto, H.: A Study on High-Speed and High-Precision Tracking Control of Large-Scale Stage Using Perfect Tracking Control Method Based on Multirate Feedforward Control, *IEEE Transactions on Industrial Electronics*, Vol. 57, No. 4, pp. 1393–1400 (2010).

[86] Eaton, J. W. and Rawlings, J. B.: Model-Predictive Control of Chemical Processes, *Chemical*

Engineering Science, Vol. 47, No. 4, pp. 705–720 (1992).

[87] Normey-Rico, J. E. and Camacho, E. F.: *Control of Dead-time Processes* (2007).

[88] Natori, K. and Ohnishi, K.: A design method of communication disturbance observer for time-delay compensation, taking the dynamic property of network disturbance into account, *IEEE Transactions on Industrial Electronics*, Vol. 55, No. 5, pp. 2152–2168 (2008).

[89] Ohnishi, W., Fujimoto, H., Sakata, K., Hara, A. and Saiki, K.: Trajectory Tracking Control for Pneumatic Actuated Scan Stage with Time Delay Compensation, in *42nd Annual Conference of IEEE Industrial Electronics Society*, pp. 5125–5130 (2016).

[90] 安藤和昭：むだ時間の Padé 近似と連分数展開による実現法, 計測自動制御学会論文集, Vol. 21, No. 11, pp. 1171–1176 (1985).

[91] 大竹雅裕：対称性による収差低減が生きるキヤノンの液晶露光装置, *O plus E*, Vol. 32, No. 9, pp. 1049–1052 (2010).

[92] 高橋一雄：露光装置技術発展の系統化調査, 独立行政法人 国立科学博物館, 119–169 pp. (2006).

[93] 小澤眞二：液晶ディスプレイ用リソグラフィー技術の現状, 電子情報通信学会論文誌. C, エレクトロニクス, Vol. J84-C, No. 12, pp. 1227–1231 (2001).

[94] 坂田晃一：FPD 露光装置と精密サーボ技術, 電気学会誌, Vol. 137, No. 1, pp. 19–22 (2017).

[95] Tokuyama, K., Fujimoto, H., Yumiza, D. and Saiki, K.: Proposal of reducing impact force control system for scan stage with decouplable structure of coarse and fine parts, in *IEEE International Conference on Mechatronics*, pp. 810–815, IEEE (2013).

[96] Yazaki, Y., Fujimoto, H., Sakata, K., Hara, A. and Saiki, K.: Application of Mode Switching Control Using Initial State Variables in Constraint Final-State Control to High-Precision Dual Stage, in *American Control Conference*, pp. 4155–4161 (2015).

[97] Kagawa, T., Sakaki, K., Tokashiki, L. R. and Fujita, T.: Accurate Positioning of a Pneumatic Servo System With Air Bearings, in *Proceedings of the JFPS International Symposium on Fluid Power*, pp. 693–698 (2002).

[98] Ramírez, I.: Modeling and tracking control of a pneumatic servo positioning system, in *2nd International Congress of Engineering Mechatronics and Automation*, pp. 1–6 (2013).

[99] Nakamura, Y., Kawakami, H. and Wakui, S.: Suppression of Anti-Resonance and Resonance in Pneumatic System of Vibration Isolator Considering Time Delay, in *41st Annual Conference of the IEEE Industrial Electronics Society*, pp. 2509–2514 (2015).

[100] Rao, Z. and Bone, G. M.: Nonlinear modeling and control of servo pneumatic actuators, *IEEE Transactions on Control Systems Technology*, Vol. 16, No. 3, pp. 562–569 (2008).

[101] Valdiero, A. C., Ritter, C. S., Rios, C. F. and Rafikov, M.: Nonlinear mathematical modeling in pneumatic servo position applications, *Mathematical Problems in Engineering*, Vol. 2011, (2011).

[102] Poon, A., Mai, R., Choi, Y., Lee, S., Yang, P.-H., Keswani, G., Hara, A. and Sakata, K.: Pneumatic Actuator for Precision Motion Control Applications, in *The 10th JFPS International Symposium on Fluid Power* (2017).

[103] Fujimoto, H., Hori, Y. and Kawamura, A.: Perfect tracking control based on multirate feedforward control with generalized sampling periods, *IEEE Transactions on Industrial Electronics*, Vol. 48, No. 3, pp. 636–644 (2001).

[104] Fujimoto, H. and Yao, B.: Multirate adaptive robust control for discrete-time non-minimum phase systems and application to linear motors, *IEEE/ASME Transactions on Mechatronics*, Vol. 10, No. 4, pp. 371–377 (2005).

[105] Fujimoto, H.: Robust Repetitive Perfect Tracking Control of HDDs Based on Re-learning Scheme, *IEEJ Journal of Industry Applications*, Vol. 2, No. 1, pp. 40–47 (2013).

[106] Fujimoto, H., Sakata, K. and Saiki, K.: Application of Perfect Tracking Control to Large-Scale High-Precision Stage, in *5th IFAC Symposium on Mechatronic Systems*, pp. 188–193 (2010).

[107] Shiraishi, T. and Fujimoto, H.: Positioning control for Piezo scanner using multirate perfect inverse model based iterative learning control, in *IEEE/ASME International Conference on Advanced Intelligent Mechatronics*, pp. 993–998 (2010).

[108] Ogata, T., Nabata, Y., Ohishi, K., Miyazaki, T., Sazawa, M., Koide, D., Takano, Y. and Tokumaru, H.: Perfect tracking control system with prediction state observer for next-generation optical disks, *Japanese Journal of Applied Physics*, Vol. 50, No. 9S1 (2011).

[109] Shimada, A. and Takeda, T.: Implementation on Robot of Multirate Manipulators Feedforward with Elastic Control Joints, *Journal of the Robotics Society of Japan*, Vol. 26, No. 7, pp. 60–66 (2008).

[110] Chen, T. and Francis, B. A.: *Optimal Sampled-Data Control Systems*, Springer (1996).

[111] 藤本博志, 堀洋一, 河村篤男：マルチレートフィードフォワード制御を用いた完全追従制御法, 計測自動制御学会論文集, Vol. 36, No. 9, pp. 766–772 (2000).

[112] 中井孝洋, 藤本博志：完全追従制御に基づく繰り返し制御を用いた PM モータの高調波電流抑制法の提案, 平成 19 年電気学会半導体電力変換研究会, No. 4, pp. 37–42 (2007).

[113] 藤田壽憲：半導体産業に向けた空気圧サーボ制御による超精密位置決め技術, 計測と制御, Vol. 54, No. 9, pp. 633–638 (2015).

[114] Halevi, Y. and Peled, I.: Absolute vibration suppression (AVS) control - Modeling, implementation and robustness, *Shock and Vibration*, Vol. 17, No. 4-5, pp. 349–357 (2010).

[115] Saito, E. and Katsura, S.: Vibration control of resonant system by using reflected wave rejection with fractional order low-pass filter, in *IEEE International Conference on Mechatronics*, pp. 853–858 (2013).

[116] Dihovicni, D. and Nedic, N.: Simulation, animation and program support for a high performance pneumatic force actuator system, *Mathematical and Computer Modelling*, Vol. 48, pp. 761–768 (2008).

[117] Hagiwara, T.: Analytic study on the intrinsic zeros of sampled-data systems, *IEEE Transactions on Automatic Control*, Vol. 41, No. 2, pp. 261–263 (1996).

[118] Rigney, B., Pao, L. Y. and Lawrence, D.: Nonminimum phase dynamic inversion for settle time applications, *IEEE Transactions on Control Systems Technology*, Vol. 17, No. 5, pp. 989–1005 (2009).

[119] Wen, J. and Potsaid, B.: An experimental study of a high performance motion control system, in *American Control Conference*, Vol. 6, pp. 5158–5163 (2004).

[120] Chen, D. and Paden, B.: Stable inversion of nonlinear non-minimum phase systems, *International Journal of Control*, Vol. 64, No. 1, pp. 81–97 (1996).

[121] Zou, Q. and Devasia, S.: Preview-Based Stable-Inversion for Output Tracking of Linear Systems, *Journal of Dynamic Systems, Measurement, and Control*, Vol. 121, No. 4, pp. 625–630 (1999).

[122] Shiraishi, T. and Fujimoto, H.: A Reference Trajectory Generation for System with Unstable Zeros Considering Negative-time Domain Analysis, in *IEEJ International Workshop on Sensing, Actuation, and Motion Control* (2015).

[123] Zundert, van J. and Oomen, T.: Stable inversion of LPTV systems with application in position-dependent and non-equidistantly sampled systems, *International Journal of Control*, Vol. 0, No. 0, pp. 1–11 (2017).

[124] Blanken, L., Isil, G., Koekebakker, S. and Oomen, T.: Flexible ILC: towards a convex approach for non-causal rational basis functions, *IFAC-PapersOnLine*, Vol. 50, No. 1, pp. 12107–12112 (2017).

[125] Ohnishi, W., Beauduin, T. and Fujimoto, H.: Preactuated multirate feedforward for a high-precision stage with continuous time unstable zeros, in *The 20th World Congress of the International Federation of Automatic Control* (2017).

[126] Sogo, T.: On the equivalence between stable inversion for nonminimum phase systems and reciprocal transfer functions defined by the two-sided Laplace transform, *Automatica*, Vol. 46, No. 1, pp. 122–126 (2010).

[127] Pintelon, R., Guillaume, P., Rolain, Y., Schoukens, J. and Van Hamme, H.: Parametric identification of transfer functions in the frequency domain-a survey, *IEEE Transactions on Automatic Control*, Vol. 39, No. 11, pp. 2245–2260 (1994).

[128] Heertjes, M. and Bruijnen, D.: MIMO FIR Feedforward Design for Zero Error Tracking Control, in *American Control Conference*, pp. 2166–2171 (2014).

[129] Hagiwara, T., Yuasa, T. and Araki, M.: Stability of the limiting zeros of sampled-data systems with zero-and first-order holds, *International Journal of Control*, Vol. 58, No. 6, pp. 1325–1346 (1993).

[130] Gross, E. and Tomizuka, M.: Experimental flexible beam tip tracking control with a truncated series approximation to uncancelable inverse dynamics, *IEEE Transactions on Control Systems Technology*, Vol. 2, No. 4, pp. 382–391 (1994).

[131] Miu, D. K.: Poles and Zeros, in *Mechatronics*, pp. 114–156, Springer-Verlag, New York (1993).

[132] Wang, H., Kim, K. and Zou, Q.: B-spline-decomposition-based output tracking with preview for nonminimum-phase linear systems, *Automatica*, Vol. 49, No. 5, pp. 1295–1303 (2013).

[133] Van Loock, W., Pipeleers, G. and Swevers, J.: B-spline parameterized optimal motion trajectories for robotic systems with guaranteed constraint satisfaction, *Mechanical Sciences*, Vol. 6, No. 2, pp. 163–171 (2015).

[134] Benosman, M. and Le Vey, G.: Stable inversion of SISO nonminimum phase linear systems through output planning: An experimental application to the one-link flexible manipulator, *IEEE Transactions on Control Systems Technology*, Vol. 11, No. 4, pp. 588–597 (2003).

[135] Graichen, K. and Zeitz, M.: Feedforward Control Design for Finite-Time Transition Problems of Nonlinear Systems With Input and Output Constraints, *IEEE Transactions on Automatic Control*, Vol. 53, No. 5, pp. 1273–1278 (2007).

[136] De Caigny, J., Camino, J. F. and Swevers, J.: Interpolating model identification for SISO linear parameter-varying systems, *Mechanical Systems and Signal Processing*, Vol. 23, No. 8, pp. 2395–2417 (2009).

[137] Smith, O. J. M.: A Controller to Overcome Dead Time, *ISA Journal*, Vol. 6, No. 2, pp. 28–33 (1959).

[138] Watanabe, K. and Ito, M.: A process-model control for linear systems with delay, *IEEE Transactions on Automatic Control*, Vol. 26, No. 6, pp. 1261–1269 (1981).

[139] Åström, K., Hang, C. and Lim, B.: A new Smith predictor for controlling a process with an integrator and long dead-time, *IEEE Transactions on Automatic Control*, Vol. 39, No. 2, pp. 343–345 (1994).

[140] Morari, M. and Zafiriou, E.: *Robust Process Control*, Prentice Hall (1989).

[141] Rahmat, M., Sunar, N. H., Salim, S. N. S., Abidin, M. S. Z., Fauzi, a. a. M. and Ismail, Z. H.: Review on Modeling and Controller Design In Pneumatic Actuator Control System, *International Journal on Smart Sensing and Intelligent Systems*, Vol. 4, No. 4, pp. 630–661 (2011).

[142] Van Varseveld, R. B. and Bone, G. M.: Accurate position control of a pneumatic actuator using on/off solenoid valves, *IEEE/ASME Transactions on Mechatronics*, Vol. 2, No. 3, pp. 195–204

(1997).

[143] Chen, C. K. and Hwang, J.: Iterative learning control for position tracking of a pneumatic actuated X-Y table, *Control Engineering Practice*, Vol. 13, No. 12 SPEC. ISS., pp. 1455–1461 (2005).

[144] Tsai, Y. C. and Huang, A. C.: Multiple-surface sliding controller design for pneumatic servo systems, *Mechatronics*, Vol. 18, No. 9, pp. 506–512 (2008).

[145] Yang, P., Choi, Y., Chang, P., Sakata, K. and Lee, S.: Control system for controlling a fluid actuator (2017).

[146] Goto, T. and Yuasa, M.: Recent Control Technology for Semiconductor Exposure Appratus, *Journal of the Society of Instrument and Control Engineers*, Vol. 52, No. 5, pp. 425–429 (2013).

[147] Shibazaki, Y., Kohno, H. and Hamatani, M.: An innovative platform for high-throughput, high-accuracy lithography using a single wafer stage, in *Proc. SPIE 7274*, pp. 1–12 (2009).

[148] Richer, E. and Hurmuzlu, Y.: A High Performance Pneumatic Force Actuator System Part 1 - Nonlinear Mathematical Model, *ASME Journal of Dynamic Systems, Measurement, and Control*, Vol. 122, No. 3, pp. 416–425 (2001).

[149] Yang, B. and Mote, C. D.: On Time Delay in Noncolocated Control of Flexible Mechanical Systems, *Journal of Dynamic Systems, Measurement, and Control*, Vol. 114, No. 3, pp. 409–415 (1992).

[150] Alli, H. and Singh, T.: On the feedback control of the wave equation, *Journal of Sound and Vibration*, Vol. 234, No. 4, pp. 625–640 (2000).

[151] Saito, E. and Katsura, S.: Vibration suppression of resonant system by using wave compensator, in *37th Annual Conference on IEEE Industrial Electronics Society*, pp. 4250–4255 (2011).

[152] Saito, E. and Katsura, S.: Compensation of Integrated Resonant and Time Delay System by Using Wave Compensator, *Automatika*, Vol. 54, No. 1, pp. 28–38 (2013).

[153] Shapiro, A. H.: *The Dynamics and Thermodynamics of Compressible Fluid Flow*, John Wiley & Sons (1953).

[154] Goodman, R. B.: *A Primer on Pneumatic Valves and Controls*, Krieger Pub Co (1997).

[155] Matsuo, K.: *Compressible fluid dynamics: theory and analysis in internal flow*, Ohmsha (2013).

[156] Park, Y.: Precision motion control of a three degrees-of-freedom hybrid stage with dual actuators, *Control Theory & Applications, IET*, Vol. 2, No. 5, pp. 392–401 (2008).

[157] Mori, K. and Munemoto, T. ; Otsuki, H. ; Yamaguchi, Y. ; Akagi, K.: A dual-stage magnetic disk drive actuator using a piezoelectric device for a high track density, *Magnetics, IEEE Transactions on*, Vol. 27, No. 6, pp. 5298–5300 (1991).

[158] Semba, T., Hirano, T., Hong, J. and Fan, L.-S.: Dual-Stage Servo Controller for HDD Using

MEMS Microactuator, *Magnetics, IEEE Transactions on*, Vol. 35, No. 5, pp. 2271–2273 (1999).

[159] Peijnenburg, A., Vermeulen, J. and Eijk, van J.: Magnetic levitation systems compared to conventional bearing systems, *Microelectronic engineering*, Vol. 83, pp. 1372–1375 (2006).

[160] Gao, W., Dejima, S., Yanai, H. and Katakura, K.: A surface motor-driven planar motion stage integrated with an XYθZ surface encoder for precision positioning, *Precision Engineering*, Vol. 28, No. 3, pp. 329–337 (2004).

[161] Ohnishi, W., Fujimoto, H., Sakata, K., Suzuki, K. and Saiki, K.: Decoupling Control for High-Precision Stages by the Center of Rotation and Gravity Hybrid-Driven Method using Multiple Actuators, in *14th IEEE International Workshop on Advanced Motion Control* (2015).

Publications

Journal articles

1. Wataru Ohnishi, Hiroshi Fujimoto, Pai-Hsueh Yang, Ping-Wei Chang, Bausan Yuan, Koichi Sakata, Atsushi Hara: Acoustic Wave Equation Based Modeling and Collocated Side Vibration Cancellation for Pneumatic Cylinder, IEEJ Journal of Industry Applications, Vol.7, No. 2, 2018.
2. 大西亘, 藤本博志: 時間軸反転による状態変数軌道生成とマルチレートフィードフォワードを用いた完全追従制御法, 電気学会論文誌 D, Vol. 137, No. 6, 2017. (Selected paper. IEEJ Journal of Industry Applications, Vol. 7, No. 1, pp.93–101 に英文翻訳版が掲載)
3. Wataru Ohnishi, Hiroshi Fujimoto, Koichi Sakata, Kazuhiro Suzuki, Kazuaki Saiki: Decoupling Control Method for High-Precision Stages using Multiple Actuators considering the Misalignment among the Actuation Point, Center of Gravity, and Center of Rotation, IEEJ Journal of Industry Applications, Vol.5, No.2, pp. 141-147, 2016.
4. 大西亘, 藤本博志, 堀洋一, 坂田晃一, 鈴木一弘, 佐伯和明: 超精密ステージにおけるオイラーの運動方程式と物体座標系の回転の非線形性と軸間干渉を補償した姿勢制御法, 電気学会論文誌 D, Vol. 134, No. 3, pp. 293-300, 2014.

Refereed Conference Publications

1. Masahiro Mae, Wataru Ohnishi, Hiroshi Fujimoto, Yoichi Hori: Perfect Tracking Control of Dual-Input Dual-Output System for High-Precision Stage in Translation and Pitching Motion, The 4th IEEJ international workshop on Sensing, Actuation, Motion Control, and Optimization, 2018/3/6-2018/3/8, Tokyo, Japan.
2. Yuma Yazaki, Takurou Nishimura, Wataru Ohnishi, Takehiro Imura, Hiroshi Fujimoto: Moving Coil Type Wireless Linear Motor based on Magnetic Resonance Coupling, 43rd Annual Conference of the IEEE Industrial Electronics Society, 2017/10/29-2017/11/1, Beijing, China.
3. Wataru Ohnishi, Thomas Beauduin, Hiroshi Fujimoto: Preactuated multirate feedforward for

a high-precision stage with continuous time unstable zeros, The 20th World Congress of the International Federation of Automatic Control, 2017/7/9-2017/7/14, Toulouse, France.

4. Wataru Ohnishi, Hiroshi Fujimoto, Pai-Hsueh Yang, Ping-Wei Chang, Bausan Yuan, Koichi Sakata, Atsushi Hara: Wave Equation Based Modeling and Vibration Cancellation for Pneumatic Cylinder, The 3rd IEEJ international workshop on Sensing, Actuation, Motion Control, and Optimization, 2017/3/6-2017/3/8, Nagaoka, Japan.
5. Wataru Ohnishi, Hiroshi Fujimoto: Tracking control method for plant with continuous time unstable zeros: Finite preactuation method based on state variable reference regeneration by redundant polynomial, 55th IEEE Conference on Decision and Control, 2016/12/12-12/14, Las Vegas, NV, USA.
6. Wataru Ohnishi, Hiroshi Fujimoto, Koichi Sakata, Atsushi Hara, Kazuaki Saiki: Trajectory Tracking Control for Pneumatic Actuated Scan Stage with Time Delay Compensation, 42nd Annual Conference of the IEEE Industrial Electronics Society, 2016/10/23-2016/10/27, Firenze, Italy.
7. Wataru Ohnishi, Hiroshi Fujimoto: Multirate Feedforward Control with State Variable Reference Generation based on Time Axis Reversal for Plant with Continuous Time Unstable Zeros, IEEE International Conference on Advanced Intelligent Mechatronics, 2016/7/12-2016/7/15, Banff, Alberta, Canada.
8. Wataru Ohnishi, Hiroshi Fujimoto, Koichi Sakata, Kazuhiro Suzuki, Kazuaki Saiki: Decoupling Control by the Center of Rotation and Gravity Hybrid-Driven Method for High-Precision Scan Stage with Multiple Actuators, The 14th International Workshop on Advanced Motion Control, 2016/4/22-2016/4/24, Auckland, New Zealand.
9. Wataru Ohnishi, Hiroshi Fujimoto, Koichi Sakata, Kazuhiro Suzuki, Kazuaki Saiki: Integrated Design of Mechanism and Control for High-Precision Stages by the Interaction Index in the Direct Nyquist Array Method, American Control Conference, 2015/7/1-2015/7/3, Chicago, America.
10. Wataru Ohnishi, Hiroshi Fujimoto, Koichi Sakata, Kazuhiro Suzuki, Kazuaki Saiki: Proposal of Decoupling Control Method for High-Precision Stages using Multiple Actuators considering the Misalignment among the Actuation Point, Center of Gravity, and Center of Rotation, The 1st IEEJ International Workshop on Sensing, Actuation, and Motion Control, 2015/3/9-2015/3/10, Nagoya, Japan.
11. Riccardo Antonello, Roberto Oboe, Stefano Bizzotto, Emanuele Siego, Yuma Yazaki, Wataru Ohnishi, Hiroshi Fujimoto: Feasible trajectory generation for a dual stage positioning system using a simplified model predictive control approach, IEEE International Conference

on Mechatronics, 2015/3/8-2015/3/8, Nagoya, Japan.

12. Wataru Ohnishi, Hiroshi Fujimoto, Koichi Sakata, Kazuhiro Suzuki, Kazuaki Saiki: Design and Control of 6-DOF High-Precision Scan Stage with Gravity Canceller, American Control Conference, 2014/6/4-2014/6/6, Portland, USA.
13. Binh Minh Nguyen, Kiyoto Ito, Wataru Ohnishi, Yafei Wang, Hiroshi Fujimoto, Yoichi Hori, Masaki Odai, Hironori Ogawa, Erii Takano, Tomohiro Inoue, and Masahiro Koyama: Dual Rate Kalman Filter Considering Delayed Measurement and Its Application in Visual Servo, The 13th International Workshop on Advanced Motion Control, 2014/3/14-2014/3/16, Yokohama, Japan.
14. Wataru Ohnishi, Hiroshi Fujimoto, Koichi Sakata, Kazuhiro Suzuki, Kazuaki Saiki: Proposal of Attitude Control for High-Precision Stage by Compensating Nonlinearity and Coupling of Euler's Equation and Rotational Kinematics, 39th Annual Conference of the IEEE Industrial Electronics Society, 2013/11/10-2013/11/13, Vienna, Austria.

Domestic conferences

1. 大西亘, 藤本博志: モード正準形を用いたマルチレートフィードフォワード制御法の基礎検討, 平成29 年メカトロニクス制御研究会/精密サーボシステムと制御技術, MEC-17-014, pp. 37–42, 2017.
2. 大西亘, 藤本博志: 連続時間不安定零点を持つ制御対象への軌道追従制御法—冗長次数多項式軌道による最適有限 Preactuation 法—, 平成 28 年メカトロニクス制御研究会/精密サーボシステムと制御技術, MEC-16-018, pp. 1–6, 2016.
3. 西村拓朗, 矢崎雄馬, 大西亘, 佐藤基, 居村岳広, 藤本博志, 堀洋一: 磁界共振結合を用いた Moving Coil 型ワイヤレスリニアモータの基礎検討, 平成 28 年メカトロニクス制御研究会/精密サーボシステムと制御技術, MEC-16-023, pp. 33–38, 2016.
4. 藤本博志, 大西亘: マルチレートフィードフォワードに基づく精密サーボのための軌道追従制御理論の新展開, 平成 28 年電気学会産業応用部門大会, 2-S3-4, pp. II-19-II24, 2016.
5. 大西亘, 藤本博志: 連続時間不安定零点を持つ制御対象への軌道追従制御法　—時間軸反転とマルチレートフィードフォワードによる安定逆系の設計—, 平成 27 年メカトロニクス制御研究会/モーションコントロール, MEC-15-047, pp. 109–114, 2015.
6. 大西亘, 藤本博志, 坂田晃一, 鈴木一弘, 佐伯和明: 複数アクチュエータの回転中心・重心点ハイブリッド駆動法による超精密ステージの非干渉化制御, 平成 27 年電気学会産業応用部門大会, Vol.2, pp. 217–220, 2015.
7. 大西亘, 藤本博志, 坂田晃一, 鈴木一弘, 佐伯和明: ナイキスト配列法における干渉指数を用いた超精密ステージの機構と制御の統合設計の提案, 平成 26 年メカトロニクス制御研究会「ナノスケールサーボのための制御技術」, MEC-14-148, pp. 1–6, 2014.

8. 大西亘, 藤本博志, 坂田晃一, 鈴木一弘, 佐伯和明: 超精密ステージにおける非線形性と軸間干渉を有する回転運動の干渉解析, 平成 25 年メカトロニクス制御研究会「ナノスケールサーボのための制御技術」, MEC-13-169, pp. 61–66, 2013.
9. 大西亘, 藤本博志, 堀洋一, 坂田晃一, 鈴木一弘, 佐伯和明: 超精密ステージにおけるオイラーの運動方程式の非線形性と軸間干渉を補償した姿勢制御の一提案, 平成 25 年産業計測制御/メカトロニクス制御合同研究会, IIC-13-101, MEC-13-101, pp. 67–72, 2013.

Review papers

1. Wataru Ohnishi, Hiroshi Fujimoto: Review on multirate feedforward: model-inverse feedforward control for nonminumum phase systems, The 4th IEEJ international workshop on Sensing, Actuation, Motion Control, and Optimization, 2018.
2. 藤本博志, 大西亘: 精密サーボ技術のための軌道追従制御理論, 電気学会誌, 電気学会, Vol. 137, No. 1, 2017.
3. 大西亘: 複数アクチュエータの回転中心・重心点ハイブリッド駆動法による超精密ステージの非干渉化制御, 精密サーボシステムを支える要素技術と制御応用, 電気学会, 2018. (出版予定)

Patent

1. 特願 2016-190382 : 移動体装置、露光装置、フラットパネルディスプレイの製造方法、およびデバイス製造方法

Awards

1. 大西亘, 部門優秀論文発表賞, 電気学会産業応用部門, 2018/3/31
2. 大西亘, 工学系研究科長賞（研究）, 東京大学大学院工学系研究科, 2018/3/22
3. 大西亘, 平成 29 年度優秀博士論文賞, 東京大学大学院工学系研究科電気系工学専攻, 2018/3/22
4. Wataru Ohnishi and Hiroshi Fujimoto, Outstanding paper award, SAMCON2018, 2018/3/7
5. 大西亘, メカトロニクス制御技術委員会優秀論文発表賞, 電気学会産業応用部門メカトロニクス制御技術委員会, 2018/1/9
6. Wataru Ohnishi, The best session presentation during the 42nd Annual Conference of the IEEE Industrial society, IEEE-IECON2016, 2016/10/27
7. 大西亘, 部門優秀論文発表賞, 電気学会産業応用部門, 2016/3/31
8. 大西亘, メカトロニクス制御技術委員会優秀論文発表賞, 電気学会産業応用部門メカトロニクス制御

技術委員会, 2016/1/8

9. 大西亘, 先端エネルギー工学優秀賞, 東京大学大学院新領域創成科学研究科先端エネルギー工学専攻, 2015/3/24
10. 大西亘, 新領域創成科学研究科長賞, 東京大学大学院新領域創成科学研究科, 2015/3/18
11. Wataru Ohnishi, Best presentation in session TT3-1: High Precision Control, The 1st IEEJ International Workshop on Sensing, Actuation, and Motion Control, 2015/3/9
12. 大西亘, メカトロニクス制御技術委員会優秀論文発表賞, 電気学会産業応用部門メカトロニクス制御技術委員会, 2015/1/7
13. 大西亘, 電気学会優秀論文発表賞 A, 電気学会, 2014/9/1
14. 大西亘, 平成 26 年度原島博学術奨励賞, 電気電子情報学術振興財団, 2014/5/28
15. 大西亘, 部門優秀論文発表賞, 電気学会産業応用部門, 2014/3/31
16. 大西亘, メカトロニクス制御技術委員会優秀論文発表賞, 電気学会産業応用部門メカトロニクス制御技術委員会, 2014/1/10
17. 大西亘, 電気学会東京支部電気学術奨励賞, 電気学会東京支部, 2013/3/31
18. 大西亘, 平成 24 年度学科長特別賞, 東京大学工学部電子情報工学科・電気電子工学科, 2013/3/26